Physical and Chemical Conditions in the Horsehead Photodissociation Region

Viviana Guzman Veloso

Thèse de Doctorat
de l'Université Pierre et Marie Curie

Spécialité
Astronomie & Astrophysique

Présentée par
Viviana Guzmán Veloso

Pour obtenir le grade de
Docteur de l'Université Pierre et Marie Curie

Sujet de la thèse :

Physical and Chemical Conditions in the Horsehead Photodissociation Region

soutenue publiquement le 26 Novembre 2013
devant le jury composé de :

M. Arnaud Belloche	Examinateur
Mme. Karine Demyk	Rapporteur
M. Jean-Hugues Fillion	Prèsident du jury
M. Guido Garay	Examinateur
Mme. Maryvonne Gerin	Directeur de thèse
M. Javier Goicoechea	Directeur de thèse
Mme. Karin Öberg	Rapporteur
M. Jèrome Pety	Directeur de thèse

Acknowledgments

First of all, I want to thank my three wonderful supervisors: Maryvonne, Jérôme and Javier. I have been very lucky to have all of you guiding me through this thesis. Thank you for teaching so much and for all the support you have given me during the past four years. I also want to thank you for making me feel I was a real collaborator and not just another student. Maryvonne, thank you for sharing your knowledge with me. Jérôme, thank you for your patience and for forcing me to learn french. My mom is especially thankful for that. Javier, thank you for always being there to answer all my questions.

I was lucky to have spend half of my time at ENS in Paris, and the second half at IRAM in Grenoble. I always felt very welcomed at both places. Special thanks to Marie-Francoise from ENS for all her help with the administration and her patience with my awful french during the first years. I also want to thank the awesome people I met at ENS: Massimo, Marc, Benjamin, Martin and Henrik. Thank you for all those coffees and beers in Paris. From IRAM, I would like to thank Brigitte for all her help with the paperwork (I would not have received my carte vitale without her). Also, thanks to Cathy and Beatrice for being so nice and helpful all the time. Special thanks to Pierre for always being willing to answer my questions. I really enjoyed working with you. I also want to thank Jan Martin and Arancha for all his help with observations from the PdBI.

I want to thank my family for all their support. To my mom and dad, for their constant encouragement to be better and for loving me no matter what. To my sister for always being there to help me when I need it. I am very grateful for the family I have. I love you all. I also want to thank Matias for his never ending support during these past four years. Thanks to all my other friends in Paris: Cinthya, Marta, Valeska and Celia; and in Grenoble: Daphnea, Nico, Susana, Anita, Nicole, Alexis and Stefano for making everything better. I would also like to thank Dennise, Myriam, Camille and Guillaume. I wish I have met you all sooner!

Finally, I thank the support from the Chilean Government through the Becas Chile scholarship program.

Abstract

Molecular lines are used to trace the structure of the interstellar medium and the physical conditions of the gas in different environments, from high-z galaxies to protoplanetary disks. To fully benefit from the diagnostic power of molecular lines, the formation and destruction paths of the molecules, including the interplay between gas-phase and grain surface chemistry, must be quantitatively understood. Well-defined sets of observations of simple template sources are key to benchmark the predictions of theoretical models.

With that motivation, this thesis is focused on the observation and analysis of an unbiased spectral line survey at 3, 2 and 1mm with the IRAM-30m telescope in the Horsehead nebula, with an unprecedented combination of bandwidth, high spectral resolution and sensitivity. Two positions were observed: the warm photodissociation region (PDR) and a cold condensation shielded from the UV field. Approximately 30 species, with up to 7 atoms plus their isotopologues, are detected. These data are complemented by high-angular resolution IRAM-PdB interferometric maps of specific species.

The results of this thesis include the detection of CF^+, a new diagnostic of the UV illuminated gas; the detection of a new species in the ISM, tentatively attributed to C_3H^+; a deep study of the abundance, spatial distribution and excitation conditions of H_2CO, CH_3OH and CH_3CN, which reveals that photo-desorption of ices is an efficient mechanism to release molecules into the gas phase; and the first detection of the complex organic molecules, HCOOH, CH_2CO, CH_3CHO and CH_3CCH in a PDR, which reveals the degree of chemical complexity reached in the UV illuminated neutral gas.

Résumé

Les raies moléculaires tracent la structure du milieu interstellaire ainsi que les conditions physiques du gaz dans différents environnements allant des galaxies à haut redshift aux disques protoplanétaires. Pour bénéficier des diagnostics moléculaires les voies de formation et de destruction des molécules doivent être comprises quantitativement, tout comme les couplages entre la chimie en phase gazeuse et solide. Des jeux bien compris de données concernant des sources simples sont essentiels pour tester les prédictions des modèles théoriques.

Cette thèse présente l'analyse d'un relevé spectral systématique à 1, 2 et 3mm avec le télescope IRAM-30m dans la Tête de Cheval, offrant une combinaison inédite de bande passante, haute résolution spectrale et sensibilité, en direction de deux positions: la région de photodissociation (PDR) et une cœure froid à proximité. Environ 30 espèces avec un maximum de 7 atomes sont détectées sans compter les isotopologues. Ces données sont complétées par des cartes interférométriques IRAM-PdBI à haute résolution d'espèces spécifiques.

Les résultats de cette thèse incluent la detection de CF^+, un nouveau diagnostic de gaz exposé à l'UV lointain; la détection d'une nouvelle molécule interstellaire, que nous attribuons au petit hydrocarbure C_3H^+; une étude approfondie des molécules organiques H_2CO, CH_3OH et CH_3CN, qui indique que la photodésorption des glaces est un mécanisme efficace pour relâcher ces molécules en phase gazeuse; et la première détection de molécules organiques complexes, comme HCOOH, CH_2CO, CH_3CHO et CH_3CCH dans une PDR, qui révèle la complexité chimique dans le gaz neutre éclairé en UV lointain.

Conditions physiques et chimiques dans la région de photo-dissociation de la Tête de Cheval

---

La Tête de Cheval: une référence observationnelle pour les modèles chimiques

Les raies moléculaires tracent permettent d'étudier la structure du milieu interstellaire ainsi que les conditions physiques du gaz dans différentes environnements allant des galaxies à haut redshift aux disques proto-planétaires. Cependant, l'interprétation des observations moléculaires est difficile délicate dans la plupart des objets. En effet, il est difficile de séparer spatialement les différentes composantes des sources à cause de leur géométrie complexe et de leur petite taille angulaire empêchent souvent de résoudre les différentes composantes de gaz, et donc de déterminer quelle type de gaz est tracée par chaque quelle molécule. Dans cet objectif, et pour pleinement bénéficier de la capacité de diagnostiques des raies moléculaires, il faut progresser dans la compréhension des chemins de formations et de destruction des molécules. Cette tâche requiert une collaboration étroite entre le dèveloppement de modèles théoriques, d'expériences de laboratoires et d'observations sur des cibles astrophysiques. L'obtention de jeux de données bien compris, et concernant des sources simples, est un point capital permettant de tester les prédictions des modèles théoriques dans des conditions les plus proches possibles des hypothèses de calcul. De ce point de vue, la nébuleuse de la Tête de Cheval est une excellente source de référence pour la physique du gaz moléculaire faiblement éclairé en UV lointain. En effet, cette source est proche (∼400 pc), elle a une géométrie simple (vue de profile) et le profil de densité est bien contraint. De plus, la Tête de Cheval est éclairée par un champ de rayonnement faible ($\chi \sim 60$ où χ représente le facteur multiplicatif appliqué à l'intensité du champ de rayonnement par rapport au champ de rayonnement interstellaire moyen au voisinage du soleil), ce qui rend cette source plus représentative de la grande majorité du gaz neutre de notre Galaxie que les autres régions de photo-dissociations (PDRs) largement étudiées dans notre Galaxie, comme la barre d'Orion et Mon R2 ($\chi \sim 10^4 - 10^5$). De plus, Les grains de poussière atteignent une température de l'ordre de $20 - 30$ K dans la Tête de Cheval, ce qui n'est pas assez chaud pour permettre l'évaporation thermique des glaces. La Tête de Cheval offre ainsi un environnement particulièrement propre pour isoler le rôle de la photo-désorption dans la chimie à la surface des grains.

Nous avons réalisé un relevé systématique de raies avec le télescope de 30m de l'IRAM pour faire de donner à la nébuleuse de la Tête de Cheval le rôle de une référence observationnelle pour les modèles chimiques. Deux positions ont été observées: la région de photodissociation (PDR) elle-même, correspondant au pic de l'emission du radical HCO, où le gas est tiède; et

le cœur dense, une condensation froide située à moins de 40″ du bord de la PDR et où HCO^+ est fortement deutéré. Le relevé couvre les bandes spectrales à 3, 2 et 1mm, qui sont idéales pour la détection des raies moléculaires provenant des niveaux rotationnels proches de l' état fondamental. Ce relevé est le tout premier qui soit réalisé avec une telle combinaison de bande passante, haute résolution angulaire et haute sensibilité. Il permet une comparaison détaillée de la chimie du gaz moléculaire dense qu'il soit éclairé (PDR) ou protégé (cœur dense) du rayonnement UV lointain. Au niveau de sensibilité atteint par ce relevé (8.1, 18.5 and 8.3 mK), la densité de raies à 3mm est d'environ 5 et 4 raies par GHz dans la PDR et le cœur dense respectivement. A 2 et 1mm, la densité de raies est typiquement de 1 raie par GHz pour les deux positions. Nous estimons la contribution des raies moléculaires au flux total du continuum à 1.2 mm à 14% pour la PDR et 16% pour le cœur dense. Environ 30 espèces chimiques (isotopologues exclus) sont détectées dans la PDR et/ou le cœur dense. Ces espèces contiennent jusqu'à 7 atomes.

Cette thèse présente les observations et l'analyse de relevé de raies "Horsehead WHISPER" (pour Wideband High-resolution Iram-30m Survey at two Positions with Emir Receivers), auxquelles s'ajoutent des cartes à hautes résolution obtenues à l'interféromètre du Plateau de Bure pour certaines molécules. Les résultats scientifiques de ce relevé incluent la détection de CF^+ (ion fluorométhylidynium), un nouveau diagnostique c de gas éclairé en UV lointain; la détection d'une nouvelle espèce du milieu interstellaire, que nous attribuons au petites hydrocarbures C_3H^+ (ion propynylidynium); la détection de molécules organiques complexes telles que H_2CO (formaldéhyde), CH_3OH (méthanol) et CH_3CN (acétonitrile), qui indiquent que la photo-désorption des glaces est une mécanisme efficace pour relacher ces molécules en phase gazeuse; et enfin la première détection de molécules organiques encore plus complexes, comme HCOOH (acide formique), CH_2CO (cétène), CH_3CHO (acétaldéhyde) et CH_3CCH (propyne) dans une PDR.

CF^+: un traceur de C^+ et une mesure de l'abondance du fluor

L'ion CF^+, détecté uniquement dans la barre d'Orion jusque là, a été observé sur le bord éclairé de la nébuleuse de la Tête de Cheval. Cet ion, qui est formé par la réaction de HF et C^+, est le deuxième réservoir le plus important de fluor après HF, là où C^+ est abondant. Les modèles théoriques prédisent qu'il y a un recouvrement important des régions d'emission de CF^+ et de C^+ au bord des nuages moléculaires. Comme CF^+ est facilement observable depuis le sol, contrairement à C^+, nous proposons de l'utiliser comme un traceur de l'ion C^+. CF^+ pourrait être un outil puissant car la raie de structure fine [C II] à 157.8 μm est le mécanisme principal de refroidissemnet du gas diffus. Or, le refroidissement du gaz est un éément crucial de la formation des étoiles, car c'est lui qui permet la condensation du gaz. Par ailleurs, la simplicité de la chimie du fluor implique que la densité de colonne de CF^+ est proportionnelle à la densité de colonne de HF. Si on suppose de plus que tout le fluor est sous forme moléculaire dans les nuages interstellaires, l'abondance du fluor peut être directement déduite des observations de CF^+. Finalement, nous avons pu résoudre spectralement les composantes hyperfines de CF^+ $J = 1 - 0$ car la Tête de Cheval présente des raies beaucoup plus étroites que d'autres PDRs comme la barre d'Orion. Nous avons comparé les fréquences mesurées avec des fréquences théoriques, obtenues à l'aide de calculs ab initio de la constante

de couplage spin-rotation de CF^+, calculs réalisés à l'occasion de ces observations. La Tête de Cheval est donc un bon laboratoire pour réaliser des études spectroscopiques précises d'espèces présentes dans du gaz éclairé en UV lointain.

Détection d'une nouvelle espèce dans l'espace et attribution potentielle à l-C_3H^+

Grâce à la sensibilité des observations et à la grande couverture spectrale du relevé de raies Horsehead WHISPER, un ensemble de 8 raies ont a été détecté dans la direction de la PDR, sans contrepartie dans les catalogues spectroscopiques publics. Les fréquences des raies observées peuvent être bien ajustées avec un modèle de rotateur linéaire, ce qui implique un état électronique fondamental $^1\Sigma$. La valeur de la constante rotationnelle déduite des mesures est proche de celle de C_3H. Nous attribuons donc les raies détectées au petit hydrocarbure C_3H^+.

Bien qu'il n'ait jamais été détecté auparavant, C_3H^+ est souvent inclus dans les réseaux chimiques parce que les réactions ions-molécules faisant intervenir ce cation font partie des voies principales de formation des petits hydrocarbures en phase gaz (Turner et al. 2000; Wakelam et al. 2010), comme par exemple C_3H et C_3H_2. Les radicaux C_3H et C_3H_2, qui sont détectés dans une grande variété de sources allant des nuages diffus aux nuages sombres, atteignent dans les PDRs une abondance 10 fois plus grande que ce que prédisent les modèles actuels en phase gazeuse. Un mécanisme de formation supplémentaire est donc nécessaire. Une possibilité pour expliquer les abondances anormalement élevées des hydrocarbures dans les PDRs est l'existence d'une chimie "destructive", opérant en plus de la chimie "constructive" habituellement invoquée. Dans ce scénario, les hydrocarbures aromatiques polycycliques (PAHs) se fragmentent en petits hydrocarbures en présence d'un champ de rayonnement dans l'UV lointain (e.g., Fuente et al. 2003; Teyssier et al. 2004; Pety et al. 2005). De la même manière, les PAHs seraient formées par photo-evaporation des trés petits grains (e.g., Berné et al. 2007; Pilleri et al. 2012). La découverte de C_3H^+, qui est une espèce intermédiaire clé dans le scénario de formation en phase gaseusze, apporte de nouvelles contraintes sur les mécanismes de formation des petits hydrocarbures. En effet, nous mesurons une abondance de C_3H^+ trop faible pour expliquer l'abondance des autres petits hydrocarbures s'ils étaient formés uniquement en phase gazeuse. C'est ainsi le premier exemple clair de formation de petites molécules à partir de plus grandes.

L'attribution des raies inconnues à l'ion l-C_3H^+ a été remise en question par Huang et al. (2013), en raison de la différence entre les valeurs des constantes spectroscopiques de C_3H^+ obtenues par leurs calculs théoriques et celles déduites de nos observations. Fortenberry et al. (2013)ont proposé l'anion C_3H^- comme un autre candidat potentiel. Cette suggestion soulève plusieurs objections. Si l'espèce inconnue était cet anion, ce serait le premier anion détecté dans la Tête de Cheval, qui plus est avec un rapport C_3H^-/C_3H^+ de 57%, c'est-à-dire le plus grand rapport anion/neutre mesuré jusqu'ici dans le milieu interstellaire. Les mêmes raies ont aussi été détectées dans plusieurs autres sources, comme la barre d'Orion (Cuadrado et al. in prep) et Srg B2 (McGuire et al. 2013), ce qui confirme la présence généralisée de ce porteur dans le milieu interstellaire. Par contre, ces raies n'ont pas été détectées dans le nuage sombre TMC-1, où tous les autres anions ont été détectés. Les observations favorisent

donc l'attribution des raies inconnues au cation, l-C_3H^+. Une mesure directe en laboratoire est néanmoins nécessaire pour prouver de manière définitive cette attribution et clore ainsi la controverse créée par les observations de la Tête de Cheval.

Photo-désorption des manteaux de glace autour des grains de poussière : H_2CO et CH_3OH

Les molécules organiques relativement simples, telles que H_2CO et CH_3OH, sont des espèces chimiques clés pour la synthèse de molécules plus complexes dans le milieu interstellaire, espèces qui pourraient finalement ensemencer les disques proto-planétaires et donc les nouveaux systèmes planétaires. Ces molècules organiques sont aussi utilisées pour mesurer la température et la densité du gaz dans de nombreuses sources astrophysiques. Comprendre leur mécanisme de formation est donc important. Le formaldéhyde et le méthanol ont tous les deux été detectés dans une grande variété d'environnements interstellaires tels que les nuages sombres, les cœurs proto-stellaires et les comêtes, avec des abondances élevées ($10^{-6} - 10^{-9}$ par rapport au nombre total de protons). Contrairement à H_2CO, qui peut être formé tout aussi efficacement en phase gazeuse que sur la surface des grains, on pense que CH_3OH est formé principalement sur les glaces, par addition successive d'atomes d'hydrogènes sur les molécules de CO absorbées sur la surface.

Nous avons observés les raies millimétriques de H_2CO et CH_3OH vers la PDR et le cœur de la Tête de Cheval. Nous avons comparé les abondances mesurées à partir des observations avec soit un modèle de PDR en phase gaz, soit un modèle incluant à la fois la chimie en phase gazeuse et la chimie à la surface des grains. Les observations indiquent que H_2CO et CH_3OH sont principalement formés à la surface des grains de poussière dans la direction de la PDR. Il s'agit probablement de l'hydrogénation successive des glaces de CO, puis de leur photo-désorption en phase gazeuse. Dans la direction du cœur dense, les observations suggèrent que H_2CO est formé principalement en phase gazeuse, alors que le méthanol reste formé à la surface des grains avant sa photo-désorption. Suggérée par les modèles, la variation du chemin principal de formation de H_2CO dans la PDR et le coeur dense est corroborée par les valeurs différentes des rapports des symétries de spin ortho et para de H_2CO, que l'on obtient à partir des observations (3 dans le coeur dense et 2 dans la PDR).

En plus des raies détectées dans le relevé, nous avons obtenues des cartes à haute résolution angulaires de H_2CO et de CH_3OH à l'aide de l'interféromètre du Plateau de Bure. La carte d'émission de H_2CO présente un pic dans la direction du cœur dense, là où CH_3OH présente un déficit d'émission. Ces observations suggèrent donc que CH_3OH est déplété dans le cœur dense. Ainsi, le CH_3OH en phase gazeuse proviendrait de l'enveloppe autour du coeur dense, alors que H_2CO serait présent à la fois dans l'enveloppe et dans le cœur dense lui-même. En effet, nous nous attendons à ce que la photo-désorption soit plus efficace dans la PDR que dans le cœur dense protégé des photons UV lointains. Nous concluons donc que la photo-désorption des glaces est un mécanisme efficace pour augmenter l'abondance en phase gazeuse de molécules dans les régions éclairées en UV lointain.

Quelques espèces azotées: CH_3CN, CH_3NC, et HC_3N

Les molécules CH_3CN et HC_3N sont facilement détectées dans les régions de formation d'étoiles (massives). En particulier, CH_3CN est un bon traceur des conditions physiques dans les régions tièdes et denses. Nous avons detecté plusieurs raies de CH_3CN et HC_3N dans la PDR et le cœur dense de la Tête de Cheval. Les molécules CH_3NC et C_3N ont aussi été détectées dans la PDR. Les chimies de HC_3N et CH_3CN sont assez différentes. En effet, nous trouvons que CH_3CN est 30 fois plus abondant dans le gaz éclairé en UV lointain que dans le gaz sombre du cœur, alors que l'abondance de HC_3N est similaire dans les deux positions. La forte abondance de CH_3CN mesurée dans la PDR est a priori surprenante parce que cette molécule complexe devrait être facilement dissociée dans les régions éclairées en UV lointain. En particulier, les modèles basés sur une chimie purement en hase gazeuse ne peuvent pas reproduire les abondances observées dans la PDR. Nous avons montré que la photo-désorption est un mécanisme efficace pour augmenter l'abondance en phase gazeuse de H_2CO et CH_3OH dans la PDR. Mais CH_3CN présente un cas encore plus extrême puisque qu'il est 30 fois plus abondant dans la PDR que dans le cœur dense, alors que H_2CO présente seulement des abondances similaires dans les deux régions. Il n'y a pas de chemin efficace de formation de CH_3CN en phase gazeuse aux faibles températures trouvées dans la Tête de Cheval. L'explication la plus probable est la production de CH_3CN à la surface des glaces à partir d'autres espèces azotées, les produits ètant ensuite photo-désorbés en phase gazeuse. La détection de CH_3NC dans la PDR, avec un rapport entre isoméres CH_3NC/CH_3CN de 0.15, suggère que CH_3NC pourrait aussi être formé à la surface des grains par isomérisation sous éclairement UV des glaces de CH_3CN.

Des molécules complexes dans les PDRs

Les molécules organiques complexes sont facilement détectées dans les régions de formation d'étoiles massives. Elles ont donc jusqu'à présent été considérées comme des traceurs de cœurs chauds. Cependant, les molécules complexes HCOOH, CH_2CO, CH_3CHO, et CH_3CCH ont été détectées dans la PDR et dans le cœur dense de la Tête de Cheval avec des abondances relatives à H_2 qui sont comparables à celles déterminées dans les cœurs chauds. Le mécanisme principal de formation de ces molécules est mal compris, bien qu'il existe un consensus autour d'une formation à la surface des grains de poussières. Au contraire de CH_3CCH, qui présente des abundances similaires dans la PDR et le coeur dense, les abondances de HCOOH, CH_2CO, et CH_3CHO sont typiquement 3.4 fois plus élevées dans la PDR que dans le coeur dense. Cela suggère que leur formation est facilitée par la présence de photons UV lointains. C'est peut-être le signe d'une photo-désorption plus efficace dans la PDR, le champ UV étant plus intense que dans le cœur dense. Mais cela peut aussi indiquer que la formation sur les grains est plus efficace dans la PDR, la mobilité des atomes et molécules sur les glaces étant accrue. Les mécanismes de formation en phase gazeuse ne peuvent pas être exclus; il est nécessaire de poursuivre les 'etudes sur la formation des molécules complexes à partir de précuseurs gazeux.

La détection de ces molécules complexes dans d'autres sources que les cœurs chauds, par exemple dans les cœurs pré-stellaires (Bacmann et al. 2012) et maintenant dans une PDR,

suggère qu'elles peuvent se former aussi bien dans le gaz froid que dans le gaz tiède éclairé en UV lointain. Nous montrons ici que ces molécules complexes peuvent survivre en présence d'éclairement UV lointain, et même que cet éclairement augmente leur abondance en phase gazeuse. Il sera donc peut-être possible de détecter ces molécules complexes dans d'autres régions éclairées en UV lointain, tels que les disques proto-planétaires.

Diagnostics chimiques

En comparant les abondances des différentes espèces chimiques dans la Tête de Cheval avec celles mesurées dans d'autres environnements, nous avons élaboré des diagnostics chimiques qui peuvent être utilisés pour déterminer les processus dominants à partir d'observations de raies moléculaires. Les rapports d'abondance suivants, $HCO/H^{13}CO^+$, $CO^+/H^{13}CO^+$, HCO^+/HOC^+ et CN/HCN, sont de bons traceurs de l'effet de l'éclairement par l'UV lointain. Le champ de rayonnement incident et la densité du gaz présent dans les PDRs peuvent ainsi être contraints par la comparaison de ces rapports d'abondance avec ceux de sources de référence. Par exemple, les rapports $HCO/H^{13}CO^+$, C_3H_2/HCO^+ et HCN/HCO^+ sont de bons traceurs de χ/n, tandis que le rapport CN/HCO^+ est un bon indicateur de la densité. Nous proposons aussi un nouvel estimateur, créé à partir de rapports d'abondance, pour classer les types de sources. Nous concluons que les caractéristiques chimiques de la PDR de la Tête de Cheval sont proches de celles du gaz diffus, et dans une moindre mesure, de celles de la galaxie à flambée de formation d'étoiles M82, tandis que les cœurs et corinos chauds ont les caractéristiques chimiques les plus éloignées de la PDR de la Tête de Cheval. En outre, la comparaisons suggère que M82 ressemble plus aux PDRs à fort èclairement UV, comme la barre d'Orion ou Mon R2, qu'à la Tête de Cheval. Les rapports d'abondances étudiés dans cette thèse utilisent des espèces aisément observables avec les instruments actuels. Ils peuvent donc être utilisés facilement pour obtenir un indicateur qualitatif du rôle des UV lointains dans différentes sources.

De l'impact des progrès instrumentaux en radioastronomie sur l'astrochimie

Avec les progrès récents en radioastronomie, l'astrochimie vit en ce moment un âge d'or. Le télescope spatial Herschel a engrangé des observations de molécules plus ou moins complexes et de la poussière en direction d'une grande variété d'environnements, comme le milieu diffus, les PDRs, les régions de formation d'étoiles, les disques proto-planétaires et les galaxies à haut-redshift, apportant de nombreux résultats nouveaux sur la chimie et la physique du milieu interstellaire. Par ailleurs, en plus des images détaillées du fond diffus cosmologique, le rayonnement cosmique fossile, le télescope spatial Planck a contribué à l'astrochimie par l'apport d'images à grande échelle de la composante froide du milieu interstellaire de notre Galaxie (poussières et raies du monoxyde de carbone). Enfin, les premières observations de l'interféromètre ALMA ont ''eté effectuées. Malgré le nombre limité d'antennes, des résultats majeurs en astrochimie ont été obtenus, portant sur la formation des étoiles et des planètes, et sur la physique des galaxies proches ou lointaines. Les futures observations de ALMA ne

manqueront pas d'apporter de nombreuses découvertes inattendues lorsque cet observatoire atteindra ses capacités nominales.

Il est prévu que les observations dans le domaine millimétrique (longueur d'onde comprise entre 1mm et 3mm) et dans des configurations *compactes* (c'est-à-dire ayant une ligne de base maximum inférieure à 1.6 km) représenteront au maximum 25% du temps alloué aux observations avec ALMA, soit environ un maximum de 3 mois par an pour cette catégorie de projet. L'objectif du projet NOEMA est de transformer l'interféromètre du plateau de Bure (PdBI) en un instrument complémentaire de ALMA en jouant simultanément sur les trois paramètres dimensionnant un interféromètre. Il s'agit premièrement de doubler le nombre d'antennes de 15 m (passage de 6 à 12, impliquant un doublement de la surface collectrice et une amélioration significative de la qualité d'imagerie par le quadruplement du nombre de lignes de base). Il s'agit ensuite d'utiliser une instrumentation innovante, en particulier une nouvelle génération de récepteurs opérant avec une bande passante totale quatre fois plus large (de 8 GHz à 32 GHz), ce qui permet un accroissement de la sensibilité en continuum par un facteur 4 et ouvre la possibilité d'observer simultanément un nombre 4 fois plus grand de raies spectrales. Ces récepteurs, qui sont les plus puissants en usage aujourd'hui, sont actuellement installés au télescope du 30m. Il s'agit enfin de doubler la plus grande ligne de base (de 800 à 1600 m) et donc de doubler la résolution angulaire actuelle ($0.2''$).

Grâce aux formidables capacités des instruments du télescope du 30m, il est possible aujourd'hui de faire des relevés complets de raies avec une sensibilité et et une résolution spectrale sans précédent dans un temps d'observation raisonnable. Le relevé de raie Horsehead WHISPER est le premier de cette catégorie, et plusieurs autres relevés sont soit en cours, ou déjà terminés. En outre, grâce à ces nouvelles capacités, chaque observation spectrale utilisant le télescope de 30m devient un mini relevé de raies. Cela fait faire un saut majeur à l'astrochimie, parce qu'il maintenant possible d'obtenir un inventaire chimique complet pour une grande variété d'environnements. Dans ce contexte, la comparaison de la chimie dans divers objets nous permettra de comprendre l'évolution chimique depuis les cœurs pré-stellaires jusqu'aux disques proto-planétaires. Dans un futur proche, chaque observation de NOEMA delivrera aussi un mini relevé de raie, mais à bien meilleure résolution angulaire, ce qui permettra de résoudre spatialement les différentes composantes du gaz. Les observations à haute résolution angulaire permettront aussi de réduire le niveau de confusion spectrale présent dans les observations actuelles de sources complexes, comme Sgr B2. Ces progrès permettront la découverte de nouvelles molécules dans le milieu instellaire, et peut-être de molécules pré-biotiques telles que la glycine, l'acide aminé le plus simple.

Au delà des relevés de raies, les nouvelles capacités des instruments de l'IRAM nous permettront d'étudier des échantillons complets de divers types de sources, et ainsi d'obtenir des statistiques sur les propriétés chmiques des différents environnements. De plus, les capacités d'imagerie des télescopes actuels et futurs nous permettront d'obtenir des informations sur la répartition spatiale de l'émission moléculaire pour de nombreuses raies simultanément. Par exemple, il est déjà possible avec le télescope de 30m de l'IRAM, d'observer simultanément plusieurs raies du méthanol et du formaldéhyde, ainsi que des raies de DCO^+, DCN and N_2H^+ dans une seule observation. Le gel de ces espèces à la surface des grains, et la formation de H_2CO et CH_3OH sur les grains peuvent ainsi être étudiés par l'intermédiaire de cartes de $200'' \times 200''$ en direction de 12 cœurs pré/proto-stellaires différents en seulement 45 heures

d'observation! Avec ALMA et NOEMA, des études similaires seront possibles sur un nombre réduit de sources mais à bien meilleure résolution angulaire. Une autre conséquence de ces nouvelles capacités est la grande quantité de données produites par chaque observation. La comparaison directe des spectres mesurés avec ceux sources simples à l'aide d'estimateurs statistiques, comme ceux discutés dans cette thèse, va devenir un outil incoutournable pour l'analyse de ces données.

Pour bénéficier au mieux de toutes les avancées dans les observations (sub)-millimétriques, de grands progrès doivent aussi être réalisés dans les outils de modélisation actuels. Cela inclut le besoin de constantes spectroscopiques, de taux d'excitation collisionnelle, de taux de photo-dissociation, et plus généralement des taux de formation et de destruction des espèces chimiques. Par ailleurs, la déduction d'abondances précises à partir des intensités de raies observées est encore un problème majeur aujourd'hui. Alors que les sources ayant une forte densité et une température importante, comme les cœurs chauds, peuvent être modélisées de manière fiable sous l'hypothèse de l'équilibre thermodynamique local (ETL), les sources ayant une plus faible densité, comme la Tête de Cheval, nécessitent une approche hors équilibre thermodynamique pour déduire les abondances. Pour ce faire, il est nécessaire de savoir comment les molécules sont excitées, et de connaître les taux d'excitation collisionnelle avec l'ensemble des partenaires de collision. Le couplage étroit entre les chimies en phases gazeuse et solide devient un autre domaine clé de l'astrochimie. Des progrès majeurs ont été réalisés ces dernières années grâce aux expériences de laboratoire. Cependant, de nombreux paramètres microphysiques liés aux processus à la surface des grains sont encore peu connus, bien qu'ils soient nécessaires pour obtenir une bonne comparaison entre les observations et les modèles théoriques.

Contents

List of Figures

List of Tables

Chapter 1

Introduction

1.1 The interstellar medium

When we look at the sky in the night, in a dark place like the Atacama desert in the north of Chile, we see a patch of light across the sky, arising from the hundreds of billions of stars contained in our Galaxy, the Milky Way. The medium between the stars is called the interstellar medium (ISM) and consists of gas and dust particles. The mass of the Galaxy is mainly in the form of dark matter, while baryons account for $\sim 10\%$ of the total mass. The mass contained in the ISM accounts for only $\sim 10\%$ of the baryonic mass of the Galaxy, while the rest is contained in stars and stellar remnants. Nevertheless, the ISM plays an important role in the evolution of a galaxy. Stars are born from the interstellar material, and in the final stages in their lives, enriched material is returned to the ISM from where new generations of stars will be born. The gas component in the ISM is dominated by hydrogen (in both mass and number fraction). Helium is the next most abundant element followed by oxygen and carbon. The precise elemental abundances of the ISM in the local neighborhood are not known, but they are thought to be similar to the elemental abundances of the Sun. The solar number abundances relative to hydrogen of He, O and C are 9.6×10^{-2}, 5.4×10^{-4} and 3.0×10^{-4}, respectively (Asplund et al. 2009). The gas-phase abundances of many elements in the ISM have been measured using interstellar absorption lines. These studies, which have been made towards many different sightlines, revealed that some elements have gas-phase abundances that are only a few percent of the solar abundance. This underabundance of elements in the gas-phase is thought to reflect the depletion of elements onto dust grains, and gives constraints to the elemental composition of interstellar grains (Draine 2011).

The bulk of the mass in the ISM is in the gas component, which is far from homogeneous. Interstellar gas is present in different ionization states and spans wide ranges of temperatures and densities. The ISM can be classified in three different phases, that are in approximate thermal pressure equilibrium with one another ($P/k \sim nT_{\rm kin} \sim 3 \times 10^3$ cm^{-3} K; Wolfire et al. 2003). The first one is the hot ionized medium (HIM) which is heated by supernova remnants to temperatures of $T_{\rm kin} \sim 10^6$ K and is very diluted ($n_{\rm H} \sim 3 \times 10^{-3}$ cm^{-3}). Embedded within the HIM, the second phase comprises two warm ($T_{\rm kin} \sim 8000$) and low density ($n_{\rm H} \sim 0.3$ cm^{-3}) components. These are the warm ionized medium (WIM) and the warm neutral medium (WNM). The last phase contains colder ($T_{\rm kin} \sim 100$) and denser ($n_{\rm H} \sim 30$ cm^{-3}) gas and is called the cold neutral medium (CNM). Two higher pressure components exist. These are the H II regions created around massive stars where the gas is heated to $T_{\rm kin} \sim 10^4$ K and densities ranges from 1 cm^{-3} to $\gtrsim 10^5$ cm^{-3}, and the gravitationally bound cold ($T_{\rm kin} = 10 - 30$) and dense ($n_{\rm H} \sim 10^3 - 10^7$ cm^{-3}) cloud cores (Hollenbach & Tielens 1999). This last component is where stars are born. The hot and

warm phases occupy most of the volume of the ISM, but the colder phases contain most of the mass.

1.1.1 Interstellar dust

The most important role of dust grains in the ISM is the shielding of molecular clouds from the UV radiation. In addition, dust grains are an important source of heating, through the photoelectric effect. They can also catalyze chemical reactions on their surface. In particular, H_2 is formed on grains.

As mentioned before, absorption line spectroscopic studies show that elements, such as C, Mg, Si, and Fe are underabundant in the gas-phase. These observations show that $\sim$2/3 of the C and $\gtrsim$90% of Mg, Si, and Fe are depleted from the gas, and could form the bulk composition of interstellar dust grains. Under this assumption, the total mass contained in dust would be 0.01% of the hydrogen mass, with 28% of the mass contributed by C, and the rest by Mg, Al, Si, Ca, Fe, Ni and O (Draine 2011).

The chemical composition of dust grains can also be constrained through the analysis of absorption features in the spectra of stars viewed through interstellar material. The strongest spectral feature in the extinction curve is the broad bump centered at $\sim$ 2175 Å due to carbonaceous material, such as graphite. Silicates are an important constituent of dust grains that produce the absorption features at 9.7 μm and 18 μm. The broad absorption feature seen at 3.4 μm, is due to the C-H stretching mode in hydrocarbons. A large number of weaker extinction features, known as the diffuse interstellar bands (DIBs), have been observed since more than 80 years but the exact nature of the chemical carriers is still not known. It is likely that a substantial fraction of the DIBs carriers are free-flying large molecules (*i.e.*, ultra-small dust grains). It has been proposed that fullerenes and hydrogenated fullerenes could be carriers of the interstellar bands (e.g., Iglesias-Groth et al. 2012). The emission features seen at 3.3, 6.2, 7.7, 8.6 and 11.3 μm correspond to the vibrational modes of polycyclic aromatic hydrocarbon (PAH) molecules (Hollenbach & Tielens 1999). In dark molecular clouds, additional absorption features are observed arising from the ices that surround the dust grains. The strongest feature is 3.1 μm band which is produced by the O-H stretching mode in H_2O ice. Other ice features include the ones at 4.67 μm, 15.2 μm and 3.53 μm, due to CO, CO_2 and CH_3OH, respectively.

Observations of absorption features also give information on the size distribution of interstellar dust grains. Models that can reproduce the dust emission and extinction in our Galaxy, include three dust components (Desert et al. 1990). These are: PAHs, which contain less than $\sim$ 1000 atoms (size $\sim$ 1 nm); Very small grains, with sizes of a few nm; and Big grains, with sizes $\sim 15 - 110$ nm. The smallest dust particles, PAHs and very small grains, have a small heat capacity, so they can be heated to high temperatures ($T \sim 100 - 1000$ K) when they absorb a single photon. They can re-emit the absorbed photon and cool down very quickly, without reaching an equilibrium temperature. They are responsible for the mid-IR continuum emission and spectral features. Big grains are in equilibrium with the radiation field, and they dominate the emission in the far-IR to sub-mm range.

Dust grains are formed in the stellar winds of late-type stars in the asymptotic giant branch (AGB) and Type II supernova remnants (SNe). These dust grains will move away

from their formation source, injecting new material into the ISM. The destruction of dust grains is dominated by sputtering and high-velocity grain-grain collisions in interstellar shock waves (Tielens et al. 1994). In the case of low velocity grain-grain collisions, which can happen in dense molecular clouds, dust grains can coagulate, increasing their size (e.g., Hirashita & Omukai 2009).

1.1.2 Molecules in the ISM

Although the typical densities of the ISM are very low compared to the densities we find in our planet[1], the interstellar gas and dust are chemically and dynamically active. Molecules are formed and destroyed in the gas and on the surface of dust grains. Interstellar matter can collapse to form new stars, and enriched material is returned to the ISM when stars die. This interaction between stars and the surrounding medium determines the evolution of galaxies.

The first molecules that were detected in the ISM are CH (Douglas & Herzberg 1941), CH^+ (Adams 1941) and CN (McKellar 1940). Since then, around 180 molecules have been detected in the interstellar medium or circumstellar shells (without taking into account isotopologues). In other galaxies, around 55 species have been detected. Table 1.1 reports the secure detections, *i.e.* tentative or disputed detections are not included. It includes the deuterated species, but it does not include other isotopologues, such as ^{13}C, ^{18}O, etc. Around 70% of the molecules detected so far, contain only one or more of the following elements: hydrogen, carbon, nitrogen and oxygen. Around 9% contain sulfur and nearly 20% contain heavier elements, such as Al, K, Si and Mg. More than 30% of the molecules contain 6 or more atoms, and are arbitrary labeled as complex[2] (Herbst & van Dishoeck 2009). All of these complex molecules are organic, as they contain carbon. The largest molecules are the fullerenes, C_{60} and C_{70}, which were recently discovered in the ISM (Cami et al. 2010; Sellgren et al. 2010). The detection of these species in various astrophysical environments has motivated the spectroscopists to review the potential of fullerenes and hydrogenated fullerenes as carriers of the DIBs. The next largest molecule, $HC_{11}N$, contains 13 atoms. Many of these species are common molecules on Earth. Others, like the molecular ions (e.g., HCO^+ and CN^-) and radicals (e.g., C_2H and C_6H) are common molecules in the ISM but exotic on earth, because they are very reactive and thus easily destroyed at the much higher densities of our planet compared to the ISM. The species listed in Table 1.1 are not all detected in the same place in the ISM. Some are common species to several different environments (e.g., H_2 and CO), but others are only found in very specific environments (e.g., N_2H^+ and DCO^+).

1.1.3 The structure of the ISM

In the mid-80s, the first CO surveys (e.g., Ungerechts & Thaddeus 1987; Bally et al. 1987), and the far-IR all-sky IRAS survey (Low et al. 1984) revealed the filamentary structure of the gas and dust in the ISM. Then, several mid-IR surveys with the *Infrared Space Observatory*

[1]The mean density of the ISM is only a few hydrogen nuclei cm^{-3}, while the density of our atmosphere at sea level is 7×10^{20} per cubic centimeter. Moreover, the typical densities in ISM clouds are lower than those achieved in the best ultra-vacuum chambers on Earth. However, because the typical sizes in the ISM are enormous, the masses are actually quite large. The hydrogen nuclei density is defined as $n_{\rm H} = n({\rm H}) + 2n({\rm H_2})$.

[2]In this thesis, I will also consider molecules that contain 4 atoms, such as H_2CO and HCOOH, as complex.

Table 1.1: List of molecules detected in the in ISM or circumstellar shells as of July 2013 (data taken from `http://www.cdms.de` and `http://www.astrochymist.org`).

			H and C			
C_2	C_{70}	CH_4	C_5H	C_2H_4	CH_2CHCH_3	$c-C_6H_6$
C_3	CH	C_2H	C_6H	$c-C_3H_2$	C_6H_2	$l-HC_6H$
C_5	CH^+	$c-C_3H$	C_7H	$l-C_3H_2$	CH_3C_2H	C_4H^-
C_{60}	CH_2	$l-C_3H$	C_8H	$l-C_4H_2$	CH_3C_4H	C_6H^-
C_{60}^+	CH_3	C_4H	C_2H_2	$l-HC_4H$	CH_3C_6H	C_8H^-
H_2	H_3^+					
			H, C and O			
CO	OH	H_2O	H_2CO	$c-H_2C_3O$	CH_3O	CH_3CH_2OH
CO^+	OH^+	H_2O+	H_2COH^+	$c-C_2H_4O$	CH_3OH	CH_3CH_2CHO
CO_2	HCO	H_3O^+	HCOOH	HC_2CHO	CH_3CHO	CH_3COOCH_3
C_2O	HCO^+	HO_2	$HOCO^+$	CH_2CHOH	CH_3OCHO	CH_3OCH_3
C_3O	HOC^+	HOOH	CH_2CO	CH_2OHCHO	CH_3COOH	$(CH_3)_2CO$
O_2					$(CH_2OH)_2$	C_2H_5OCHO
			H, C and N			
N_2	CN	HC_3NH^+	$HC_{11}N$	HC_2NC	CH_2CCHCN	CH_3CHNH
NH	C_3N	HC_3N	H_2CN	HNCNH	CH_3CN	CH_3CH_2CN
NH_2	C_5N	$l-HC_4N$	CH_2NH	HNCHCN	CH_3NC	$n-C_3H_7CN$
N_2H^+	HNC	HC_5N	CH_2CN	NH_2CN	CH_3NH2	CN^-
NH_3	HCN	HC_7N	HNC_3	NH_2CH_2CN	CH_3C_3N	C_3N^-
	$HCNH^+$	HC_9N	HC_2N	CH_2CHCN	CH_3C_5N	C_5N^-
	Species containing S				H, C, O and N	
SH	SH^+	NS	H_2S	NO	HNCO	NH_2CHO
CS	SO	HNCS	HCS^+	N_2O	HCNO	CNCHO
C_2S	SO^+	HSCN	H_2CS	HNO	HOCN	CH_3CONH_2
C_3S	SO_2	OCS	CH_3SH			OCN^-
			Species containing F, Al, K, Na, Cl, Si, P, Mg, Fe and Ti			
HF	AlNC	HCl	SiC	$c-SiC_2$	CP	MgCN
CF^+	AlCl	HCl^+	SiO	$c-SiC_3$	PO	MgNC
AlF		H_2Cl^+	SiN	SiC_4	PN	FeCN
AlO	KCN	KCl	SiS	SiCN	HCP	TiO
AlOH	NaCN	NaCl	SiH_4	SiNC	CCP	TiO_2
			Deuterated species			
HD	HDO	D_2CO	C_2D	ND	N_2D+	D_2S
H_2D^+	D_2O	CH_2DOH	c-C_3HD	NH_2D	DCN	HDS
HD_2^+	DCO^+	CH_3OD	c-C_3D_2	NHD_2	DNC	HDCS
NH_3D^+	HDCO	CD_3OH	C_4D	ND_3	CH_2DCN	D_2CS

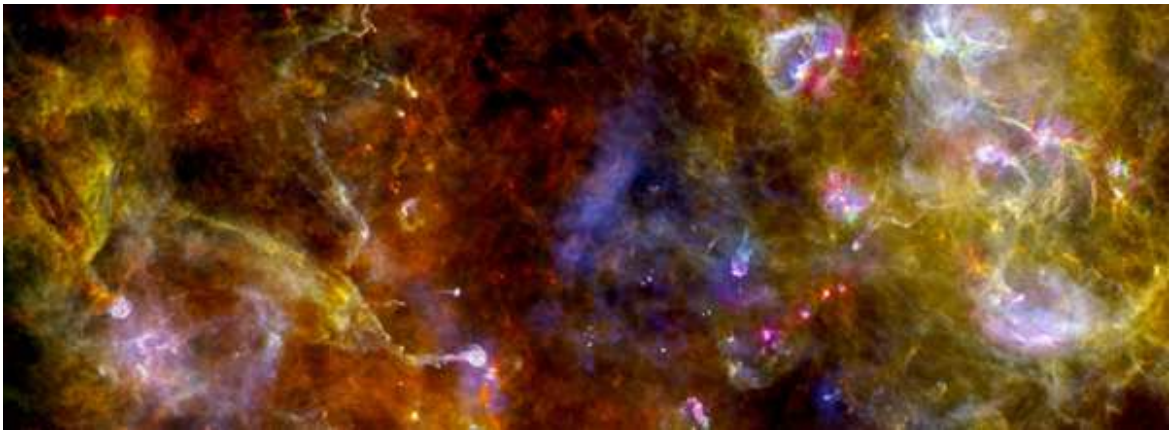

Figure 1.1: Infrared view of Cygnus X viewed by Herschel, revealing the complex filamentary structure of the cool gas and dust. Credit: ESA/Herschel/Gould Belt Survey

(e.g., Perault et al. 1996) and the *Spitzer* (e.g., Benjamin et al. 2003) telescope revealed the filamentary structure of the cold dust, regions that are now known as infrared dark clouds (IRDC).

Dark clouds show a hierarchical structure. The contain embedded clumps which are defined as coherent regions in position-position-velocity space. Usually, CO isotopologues are used to define them. Within clumps there are cores, which are the smallest and densest units inside molecular clouds, and are defined as gravitationally bound, single-peaked regions out of which individual stars or simple stellar systems form (Bergin & Tafalla 2007). Table 1.2 shows typical parameters for clouds, clumps and cores.

Recent observations with the *Herschel Space Observatory* have confirmed the complex large-scale filamentary structure of the ISM (see Fig. 1.1), and show that filaments are truly ubiquitous in molecular clouds and that numerous dense cores are located along the filaments (e.g., Men'shchikov et al. 2010; Ward-Thompson et al. 2010; André et al. 2010). These filaments share common properties, such as a characteristic width (~ 0.1 pc), but present a large range in column density, from $N_{\rm H_2} = 2\times10^{20}$ cm^{-3} for the most tenuous, to $N_{\rm H_2} = 10^{23}$ cm^{-3} for the densest ones (Arzoumanian et al. 2011). In most cases, prestellar cores, that eventually form stars, are observed in the densest filaments, which are likely gravitationally unstable. The observed association between filaments and cores suggests that prestellar cores result

Table 1.2: Properties of clouds, clumps and core. Table adapted from Bergin & Tafalla (2007).

	Cloud	Clumps	Cores
Mass ($M_\odot$)	$10^3 - 10^4$	$50 - 500$	$0.5 - 5$
Size (pc)	$2 - 15$	$0.3 - 3$	$0.03 - 0.2$
Density (cm^{-3})	$50 - 500$	$10^3 - 10^4$	$10^4 - 10^5$
Gas temperature (K)	$10 - 30$	$10 - 20$	$8 - 12$

from the gravitational fragmentation of filaments in the cold ISM. In this scenario, filaments would form first within molecular clouds as a result of large-scale magneto-hydrodynamic (MHD) turbulence (André et al. 2010).

1.2 Photon-dominated Regions

Photon-dominated regions (PDRs), also called photodissociation regions, are regions where the physics and chemistry of the dust and gas is regulated by the far-UV (6 eV< $h\nu$ <13.6 eV) radiation arising from nearby massive stars. The presence of PDRs in the ISM was first established by the observations of bright O I 63 μm and C II 158 μm fine structure lines towards massive star forming regions (Russell et al. 1980, 1981; Melnick et al. 1979; Storey et al. 1979). These studies revealed the presence of a predominantly neutral layer of gas located between the H II region and the dense molecular cloud, where atomic and molecular hydrogen coexist. In order to explain these observations and understand the interaction between radiation and interstellar clouds, the first PDR models were developed (e.g., Tielens & Hollenbach 1985b,a; Sternberg & Dalgarno 1989). Since then, and with the advent of instrumental improvements at IR and (sub-)millimeter wavelengths, the study of PDRs became an important field in astronomy. Indeed, we now know that the majority of the interstellar material is found in PDRs. All of the atomic and at least >50% of the molecular gas in the Galaxy is found in PDRs (Hollenbach & Tielens 1999). Therefore, many different environments are studied in the frame of PDRs. In addition to the interstellar clouds near massive stars, this includes the reflection nebulae, circumstellar envelopes around evolved stars, like red giants and AGB stars, starburst galaxies, protoplanetary disks, diffuse clouds, etc. The IR and sub-millimeter line emission of galaxies is dominated by PDRs. This includes the fine structure lines of C^+,

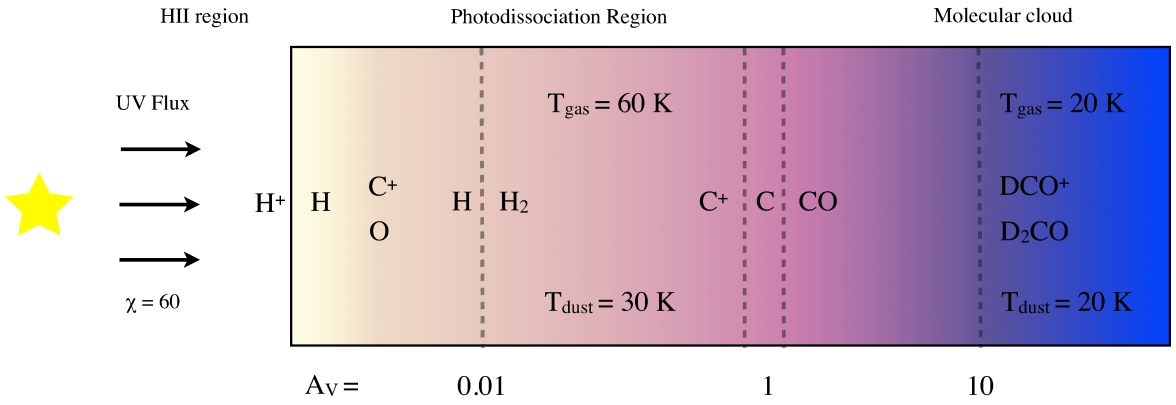

Figure 1.2: A schematic diagram of a photodissociation region. The PDR is illuminated from the left by a radiation field of $\chi = 60$ relative to the Draine field (Draine 1978). The radiation field, the gas and dust temperatures decrease towards the inner layers of the cloud. Hydrogen goes from being primarily atomic to molecular at $A_V \sim 0.01$ mag. Deeper inside, at $A_V \sim 1$ mag, carbon goes quickly from being ionized to neutral, and finally most of the carbon is found in CO. At $A_V \gtrsim 10$ mag, species start to freeze-out onto grains and deuterated species, such as DCO^+ and D_2CO, can be found.

C, O and Si, H_2 ro-vibrational lines, PAH features, and rotational lines from molecules, like CO.

A schematic diagram of a PDR is shown in Fig. 1.2. The illuminating star, located at the left side of the molecular cloud, illuminates the cloud with an incident far-UV flux of $\chi = 60$ in Draine units[3]. The first layers of the gas surrounding the star, absorb the Lyman continuum photons and form an H II region. The FUV photons can penetrate the next layers of the cloud. Atoms, such as H and O become neutral, while C is primarily ionized. Deeper inside, at $A_V \sim 0.01$ mag, hydrogen becomes molecular, and at $A_V \sim 1$ mag there is the transition between C^+, C and CO. In the inner layers of the cloud, where the gas temperature has decreased considerably ($T_{\rm kin} \sim 20$ K), deuterated species start to form.

1.3 Physical and chemical processes in PDRs

The key actors in the structure and composition of the illuminated matter are the far-UV photons. The structure in density of the medium and the intensity of the incident radiation field will determine how far inside the cloud the far-UV photons will penetrate, and hence the location of the transition between H and H_2, and between C^+, C and CO. Far-UV photons will also regulate the chemistry and the thermal balance of the gas. The most important physical and chemical processes taking place in PDRs are described next.

1.3.1 Penetration of far-UV radiation

The distribution of the gas and dust plays an important role in the way radiation will transfer throughout the cloud. Photons will penetrate much deeper in clumpy regions than in homogeneous clouds. The penetration of the far-UV radiation is regulated mainly by dust grain absorption, but also by dust scattering and discrete absorption lines from the most abundant species, *i.e.*, H, H_2 and CO (Goicoechea & Le Bourlot 2007).

PAHs absorb 5% of the far-UV radiation, while larger dust grains absorb the rest and reradiate it as far-infrared continuum. The absorption of photons by PAHs, leads to the ejection of electrons into the gas-phase, and is an important heating mechanism of the gas, as will be discussed in section 1.3.2.1. The absorption of far-UV photons depends strongly on the properties of the grains. Standard properties include a power law function[4] for the grain size distribution, known as the MRN law (Mathis et al. 1977), and a typical absorption cross section of 10^{-17} cm^{-2} per C atom.

Absorption by molecules is dominated by atomic H Lyman lines and molecular H_2 electronic transitions. The case of H_2 is particularly important. H_2 absorbs far-UV photons via Lyman and Werner electronic transitions in the $912 - 1100$ Å range. This process, known as H_2 pumping, is followed by the radiative decay, or fluorescence, from the electronically excited states to either the vibrational continuum or to an excited vibrational state of the

[3]The incident far-UV flux is usually expressed in units of the Habing field or the Draine field. The Habing field corresponds to an average interstellar flux of $G_0 = 1.6 \times 10^{-3}$ erg cm^{-2} s^{-1} (Habing 1968). This is equivalent to a radiation field of $\chi = 1.7$ using the Draine field (Draine 1978).

[4]$dn(a) \propto a^{\alpha} da$, where $dn(a)$ is the number of grains per unit volume, a is the radius of the grain and $\alpha = -3.5$

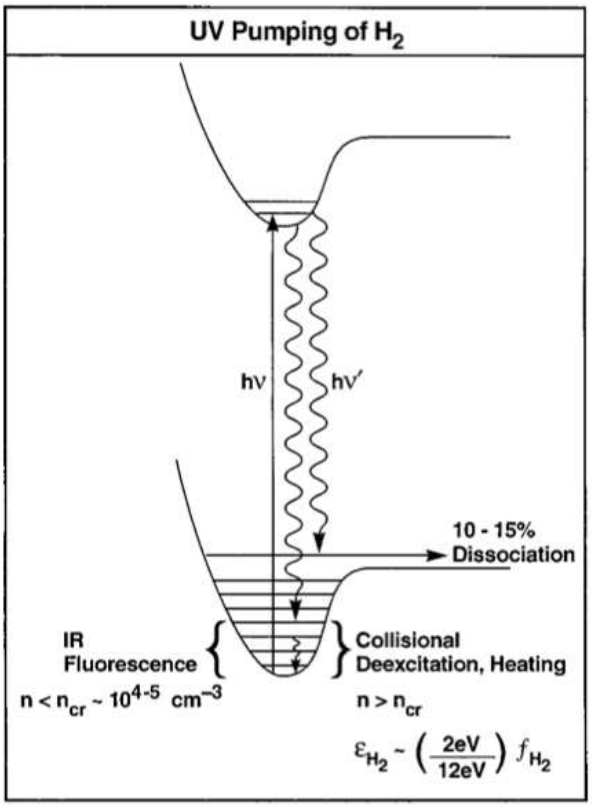

Figure 1.3: The far-UV pumping of H_2 is followed in $10-15\%$ of the time by fluorescence to the vibrational continuum of the ground electronic state, which leads to dissociation. Most of the time the fluorescence will leave the H_2 vibrationally excited in the ground electronic state, and the following collisional deexcitation will heat the gas. Figure from Hollenbach & Tielens (1999).

ground electronic state. In the first case, that occurs $10-15\%$ of the time, the H_2 molecule dissociates (see Fig. 1.3). When the absorption line becomes optically thick, H_2 forms a protective layer that shields the cloud from the far-UV radiation. In clouds that are illuminated by moderate radiation fields, *i.e.*, when $G_0/n_{\rm H} \lesssim 4\times10^{-2}$ cm^{-3}, this so-called H_2 self-shielding, becomes important and most of the photons that can pump H_2 ($h\nu \geq 11.2$ ev) are absorbed by H_2 rather than dust. In the second case, the vibrationally excited states can cascade down to the ground vibrational state through the emission of IR photons. The H_2 rovibrational line at 2.12 μm is often the brightest of these lines, and is easily detected from ground based telescopes.

1.3.2 Thermal balance

At steady state, the kinetic temperature at each position of the cloud is determined by equating the gas heating and cooling mechanisms. The heating of the gas involves the transfer of energy from the impinging far-UV photons and cosmic rays to kinetic energy of the gas. The cooling, on the other hand, involves the conversion of kinetic energy to photons emitted by atoms and molecules that can escape the cloud. Fig. 1.4 shows the main heating and cooling mechanisms in a PDR that is illuminated by a radiation field of $\chi = 60$ in Draine units (Draine 1978).

1.3.2.1 Heating mechanisms

The dominant heating mechanisms in PDRs are the photoelectric effect on PAH and small dust grains and the collisional de-excitation of vibrationally excited H_2 molecules. The formation of H_2 on dust grains followed by collisional de-excitation can also dominate under certain physical conditions.

Photoelectric heating by dust: When a far-UV photon is absorbed by a dust grain it will create energetic electrons (of a few eV) that may diffuse in the grain, reach the surface and be ejected at high speed into the gas. This electron, which carries an important fraction of the energy of the original photon, will then collide with molecules increasing the kinetic energy of the gas. The efficiency of the photoelectric heating effect depends on the size and the charge of the grain. For the electron to be ejected, it first needs to overcome the potential barrier, which is larger if the grain is positively charged. PAH and very small dust grains are the most efficient ones at heating the gas through this process (D'Hendecourt & Leger 1987; Lepp & Dalgarno 1988; Verstraete et al. 1990; Bakes & Tielens 1994). Grains with less than 1500 C atoms ($a = 15$ Å) contribute to half of the photoelectric heating, while grains with $1500 - 4.5 \times 10^5$ C atoms ($a = 15 - 100$ Å) are responsible for the other half (Bakes & Tielens 1994).

H_2 pumping followed by collisional de-excitation: Collisions between H_2 vibrationally excited through far-UV pumping, and other abundant species, like H atoms, will de-excite the H_2 molecule and transfer the vibrational energy to kinetic energy through each collision.

H_2 formation on grains followed by collisional de-excitation: When an H_2 molecule is formed on the surface of dust grains, it releases 4.5 eV. Part of this energy will heat the grain, another part will be converted into internal energy of the H_2 molecule, and the rest will be used to eject the newly formed molecule into the gas. The released H_2 molecules will then heat the gas through collisions with other molecules. The formation of H_2 on the surfaces of dust grains through the Eley-Rideal mechanism[5], followed by collisional de-excitation becomes the dominant source of heating at the edges of dense high-illuminated molecular clouds, where H_2 self-shielding is not yet fully efficient (Le Bourlot et al. 2012).

Gas-grain collisions: The kinetic temperature of the gas may be different from the temperature of the dust grains. At the edges of PDRs, dust grains are colder than the gas. If the density is large, collisions between molecules and dust grains can transfer energy to the gas and heat it. This heating mechanism dominates in the densest parts of molecular clouds.

Collisional de-excitation of H_2 dominates at high densities. Other heating mechanisms are cosmic ray ionization and excitation, ionization of C, and the pumping of gas species by far-UV photons emitted by warm dust grains followed by collisional de-excitation. The energy released in exothermic chemical reactions can be important for $A_V > 4$ mag.

1.3.2.2 Cooling mechanisms

The gas in PDRs is cooled by the emission of atomic fine-structure lines and by molecular rotational lines following collisional excitation. The dominant cooling lines at the surfaces of

[5]Grain surface chemistry and the formation mechanisms of the H_2 molecule will be further described in section 1.3.3.2

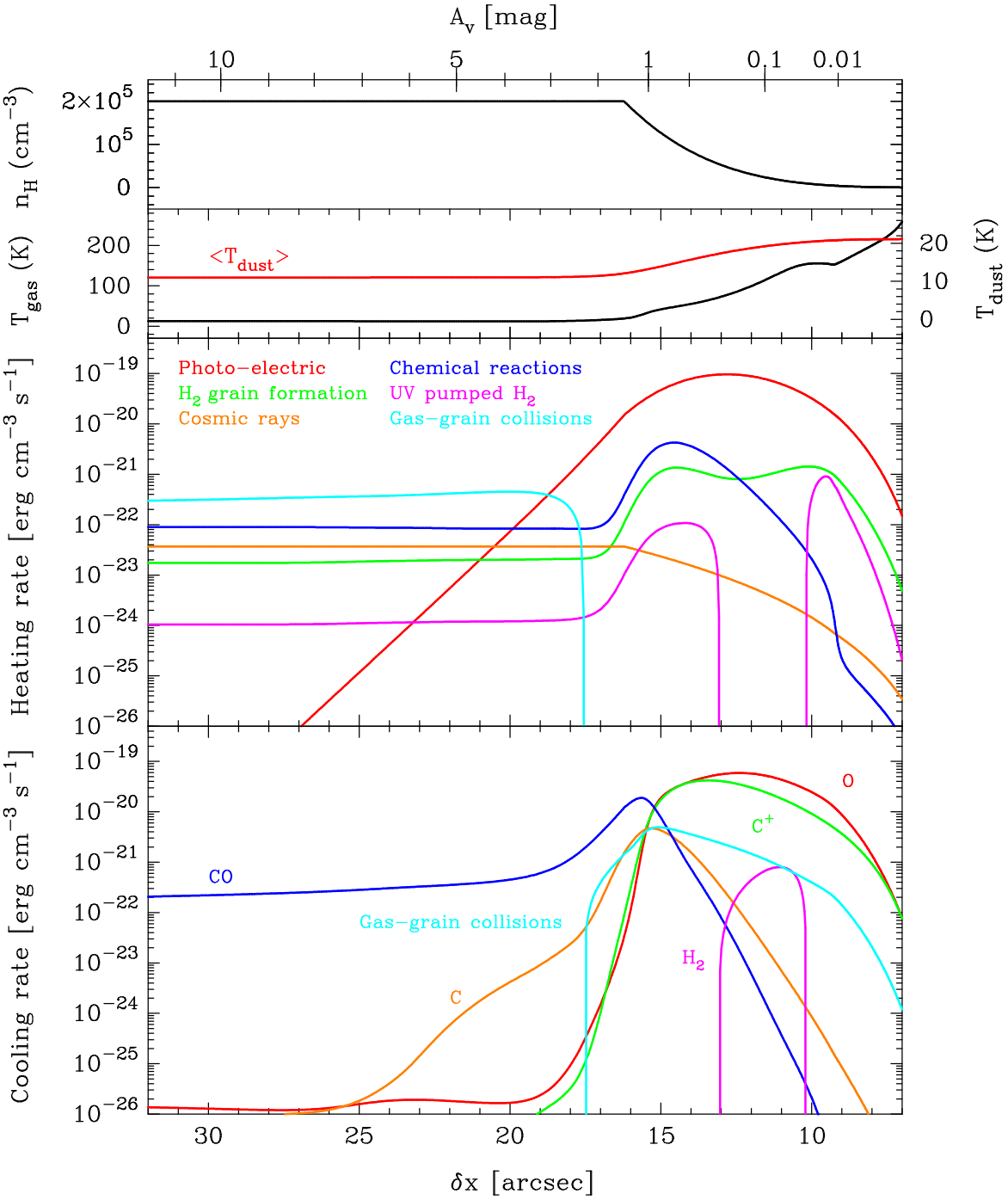

Figure 1.4: PDR models showing the steep density and temperature gradients (two upper panels) for a model with an incident radiation field of $\chi = 60$, and the contribution of different physical processes to the heating (middle panel) and cooling (lower panel) rates as a function of depth in a cloud. The illuminating star is at the right of the figure.

Table 1.3: Main gas-phase reaction in PDRs.

	Reaction	Example
Photodissociation	$AB + h\nu \rightarrow A + B$	$CO + h\nu \rightarrow C + O$
Ionization	$A + h\nu \rightarrow A^+ + e^-$	$C + h\nu \rightarrow C^+ + e^-$
Radiative association	$A + B \rightarrow AB + h\nu$	$C^+ + H_2 \rightarrow CH_2^+ + h\nu$
Neutral-neutral	$A + B \rightarrow C + D$	$O + CH_3 \rightarrow H_2CO + H$
Ion-molecule	$A^+ + B \rightarrow C^+ + D$	$C^+ + HF \rightarrow CF^+ + H$
Charge-transfer	$A^+ + B \rightarrow A + B^+$	$H^+ + O \rightarrow H + O^+$
Dissociative recombination	$AB^+ + e^- \rightarrow A + B$	$CF^+ + e^- \rightarrow C + F$

PDRs are the C II 158 μm and O I 63 μm and 146 μm fine structure lines. The energy emitted through these lines is of order $10^{-3} - 10^{-2}$ of the IR energy absorbed by dust grains (Tielens & Hollenbach 1985b). Other important cooling lines at the surface of the cloud are the Si II 35 μm fine structure line, the H_2 rovibrational line at 2.12 μm and the H_2 rotational lines at 12, 17 and 28 μm. Note that H_2 can contribute to both heating and cooling of the gas (see Fig. 1.4). The cooling through H_2 emission lines is most efficient in the outer layers of the PDR, around $A_V \sim 0.1$ mag. In high-density high-illuminated clouds, where the gas can reach $T_{\rm kin} \geq 5000$ K, the Fe II 1.26 μm and 1.64 μm, O I 6300 Å and S II 6730 Å fine structure lines are also important. Deeper inside the cloud, the C I 609 μm and 370 μm fine structure lines and the mid- and high-J CO rotational lines dominate the cooling. In dense clouds ($n_{\rm H} \gtrsim 10^6$ cm^{-3}), H_2O emission lines can contribute significantly to the cooling (Gonzalez Garcia et al. 2008). In this case H_2O is excited by infrared photons that are emitted by hot dust grains at the edge of the cloud and that penetrate deep inside the cloud. Interstellar dust grains also contribute to the cooling of the cloud by thermally re-emitting in the infrared the radiation they previously absorbed in the far-UV.

1.3.3 Chemistry

1.3.3.1 Gas phase chemistry

In the gas phase, chemistry is driven by two-body reactions. Due to the very low densities in the ISM, three-body reactions have very low probabilities, and can be thus neglected. Table 1.3 summarizes the main type of reactions in the gas-phase.

The most important gas-phase process in PDRs involve photons, due to the high far-UV flux. Photodissociation fragments molecules, such as CO, into smaller species. This is the dominant destruction mechanism of the molecules. Far-UV photons can also ionize species, such as C. This way, C^+, C and O can remain abundant in the PDR. Deeper inside the cloud, where the radiation field has been attenuated considerably, cosmic rays can still ionize atoms and molecules, producing species such as HCO^+, H_3O^+ and H_3^+. Cosmic rays can also excite H_2, which later de-excites leading to a constant source of secondary far-UV photons, that can then photo-dissociate other molecules. In radiative association reactions, the collision between two species leads to a product that is stabilized through the emission of a photon

that takes away the excess energy. One example is the radiative association of C^+ with H_2, leading to CH_2^+,

Neutral-neutral reactions are usually exothermic, but they often present activation barriers because the bond between atoms has to be broken in order to rearrange the molecule. Some neutral-neutral reactions involving atoms or radicals, such as C and OH, have no activation energy and are thus important in cold environments. Ion-neutral reactions are faster than the neutral-neutral ones because the dipole moment induced by the ion on the neutral species creates an attraction force, that increases the cross section of the reaction and overcomes any activation barrier. This type of reactions are important in PDRs, because ions are abundant.

Recombination with electrons and charge transfer reactions between species are important for the ionization balance of the gas. One important charge transfer is the one between H^+ and O, where H^+ is produced by cosmic-ray ionization. The charge transfer of C^+ to S is an important source of neutral C in the C^+/C/CO transition layers of PDRs. In highly illuminated PDRs, CO can be formed from the charge-transfer between CO^+ and H. Charge-transfer reactions between cations, such as C^+, S^+ and Si^+, and PAHs are also important in PDRs, as they can appreciably increase the column density of neutral atoms through the PDR. In the dissociative recombination reactions, an ion captures a free electron and forms a neutral species in an excited electronic state, that can then dissociate into two neutral species. The dissociative electron recombination of CH^+ to C can be an important source of C in warm, high-density PDRs. PAH cations can also capture free electrons to recombine. This last process is balanced by the photoelectric effect, where electrons are ejected from the surface of PAHs.

1.3.3.2 Grain surface chemistry

Dust grains are chemically active in the ISM. Atoms and molecules can be absorbed onto their surfaces, they can move and encounter other atoms or molecules, react with them to form more complex species, and they can be desorbed back into the gas phase.

There are two types of interactions between the atoms and the surface of dust grains. The first one, called physisorption, is a weak force through Van der Waals interactions, with binding energies of ~ 0.01 eV. The other one, called chemisorption, is a strong force through chemical bonds, with binding energies of ~ 1 eV. Fig. 1.5 shows the interaction energy profile between an atom and the surface, where the two types of interaction are summarized. Gas-phase atoms can easily enter physisorbed sites and become physisorbed atoms. In contrast, in order for a gas-phase atom to enter a chemisorbed site, it first has to overcome a barrier that depends on the gas temperature. Adsorbed atoms can migrate from site to site by tunneling effects and thermal hopping. At low temperatures, physisorbed atoms can easily migrate on the surface of grains to other physisorbed sites. Physisorbed atoms can also migrate to chemisorbed sites, depending on the barrier against chemisorption. At higher temperatures, the physisorbed species evaporate, while chemisorbed species can remain on the surface.

Molecules can be formed on the surface of dust grains through two mechanisms: the Langmuir-Hinshelwood mechanism, that involves physisorbed species, and the Eley-Rideal mechanism, that involves chemisorbed species (see Fig. 1.6). In the Langmuir-Hinshelwood

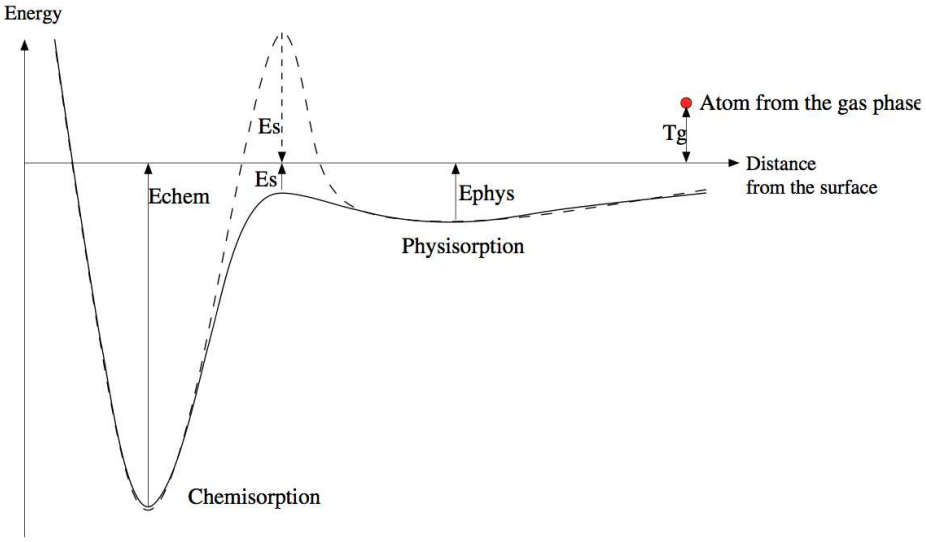

Figure 1.5: The interaction between an atom and the surface of a dust grain, showing the energy binding through physisorption ($E_{\rm phys}$) and through chemisorption ($E_{\rm chem}$). The dashed line displays a surface with a high barrier against chemisorption, while the continuous line displays a surface with no barrier. Figure from Cazaux & Spaans (2009).

mechanism, physisorbed atoms diffuse on the surface, encounter another physisorbed atom and form a molecule. They can also leave the surface through thermal desorption or another desorption process such as photodesorption. In the Eley-Rideal mechanism, an impinging gas-phase atom reaches an occupied chemisorbed site and react with it to form a molecule. The formation rate by the Langmuir-Hinshelwood mechanism depends on the dust temperature (allowing diffusion of species on the surface), while the formation rate by the Eley-Rideal mechanism depends on the gas temperature (allowing gas-phase atoms to reach a chemisorbed atom).

H_2 formation on grains: The formation of H_2 has been extensively studied in the past. Theoretical models including only the Langmuir-Hinshelwood mechanism find that H_2 can only be formed at low grain temperatures ($T_{\rm dust} \simeq 10 - 20$ K) (Biham & Lipshtat 2002; Le Petit et al. 2009). On the other side, H_2 is observed in a wide range of physical conditions, showing that it can also be formed at larger grain temperatures (even higher than 30 K). Therefore, the H_2 formation rate has been historically set to a standard value of $3 \times 10^{-17} n_{\rm H}\ n({\rm H})\ {\rm cm}^{-3}\ {\rm s}^{-1}$ derived from far-UV observations of H_2 in absorption in diffuse interstellar medium (Jura 1974; Gry et al. 2002). In the past few years, detailed models have been developed to understand the exact mechanisms responsible for such an efficient H_2 formation in a wide range of physical conditions. Recent models including both the Langmuir-Hinshelwood and the Eley-Rideal mechanisms are able to form H_2 in regions where the dust temperature is higher than 25 K (Le Bourlot et al. 2012). The Eley-Rideal mechanism involving chemisorbed sites is thus important for the formation of H_2 in regions where the gas and dust grains are warm, as physisorbed species are desorbed.

The newly formed species on the surface of dust grains can be desorbed into the gas-

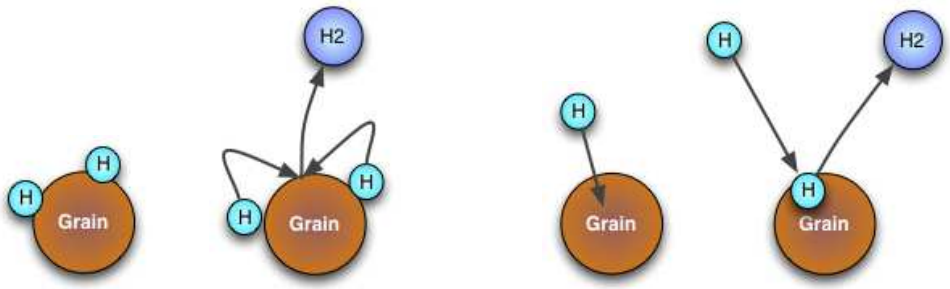

(a) Langmuir-Hinshelwood (b) Eley-Rideal

Figure 1.6: A schematic diagram of the two mechanisms to form molecules on the surface of dust grains. In (a), two physisorbed H atoms migrate on the surface of the grain, and when they meet H_2 is formed. In (b), a gas-phase H atom hits a chemisorbed H atom to form H_2.

phase either through thermal or non-thermal processes. Thermal desorption dominates in regions where dust grains reach high temperatures, like in hot cores and hot corinos (e.g., Jørgensen et al. 2005; Bisschop et al. 2007; Bottinelli et al. 2007), but also in highly far-UV illuminated PDRs, like in the Orion bar (Leurini et al. 2010). Non-thermal desorption by far-UV photons (photodesorption) dominates in colder regions, either UV-shielded dense cores where secondary UV photons are produced by the interaction between cosmic rays and H_2 molecules (e.g., Caselli et al. 2012) or in low-UV illumination PDRs, like the Horsehead nebula, where dust grains are too cold to sublimate their ices. Laboratory experiments have shown that this mechanism can be efficient (Öberg et al. 2009a,b). Chemical desorption, where the newly formed species is directly released into the gas due to the exothermicity of the reaction, can also be an efficient mechanism to release molecules into the gas phase (Dulieu et al. 2013)

1.4 Aims and structure of this thesis

Thanks to the powerful capabilities of radio-telescopes and the progress in laboratory techniques, astrochemistry has entered a completely new era. The improvements in both quality and speed of astronomical observations, enable us to observe and identify the numerous *fingerprints* of molecules in the Universe in a matter of days, while it took years before. Molecular lines are used to trace the structure of the interstellar medium and the physical conditions of the gas in different environments, from high-z galaxies to proto-planetary disks. The final goal of these studies is to answer key questions, like how planets, stars and galaxies form. But this is challenging because most objects in the sky cannot be resolved spatially, so it is difficult to know which specific region each molecule really traces. Therefore, to fully benefit from the diagnostic power of molecular lines, the formation and destruction paths of molecules must be quantitatively understood. In order to do this, sophisticated models are being developed but they need to be benchmarked with well-defined sets of observations of template sources. A good template source is one that is close-by, in order to spatially resolve the different components of the gas, and one that has a simple geometry, in order to ease the

comparison with chemical models. The work presented in this thesis is motivated by these needs.

The thesis is structured as follows. The Horsehead nebula is presented in Chapter 2, with a summary of the main observational results to date. At the end of this Chapter, I describe the Horsehead WHISPER line survey. The main results of this survey are presented in the following Chapters. In Chapters 3 and 4, I present the observations of simple molecules, namely CF^+ and C_3H^+, respectively. The next three Chapters contain observations of more complex molecules. H_2CO and CH_3OH presented in Chapter 5. The nitrile molecules, CH_3CN, CH_3NC and HC_3N are presented in Chapter 6. The complex molecules HCOOH, CH_2CO, CH_3CHO and CH_3CCH are presented in Chapter 7. A comparison between the chemistry in the Horsehead and other environments is given in Chapter 8. A summary of the main results of the Horsehead WHISPER line survey is given in Chapter 9, as well as some perspectives.

Chapter 2

The Horsehead nebula as a template PDR

2.1 The Horsehead nebula

In 1811 William Herschel published his 52 regions of *extensive diffuse nebulosity*, and the area around the star ζ Orionis (Alnitak) in Orion's belt was one of them (Herschel 1811). But it was not until 1888 that the first photographic plate (B2312) of the Orion region was taken by W. H. Pickering at the Harvard College Observatory. The plate was examined later that same year by Williamina Fleming, who discovered a dark patch and described it as "a semicircular indentation 5 minutes in diameter 30 minutes south of Zeta". In the next 30 years several new photographs of this object were published and discussed (e.g. Roberts 1903; Wolf 1903; Keeler 1908; Barnard 1913). At this point it was clear that this *dark object* seen in the photographs was a dark physical body between the stars. The nebula later received the scientific name B33 in the catalog of Barnard (1919). Since then, the Horsehead nebula became one of the most famous and easily-recognizable objects in the sky. The first observations of the Horsehead at millimeter wavelengths were made for ^{12}CO (Stark & Bally 1982) and NH_3 (Sandell et al. 1986) with an angular resolution of $2'$. Later, Suzuki et al. (1987) made a (low-quality) map of CO$(1-0)$ line with the NRO 45 m telescope at $15''$ angular resolution. Further observations include maps of CS (Lada et al. 1991), C II (Zhou et al. 1993), ^{13}CO (Kramer et al. 1996) and CI (Philipp et al. 2006).

At visible wavelengths the Horsehead nebula appears as a dark patch against the bright Hα emission from the H II region IC 434 (see lower right panel in Fig. 2.1). At mid-IR and radio wavelengths the nebula is bright due to dust and molecular emission (see lower left panel in Fig. 2.1). Two OB-systems are located near the Horsehead nebula, ζ Ori to the north and σ Ori to the west. However, ζ Ori ($d = 250 \pm 50$ pc) is located further away from the Horsehead than σ Ori ($d = 352 \pm 113$ pc), as shown by Hipparcos determinations of their distances (Perryman et al. 1997). The western edge of the Orion B molecular cloud or L1630, the Horsehead parent cloud, is therefore mainly illuminated by σ Ori at a projected linear distance of 3.5 pc (or 0.5° from the cloud). σ Ori is a O9.5V binary system (Warren & Hesser 1977) with an effective temperature of ~ 34.600 K (Schaerer & de Koter 1997)

The incident radiation field that has shaped the molecular cloud into the famous Horsehead is also compressing and heating the gas and dust, forming a PDR at the western edge of the nebula. The Horsehead nebula is thus not only a beautiful object, but also an interesting laboratory to study the interaction between the far-UV radiation and the gas and dust in molecular clouds.

Figure 2.1: *Upper panel:* A deep exposure of the Orion B molecular cloud. Credit: Rogelio Bernal Andreo (Deep Sky Colors). *Lower left panel:* The Horsehead nebula see in the near-infrared by the Hubble Space Telescope. Credit: NASA, ESA, and the Hubble Heritage Team (AURA/STScI). *Lower right panel*: The Horsehead nebula seen at visible wavelengths by the VLT (composite of B,V and R bands)

2.1.1 A dense PDR seen edge-on

Abergel et al. (2003) observed the nebula with the ISOCAM on board the ISO satellite at $5 - 18$ μm with $6''$ angular resolution. The images, which are dominated by the emission of PAHs (Polycyclic Aromatic Hydrocarbons), revealed a very thin ($\sim 10''$ or $\sim$0.02 pc) filament delineating the illuminated edge of the nebula. This indicated that the Horsehead PDR is

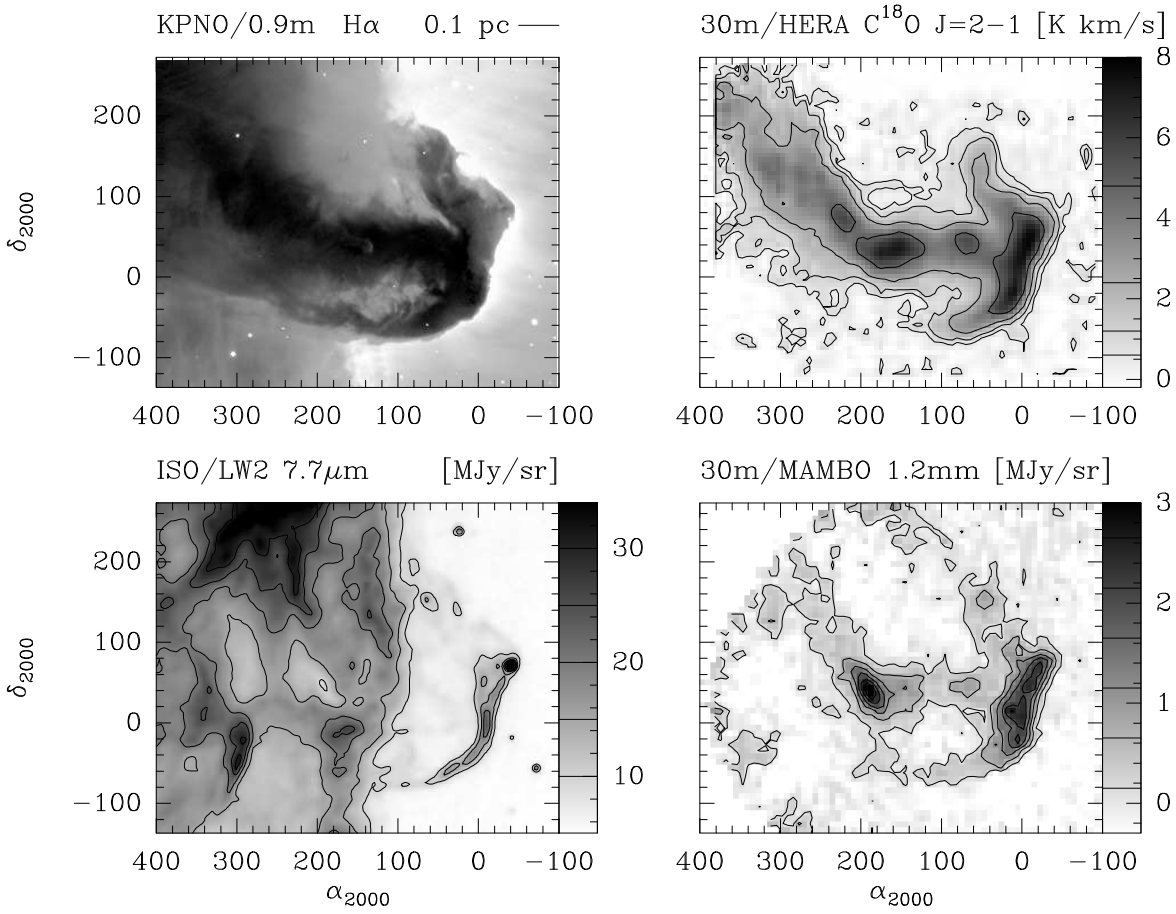

Figure 2.2: The Horsehead nebula seen at different wavelengths. *Upper left:* H_α line emission obtained at the 0.9 m KPNO telescope. Credit: B. Reipurth and J. Bally. *Upper right:* Integrated emission map of $C^{18}O$ $J = 2 - 1$ (Hily-Blant et al. 2005). *Lower left:* Continuum emission around 7 μm (Abergel et al. 2003). *Lower right:* Continuum emission at 1.2 mm (Hily-Blant et al. 2005).

seen nearly edge-on, as a large inclination would produce a broader filament (see lower left panel in Fig. 2.2). Assuming a distance of 400 pc (from the study of the distances to B stars in the Orion association by Anthony-Twarog 1982), the incident radiation field is $\chi \simeq 60$ times the mean interstellar radiation field as determined by Draine (1978).

Habart et al. (2005) obtained high-resolution ($\sim 1''$) images of the H_2 line emission at 2.12 μm with the SOFI instrument on the NTT telescope. The H_2 fluorescent emission is very sensitive to both the far-UV radiation field and the gas density. The data revealed extremely sharp ($\sim 5''$ or 0.01 pc) and bright filaments spatially coincident with the PAH emission. Habart et al. (2005) modeled the emission of H_2, CO and PAHs to study the gas density structure along the PDR. They concluded that in order to explain the observed spatial stratification, as well as the absolute intensities and intensity ratios of the different tracers, the density must follow a steep gradient at the cloud edge, rising from $n_H \simeq 10^4$ cm^{-3} to $n_H = 10^5$ cm^{-3} in less than $10''$ (i.e. 0.02 pc), at a roughly constant thermal pressure

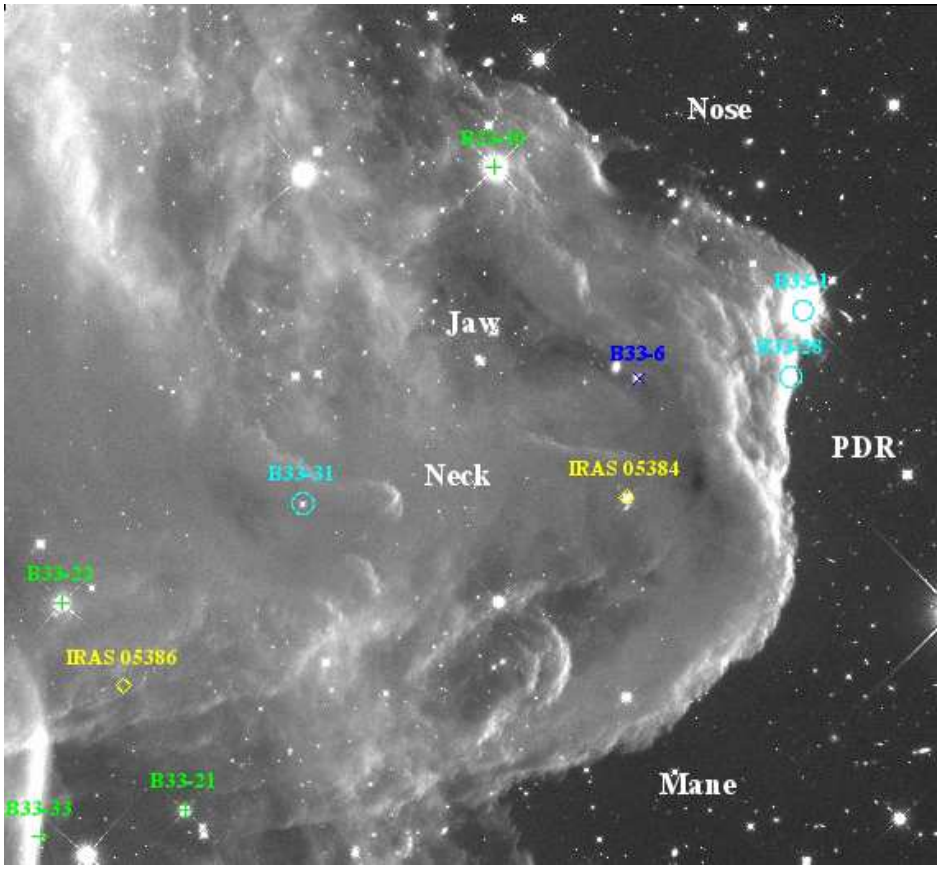

Figure 2.3: Locations of bona fide YSOs (cyan circles), candidate YSOs (green crosses) and IRAS sources (yellow diamonds) overlaid on the near-IR Hubble image. The main sections of the Horsehead (nose, PDR, mane, jaw and neck) are also indicated.

($P = 4 \times 10^6$ K cm^{-3}) more than 100 times larger than the mean ISM pressure ($P \sim 2.5 \times 10^4$K cm^{-3}; Boulares & Cox 1990)

Figure 2.3 displays an optical image of the Horsehead showing the top of the Horsehead (western ridge) from the nose to the mane. It also shows the throat (neck) of the Horsehead. These names were given by Pound et al. (2003) and Hily-Blant et al. (2005). The protostars identified in the Horsehead are also marked (see next section).

2.1.2 Star formation in the Horsehead

The Orion molecular cloud complex is the closest giant star-forming complex to the Sun. It contains two major giant molecular clouds: L1641 (Orion A) and L1630 (Orion B). The Orion B Molecular Cloud is shown in the upper panel in Fig. 2.1. This giant molecular cloud contains several well-known star-forming regions such as NGC 2071, NGC 2068, M 78 (HH 19-27), NGC 2024 and NGC 2023.

The Horsehead nebula itself is also an active site of star formation. Reipurth & Bouchet (1984) were the first ones to search for embedded young stars in the Horsehead. They

identified an infrared source, B33-1, at the western edge in the mane of the Horsehead, which has a large infrared excess. This source was later identified by IRAS (IRAS 05383-0228). They also detected a faint infrared source, B33-6, between the jaw and the throat of the Horsehead. They suggested that the cavity that starts at the jaw and extends to the northeast was produced by a collimated jet emanating from this star. However, this source was not detected by IRAS and has no infrared excess. Pound et al. (2003) suggested that it could be a very cool, deeply embedded source, perhaps of Class 0. Sandell et al. (1986) identified two other IRAS source, IRAS 05384-0229 to the southwest and IRAS 05386-0229 to the southeast of the Horsehead (see Fig. 2.3). Bowler et al. (2009) made an infrared census of star formation in the Horsehead. They identified two bona fide young stellar objects (YSOs), B33-1 and B33-28, at the western edge of the PDR and one Class II YSO, B33-31, to the east in the neck of the Horsehead. B33-28 is optically invisible and therefore they concluded that it is either embedded or is emerging on the other side of the Horsehead. They also identified five candidate young stars (B33-10, B33-21, B33-22, B33-25 and B33-33), but their association with the Horsehead is unclear. B33-10 is located in the nose the Horsehead, while B33-21, B33-22, B33-25 and B33-33 are located to the east, in the outer neck of the Horsehead.

Ward-Thompson et al. (2006) studied the dust emission at 450 and 850 μm in the Horsehead and found two dense condensations. The first one, called B33-SMM1, is associated with the top of the Horsehead (the western ridge). The other one, called B33-SMM2, is associated to the middle neck. They estimated a mass for the clumps of 2 $M_\odot$ (B33-SMM1) and 4 $M_\odot$ (B33-SMM2). B33-SMM1 is not gravitationally bound but is being confined by the external pressure from the H II region and may undergo triggered star formation. B33-SMM2 is in approximate gravitational equilibrium, consistent with it being formed before σ Ori was born, but its collapse may also eventually be triggered by the expansion of the external H II region.

2.1.3 Formation and evolution of the Horsehead

Reipurth & Bouchet (1984) were the first ones to propose a formation scenario for the Horsehead nebula. They suggested that the Horsehead will become a Bok globule, which is a condensation that has survived the destruction of its parent cloud by nearby OB stars (Reipurth 1983). Following this work, Pound et al. (2003) classified the Horsehead in the category of pillars, such as the "pillars of creation" in the Eagle nebula (M16). Despite detailed observations and theoretical models, there is no clear consensus on how pillars, also called *elephant trunks*, are formed. Proposed formation mechanisms include instabilities at the interfaces between H II regions and molecular clouds that grow in time (e.g., Whalen & Norman 2008), and preexisting density enhancements in the parent cloud that will create shadowed regions behind dense clumps where gas can accumulate (e.g., Mackey & Lim 2010). Tremblin et al. (2012) showed that an initial curvature of the cloud at the edge of the H II region will lead to the formation of pillars.

Pound et al. (2003) made the first CO $J = 1 - 0$ interferometric map (10" resolution) of the Horsehead with the BIMA interferometer. They analyzed the velocity field of the nebula and found a velocity gradient of 5 $\mathrm{km\,s^{-1}\ pc^{-1}}$ from the northeast to the southwest. They also estimated a formation timescale of the Horsehead to be ~ 0.5 Myr and a survival time of

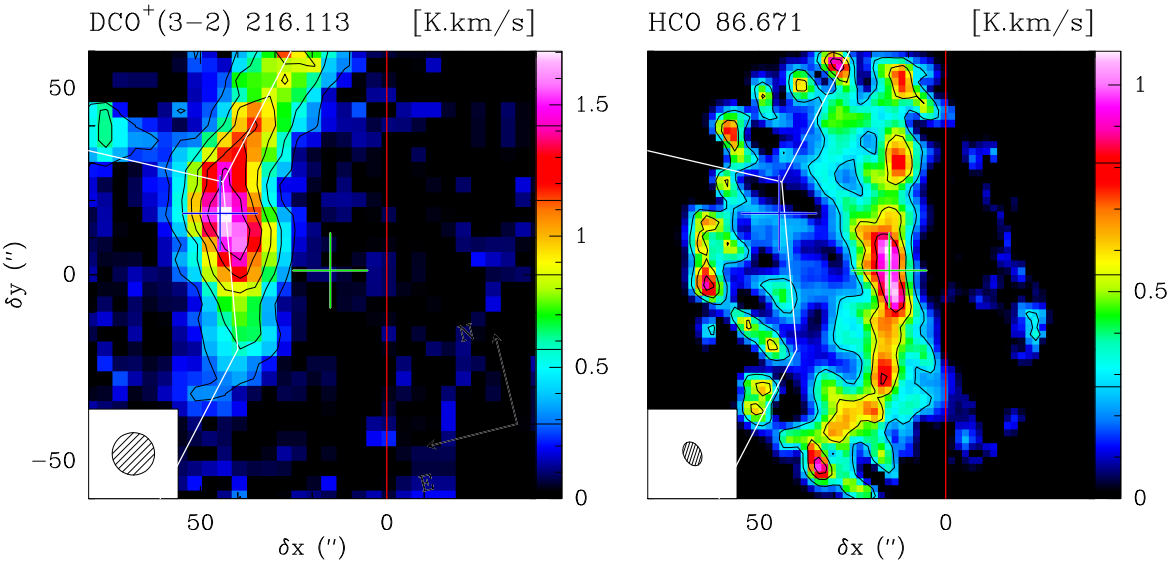

Figure 2.4: Integrated intensity maps of the Horsehead edge. Maps were rotated by 14° counter-clockwise around the projection center, located at $(\delta x, \delta y) = (20'', 0'')$, to bring the exciting star direction in the horizontal direction and the horizontal zero was set at the PDR edge, delineated by the red vertical line. The crosses show the positions of the PDR (green) and the dense-core (blue).

5 Myr. Hily-Blant et al. (2005) then made a map of the $C^{18}O$ $J = 2-1$ line (see upper right panel in Fig. 2.2), which unlike the CO $J = 1-0$ line is an optically thin tracer and therefore reveals the inner layers of the nebula. These observations showed that the Horsehead is rotating around the neck axis with a rotation period of 4 Myr, that is comparable to the 5 Myr lifetime estimated by Pound et al. (2003). Hily-Blant et al. (2005) suggested that the origin of the Horsehead could be linked to a pre-existent rotation of this region of L1630 that survived the incident radiation field from σOri, where the nose and mane would have been progressively detached from the neck due to the centrifugal force.

2.1.4 Two different environments less than 40" away

Gerin et al. (2009) observed interferometric maps (5″) of the HCO and $H^{13}CO$ ground state lines towards the Horsehead edge. They detected bright HCO emission delineating the illuminated edge of the nebula, and faint emission toward the shielded molecular cloud. The HCO emission almost coincides with the PAH and CCH emission. At the emission peak, HCO reaches a similar abundance to HCO^+ ($1 - 2 \times 10^{-9}$ with respect to H_2). At this position, the gas is warm ($T_{\rm kin} \sim 60$ K) and relatively dense ($n_{\rm H} \sim 6 \times 10^4$ cm^{-3}). Gerin et al. (2009) proposed that HCO is a good tracer of dense far-UV illuminated gas. On the other side, Pety et al. (2007) detected very bright DCO^+ lines in the Horsehead, arising from a dense ($n_{\rm H} \geq 2 \times 10^5$ cm^{-3}) and cold ($T_{\rm kin} \leq 20$ K) condensation less than 40″ away from the UV-illuminated edge of the nebula. This dense core is confined by the pressure from the external far-UV radiation field (Ward-Thompson et al. 2006). A large DCO^+/HCO^+

Table 2.1: Summary of abundances towards the PDR and dense core. The column density of H_2 is also given.

Species	Beam	PDR		Core		Ref.
	($''$)	Abundance	Offsets	Abundance	Offsets	
$N(H_2)$	11	1.9×10^{22}	(-5,0)	2.9×10^{22}	(20,22)	4,5,6,7
$C^{18}O$	6.5×4.3	1.9×10^{-7}	(-6,4)			1
C_2H	7.2×5.0	1.4×10^{-8}	(-6,4)			1
c-C_3H	28	2.7×10^{-10}	(-10,0)			2
l-C_3H	28	1.4×10^{-10}	(-10,0)			2
c-C_3H_2	6.1×4.7	1.1×10^{-9}	(-6,4)			1
l-C_3H_2	27	$< 4.6 \times 10^{-11}$	(-10,0)			2
C_4H	6.1×4.7	1.0×10^{-9}	(-6,-4)			1
C_6H	28	2.2×10^{-11}	(-6,4)			3
CS	10	2.0×10^{-9}	(4,0)	2.9×10^{-9}	(21,15)	4
$C^{34}S$	16	9.2×10^{-11}	(4,0)	9.1×10^{-11}	(21,15)	4
HCS^+	29	1.7×10^{-11}	(4,0)	1.2×10^{-11}	(21,15)	4
HCO	6.7×4.4	8.4×10^{-10}	(-5,0)	8.0×10^{-11}	(20,22)	5
HCO^+	28	9.0×10^{-10}	(-5,0)	3.9×10^{-9}	(20,22)	6
$H^{13}CO^+$	6.8×4.7	1.5×10^{-11}	(-5,0)	6.5×10^{-11}	(20,22)	6
HOC^+	27.5	4.0×10^{-12}	(-5,0)	-	(20,22)	6
CO^+	10.4	$< 5.0 \times 10^{-13}$	(-5,0)	-	(20,22)	6
DCO^+	12	-	(-5,0)	8.0×10^{-11}	(20,22)	6,7

References: (1) Pety et al. (2005); (2) Teyssier et al. (2004); (3) Agúndez et al. (2008); (4) Goicoechea et al. (2006); (5) Gerin et al. (2009); (6) Goicoechea et al. (2009b); (7) Pety et al. (2007);

abundance ratio (≥ 0.02) is inferred at the DCO^+ emission peak. These two species, namely HCO and DCO^+ thus trace two different environments in the Horsehead (see Fig. 2.4). HCO traces the warm UV-illuminated edge, while DCO^+ traces the cold UV-shielded layers of the nebula. We therefore refer to these two environments as the PDR, corresponding to the peak of the HCO emission, and the dense core, corresponding to the peak of the DCO^+ emission.

2.1.5 Chemistry in the Horsehead

Table 2.1 summarizes the molecules detected towards the PDR and dense core position in the Horsehead (*before this work*).

- **Carbon chemistry:** The carbon chemistry will be described in Chapter 4.
- **Sulfur chemistry:** The main sulfur bearing species in molecular clouds are S^+, S, SO, CS and H_2S. Because the observed abundances of these species in dark clouds are too low compared to standard chemical models predictions, it was assumed that sulfur-bearing molecules are depleted onto grains in these regions. Goicoechea et al. (2006)

studied the emission of CS and HCS^+ in the PDR of the Horsehead and found that the sulfur abundance required to reproduce the observations is very close to the solar sulfur elemental abundance. Therefore, they showed that the gas sulfur depletion in the Horsehead PDR is orders of magnitude lower than in previous studies of the sulfur chemistry. This implies that there is something important lacking in the chemical models or that an important sulfur-bearing carrier is missing.

- **Electron abundance:** The electron abundance ($[e^-] = n_e/n_H$) plays a fundamental role in the chemistry and dynamics of interstellar gas. Electron can excite molecules with large dipole moments, such as CH_3CN. Goicoechea et al. (2009b) investigated the electron abundance gradient across the edge of the Horsehead nebula, using observations of DCO^+, $H^{13}CO^+$ and HOC^+. They showed that the ionization fraction follows a steep gradient in the edge of the Horsehead, with a scale length of ~ 0.05 pc (or $\sim 25''$), from $[e^-] \simeq 10^{-4}$ (or $n_e \sim 1 - 5$ cm^{-3}) in the PDR to a few times $\sim 10^{-9}$ in the core. They also confirmed that PAH^- anions play a role in the charge balance of the cold and neutral gas if their abundance is significant ($[PAH] > 10^{-8}$).

2.2 Spectral line surveys

Unbiased spectral line surveys covering large frequency ranges are the best tools to obtain an inventory of the chemical composition. They provide as many transitions as possible for each species, with well separated upper energy levels. This makes possible to correctly identify the molecular species and to accurately compute their abundances. Therefore, line surveys have led to the discovery of most of the species detected up to date in the interstellar medium. Most of these surveys have been made toward Galactic sources where molecular lines are abundant and bright. The source sample includes the evolved star IRC +10216 (Johansson et al. 1984, 1985; Avery et al. 1992; Groesbeck et al. 1994; Cernicharo et al. 2000), the star-forming regions Sgr B2 (Cummins et al. 1986; Turner 1989, 1991; Sutton et al. 1991; Nummelin et al. 2000; Friedel et al. 2004) and Orion KL (Johansson et al. 1984, 1985; Blake et al. 1987; Jewell et al. 1989; Turner 1989, 1991; Schilke et al. 1997, 2001a; Lee et al. 2001; Comito et al. 2005; Tercero et al. 2010), and the dark cloud TMC-1 (Kaifu et al. 2004). Table 2.2 summarizes recent (sub-)millimeter line surveys towards galactic sources and galaxies. Within these surveys hundreds of spectral lines are detected, where a non-negligible fraction remains unidentified. For example, in Orion KL Tercero et al. (2010) detected 14400 spectral features, where ∼70% have been identified and attributed to 43 different molecules. In the carbon-rich star, IRC+10216, the line survey carried by Cernicharo et al. (2000) resulted in 380 lines detected, of which 317 were identified and attributed to 30 different molecules. Within the line surveys mentioned above for this source, about 60 species have been identified. In other Galaxies, less molecules have been detected. For example, in the line survey of Aladro et al. (2011) towards M82, 69 spectral features were detected corresponding to 18 different molecules.

Table 2.2: Summary of recent (sub-)millimeter line survey.

Object	Frequency range (GHz)	Telescope	Reference
Galactic sources			
IRC+10216	129–172.5	IRAM-30m	Cernicharo et al. (2000)
	488–1901	Herschel	Cernicharo et al. (2010)
Mon R2	87.5–95, 103–110.6, 204.6–220	IRAM-30m	Ginard et al. (2012)
Orion-KL	80–115.5, 130–178, 197–281	IRAM-30m	Tercero et al. (2010)
	325–360	CSO	Schilke et al. (1997)
	607–725	CSO	Schilke et al. (2001b)
	795–903	CSO	Comito et al. (2005)
	479.5–1280, 1426–1906.8	Herschel	Bergin et al. (2010)
Sgr B2	479.5–1280, 1426–1906.8	Herschel	Bergin et al. (2010)
	80–116, 201.8–204.6, 205–217.7	IRAM-30m	Belloche et al. (2013)
	80–116, 201.8–204.6, 205–217.7	IRAM-30m	Belloche et al. (2008a)
Galaxies			
Arp 220	202–242	SMA	Martín et al. (2011)
NGC 253	129–175	IRAM-30m	Martín et al. (2006)
M82	130–175, 241–260	IRAM-30m	Aladro et al. (2011)
PKS 1830-211	30–50	ATCA	Muller et al. (2011)
NGC 1068	86.2–115.6	IRAM-30m	Aladro et al. (2013)

2.3 The Horsehead WHISPER line survey

The Horsehead WHISPER (Wideband High-resolution Iram-30m Surveys at two Positions with Emir Receivers, PI: J. Pety) survey is a complete and unbiased line survey of the Horsehead. Two positions were observed, namely the PDR and the dense core. The observation of these two different positions enables a detailed comparison of the chemistry of the UV-illuminated and UV-shielded gas. The survey covers the 3, 2 and 1 mm bands with an unprecedented combination of bandwidth (36GHz at 3mm, 25GHz at 2mm and 76GHz at 1mm), high spectral resolution (49 kHz at 3 and 2 mm; and 195 kHz at 1 mm), and high sensitivity (median noise 8.1 mK, 18.5 mK and 8.3mK, respectively). The total telescope time used to complete this project is ∼145 hours.

Fig.2.5 shows the full survey in the three bands for the two positions. The number of lines detected per band (with $S/N > 5$) at each positions are shown in the left panel of Fig. 2.6. Most of the detected lines are in the 3 mm band at both positions. The 2 mm spectrum has the lowest sensitivity of the three spectra and covers a smaller frequency range, which could explain the low number of detected lines compared to the other bands. This is because the 2 mm EMIR reciever at the 30 m was a SSB (Single Side Band, 4 GHz bandwidth) receiver, while the 1 and 3 mm EMIR receivers are 2SB (side band separated mixers, 8 GHz bandwidth) receivers. The 2 mm EMIR receiver has been upgraded to a 2SB mixer at the end of September 2013. From now on, it will thus be possible to do 2 mm line surveys with similar sensitivity to those at 3 and 1 mm, in a similar observing time. In the right panel of Fig. 2.6, the distribution of the density of detected lines (with $S/N > 5$) is shown. The line density is, on average, 5 lines/GHz (3 mm), 1 lines/GHz (2 mm) and 1 lines/GHz (1 mm)

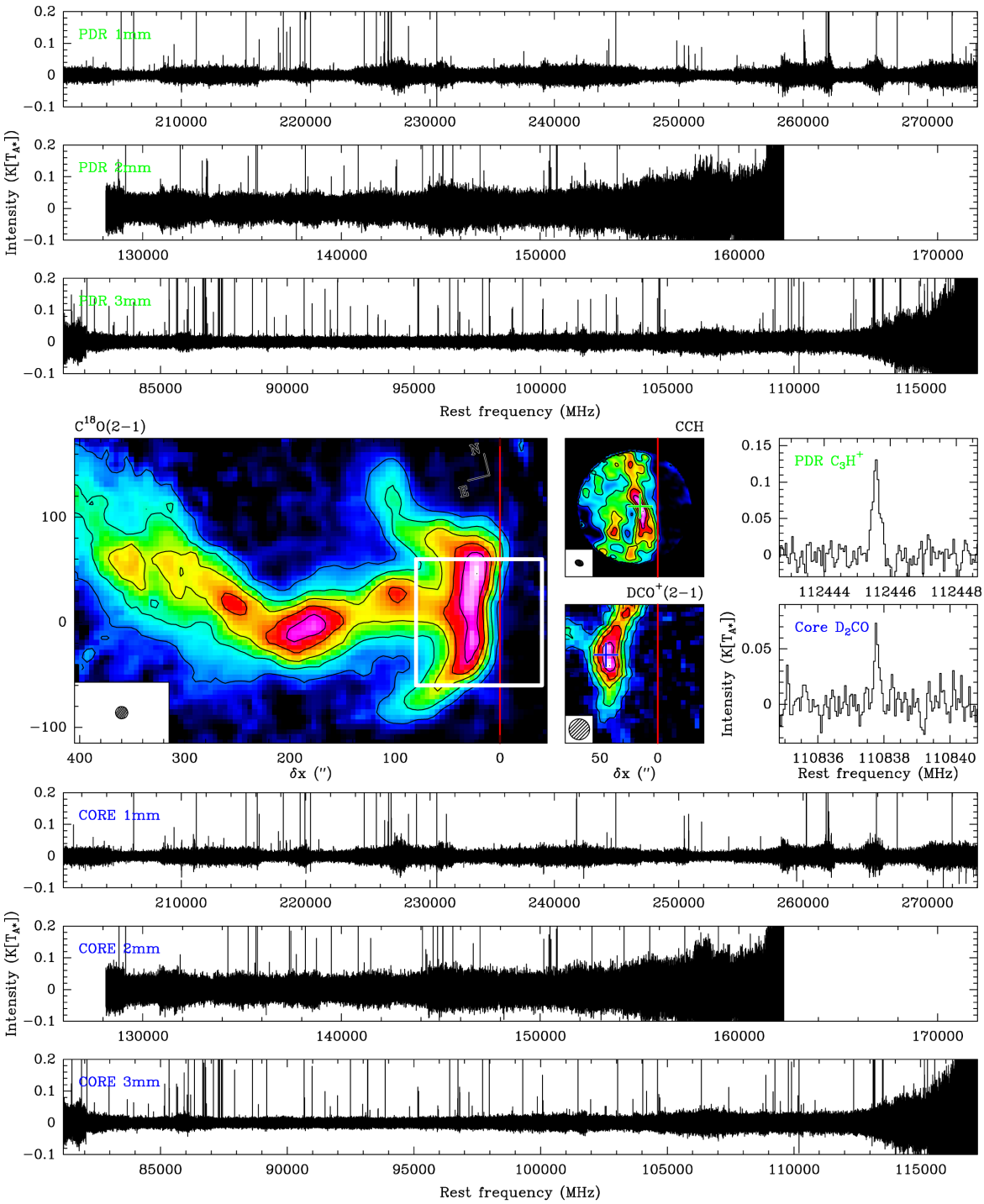

Figure 2.5: 1 mm, 2 mm and 3 mm spectra at two positions located inside the white square on the $C^{18}O(2-1)$ integrated emission map (wide, left image; IRAM-30 m/HERA; Hily-Blant et al. 2005): 1) the PDR marked by the green cross on the CCH emission map (middle, top image; IRAM-PdBI; Pety et al. 2005), and 2) the dense core marked by the blue cross on the DCO^+ emission map (middle, bottom image; IRAM-30 m/CD; Pety et al. 2007). The middle right panels display two lines zoomed from the line surveys.

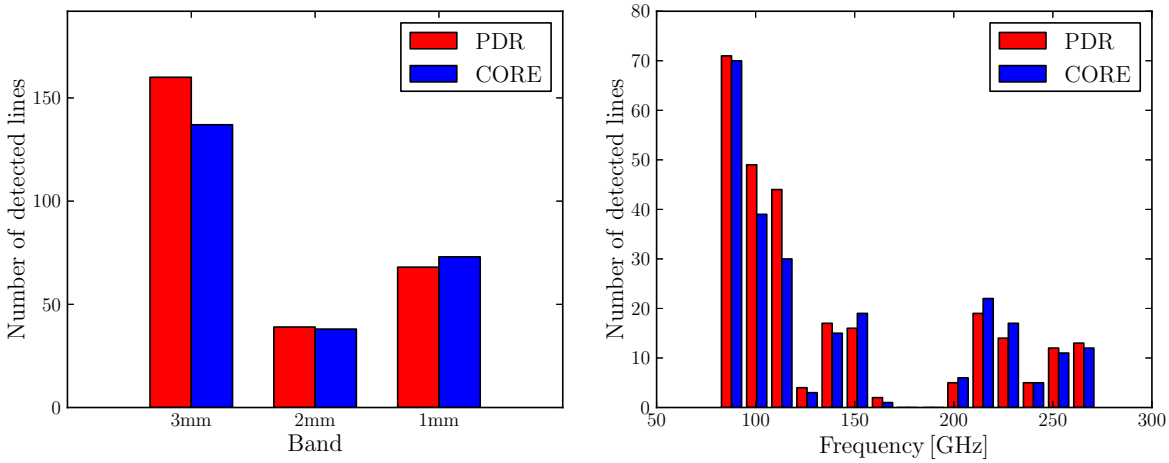

Figure 2.6: *Left:* Total number of lines detected at the PDR and dense core in each band. *Right:* Distribution of the density of lines (averaged over 15 GHz intervals) detected at the PDR and dense core.

at the PDR, and 4 lines/GHz (3 mm), 1 lines/GHz (2 mm) and 1 lines/GHz (1 mm) at the dense core. It is interesting to note that a similar number of lines are detected at the PDR and dense core positions.

A cumulative distribution of the number of lines as a function of their integrated intensities is shown in Fig. 2.7. The number of lines with integrated intensities larger than 0.1 and 10 $\mathrm{K\,km\,s^{-1}}$ can be roughly fitted by a power law of slope -0.9. The power law breaks down at the lower and higher end of the distribution. The same slope has been found in other millimeter surveys (e.g., Schilke et al. 2001b; Comito et al. 2005; Caux et al. 2011).

At the PDR, the total line flux is 77, 11 and 68 $\mathrm{K\,km\,s^{-1}}$ at 3, 2 and 1 mm, respectively. At the dense core, the total line flux is 88, 20 and 69 $\mathrm{K\,km\,s^{-1}}$ at 3, 2 and 1 mm, respectively. Around 75% of the total line flux is due to the emission of CO and its isotopologues at both positions. The contribution of molecular lines to the total flux at 1.2 mm is estimated to be 14% at the PDR and 16% at the dense core.

The species detected (with $S/N > 5$) and identified in the survey are listed in Table 2.3. Approximately 30 species (plus their isotopologues) are detected with up to 7 atoms in the PDR and the dense core. In Table 2.3, the species in red are only detected at the PDR, while the species in blue are only detected at the dense core. Species in black are detected at both positions. It is interesting to note that most of the species are detected at both positions. However, for a few species, the emission detected at one of the positions is actually beam pick-up from the other position (e.g., CF^+). In addition, for a few species detected at the dense core, the emission arises from the illuminated skin of the cloud and not from the dense core itself (e.g., HCO). A few species are detected only at one of the two positions, and show the different chemistries present in the PDR and dense core. The dense core is characterized by the presence of deuterated species (e.g., CCD, D_2CO, DCN and N_2D^+), while the PDR is characterized by the presence of radicals and reactive species (e.g., $HOC^+$and ^{13}CCH).

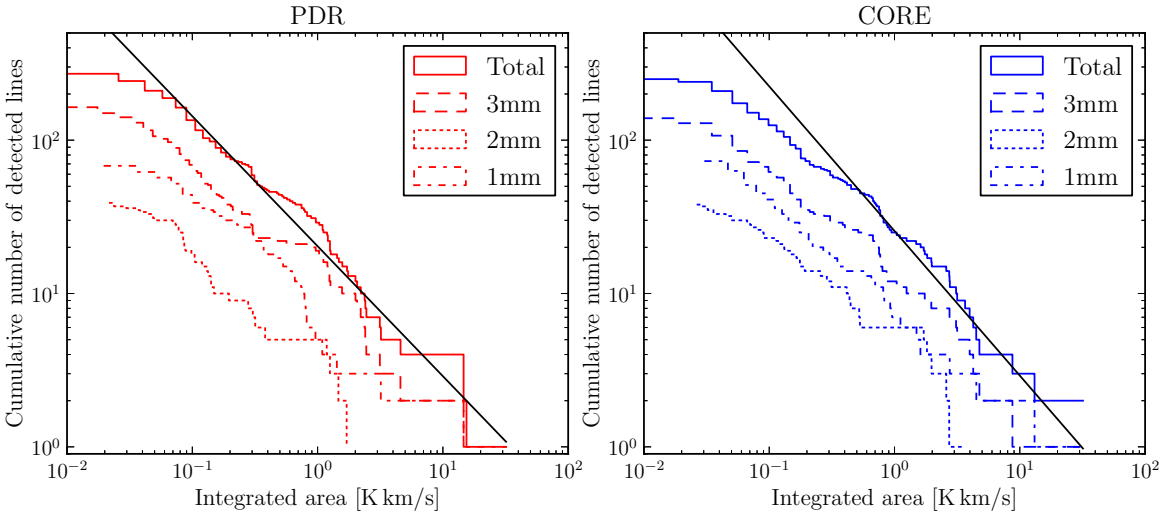

Figure 2.7: Number of lines with integrated line areas larger than a given threshold. The solid line shows the best power-law fit for integrated intensities between 0.1 and 10 $\mathrm{K\,km\,s^{-1}}$.

Table 2.3: Summary of species detected in the Horsehead WHISPER line survey with $S/N \geq 5$. Species in blue are only detected in the dense core, and species in red are only detected in the PDR. Species in black are detected in both positions.

^{12}CO	$c-C_3H$	$HC^{17}O^+$	CH_3CCH	$HN^{13}C$	NH_2D	HDS
^{13}CO	$l-C_3H$	HOC^+	CN	$H^{15}NC$	N_2D^+	H_2CS
$C^{17}O$	$c-C_3H_2$	H_2CO	^{13}CN	CH_3CN	CS	SO
$C^{18}O$	$l-C_3H_2$	$H_2{}^{13}CO$	$C^{15}N$	CH_3NC	^{13}CS	SO_2
$^{13}C^{18}O$	C_3HD	CH_3OH	HCN	HC_3N	$C^{33}S$	^{34}SO
C_2H	HCO	CH_2CO	HNC	CCO	$C^{34}S$	SO^+
CCD	DCO^+	CH_3CHO	DCN	NO	CCS	NS
^{13}CCH	HCO^+	HDCO	DNC	HNO	OCS	SiO
$C^{13}CH$	$H^{13}CO^+$	D_2CO	$H^{13}CN$	HNCO	HCS^+	CF^+
C_4H	$HC^{18}O^+$	HCOOH	$HC^{15}N$	N_2H^+	HDCS	

Part I

Simple molecules

Chapter 3

CF^+ Fluoromethylidynium

In this section, I will present the results of the first paper in the Horsehead WHISPER line survey series, which consists in the second detection of CF^+ in the ISM.

3.1 Introduction

Of the ∼180 molecules that have been detected in the interstellar medium or in circumstellar envelopes so far, ∼85% contain one or more of the following elements: hydrogen, carbon, nitrogen, oxygen, silicon and sulfur, and only 3 molecules contain fluorine. These are HF, CF^+ and AlF. The first two have been detected in the interstellar medium, while AlF has only been detected in the envelope of the carbon-rich object IRC +10216 (Cernicharo & Guelin 1987; Ziurys et al. 1994).

3.1.1 Fluorine chemistry

Fluorine atoms are unique because they can react exothermically with H_2 to form HF, the only neutral diatomic hydride which is more strongly bound than H_2 (the dissociation energy of HF is 5.87 eV, while the one of H_2 is 4.48 eV). As a consequence theoretical models predict that HF will become the dominant fluorine reservoir in molecular clouds ($H_2/H > 1$), over a wide range of physical conditions (Zhu et al. 2002; Neufeld et al. 2005; Neufeld & Wolfire 2009). The fluorine chemistry is thus initiated by reactions between F and H_2,

$$F + H_2 \rightarrow HF + H. \tag{3.1}$$

HF is destroyed by photodissociation, and by reactions with He^+, H_3^+ and C^+. The reactions with C^+ lead to the formation of the fluoromethylidynium ion, CF^+,

$$HF + C^+ \rightarrow CF^+ + H \tag{3.2}$$

In UV-irradiated cloud surfaces where C^+ is abundant, CF^+ is expected to be the second most important fluorine reservoir. In these regions, HF will remain the dominant reservoir of fluorine, but CF^+ can account for as much as $\sim 1\%$ of the gas-phase fluorine abundance (Neufeld & Wolfire 2009). CF^+ is destroyed mainly by reactions with electrons, but photodissociation can be important in regions that are exposed to strong radiation fields,

$$CF^+ + e^- \rightarrow C + F \tag{3.3}$$

$$CF^+ + h\nu \rightarrow C^+ + F. \tag{3.4}$$

3.1.2 CF^+ and HF in the interstellar medium

Following the theoretical study of Neufeld et al. (2005), which predicted that CF^+ could be abundant enough to be detected in UV-irradiated cloud surfaces, where C^+ is the dominant carbon reservoir, the authors searched for the low-energy rotational lines of CF^+ toward the Orion Bar. Neufeld et al. (2006) reported the first detection of the $J = 1 - 0$, $J = 2 - 1$ and $J = 3 - 2$ rotational transitions of CF^+, and infer a CF^+ abundance of $\sim 10^{-10}$. This provided support to the theoretical model of fluorine chemistry, and opened the possibility of detecting the $J = 1 - 0$ transition of HF with Herschel in the following years.

HF was detected for the first time in its $J = 2 - 1$ transition (2.5 THz) by Neufeld et al. (1997). The line was observed in absorption toward the far-infrared continuum source Sgr B2, with the Infrared Space Observatory (ISO) at low spectral resolution. More recently, the HF $J = 1 - 0$ transition at 1.2 THz has been routinely observed with Herschel/HIFI at high spectral resolution, towards the envelope of the carbon star IRC +10216 (Agúndez et al. 2011), and also in absorption against strong continuum sources (e.g., Neufeld et al. 2010; Sonnentrucker et al. 2010; Monje et al. 2011a; Emprechtinger et al. 2012). These studies revealed that HF is ubiquitous in Galactic molecular clouds and has the potential to become an excellent tracer of molecular gas in diffuse clouds. From observations of ^{13}CO and CH, they estimated the H_2 column density, and derived a relative abundance of $N(HF)/N(H_2) = (1 - 2) \times 10^{-8}$ in diffuse molecular clouds, with an average value of 1.4×10^{-8}. This value is about two times lower than the abundance predicted by theory of $N(HF)/N(H_2) = 3.6 \times 10^{-8}$, if one assumes the interstellar gas-phase abundance of fluorine to be $N(F)/N_H = 1.8 \times 10^{-8}$. This last value is the one found in diffuse cloud sight lines, where fluorine is expected to be mainly in its atomic form (Federman et al. 2005; Snow et al. 2007).

More recently, Indriolo et al. (2013) derived the abundance ratio $N(HF)/N(H_2)$ in diffuse molecular clouds towards three background sources, where the H_2 column density was previously determined directly from observations of H_2. This allowed them to remove the uncertainties associated to the relation between the column density of H_2 and the tracer molecule (CH and CO), and compute a more accurate value for the HF abundance. They derived relative abundances of $N(HF)/N(H_2) = (0.3 - 1.2) \times 10^{-8}$, which are well below the predicted value, but in agreement with the previous studies. They also detected HF absorption from warm gas associated with a massive protostar. They derived $N(HF)/N(H_2) = (1.7 - 2.9) \times 10^{-8}$ for this component. The observed underabundance of gas-phase HF compared to the predicted value if nearly all gas-phase fluorine is in the form of HF may indicate that 1) the gas-phase abundance of fluorine is lower than expected, 2) not all fluorine is in its molecular form, which could be due to a larger destruction rate of HF, and/or 3) it could also be the result of the freeze-out of HF onto dust grains.

Besides diffuse foreground clouds, HF has been detected in dense molecular clouds, in absorption toward the high-mass star-forming region Orion KL (Phillips et al. 2010) and in NGC 6334 I (Emprechtinger et al. 2012). A lower limit on the HF abundance of $N(HF)/N(H_2) = (1.6 - 5.0) \times 10^{-10}$ was found for these sources, which is ∼100 times lower than the HF abundance found in diffuse clouds, suggesting that HF is efficiently depleted onto grains in dense regions.

HF has also been detected in emission toward the Orion Bar photodissociation region (van

der Tak et al. 2012). They find a relative abundance of $N(\mathrm{HF})/N(\mathrm{H_2}) = (3-4)\times10^{-8}$, which is consistent with the theoretical prediction. Finally, HF has been detected in extragalactic sources, including active galactic nuclei (AGNs), Mrk 231 (van der Werf et al. 2010), Arp 220 (Rangwala et al. 2011) and the Cloverleaf (Monje et al. 2011b).

3.1.3 The importance of C^+

C^+ is a key species in the interstellar medium. It is an important tracer of the neutral gas where CO has not yet been able to form (Langer et al. 2010). C^+ is present in the warm ionized medium, e.g., HII regions. It is the dominant gas phase reservoir of carbon in the diffuse interstellar medium and its fine structure transition, that lies at 1.9 THz (158μm), is the main cooling mechanism of the diffuse gas. The cooling of the gas, which allows the gas to compress, is a crucial step in the star formation process. Herschel/HIFI has observed this line in the ISM (e.g., GOT C^+ key program by Langer et al. 2010) but with limited spatial resolution (12"). It is now also possible to observe this line with SOFIA at 15" resolution (e.g., Mookerjea et al. 2012). It is possible to observe the C^+ line with ALMA in high-redshift galaxies. Unfortunately, we cannot obtain interferometric observations of C^+ in the local Universe, because its rest-frame emission cannot be observed from ground-based telescopes. It is therefore of great interest to find tracers of C^+ that can be observed from the ground at much higher spatial resolution, for example with ALMA and NOEMA.

3.1.4 CF+ hyperfine structure

CF^+ has a non-zero nuclear spin ($I = 1/2$). The coupling between the rotational angular momentum J and the spin angular momentum I, through $\mathbf{F} = \mathbf{J} + \mathbf{I}$, produces the splitting of the energy levels. The total angular momentum F can have the values $F = I + J, I + J - 1, ..., |I - J|$. The energy of the resulting hyperfine structure is given by

$$E = E_J + \frac{C_I}{2}[F(F+1) - I(I+1) - J(J+1)] \tag{3.5}$$

where C_I is the spin rotation constant. This way, the energy of the low-lying rotational levels ($E_{J,F}$) is

- $J = 0$, $F = \frac{1}{2}$

$$E_{0,\frac{1}{2}} = 0 \tag{3.6}$$

- $J = 1$, $F = \frac{1}{2}, \frac{3}{2}$

$$E_{1,\frac{1}{2}} = E_1 - C_I \tag{3.7}$$

$$E_{1,\frac{3}{2}} = E_1 + \frac{C_I}{2} \tag{3.8}$$

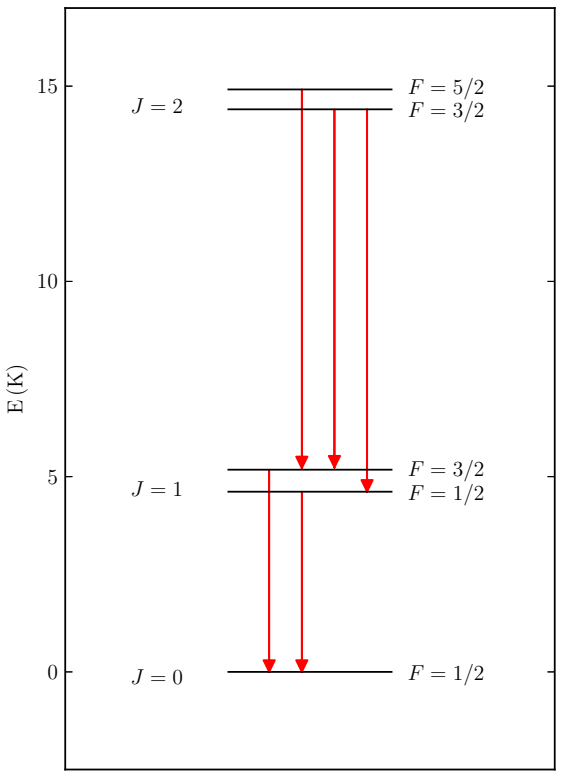

Figure 3.1: Lower energy level diagram of CF^+. The hyperfine splitting of the $J = 1$ and $J = 2$ levels is not to scale. The arrows indicate the transitions detected in the Horsehead.

- $J = 2$, $F = \frac{3}{2}, \frac{5}{2}$

$$E_{2,\frac{3}{2}} = E_2 - \frac{3}{2}C_I \tag{3.9}$$

$$E_{2,\frac{5}{2}} = E_2 + C_I \tag{3.10}$$

A diagram is shown in Fig. 3.1 with the low-energy levels of CF^+. The frequency splitting of the two hyperfine lines is equal to 3/2 C_I for the $J = 1 - 0$ transition. For the $J = 2 - 1$ transition, there are three hyperfine lines separated by C_I and 5/2 C_I from the strongest transition (Townes & Schawlow 1975).

3.2 Detection of CF^+ in the Horsehead

We detected the $J = 1 - 0$ and $J = 2 - 1$ low-energy rotational lines of CF^+ towards the PDR and dense core positions in the Horsehead (see Fig. 3.1). This is the second detection of this species in the ISM. The region was also mapped in both transitions to study the spatial distribution of the emission. The results are published in Guzmán et al. (2012a) and Guzmán et al. (2012b), and here we summarize the main results.

3.2.1 Results

- We find that the emission arises mostly at the illuminated edge of the nebula, but it is also detected towards the dense core arising from its lower density skin. Because the theoretical models predict that there is a significant overlap between CF^+ and C^+, we propose that CF^+ can be used as a proxy of C^+, that can be observed from ground-based telescopes, unlike C^+ for which we need to go to space.

- We derive a column density of $N(CF^+) = (1.5 - 2.0) \times 10^{12}$ cm^{-2} in the PDR position, and an upper limit of $N(CF^+) \leq 4.4 \times 10^{11}$ cm^{-2} towards the dense core. This translates into an abundance of $(4.9 - 6.5) \times 10^{-10}$ with respect to H nuclei in the PDR.

- Given the simple chemistry of fluorine, the CF^+ column density is proportional to the column density of HF. Hence, if all fluorine is in its molecular form, the elemental abundance of fluorine can be derived directly from CF^+ observations. We infer F/H $= (0.6 - 1.5) \times 10^{-8}$ in good agreement with the one found in diffuse molecular clouds (Sonnentrucker et al. 2010), and somewhat lower than the solar value (Asplund et al. 2009) and the one found in the diffuse atomic gas (Snow et al. 2007).

- The CF^+ $J = 1 - 0$ line is double-peaked in contrast to other millimeter lines in the Horsehead, and the one detected in the Orion Bar. The double-peaked profile was first thought to be of kinematic origin, but these observations stimulated the theoretical computation of the fluorine spin rotation constant of CF^+ in order to see if the two peaks corresponded to the hyperfine components of CF^+. The CF^+ spin rotation constant was determined by means of quantum chemical calculations by J. Gauss. The derived theoretical value is $C_I = 229.2$ kHz. This value is higher than, e.g., the ^{13}CO value of 32.6 kHz (Cazzoli et al. 2004). This makes CF^+ a spectroscopically peculiar ion. Indeed, in Guzmán et al. (2012a), when the CF^+ spin rotation constant was not known, we extrapolated from the spectroscopy of ^{13}CO, and significantly underestimated the hyperfine splitting of the $J = 1 - 0$ line by assuming a value of about 165 kHz. The computed value of the spin rotation constant agrees with the fact that the hyperfine splittings were not observed in the experiments of Cazzoli et al. (2010). We find that the observed line profile is well fitted by the computed hyperfine components. The observed CF^+ double-peak line profile can then be fully explained spectroscopically. Because lines are broader in the Orion Bar, the CF^+ hyperfine splitting was not resolved there. The Horsehead, showing narrow emission lines, is a good laboratory for precise spectroscopic studies of species present in UV-illuminated environments.

A&A 543, L1 (2012)
DOI: 10.1051/0004-6361/201219449

Astronomy & Astrophysics

Letter to the Editor

The IRAM-30m line survey of the Horsehead PDR

I. CF^+ as a tracer of C^+ and as a measure of the fluorine abundance

V. Guzmán[1], J. Pety[1,2], P. Gratier[1], J. R. Goicoechea[3], M. Gerin[2], E. Roueff[4], and D. Teyssier[5]

[1] IRAM, 300 rue de la Piscine, 38406 Saint Martin d'Hères, France
e-mail: [guzman;pety;gratier]@iram.fr
[2] LERMA – LRA, UMR 8112, Observatoire de Paris and École normale Supérieure, 24 rue Lhomond, 75231 Paris, France
e-mail: maryvonne.gerin@lra.ens.fr
[3] Centro de Astrobiología, CSIC-INTA, Carretera de Ajalvir, Km 4, Torrejón de Ardoz, 28850 Madrid, Spain
e-mail: jr.goicoechea@cab.inta-csic.es
[4] LUTH UMR 8102, CNRS and Observatoire de Paris, Place J. Janssen, 92195 Meudon Cedex, France
e-mail: evelyne.roueff@obspm.fr
[5] European Space Astronomy Centre, ESA, PO Box 78, 28691 Villanueva de la Caada, Madrid, Spain
e-mail: dteyssier@sciops.esa.int

Received 20 April 2012 / Accepted 2 June 2012

ABSTRACT

C^+ is a key species in the interstellar medium, but its 158 μm fine structure line cannot be observed from ground-based telescopes. Current models of fluorine chemistry predict that CF^+ is the second-most important fluorine reservoir in regions where C^+ is abundant. We detected the $J = 1–0$ and $J = 2–1$ rotational lines of CF^+ with high signal-to-noise ratio toward the photo-dissociation region and dense core positions in the Horsehead. Using a rotational diagram analysis, we derive a column density of $N(CF^+) = (1.5–2.0) \times 10^{12}$ cm^{-2}. Because of the simple fluorine chemistry, the CF^+ column density is proportional to the fluorine abundance. We thus infer the fluorine gas-phase abundance to be F/H = $(0.6–1.5) \times 10^{-8}$. Photochemical models indicate that CF^+ is found in the layers where C^+ is abundant. The emission arises in the UV-illuminated skin of the nebula, tracing the outermost cloud layers. Indeed, CF^+ and C^+ are the only species observed to date in the Horsehead with a double-peaked line profile caused by kinematics. We therefore propose that CF^+, which is detectable from the ground, can be used as a proxy of the C^+ layers.

Key words. astrochemistry – ISM: clouds – ISM: molecules – ISM: individual objects: Horsehead nebula – radio lines: ISM

1. Introduction

C^+ is a key species in the interstellar medium. First, it is an important tracer of the neutral gas where CO has not yet been able to form (Langer et al. 2010). Second, it is the dominant gas phase reservoir of carbon in the diffuse interstellar medium and its fine structure transition ($^2P_{3/2}$–$^2P_{1/2}$ 157.8 μm, 1.9 THz) is the main cooling mechanism of the diffuse gas. Unfortunately, its rest-frame emission cannot be observed from ground-based telescopes. With *Herschel* and SOFIA it is now possible to observe this line from space and from the stratosphere, respectively, but with limited spatial resolution (12″ and 15″, respectively). It is therefore of great interest to find tracers of C^+ that can be observed from the ground at much higher spatial resolution, for example with the Atacama Large Millimeter Array (ALMA) or the NOrthern Extended Millimeter Array (NOEMA).

The chemistry of fluorine was studied by Neufeld et al. (2005). Although there are still uncertainties in some reaction rate coefficients (e.g. CF^+ photodissociation), the current models predict that CF^+ is present in regions where C^+ and HF are abundant, because it is produced by reactions between these species and destroyed mainly by electrons. In these regions CF^+ is the second-most important fluorine reservoir after HF. The ground rotational transition of HF, which lies at THz frequencies, was first detected with the *Herschel*/HIFI in the diffuse interstellar medium through absorption measurements (Neufeld et al. 2010) and in emission in the Orion Bar (van der Tak et al. 2012). Neufeld et al. (2010) found a lower limit for the HF abundance of 6×10^{-9} relative to hydrogen nuclei, providing support to the theoretical prediction that HF is the dominant fluorine reservoir among a wide variety of interstellar conditions. Unlike HF and C^+, CF^+ rotational lines can be observed from the ground. However, up to now there has been only one detection of CF^+ toward the Orion Bar (Neufeld et al. 2006).

In this Letter we report the detection of CF^+ at the HCO and DCO^+ peak emission, corresponding to the photo-dissociation region (PDR) and dense core environments in the Horsehead nebula, respectively (Pety et al. 2007; Gerin et al. 2009). We then infer the gas phase fluorine abundance.

2. Observations and data reduction

Figure 1 displays deep integrations of the $J = 1–0$ and $J = 2–1$ low-energy rotational lines of CF^+ with the IRAM-30m telescope centered at the PDR and the dense core, located at (δRA, δDec) = (−5″, 0″) and (20″, 22″) with respect to the projection center, with 49 kHz spectral resolution at both frequencies. These observations were obtained as part of the Horsehead WHISPER project (Wideband High-resolution Iram-30m Surveys at two Positions with Emir Receivers). A presentation of the whole survey and the data reduction process will be given in Pety et al. (in prep.).

Table 1. Observation parameters for the maps.

Line	Frequency GHz	Instrument	$F_{\rm eff}$	$B_{\rm eff}$	Beam arcsec	PA °	Int. time[a] h	$T_{\rm sys}$ K ($T_{\rm A}^*$)	Noise K ($T_{\rm mb}$)	Obs. date
HCO $1_{0,1}$ 3/2, 2–$0_{0,0}$ 1/2, 1	86.670760	PdBI/C&D	0.95	0.78	6.7×4.4	16	6.5	150	0.09	2006–2007
CF^+ 1–0	102.587533	30 m/EMIR	0.94	0.79	25.4	0	2.5	88	0.03[b]	Jan. 2012
CF^+ 2–1	205.170520	30 m/EMIR	0.94	0.64	11.4	0	3.4	220	0.18[c]	Jan. 2012
DCO^+ 3–2	216.112582	30 m/HERA	0.90	0.52	11.4	0	1.5	230	0.10	Mar. 2006

Notes. Their projection center is $\alpha_{2000} = 05^{\rm h}40^{\rm m}54.27^{\rm s}$, $\delta_{2000} = -02°28'00''$. [(a)] On-source integration time. The noise values are for a spectral resolution of [(b)] 0.114 km s^{-1} and [(c)] 0.057 km s^{-1}.

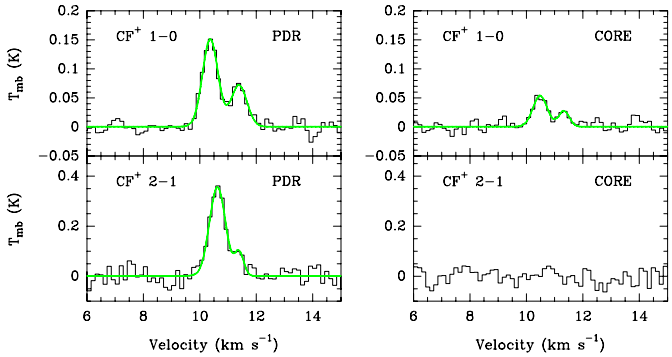

Fig. 1. Deep integrations toward the PDR and core positions. The green lines are double Gaussian fits.

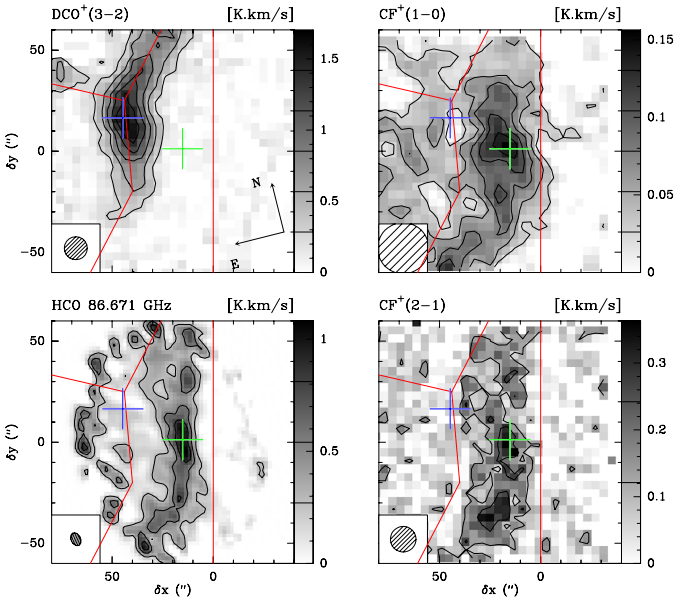

Fig. 2. Integrated intensity maps of the Horsehead edge. Maps were rotated by 14° counter-clockwise around the projection center, located at $(\delta x, \delta y) = (20'', 0'')$, to bring the exciting star direction in the horizontal direction and the horizontal zero was set at the PDR edge, delineated by the red vertical line. The crosses show the positions of the PDR (green) and the dense core (blue). The spatial resolution is plotted in the bottom left corner. Values of the contour levels are shown in the color look-up table of each image (first contour at 2σ and 2.5σ for CF^+1–0 and 2–1 respectively). The emission of all lines is integrated between 10.1 and 11.1 km s^{-1}.

The CF^+ $J = 1$–0 and $J = 2$–1 maps displayed in Fig. 2 were observed simultaneously during seven hours of good winter weather (2 mm of precipitable water vapor) using the EMIR sideband-separation receivers at the IRAM-30m. We used the position-switching, on-the-fly observing mode. The off-position offsets were (δRA, δDec) = ($-100''$, $0''$), i.e. into the HII region ionized by σOri and free of molecular emission. We observed along and perpendicular to the direction of the exciting star in zigzags, covering an area of $100'' \times 100''$. A description of the HCO and DCO^+ observations and data reductions, which are also displayed in Fig. 2, can be found in Gerin et al. (2009) and Pety et al. (2007). Table 1 summarizes the observation parameters for all these maps.

The maps were processed with the GILDAS[1] softwares (Pety 2005). The IRAM-30m data were first calibrated to the $T_{\rm A}^*$ scale using the chopper-wheel method (Penzias & Burrus 1973), and finally converted into main-beam temperatures ($T_{\rm mb}$) using the forward and main-beam efficiencies ($F_{\rm eff}$ & $B_{\rm eff}$) displayed in Table 1. The resulting amplitude accuracy is ~10%. The resulting spectra were then baseline-corrected and gridded through convolution with a Gaussian to obtain the maps.

3. Results

3.1. Line profiles

Two velocity peaks for the $J = 1$–0 line are clearly seen at both positions in Fig. 1. The second velocity peak is marginal for the $J = 2$–1 line. Table 2 presents the results of dual Gaussian fits. The centroid velocity of each peak is significantly shifted between the two CF^+ transitions. We have carefully checked that neither peak is a residual line incompletely rejected from the image side band. This doubled-peak behavior is unexpected because all species without an hyperfine structure detected previously at millimeter wavelengths in the Horsehead present a simple velocity profile centered close to 10.7 km s^{-1}. The only other species detected to date with a clear double peak emission profile is C^+ toward the illuminated edge of the cloud (*Herschel*/HIFI, Teyssier et al., in prep.).

The most obvious explanation would be that the higher velocity peak corresponds to another line from another species. However, there are no other lines in the public line catalogs (Pickett et al. 1998; Müller et al. 2001) near this frequency besides CF^+. Another possible explanation would be that the two peaks correspond to different hyperfine components that are caused by the fluorine nuclei. To our knowledge, there are no hyperfine structure studies on CF^+. However, because the molecule is isoelectronic with CO, one can try to rely on ^{13}CO spectroscopy since the nuclear spin of ^{13}C is 1/2, as for the fluorine nucleus. The magnetic dipolar coupling constant scales approximately with the rotational constant and the magnetic moment of the nucleus for $^1\Sigma$ electronic ground states (Reid & Chu 1974). This allows us to derive a coupling constant of approximately 110 kHz, and an hyperfine splitting of 165 kHz (110 kHz) for the $J = 1$–0 ($J = 2$–1) transitions, well below

[1] See http://www.iram.fr/IRAMFR/GILDAS for more information about the GILDAS softwares.

Table 2. Gaussian fit results.

Line	Line area K km s^{-1}	Velocity km s^{-1}	Width km s^{-1}	T_{peak} K
		PDR		
CF$^+$ J = 1−0	0.10 ± 0.01	10.36 ± 0.02	0.65 ± 0.04	0.15
	0.05 ± 0.01	11.38 ± 0.03	0.66 ± 0.09	0.07
CF$^+$ J = 2−1	0.25 ± 0.02	10.62 ± 0.02	0.67 ± 0.06	0.36
	0.04 ± 0.02	11.39 ± 0.06	0.38 ± 0.17	0.09
		CORE		
CF$^+$ J = 1−0	0.03 ± 0.01	10.47 ± 0.04	0.60 ± 0.08	0.05
	0.01 ± 0.01	11.32 ± 0.06	0.45 ± 0.20	0.03
CF$^+$ J = 2−1	<0.05[a]	10.7[a]	0.5[a]	0.09[a]

Notes. [(a)] Upper limit for a fixed velocity, linewidth and a $T_{peak} = 2\sigma_{rms}$.

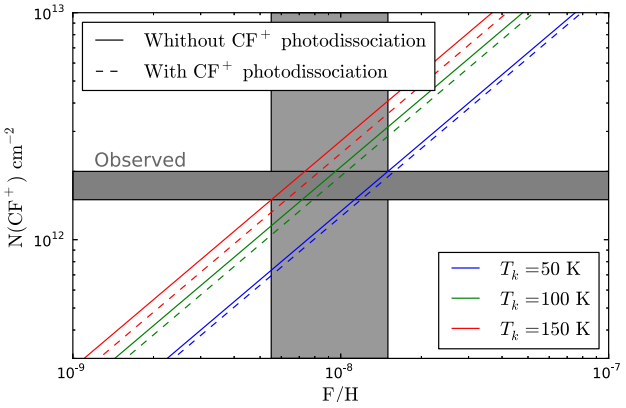

Fig. 3. Relation between the CF$^+$ column density and F/H.

the observations. In addition, the respective intensities do not follow the theoretical predictions. Therefore, this possibility is unlikely. The profile is not caused by self-absorption because the CF$^+$ opacities are low ($\tau \lesssim 1$). We therefore attribute the complex line profiles to kinematics in the CF$^+$ emitting layers.

3.2. CF$^+$ spatial distribution

Figure 2 presents the CF$^+$, HCO and DCO$^+$ integrated line intensity maps. The CF$^+$ emission is concentrated toward the edge of the Horsehead, delineating the western edge of the DCO$^+$ emission. A more extended and fainter emission is detected in the CF$^+$ J = 1−0 map but not in the J = 2−1 map, which has a lower signal-to-noise ratio. The intensity peak of the CF$^+$ J = 1−0 line coincides with the intensity peak of the HCO emission (shown by the green cross), which traces the far-UV illuminated matter (Gerin et al. 2009). The J = 2−1 transition also peaks near the HCO emission peak.

We have checked that beam pick-up contamination from the PDR is negligible at the core position (<7%), even with the large beam size (~25″) of the 30 m at 102 GHz. The emission then arises in the line of sight toward the core but not necessarily in the cold gas associated with the core. Indeed, we expect the CF$^+$ emission to arise in the outer layers of the nebula, delineating the edge as shown by the maps. This emission is likely to arise in the warmer and more diffuse material of the skin layers toward the core line of sight. Furthermore, there is a minimum of the emission in the CF$^+$1−0 map toward the dense core position. This confirms that the CF$^+$ emission is associated to the diffuse envelope. Molecular emission from the lower density cloud surface was already mentioned by Goicoechea et al. (2006) and Gerin et al. (2009) to explain the CS and HCO emission, respectively.

3.3. Column densities and abundances

The CF$^+$ column density was estimated assuming that the emission is optically thin and that the emission fills the 30 m beam. We inferred an excitation temperature of 10 K, based on a rotational diagram built with the integrated line intensities of the two detected transitions. Assuming T_{ex} = 10 K for all rotational levels, the beam averaged column density is $\simeq(1.5–2.0)\times10^{12}$ cm^{-2} in the PDR. This value is similar to the column density found in the Orion Bar by Neufeld et al. (2006). In the next section, we will show that the CF$^+$ emission arises at the illuminated edge of the nebula. Goicoechea et al. (2009a) found that the [O I]63 μm fine structure line, which also arises at the edge of the nebula, was best reproduced with a gas density of $n_H \simeq 10^4$ cm^{-3}. Thus, assuming this density and a cloud depth $l \sim 0.1$ pc (Habart et al. 2005), the CF$^+$ column density translates into an abundance of $\simeq(4.9–6.5) \times 10^{-10}$ with respect to H nuclei. Taking the same excitation temperature of 10 K, we computed a column density toward the core of $\simeq 4.4 \times 10^{11}$ cm^{-2}. We consider this as an upper limit for the model in Sect. 3.4 because CF$^+$ is found in the surface layer, which is not taken into account by our unidimensional photochemical model.

3.4. CF$^+$ chemistry

CF$^+$ is formed through the following chemical path:

$$F + H_2 \rightarrow HF + H$$

$$HF + C^+ \xrightarrow{k_1} CF^+ + H$$

and destroyed by dissociative recombination with electrons (Neufeld et al. 2006) and by far-UV photons:

$$CF^+ + e^- \xrightarrow{k_2} C + F$$

$$CF^+ + h\nu \xrightarrow{k_{pd}} C^+ + F.$$

The reactions rates are $k_1 = 7.2 \times 10^{-9}(T/300)^{-0.15}$ cm^3 s^{-1} (Neufeld et al. 2005) and $k_2 = 5.3 \times 10^{-8}(T/300)^{-0.8}$ cm^3 s^{-1} (Novotny et al. 2005). The CF$^+$ photodissociation rate k_{pd} is not known. Nevertheless, assuming a rate of 10^{-9} exp($-2.5\,A_V$) s^{-1}, we estimate that this contribution is negligible compared to the dissociative recombination in low far-UV field PDRs like the Horsehead. However, it might not be negligible in regions with high-radiation fields ($\chi \simeq 10^4–10^5$), like the Orion Bar. In the following we therefore assumed that $k_{pd} = 0$. Because 1) the fluorine chemistry is simple, 2) the electron abundance is given by the ionization of carbon $n(e-) \sim n(C^+)$ and 3) HF is the major reservoir of fluorine $n(HF) \sim n(F)$, it can be shown that the CF$^+$ column density is proportional to the fluorine gas phase abundance ([F] = F/H), i.e.

$$N(CF^+) \simeq \frac{k_1}{k_2}[F]\, n_H\, l \qquad \left[\mathrm{cm}^{-2}\right].$$

From our CF$^+$ observations we find F/H $\simeq$ (0.6–1.5) $\times 10^{-8}$ in the Horsehead PDR (see Fig. 3), in good agreement with the solar value (2.6×10^{-8}; Asplund et al. 2009) and the one found in the diffuse atomic gas (1.8×10^{-8}; Snow et al. 2007). Sonnentrucker et al. (2010) also derived F/H $\simeq$ (0.5–0.8) $\times 10^{-8}$ in diffuse molecular clouds detected in absorption with the *Herschel*/HIFI.

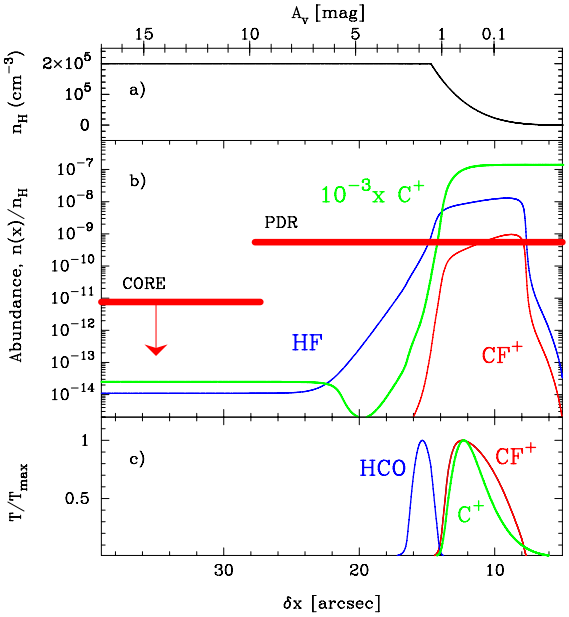

Fig. 4. Photochemical model of the Horsehead PDR. A_V increases from right to left; the PDR edge, delineated by the red vertical line in Fig. 2, corresponds to $A_V = 0$. **a)** Horsehead density profile $n_H = n(H) + 2n(H_2)$. **b)** Predicted abundance of CF^+ in red, HF in blue and C^+ in green. The red horizontal bars show the measured CF^+ abundances, and their length represents the beam size. **c)** Predicted intensity profiles.

To understand the CF^+ abundance profile as a function of depth, we used a one-dimensional, steady-state photochemical model (Meudon PDR code, Le Bourlot et al. 2012; Le Petit et al. 2006). The version of the Meudon PDR model we used includes the Langmuir Hinshelwood and Eley-Rideal mechanisms to describe the formation of H_2 on grain surfaces. The physical conditions in the Horsehead have already been constrained by our previous observational studies and we kept the same assumptions for the steep density gradient (displayed in the upper panel of Fig. 4), radiation field ($\chi = 60$ times the Draine 1978, mean interstellar radiation field), elemental gas-phase abundances (see Table 6 in Goicoechea et al. 2009b) and cosmic ray primary ionization rate ($\zeta = 5 \times 10^{-17}$ s^{-1} per H_2 molecule). We used the Ohio State University (osu) pure gas-phase chemical network, and included fluorine adsorption and desorption onto grains.

The predicted CF^+, HF and C^+ abundance profiles are shown in Fig. 4b. The HF and CF^+ abundances decrease rapidly for $A_V > 1$. The model agrees well with the observed CF^+ abundance in the PDR, shown by the horizontal bars. The model predicts that there is a significant overlap between CF^+ and C^+. Moreover, the abundance ratio between these two species remains quite constant along the illuminated side of the cloud, i.e. $A_V < 4$, as shown in Fig. 4c. The CF^+ emission arises in the outermost layers of the cloud ($A_V \sim 0.5$), which are directly exposed to the far-UV field, where the gas is less dense. The predicted spatial distribution of the CF^+ emission is shown in Fig. 4d. We expect a narrow filament (~5″) shifted in the illuminated part of the PDR with respect to the HCO emission, which has already been shown to trace the far-UV illuminated molecular gas (Gerin et al. 2009).

4. Conclusions

We have detected the $J = 1–0$ and $J = 2–1$ rotational lines of CF^+ with high signal-to-noise ratio toward the PDR and core positions in the Horsehead. We have also mapped the region, and found that the emission arises mostly at the illuminated edge of the nebula (PDR), but it is also detected toward the dense core arising from its lower density skin. CF^+ is unique because its column density is proportional to the elemental abundance of fluorine. In the Horsehead PDR we found $N \simeq (1.5–2.0) \times 10^{12}$ cm^{-2} and inferred F/H $\simeq (0.6–1.5) \times 10^{-8}$. Our model of the fluorine chemistry predicts that CF^+ accounts for 4–8% of all fluorine. CF^+ is found in the layers where C^+ is abundant because it is formed by reactions between HF and C^+. In these regions the ionization fraction is high (see Goicoechea et al. 2009b) and CF^+ destruction is dominated by dissociative recombination with electrons. The CF^+ emission has two velocity components. The possibility that we are resolving the hyperfine structure is unlikely, but a corresponding theoretical or experimental study would allow us to derive the velocity structure unambiguously. Although the CF^+ line profile is not exactly the same as the C^+ line profile, they are the only species in the Horsehead with a double-peaked profile of kinematic origin measured to date. The complex line profile of both CF^+ and C^+ therefore confirms that they trace the gas directly exposed to the far-UV radiation, which shows a completely different kinematics than the following layers traced by other species, like HCO. We therefore propose that CF^+ can be used as a proxy of the C^+ layers that can be observed from the ground. We will check this by comparing our findings with a *Herschel*/HIFI map of the C^+ emission in the Horsehead.

Acknowledgements. We thank the anonymous referee for useful comments that improved the Letter. V.G. acknowledges support from the Chilean Government through the Becas Chile scholarship program. This work was also funded by grant ANR-09-BLAN-0231-01 from the French *Agence Nationale de la Recherche* as part of the SCHISM project. J.R.G. thanks the Spanish MICINN for funding support through grants AYA2009-07304 and CSD2009-00038. J.R.G. is supported by a Ramón y Cajal research contract from the Spanish MICINN and co-financed by the European Social Fund.

References

Asplund, M., Grevesse, N., Sauval, A. J., & Scott, P. 2009, ARA&A, 47, 481
Draine, B. T. 1978, ApJS, 36, 595
Gerin, M., Goicoechea, J. R., Pety, J., & Hily-Blant, P. 2009, A&A, 494, 977
Goicoechea, J. R., Pety, J., Gerin, M., et al. 2006, A&A, 456, 565
Goicoechea, J. R., Compiègne, M., & Habart, E. 2009a, ApJ, 699, L165
Goicoechea, J. R., Pety, J., Gerin, M., Hily-Blant, P., & Le Bourlot, J. 2009b, A&A, 498, 771
Habart, E., Abergel, A., Walmsley, C. M., Teyssier, D., & Pety, J. 2005, A&A, 437, 177
Langer, W. D., Velusamy, T., Pineda, J. L., et al. 2010, A&A, 521, L17
Le Bourlot, J., Le Petit, F., Pinto, C., Roueff, E., & Roy, F. 2012, A&A, 541, A76
Le Petit, F., Nehmé, C., Le Bourlot, J., & Roueff, E. 2006, ApJS, 164, 506
Müller, H. S. P., Thorwirth, S., Roth, D. A., & Winnewisser, G. 2001, A&A, 370, L49
Neufeld, D. A., Wolfire, M. G., & Schilke, P. 2005, ApJ, 628, 260
Neufeld, D. A., Schilke, P., Menten, K. M., et al. 2006, A&A, 454, L37
Neufeld, D. A., Sonnentrucker, P., Phillips, T. G., et al. 2010, A&A, 518, L108
Novotny, O., Mitchell, J. B. A., LeGarrec, J. L., et al. 2005, J. Phys. B At. Mol. Phys., 38, 1471
Penzias, A. A., & Burrus, C. A. 1973, ARA&A, 11, 51
Pety, J. 2005, in SF2A-2005: Semaine de l'Astrophysique Française, ed. F. Casoli, T. Contini, J. M. Hameury, & L. Pagani, 721
Pety, J., Goicoechea, J. R., Hily-Blant, P., Gerin, M., & Teyssier, D. 2007, A&A, 464, L41
Pickett, H. M., Poynter, R. L., Cohen, E. A., et al. 1998, J. Quant. Spec. Radiat. Transf., 60, 883
Reid, R. V., & Chu, A. H.-M. 1974, Phys. Rev. A, 9, 609
Snow, T. P., Destree, J. D., & Jensen, A. G. 2007, ApJ, 655, 285
Sonnentrucker, P., Neufeld, D. A., Phillips, T. G., et al. 2010, A&A, 521, L12
van der Tak, F. F. S., Ossenkopf, V., Nagy, Z., et al. 2012, A&A, 537, L10

A&A 548, A94 (2012)
DOI: 10.1051/0004-6361/201220174

Astronomy & Astrophysics

The hyperfine structure in the rotational spectrum of CF^+ *(Research Note)*

V. Guzmán[1], E. Roueff[2], J. Gauss[3], J. Pety[1,4], P. Gratier[1], J. R. Goicoechea[5], M. Gerin[4], and D. Teyssier[6]

[1] IRAM, 300 rue de la Piscine, 38406 Saint-Martin d'Hères, France
e-mail: guzman@iram.fr
[2] LUTH UMR 8102, CNRS and Observatoire de Paris, Place J. Janssen, 92195 Meudon Cedex, France
[3] Institut für Physikalische Chemie, Universität Mainz, 55099 Mainz, Germany
[4] LERMA – LRA, UMR 8112, Observatoire de Paris and École normale Supérieure, 24 rue Lhomond, 75231 Paris, France
[5] Centro de Astrobiología, CSIC-INTA, Carretera de Ajalvir, Km 4, Torrejón de Ardoz, 28850 Madrid, Spain
[6] European Space Astronomy Centre, ESA, PO Box 78, 28691 Villanueva de la Cañada, Madrid, Spain

Received 6 August 2012 / Accepted 1 November 2012

ABSTRACT

Context. CF^+ has recently been detected in the Horsehead and Orion Bar photo-dissociation regions. The $J = 1–0$ line in the Horsehead is double-peaked in contrast to other millimeter lines. The origin of this double-peak profile may be kinematic or spectroscopic.
Aims. We investigate the effect of hyperfine interactions due to the fluorine nucleus in CF^+ on the rotational transitions.
Methods. We compute the fluorine spin rotation constant of CF^+ using high-level quantum chemical methods and determine the relative positions and intensities of each hyperfine component. This information is used to fit the theoretical hyperfine components to the observed CF^+ line profiles, thereby employing the hyperfine fitting method in GILDAS.
Results. The fluorine spin rotation constant of CF^+ is 229.2 kHz. This way, the double-peaked CF^+ line profiles are well fitted by the hyperfine components predicted by the calculations. The unusually large hyperfine splitting of the CF^+ line therefore explains the shape of the lines detected in the Horsehead nebula, without invoking intricate kinematics in the UV-illuminated gas.

Key words. astrochemistry – ISM: clouds – ISM: molecules – ISM: individual objects: Horsehead nebula – radio lines: ISM

1. Introduction

Up to now, CF^+ has only been detected in two photo-dissociation regions (PDR), namely the Horsehead mane (Guzmán et al. 2012) and the Orion bar (Neufeld et al. 2006). In contrast to other mm lines in the Horsehead, the CF^+ $J = 1–0$ (102.587 GHz) line is double-peaked. Guzmán et al. (2012) proposed three possible explanations: 1) the CF^+ line suffers from self-absorption; 2) the complex CF^+ line profile is caused by kinematics; or 3) the two peaks correspond to different hyperfine components caused by the fluorine nuclei. As the CF^+ opacities are low ($\tau \lesssim 1$), the radiative transfer explanation could be ruled out. However, Guzmán et al. (2012) could not distinguish between the remaining possibilities for two reasons. First, CF^+ is expected to coexist with C^+, because CF^+ is formed by the reaction of HF with C^+. This implies that the lines of both C^+ and CF^+ may share similar kinematics and indeed the 157.8 μm C^+ line is double-peaked. Second, no experimental or theoretical investigation of the hyperfine structure of CF^+ was available. The most recent spectroscopic study of CF^+ did not consider the hyperfine structure because the experiments were not able to resolve the hyperfine components (Cazzoli et al. 2010). High-level quantum chemical calculations reported in the following now allow us to determine the hyperfine splitting. It is thus possible to establish the spectroscopic origin of the double-peak line in the Horsehead PDR.

2. Hyperfine structure

CF^+ has a $^1\Sigma^+$ electronic ground state with a dipole moment of 1.04 Debye (Peterson et al. 1990). The fluorine nuclei has a non-zero nuclear spin ($I = 1/2$). Therefore, the rotational and spin angular momenta are coupled through $\boldsymbol{J} + \boldsymbol{I} = \boldsymbol{F}$. This implies that the total angular momentum F can have the values $F = I+J, I+J-1, ..., |I-J|$, where J is the rotational and I the nuclear spin quantum number. The various combinations of these quantum numbers are responsible for the hyperfine splitting of the energy levels, which are given by

$$E = E_J + \frac{C_I}{2}\left[F(F+1) - I(I+1) - J(J+1)\right], \quad (1)$$

with C_I as the spin rotation constant. The frequency splitting of the two hyperfine lines is equal to $3/2\ C_I$ for the $J = 1–0$ transition. For the $J = 2–1$ transition, there are three hyperfine lines separated by C_I and $5/2\ C_I$ from the strongest transition (Townes & Schawlow 1975).

The CF^+ spin rotation constant has been determined by means of quantum chemical calculations (see, e.g., Puzzarini et al. 2010, for details). To ensure high accuracy, the computations were performed at the coupled-cluster singles and doubles level augmented by a perturbative treatment of triple excitations (CCSD(T), Raghavachari et al. 1989) together with atomic-orbital basis sets from Dunning's cc-pCVXZ hierarchy with $X = Q$, 5, and 6 (Woon & Dunning 1995). Rotational London orbitals (Gauss et al. 1996) were used in all calculations. Furthermore, zero-point vibrational effects were accounted for in a perturbative manner as described in Auer et al. (2003) at the CCSD(T)/cc-pCVQZ level. The values computed for r(CF) = 1.154089 Å are 227.5 kHz (cc-pCVQZ), 228.5 kHz (cc-pCV5Z), and 228.7 kHz (cc-pCV6Z), respectively. Vibrational corrections

Table 1. Hyperfine splitting shifts with respect to the strongest transition and relative intensities.

Transition $J \rightarrow J-1$	Component $F \rightarrow F'$	Shift Freq. (kHz)	Shift Vel. (km s^{-1})	Rel. intensity %
1–0	3/2–1/2	0	0.00	66.7
	1/2–1/2	–343.8	1.00	33.3
2–1	5/2–3/2	0.00	0.00	60.0
	3/2–1/2	–229.2	0.33	33.4
	3/2–3/2	–573.0	0.84	6.66

amount to 0.55 kHz, thus leading to a final theoretical value of 229.2 kHz for the spin rotation constant of CF^+. All calculations were performed with the quantum chemical program package CF [1].

Table 1 gives the resulting hyperfine frequency shifts together with the relative line intensities, taking a CF^+ spin rotation constant of 229.2 kHz. This value is higher than, e.g., the ^{13}CO value of 32.6 kHz (Cazzoli et al. 2004). This makes CF^+ a spectroscopically peculiar ion. Indeed, extrapolating from the spectroscopy of ^{13}CO, Guzmán et al. (2012) significantly underestimated the hyperfine splitting of the $J = 1-0$ line by assuming a value of about 165 kHz. The computed value of the spin rotation constant agrees with the fact that the hyperfine splittings were not observed in the experiments of Cazzoli et al. (2010).

3. Comparison with observations

The hyperfine fitting method available in the GILDAS/CLASS software[2] was used to fit the CF^+ hyperfine components to the available astronomical data. The fits and their residuals are shown in Fig. 1. Table 2 gives the results of the fits, namely the local standard of rest (LSR) velocity, the linewidth, and the total opacity of the line. The observed lines are well fitted and the column density inferred from the fitted total opacity is $N = (1.8–3.5) \times 10^{12}$ cm^{-2}, i.e., less than a factor two from the value inferred in Guzmán et al. (2012). The frequency splitting and relative intensities of the two peaks in the CF^+ $J = 1-0$ line emission profile are consistent with two hyperfine components due to the fluorine nucleus. The two strongest hyperfine components in the $J = 2-1$ line are separated by only 0.3 km s^{-1} at the LSR velocity associated to the Horsehead nebula while the typical linewidth of the lines is ~0.6 km s^{-1}. The velocity separation of the third hyperfine component is much larger, but its relative intensity is weak (less than 10%). Therefore, the three hyperfine components are not easily disentangled at 1 mm. Nevertheless, the line profile is also compatible with the computed hyperfine splitting, as shown on the residuals. The fitted velocities for both lines are 10.7 km s^{-1}; i.e., they are equal to the usual systematic velocity of all the lines detected in the Horsehead WHISPER survey (PI: J. Pety). This way, the observed CF^+ double-peak profile can be fully explained spectroscopically. This result demonstrates the importance of multidisciplinary collaborations to interpret astrophysical observations.

The difference in typical linewidth explains why the hyperfine splitting was not detected in the Orion bar (1.5–3.0 km s^{-1}, Neufeld et al. 2006). The Horsehead (showing narrow emission lines) is a perfect laboratory for precise spectroscopic studies of species present in UV-illuminated environments.

[1] See http://www.cfour.de for more information about the CF package.

[2] See http://www.iram.fr/IRAMFR/GILDAS for more information about the GILDAS softwares.

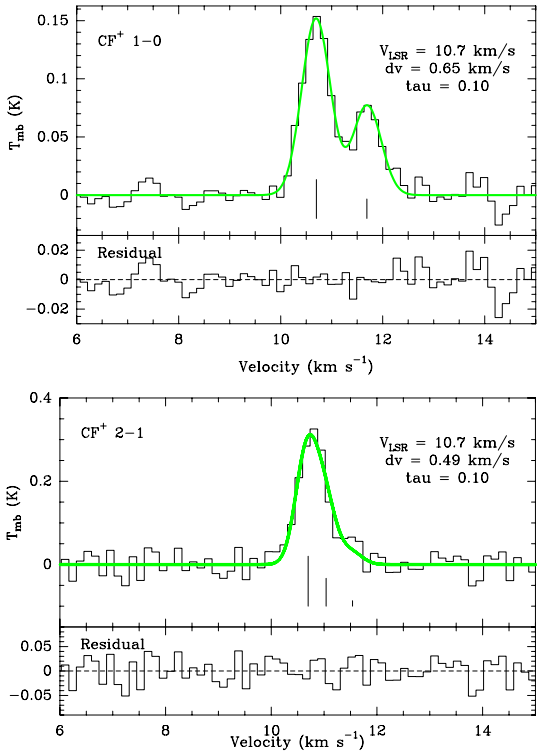

Fig. 1. CF^+ $J = 1-0$ and $J = 2-1$ line profiles detected toward the Horsehead PDR. The vertical lines indicate the positions and the relative intensities of the hyperfine components. The green lines display the hyperfine fit performed with the CLASS tool in GILDAS. The fit residuals are shown in the bottom panels.

Table 2. Results of the hyperfine component fit.

Line	v_{LSR} K	Width km s^{-1}	τ_{main}
$J = 1-0$	10.70 ± 0.01	0.65 ± 0.02	0.10 ± 0.96
$J = 2-1$	10.70 ± 0.02	0.49 ± 0.05	0.10 ± 0.45

Acknowledgements. V.G. acknowledges support from the Chilean Government through the Becas Chile scholarship program. This work was also funded by grant ANR-09-BLAN-0231-01 from the French *Agence Nationale de la Recherche* as part of the SCHISM project and in Mainz by the Deutsche Forschungsgemeinschaft through grant GA 370/5-1. J.R.G. thanks the Spanish MICINN for support through grants AYA2009-07304 and CSD2009-00038. J.R.G. is also supported by a Ramón y Cajal research contract from the Spanish MICINN and co-financed by the European Social Fund.

References

Auer, A. A., Gauss, J., & Stanton, J. F. 2003, J. Chem. Phys., 118, 10407
Cazzoli, G., Puzzarini, C., & Lapinov, A. V. 2004, ApJ, 611, 615
Cazzoli, G., Cludi, L., Puzzarini, C., & Gauss, J. 2010, A&A, 509, A1
Gauss, J., Ruud, K., & Helgaker, T. 1996, J. Chem. Phys., 105, 2804
Guzmán, V., Pety, J., Gratier, P., et al. 2012, A&A, 543, L1
Neufeld, D. A., Schilke, P., Menten, K. M., et al. 2006, A&A, 454, L37
Peterson, K., Woods, R. C., Rosmus, P., & Werner, H.-J. 1990, J. Chem. Phys., 93, 1889
Puzzarini, C., Stanton, J. F., & Gauss, J. 2010, Int. Rev. Phys. Chem., 29, 273
Raghavachari, K., Trucks, G. W., Pople, J. A., & Head-Gordon, M. 1989, Chem. Phys. Lett., 157, 479
Townes, C. H., & Schawlow, A. L. 1975, Microwave spectroscopy
Woon, K., & Dunning, T. H. 1995, J. Chem. Phys., 103, 4572

Chapter 4

C_3H^+ Propynylidynium

In this section, I will present the results of the second paper in the Horsehead WHISPER line survey series, which consists in the first detection of a new species in the ISM, that we tentatively attribute to the hydrocarbon C_3H^+.

4.1 Introduction

Carbon is the fourth most abundant element in the interstellar medium. Hence, carbon, in its neutral or ionized forms, is one of the main reactants in chemical networks. Moreover, ∼75% of the molecules that have been detected in the ISM or in circumstellar envelopes so far, contain at least one carbon atom. Two important examples include CO, the second most abundant species in the ISM, and a widely used tracer of H_2 in molecular clouds; and C^+, an important gas coolant over a wide range of physical conditions. In addition, a large fraction of the total carbon in the ISM is locked in dust grains and PAH, which contribute to the interstellar extinction, the dust thermal emission and contribute to the gas heating through the photoelectric effect. The carbon chemistry is thus important for understanding the structure and evolution of the ISM.

4.1.1 Chemistry of small hydrocarbons

Carbon chains and rings are ubiquitous molecules in the ISM. Small hydrocarbons (with 1 to 3 carbon atoms), are key actors in the formation of larger hydrocarbons chains and carbon clusters. The chemistry of carbon is complex. In the gas phase, it is initiated by reactions of C^+ with H_2, leading to CH_2^+. This first step is slow because the reaction between C^+ and H_2 has a large endothermicity. Then, CH_2^+ reacts with molecular hydrogen to form CH_3^+. The following reactions with C^+, H_2 and electrons lead to the formation of C_2H_2, which can later be photodissociated into C_2H or can react with C^+ to form C_3H^+. Subsequent reactions with molecular hydrogen and electrons can then lead to the formation the small hydrocarbons C_3H and C_3H_2 (Turner et al. 2000; Wakelam et al. 2010).

$$\begin{array}{l} \xrightarrow{H_2} C_3H_2^+ \xrightarrow{e^-} C_3H \\ C_2H_2 \xrightarrow{C^+} C_3H^+ \\ \xrightarrow[H_2]{} C_3H_3^+ \xrightarrow{e^-} C_3H_2 \end{array} \tag{4.1}$$

C_2H_2, C_2H and both linear and cyclic forms of C_3H and C_3H_2 have been detected in the ISM and in the circumstellar shells of evolved stars. These last three have been observed in

the diffuse medium (e.g., Liszt et al. 2012), and all four have been detected in dark clouds (Turner et al. 2000), carbon rich envelopes around evolved stars (e.g., Millar et al. 2000; Cernicharo et al. 2000; Zhang et al. 2009). C_2H_2, C_2H and c-C_3H_2 have also been detected in protoplanetary disks (Dutrey et al. 1997; Qi et al. 2013; Gibb et al. 2007). In nearby gas-rich active galaxies, C_2H and c-C_3H_2 have been detected as well (e.g., Jiang et al. 2011; Aladro et al. 2011).

4.1.2 The abundance of hydrocarbons in PDRs

Small hydrocarbons are abundant and ubiquitous in PDRs. They can be as abundant in PDRs as they are found to be in dark, well shielded clouds, such as L134N and TMC-1, (Fuente et al. 2003; Teyssier et al. 2004). In the PDRs, NGC 7023, Orion Bar and NGC 7027, Fuente et al. (2003) found c-C_3H_2 abundances of $10^{-10} - 10^{-8}$. Teyssier et al. (2004) observed the emission from the small hydrocarbons CCH, c-C_3H_2 and C_4H with medium spatial resolution ($30''$) in three PDRs, including the Horsehead, with radiation fields between 60 and 600 (Draine 1978, in Draine units;). They showed that the small hydrocarbons are also present in the edge of the PDR, and derived similar abundances to the ones found by Fuente et al. (2003). The high abundances of small hydrocarbons found in these FUV-illuminated regions was a surprise because they were expected to be destroyed by the incident radiation field. Pety et al. (2005) continued this work in the Horsehead and obtained high spatial resolution observations of the same species. The observations showed that the emission from these small hydrocarbons arises from the far-UV illuminated edge of the nebula. They found the C_2H emission correlates very well with the emission of c-C_3H_2 and C_4H, suggesting a common formation path. A tight correlation between C_2H and c-C_3H_2 has also been observed in diffuse clouds (Lucas & Liszt 2000; Gerin et al. 2011). The mid-IR emission due to PAH also spatially correlates very well with the distribution of carbon chains in the Horsehead nebula. PDR models including pure gas-phase chemistry fail to reproduce the abundance inferred from the observations of these small hydrocarbons. The observed abundances are typically one to two orders of magnitude higher than the predictions of the models.

More recently, Pilleri et al. (2013) studied the emission of the small hydrocarbons CH, C_2H and c-C_3H_2, in the neighborhood of the ultracompact HII region Monoceros R2. They found that the emission of c-C_3H_2 is concentrated towards the more illuminated layers of the PDR, while C_2H emission is more extended. An abundance of $10^{-9} - 10^{-8}$ for C_2H, and $10^{-11} - 10^{-10}$ for C_3H_2, was inferred. They compared their results with others PDRs, and found that the abundance of C_2H is quite constant in all PDRs, whereas the abundance of c-C_3H_2 is higher in low-UV PDRs, with $N(c\text{-}C_3H_2)/N(C_2H) \simeq 0.008 - 0.08$ from high- to low-UV illuminated PDRs.

The rapid photodissociation rates of the small hydrocarbons, and the high abundances observed in PDRs reveal the existence of an efficient formation mechanism in FUV-illuminated regions that injects hydrocarbons continuously in the PDR. Several authors have proposed that a possible explanation for the discrepancy between models and observations, is that the incident radiation field can fragment PAHs and small carbon grains into small hydrocarbons (e.g., Fuente et al. 2003; Teyssier et al. 2004; Pety et al. 2005, and references therein). The fact that PAH are abundant molecules in PDRs, and the excellent correlation between PAH

emission and hydrocarbon emission observed in PDRs supports this scenario.

PAHs have also been observed in the HII region IC 434 up to a distance of $\sim 20''$ from the ionisation front (Compiègne et al. 2007). It is not clear how PAH can survive in such harsh environments. In the Horsehead, it could be due to the moderate radiation field and it could also be related to the continuous photoevaporation of the Horsehead nebula which brings "fresh" matter into the HII region.

Another possibility to explain the high abundance of small hydrocarbons in PDRs, is that they could form deeper inside the cloud and are transported to the surface by turbulent mixing (Lesaffre et al. 2007; Gerin et al. 2007). Rimmer et al. (2012) also proposed that a variation of the cosmic ray ionization rate with depth could improve the agreement between observations and models, but only for C_2H.

4.2 A new molecule in space: Tentative detection of l-C_3H^+ in the Horsehead

Within the Horsehead WHISPER line survey, we found a line around 89.957 GHz (T_{peak}=89 mK) toward the PDR position, that could not be associated to any transition listed in the public line catalogs. Assuming the associated molecule is a linear rigid rotor we found a consistent set of 8 unidentified lines (including the 89.957 GHz line), and derived a rotational constant $B = 11244.9512 \pm 0.0015$ MHz, which is close to that of l-C_3H ($B = 11189.1033 \pm 84$ MHz; Caris et al. 2009). We attribute the detected lines to the small hydrocarbon l-C_3H^+, and derive an abundance relative to total H nuclei of $(1.9 - 4.2) \times 10^{-11}$ at the PDR position.

The lines are not detected toward the dense core position. We observed a cut along the PDR, to constrain the spatial distribution of the l-C_3H^+ emission perpendicular to the photo-dissociation front, and found that indeed the emission is concentrated toward the illuminated edge of the nebula, with a similar spatial distribution to radical species such as HCO, and other small hydrocarbons such as C_2H.

The detection of C_3H^+, which is an intermediate species in the gas-phase formation scenario (as shown by the chemical path 4.1), brings further constraints to the formation pathways of the small hydrocarbons. We derive a l-C_3H^+ abundance that is consistent with pure gas-phase models. This implies that the abundance of the chemically related hydrocarbons should be much smaller than what is observed if pure gas-phase chemistry is the only formation pathway. This supports the so called *Top-Down* scenario described before, where PAHs are fragmented into small hydrocarbons in PDRs due to the strong UV fields, and where in the same way, PAHs are formed by the photo-destruction of very small grains (e.g., Berné et al. 2007; Pilleri et al. 2012). This is the first clear example of the formation of small molecules from larger ones, thanks to the detection of C_3H^+.

Recently, Huang et al. (2013) performed high-accuracy quantum chemical calculations to compute the spectroscopic constants of C_3H^+. They computed a B rotational constant that agrees, to within 20 MHz (a typical level of accuracy), with the value we derive in the Horsehead. On the other hand, the first order centrifugal distortion term D, differs by more than 40%, while the second order centrifugal distortion constant H differs by three orders of magnitude, compared to values inferred in the Horsehead. They therefore questioned

the assignment of the detected lines in the Horsehead to the hydrocarbon cation l-C_3H^+. Fortenberry et al. (2013) proposed that a more plausible candidate is the hydrocarbon anion l-C_3H^-. However, several observational facts favor the assignment of the unknown lines to l-C_3H^+ instead of the anion. First, no other anions have been detected in the Horsehead PDR. Agúndez et al. (2008) searched for anions in the Horsehead PDR without success, and derived the upper limits $C_4H^-/C_4H \leq 0.033$, $C_6H^-/C_6H \leq 8.9$, and $CN^-/CN \leq 0.55$. If the unknown species is the anion, the ratio of C_3H^- to neutral C_3H would be $\sim 57\%$, which is higher than any anion to neutral ratio detected in the ISM so far. Second, the lines were not detected in the dark cloud TMC 1, where other anions have been already detected. The lines have also been detected in the Orion Bar (Cuadrado et al. in prep) and in absorption in Sgr B2 (McGuire et al. 2013), where several other molecular cations have been observed. Third, the cyclic form of C_3H^- is more stable than the linear form. Hence, one would expect to also detect c-C_3H^- if l-C_3H^- is present, as c-C_3H is found to be more abundant than l-C_3H in the Horsehead PDR. The discussion presented by Huang et al. (2013) is based on theoretical calculations. A direct measurement in the laboratory is necessary to provide a definitive assignment and close the controversy.

A&A 548, A68 (2012)
DOI: 10.1051/0004-6361/201220062

Astronomy & Astrophysics

The IRAM-30 m line survey of the Horsehead PDR

II. First detection of the l-C_3H^+ hydrocarbon cation⋆

J. Pety[1,2], P. Gratier[1], V. Guzmán[1], E. Roueff[3], M. Gerin[2], J. R. Goicoechea[4], S. Bardeau[1], A. Sievers[5], F. Le Petit[3], J. Le Bourlot[3], A. Belloche[6], and D. Talbi[7]

[1] IRAM, 300 rue de la Piscine, 38406 Saint Martin d'Hères, France
e-mail: [pety;gratier;guzman;bardeau]@iram.fr
[2] LERMA, UMR 8112, CNRS and Observatoire de Paris, 61 avenue de l'Observatoire, 75014 Paris, France
e-mail: maryvonne.gerin@lra.ens.fr
[3] LUTH, UMR 8102, CNRS and Observatoire de Paris, Place J. Janssen, 92195 Meudon Cedex, France
e-mail: evelyne.roueff@obspm.fr
[4] Centro de Astrobiología. CSIC-INTA. Carretera de Ajalvir, Km 4. Torrejón de Ardoz, 28850 Madrid, Spain
e-mail: jr.goicoechea@cab.inta-csic.es
[5] IRAM, 7 Avenida Pastora, Granada, Spain
e-mail: sievers@iram.es
[6] Max-Planck Institut für Radioastronomie, Auf dem Hügel 69, 53121 Bonn, Germany
e-mail: belloche@mpifr-bonn.mpg.de
[7] LUPM, UMR 5299, Université Montpellier 2, Place Eugène Bataillon, 34095 Montpellier Cedex 05, France
e-mail: dahbia.talbi@univ-montp2.fr

Received 19 July 2012 / Accepted 11 October 2012

ABSTRACT

Context. Pure gas-phase chemistry models do not succeed in reproducing the measured abundances of small hydrocarbons in the interstellar medium. Information on key gas-phase progenitors of these molecules sheds light on this problem.
Aims. We aim to constrain the chemical content of the Horsehead mane with a millimeter unbiased line survey at two positions, namely the photo-dissociation region (PDR) and the nearby shielded core. This project revealed a consistent set of eight unidentified lines toward the PDR position. We associate them to the l-C_3H^+ hydrocarbon cation, which enables us to constrain the chemistry of small hydrocarbons. We observed the lowest detectable J line in the millimeter domain along a cut toward the illuminating direction to constrain the spatial distribution of the l-C_3H^+ emission perpendicular to the photo-dissociation front.
Methods. We simultaneously fit 1) the rotational and centrifugal distortion constants of a linear rotor; and 2) the Gaussian line shapes located at the eight predicted frequencies. A rotational diagram is then used to infer the excitation temperature and the column density. We finally compare the abundance to the results of the Meudon PDR photochemical model.
Results. Six out of the eight unidentified lines observable in the millimeter bands are detected with a signal-to-noise ratio from 6 to 19 toward the Horsehead PDR, while the two last ones are tentatively detected. Mostly noise appears at the same frequency toward the dense core, located less than 40″ away. Moreover, the spatial distribution of the species integrated emission has a shape similar to radical species such as HCO, and small hydrocarbons such as C_2H, which show enhanced abundances toward the PDR. The observed lines can be accurately fitted with a linear rotor model, implying a $^1\Sigma$ ground electronic state. The deduced rotational constant value is $B = 11\,244.9512 \pm 0.0015$ MHz, close to that of l-C_3H.
Conclusions. This is the first detection of the l-C_3H^+ hydrocarbon in the interstellar medium. Laboratory spectroscopy is underway to confirm these results. Interferometric imaging is needed to firmly constrain the small hydrocarbon chemistry in the Horsehead.

Key words. surveys – photon-dominated region (PDR) – ISM: lines and bands – ISM: individual objects: Horsehead nebula – line: identification

1. Introduction

Molecular ions play an important role in the physics and chemistry of the insterstellar medium. They trace the gas physical conditions, e.g., its ionization rate and its ionization fraction (see for example Goicoechea et al. 2009), and they participate in the coupling of the gas with the magnetic field. Moreover, molecular ions are key species in the gas phase synthesis of molecules because ion-molecule reactions most often have no activation barrier.

Simple hydrocarbon molecules, such as C_2H, C_3H, and C_3H_2 have been detected in a wide variety of sources from diffuse (e.g. Lucas & Liszt 2000) to dark clouds (e.g. Wootten et al. 1980; Mangum & Wootten 1990). The high abundances found at the UV-illuminated edges of molecular clouds or photo-dissociation regions (PDRs) cannot be reproduced by current pure gas-phase models (Fuente et al. 2003; Teyssier et al. 2004). Pety et al. (2005) proposed another chemical route, namely the photo-erosion of Polycyclic Aromatic Hydrocarbons (PAHs)

⋆ Based on observations obtained with the IRAM-30 m telescope. IRAM is supported by INSU/CNRS (France), MPG (Germany), and IGN (Spain).

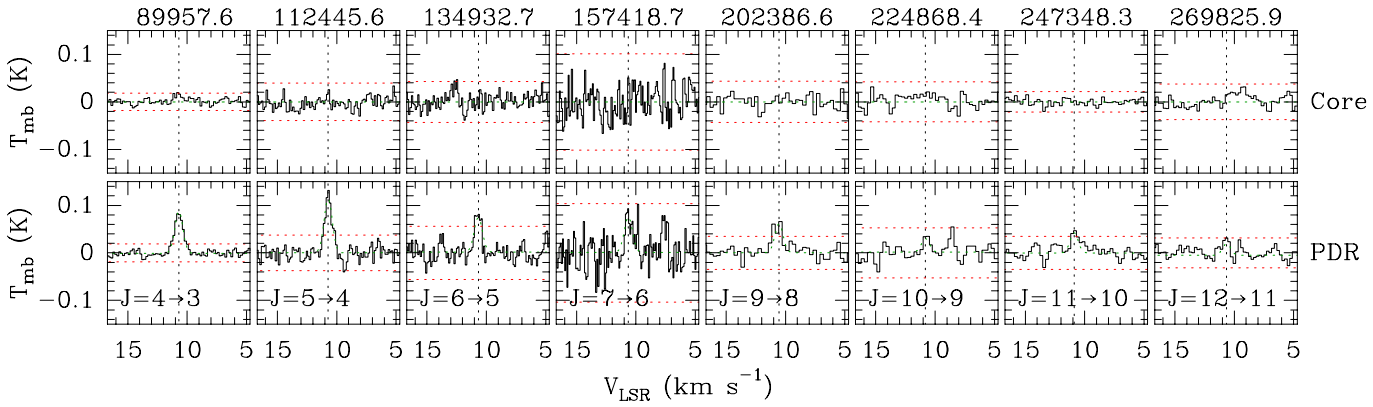

Fig. 1. Millimeter lines attributed to the l-C_3H^+ cation in the PDR (*lower panels*) and the dense core (*upper panels*) positions. The numbers above each panel are the line rest frequencies in MHz. The spectra and the Gaussian fits are shown as black histograms and green curves, respectively. The inferred rest frequencies are displayed as vertical dotted black lines for v_{lsr} = 10.7 km s^{-1} and $\pm 3\sigma$ noise levels as horizontal dotted red lines.

and small carbon grains to produce these hydrocarbons. Rimmer et al. (2012) showed that using a column-dependent cosmic ray ionization rate slightly improves the agreement between models and observations in the Horsehead PDR. Ion-molecule reactions with the C_2H^+ and C_3H^+ cations are thought to be the most important gas-phase channels to form small hydrocarbons (Turner et al. 2000; Wakelam et al. 2010), but they have not yet been observed in the interstellar medium. Constraining the abundances of these intermediate hydrocarbon cations will shed light on the formation routes of hydrocarbons.

In this paper, we report the first detection in the interstellar medium of the l-C_3H^+ hydrocarbon cation toward the Horsehead PDR (more precisely, at the peak of the HCO emission, Gerin et al. 2009). Section 2 describes the observations. Sections 3 and 4 explain how we inferred the spectroscopic parameters associated with the set of unidentified lines, and why we attribute these to l-C_3H^+. Section 5 discusses the determination of the l-C_3H^+ abundance and its chemistry.

2. Observations

The Horsehead WHISPER project (Wideband High-resolution Iram-30 m Surveys at two Positions with Emir Receivers, PI: J. Pety) is a complete unbiased line survey of the 3, 2, and 1 mm bands that is being completed at the IRAM-30 m telescope. Two positions are observed: 1) the "HCO peak" (RA = $5^h40^m53.936^s$, Dec = $-2°28'00''$, J2000), which is characteristic of the photo-dissociation region at the surface of the Horsehead nebula (Gerin et al. 2009); and 2) the "DCO^+ peak" (RA = $5^h40^m55.61^s$, Dec = $-2°27'38''$, J2000), which belongs to a cold and shielded condensation located less than 40″ away from the PDR edge, where HCO^+ is highly deuterated (Pety et al. 2007). The combination of the new EMIR receivers and Fourier transform spectrometers at the IRAM-30 m telescope yields a spectral survey with unprecedented combination of bandwidth (36 GHz at 3 mm, 19 GHz at 2 mm, and 76 GHz at 1 mm), spectral resolution (49 kHz at 3 and 2 mm; and 195 kHz at 1 mm), and sensitivity (median noise 8.1 mK, 18.5 mK, and 8.3 mK, respectively). A detailed presentation of the observing strategy and data reduction process will be given in another paper. In short, any frequency was observed with two different frequency tunings and the Horsehead PDR and dense core positions were alternatively observed every 15 min. The total observing time amounted to one hour per frequency setup and position.

In the analysis of the survey, we found an 89 mK line peak around 89.957 GHz, that could not be associated to any transition listed in the common public catalogs: CDMS[1] (Müller et al. 2001), JPL[2] (Pickett et al. 1998), and splatalogue[3]. The observing strategy allowed us to rule out that the detected line is a ghost line incompletely rejected from a strong line in the image side band (the typical rejection of the EMIR sideband separating mixers is 13 dB). Our search for an identification started with the simplest assumption, i.e., the associated species is a linear rigid rotor. The frequency of the transition ($J + 1 \rightarrow J$) is then given by

$$\nu = 2B\,(J + 1), \tag{1}$$

where B is the rotational constant. In this simple model, the ratio of line frequencies depends only on the ratio of $J + 1$ values. We thus could predict different sets of frequencies to search for companion lines associated to the same species, each set associating a given $J + 1 \rightarrow J$ transition to the frequency of the detected unidentified line, i.e., ~89.957 GHz. The only set of frequencies that consistently brings five other detected lines and two more tentative detections less than 1 MHz from the frequency predictions was the one which associates the 89.957 GHz unidentified line to the $J = 4 \rightarrow 3$ transition of a linear rigid rotor. Using the `WEEDS` extension (Maret et al. 2011) of the `GILDAS/CLASS` software[4] (Pety 2005), we quickly ruled out the assignment of any of the detected unidentified lines to other possible species because the potential candidate species were complex molecules for which many other expected transitions were not detected in the survey.

Figure 1 displays the spectra at the Horsehead PDR and dense core positions of the consistent set of eight unidentified lines, which lie in the millimeter frequency bands. Even though the weather conditions, the pointing and focus corrections, and the tuning setups were shared for the two observed positions, the unidentified lines were detected with a profile, integrated signal-to-noise ratio between 3 and 19 at the PDR position,

[1] http://www.astro.uni-koeln.de/cdms/
[2] http://spec.jpl.nasa.gov/
[3] http://www.splatalogue.net
[4] See http://www.iram.fr/IRAMFR/GILDAS for more information about the `GILDAS` softwares.

Table 1. Results for the simultaneous fit of the l-C_3H^+ line parameters (bottom) and the associated spectroscopic modeling (top).

Order	$\ln(\mathcal{L})^a$	Parameter^b	Value	Unit
Second	2797.9	B	11 244.9474 ± 0.0007	MHz
		D	7.652 ± 0.011	kHz
Third	2802.5	B	11 244.9512 ± 0.0015	MHz
		D	7.766 ± 0.040	kHz
		H	0.56 ± 0.19	Hz

Transition	Frequency	Resolutions		Offset^c	RMS noise^c	$T_{peak}{}^c$	W^c	SNR	A_{ul}	E_u	g_u
	MHz	arcsec	kHz	mK	mK	mK	mK km s^{-1}		s^{-1}	K	
$J = 4 \rightarrow 3$	89 957.625 ± 0.004	27.3	49	−0.8 ± 0.5	5.8 ± 0.4	89	77 ± 4	19	3.5×10^{-5}	10.8	9
$J = 5 \rightarrow 4$	112 445.642 ± 0.005	21.9	49	+0.2 ± 1.0	13.9 ± 0.7	115	99 ± 7	15	6.8×10^{-5}	16.2	11
$J = 6 \rightarrow 5$	134 932.733 ± 0.010	18.2	49	+1.7 ± 1.2	17.6 ± 0.9	72	62 ± 7	10	1.2×10^{-4}	22.7	13
$J = 7 \rightarrow 6$	157 418.719 ± 0.016	15.6	49	+1.3 ± 2.1	33.2 ± 1.5	75	65 ± 11	6	1.9×10^{-4}	30.2	15
$J = 8 \rightarrow 7$	179 903.429 ± 0.024	d	–	–	–	–	–	–	2.9×10^{-4}	38.8	17
$J = 9 \rightarrow 8$	202 386.678 ± 0.029	12.2	195	+0.6 ± 1.5	13.1 ± 1.0	62	54 ± 8	7	4.1×10^{-4}	48.6	19
$J = 10 \rightarrow 9$	224 868.302 ± 0.033	10.9	195	+1.7 ± 1.7	15.6 ± 1.2	30	26 ± 9	3	5.7×10^{-4}	59.4	21
$J = 11 \rightarrow 10$	247 348.134 ± 0.046	9.9	195	+0.0 ± 1.2	11.5 ± 0.8	45	39 ± 6	6	7.6×10^{-4}	71.2	23
$J = 12 \rightarrow 11$	269 826.003 ± 0.082	9.1	195	−5.3 ± 1.3	12.3 ± 0.9	25	21 ± 7	3	9.9×10^{-4}	84.2	25

Notes. $^{(a)}$ $\mathcal{L}$ is the fit likelihood. $^{(b)}$ Parameters for a linear rotor developed to second and third orders (see Sect. 2). $^{(c)}$ Results of the simultaneous Gaussian fits using the third-order model to predict the frequencies. The common line width is 0.81 ± 0.03 km s^{-1}. $^{(d)}$ Outside of the EMIR receiver tuning range.

while only two-sigma upper limits of typically 25 mK km s^{-1} for a 0.8 km s^{-1} linewidth could be derived at the dense core position. The only exception is the $J = 4–3$ line, which is tentatively detected toward the dense core. Assuming that the emission arises from a Gaussian filament of 12″ full width at half maximum centered on the PDR (see Gerin et al. 2009), 27% of the emission detected at the core position is explained by beam pickup from the PDR. The remaining emission could arise in the lower density skin of the dense core, already detected in HCO (Gerin et al. 2009) and CF^+ (Guzmán et al. 2012a,b). In summary, the eight (tentatively) detected lines in the PDR are *unlikely* to be observing artifacts.

3. Associated spectroscopic constants

To compute the spectroscopic parameters associated with the set of unidentified lines, we used higher order improvements to the simple model of a linear rotor. The second and third order corrections, which include the effect of the centrifugal distortion, predict that the frequency of the $J + 1 \rightarrow J$ transition is

$$\nu = 2B(J+1) - 4D(J+1)^3, \quad \text{and} \tag{2}$$

$$\nu = 2B(J+1) - 4D(J+1)^3 + H(J+1)^3[(J+2)^3 - J^3], \tag{3}$$

where D and H are the centrifugal distortion constants to the second and third order, respectively.

Using these expressions, it is possible to generate the sum of 1) Gaussian white noise; 2) a baseline offset; and 3) Gaussian line profiles at the eight predicted frequencies of arbitrary areas and line widths. This allows us to *simultaneously* fit the noise level, a residual baseline offset, and the Gaussian parameters (areas and line widths) as well as the rotational and centrifugal distortion constants associated with these models. In practice, it is very difficult to make the fit converge with the eight lines because of the limited signal-to-noise ratio of some of them. We therefore assume that the eight lines have the same line width. This is likely for two reasons. First, the line width is dominated by the turbulent velocity field and the lines are probably emitted from the same gas cells because the range of energy probed by the eight transitions is relatively narrow (from 10 to 80 K). Second, the velocity gradient in the plane of the sky is shallow, ensuring that the line width does not evolve significantly when the beam size changes with frequency. This assumption enables a quick fit convergence when we start the fit with the following initial values: $B = 11.2$ GHz, $D = 5$ kHz, $H = 1$ Hz, zero offsets, 10 mK noise levels, and 1 km s^{-1} common linewidth. Appendix A discusses why the third order model gives the best fit to the data and Table 1 gives the results of the fits (both the Gaussian line parameters and the spectroscopic constants).

Because laboratory measurements are not available, the only unambiguous frequency available is the one measured in the local standard of rest (LSR) frame, ν_{lsr}. The frequency given in the source frame, ν_{sou}, assumes an LSR systemic velocity of the source, v_{lsr}. These frequencies are linked through $\nu_{sou} = \nu_{lsr}\,[1 - (v_{lsr}/c)]$, where c is the speed of light. The systemic velocity may vary from species to species because of different coupling between the gas kinematics and its chemistry and/or line-shape variations due to optical-depth effects. The analysis of the unambiguously attributed detected lines in the survey shows that the possible range of LSR systemic velocities in the Horsehead PDR is quite narrow, ~0.2 km s^{-1} around 10.7 km s^{-1} (see Fig. A.1 which displays different lines of several hydrocarbons). All frequencies quoted here accordingly assume an LSR velocity of 10.7 km s^{-1}. The derived spectroscopic parameters may therefore need to be slightly linearly scaled.

4. Attribution of the lines to the l-C_3H^+ cation

The unidentified lines were all detected at the PDR position, but not at the dense core position. We thus complemented these data with a cut from the H region into the molecular cloud along the direction of the exciting star, σ Ori, i.e., perpendicular to the photo-dissociation front. Figure 3 displays the integrated intensity emission of the $J = 4–3$ unidentified line as a function of the angular distance from the photo-dissociation front, along with the emission of HCO, $H^{13}CO^+$, and C_2H species (Table 2 defines the observed lines). All these lines were observed simultaneously with the IRAM-30 m telescope during 4 h

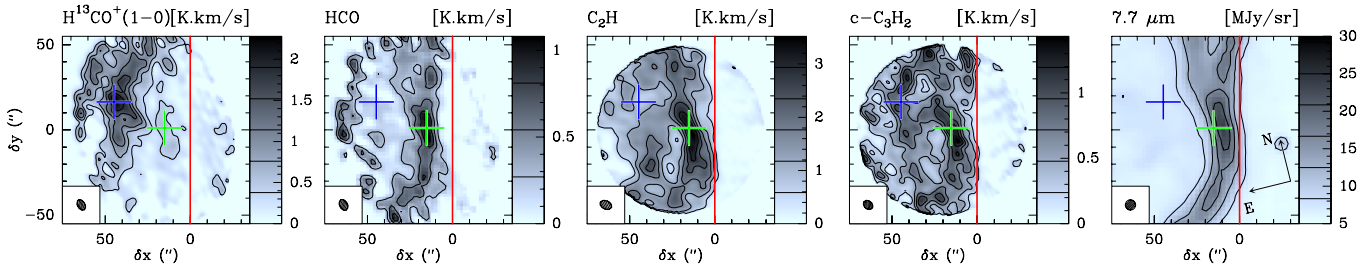

Fig. 2. High angular resolution maps of the integrated intensity of $H^{13}CO^+$, HCO, C_2H, and c-C_3H_2, and the 7.7 μm PAH emission. Maps are rotated by 14° counter-clockwise around the projection center, located at $(\delta x, \delta y) = (20'', 0'')$, to bring the illuminated star direction in the horizontal direction. The horizontal zero is set at the PDR edge. The emission of all lines is integrated between 10.1 and 11.1 km s^{-1}. Displayed integrated intensities are expressed in the main beam temperature scale. Contour levels are shown in the grey-scale lookup tables. The red vertical line shows the PDR edge and the blue and green crosses show the dense core and PDR positions, respectively.

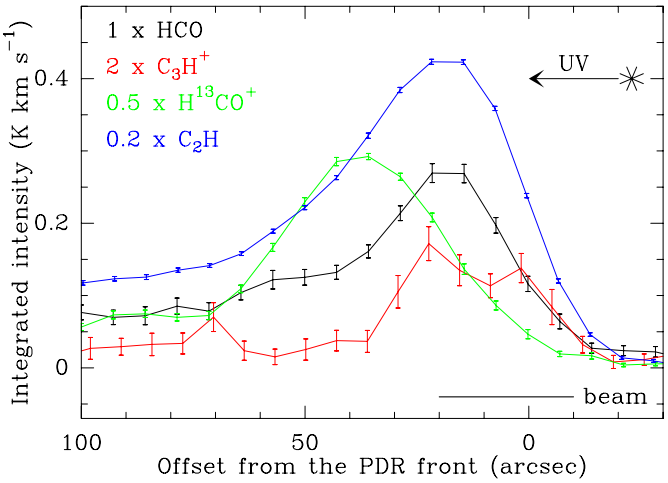

Fig. 3. Integrated intensity profiles across the PDR photo-dissociation front of the l-C_3H^+, HCO, $H^{13}CO^+$, and C_2H species (IRAM-30 m). The cut would appear horizontal at $\delta y = 0''$ in Fig. 2. The observed lines are summarized in Table 2.

of mild summer weather (typically 11 mm of precipitable water vapor), but they all were well-detected nevertheless. At 29″ resolution, it is clear that the unidentified species cut peaks in the UV-illuminated part of the Horsehead mane in the same way as HCO and C_2H, while $H^{13}CO^+$ peaks in the dense core, shielded from the UV field. This led us to conclude that the species is a reactive molecule with a spatial distribution similar to small hydrocarbon chains. For reference, Fig. 2 displays the integrated intensity emission of the same lines, imaged at ∼6″ with the Plateau de Bure Interferometer (Pety et al. 2007; Gerin et al. 2009; Pety et al. 2005), plus the 7.7 μm PAH emission imaged at ∼6″ with ISO (Abergel et al. 2003).

The quality of the spectroscopic fit suggests that the molecule is a linear rotor with a $^1\Sigma$ electronic ground state, i.e., with a closed electronic shell. The rotational constant is $B \sim 11.24$ GHz, which implies the presence of several heavy atoms in the species. According to the literature, the most probable candidate is the l-C_3H^+ cation. Indeed, ab initio calculation implies that 1) the linear structure is the most stable; 2) it has the right electronic state; and 3) the computed rotational constant value is about 11.1 GHz (Radom et al. 1976; Wilson & Green 1980, 1982; Cooper & Murphy 1988; Ikuta 1997). Experimental spectroscopic confirmation for this cation is being performed at the PhLAM laboratory in Lille (Bailleux & Margules, priv. comm.).

Table 2. Lines simultaneously observed in the cut displayed in Fig. 3.

Species	Transition	Frequency MHz
$H^{13}CO^+$	$J = 1-0$	86 754.2884
HCO	$1_{0,1}, 1/2, 1-0_{0,0}, 1/2, 1$	86 777.4600
C_2H	$N = 1-0, J = 3/2-1/2, F = 2-1$	87 316.8980
l-C_3H^+	$J = 4-3$	89 957.6250

Wilson & Green (1980) estimated the dipole moment of this cation to be 2.6 Debye, but this is a rather old value. We therefore computed it again with more sophisticated ab initio techniques of quantum chemistry, as implemented in the MOLPRO suite of programs[5]. We used the CASSCF-MRCI level of theory with the correlation-consistent aug-cc-pVQZ basis sets of Woon & Dunning (1993) for all atoms. The active space of the CASSCF included the $n = 2$ orbitals of carbon and the 1S orbital of H. The geometry was first optimized at the CASSCF level, leading to bond distances for l-C_3H^+ (1.090 Å, 1.246 Å, 1.355 Å) that perfectly match the results obtained in Ikuta (1997). The dipole moment was then computed at the center of mass of the molecule for the CASSCF optimized geometry. The resulting dipole moment of l-C_3H^+ is 3 Debye at the CASSCF-MRCI level of theory, i.e., close to the initial value of Wilson & Green (1980). We used the new value to compute the column density of l-C_3H^+.

5. l-C_3H^+ abundance and chemistry

We used the formalism of the rotational diagram to estimate the column density of l-C_3H^+. Goldsmith & Langer (1999) give the expressions for the level energies, the quantum level degeneracies, the Einstein coefficients, and the partition function $Z(T)$ for a rigid rotor of dipole moment, μ. For instance, the Einstein coefficients are given by

$$A_{J+1\rightarrow J} = \frac{64\pi^4\nu^3\mu^2}{3\,h\,c^3}\,\frac{J+1}{2J+3}, \quad (4)$$

where h and c are the Planck constant and the light speed, respectively. Using these formula, we are able to compute the rotational diagram, assuming 1) that the lines are optically thin ($\tau < 1$); and 2) that the l-C_3H^+ emission is co-spatial with the illuminated filament of the C_2H emission, i.e., it approximately fills as a Gaussian filament of ∼12″ width in the δx direction, infinite size

[5] Werner & Knowles, MOLPRO (version 2002.6) package of ab initio 254 programs, 2002.

Table 3. Comparison of the measured and modeled abundances with respect to the number of protons at three different positions across the PDR front.

	δx	C_2H		c-C_3H_2		C_3H^+	
	["]	Measured[a]	Modeled	Measured[a]	Modeled	Measured[b]	Modeled
Cloud	24.9	$(0.6–1.9) \times 10^{-9}$	1.2×10^{-10}	$(2.2–8.6) \times 10^{-11}$	1.8×10^{-11}	–	5.0×10^{-14}
IR peak	13.2	$(0.9–2.7) \times 10^{-8}$	2.7×10^{-9}	$(0.5–2.6) \times 10^{-9}$	5.7×10^{-12}	$(1.9–4.2) \times 10^{-11}$	1.0×10^{-11}
IR edge	7.4	$(0.8–3.7) \times 10^{-8}$	9.7×10^{-10}	$(0.4–3.8) \times 10^{-9}$	1.3×10^{-12}	–	3.7×10^{-12}

Notes. [(a)] Pety et al. (2005), deduced from observations at ~6″-resolution. [(b)] This work, using a simple source model to compute the beam dilution.

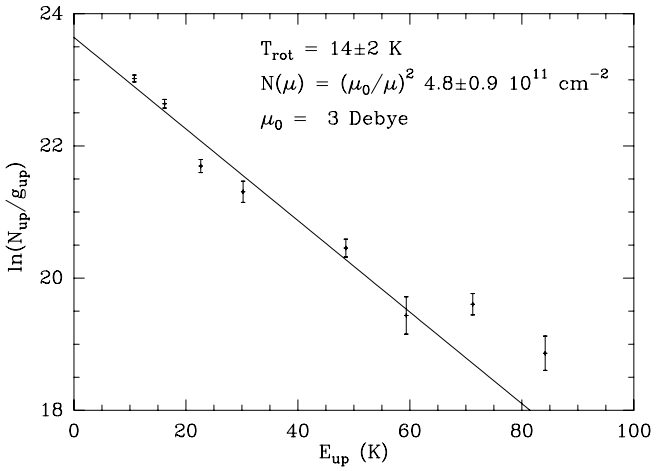

Fig. 4. Rotational diagram of l-C_3H^+ at the PDR position.

in the δy direction, and centered at the HCO peak (see Fig. 2). The filling factors are 0.4, 0.6, and 0.8 at 90, 157, and 270 GHz, respectively. Figure 4 displays the diagram for $\mu_0 = 3$ Debye (this work). The rotational temperature inferred from the observations is independent of the dipole moment because it scales with the slope of the rotational diagram, while the column density scales as μ^{-2}. The typical rotational temperature and column density thus are 14 ± 2 K and $(\mu_0/\mu)^2\ (4.8 \pm 0.9) \times 10^{11}$ cm^{-2}, respectively.

We took advantage of the Horsehead WHISPER survey to make a consistent summary of the small hydrocarbon detections in the Horsehead PDR. The spectra of the detected lines in the 3 mm band of C_2H, c-C_3H, l-C_3H, c-C_3H_2, l-C_3H_2, and C_4H are displayed in Fig. A.1 and their Gaussian fit results are summarized in Table A.1. The integrated intensities of the lines are consistent with the results published by Teyssier et al. (2004, 2005). We accordingly just summarized their column densities and abundances in Table 4. Pety et al. (2005) presented higher angular (typically 6″) observations of C_2H and c-C_3H_2 obtained with the Plateau de Bure Interferometer. The associated abundances at three different positions (the "IR peak" close to the usual "HCO peak", one position named "cloud" representative of the UV-shielded material, and one position named "IR edge" closer to the H region) are summarized in Table 3. The comparison of Tables 3 and 4 indicates that the C_2H and c-C_3H_2 abundances measured at a typical resolution of 25−28″ falls in the uncertainty range of abundances measured at a four times better resolution with PdBI. This means that their emission more or less fills the 25−28″ beam, even though it is substructured into filaments (see Fig. 2). Indeed, if we had assumed that the l-C_3H^+ emission fills the beam at every measured frequency, the inferred l-C_3H^+ abundance would have only be reduced by a factor 2.

Table 4. Column densities and abundances with respect to the number of protons, i.e., [X] = 0.5 N(X)/N(H_2), toward the PDR position, from single-dish observations at resolutions between 25 and 28″.

Molecule	Column density cm^{-2}	Abundance
H_2	$7.2 \pm 2.4 \times 10^{21}$	0.5
C_2H	$1.6 \pm 0.2 \times 10^{14}$	$1.1 \pm 0.4 \times 10^{-8}$
c-C_3H	$3.9 \pm 0.5 \times 10^{12}$	$2.7 \pm 1.0 \times 10^{-10}$
l-C_3H	$2.1 \pm 0.7 \times 10^{12}$	$1.4 \pm 0.7 \times 10^{-10}$
c-C_3H_2	$9.3 \pm 0.2 \times 10^{12}$	$6.4 \pm 2.1 \times 10^{-10}$
l-C_3H_2	$2.7 \pm 0.5 \times 10^{12}$	$1.9 \pm 1.1 \times 10^{-10}$

We finally compared the derived abundances with a one-dimensional, steady-state photochemical model (Meudon PDR model, Le Bourlot et al. 2012; Le Petit et al. 2006). The used version of the Meudon PDR code includes the Langmuir-Hinshelwood and Eley-Rideal mechanisms to describe the formation of H_2 on grains (Le Bourlot et al. 2012), and surface reactions for other species (Le Bourlot et al., in prep.). The physical conditions in the Horsehead have already been constrained by our previous observational studies and we kept the same assumptions for the steep density gradient, radiation field ($\chi = 60$ in Draine units, see Abergel et al. 2003), elemental gas-phase abundances (see Table 6 in Goicoechea et al. 2006) and cosmic ray primary ionization rate ($\zeta = 5 \times 10^{-17}$ s^{-1} per H_2 molecule, Goicoechea et al. 2009).

We used the Ohio State University (osu) pure gas-phase chemical network upgraded for photochemical studies. C_3H^+ is produced by reactions between C_2H_2 and C^+. Then, C_3H^+ is thought to produce $C_3H_2^+$, and $C_3H_3^+$ through reactions with H_2, which later recombines with electrons to form C_3H and C_3H_2

$$C_2H_2 \xrightarrow{C^+} C_3H^+ \begin{array}{l} \xrightarrow{H_2} C_3H_2^+ \xrightarrow{e^-} C_3H \\ \xrightarrow{H_2} C_3H_3^+ \xrightarrow{e^-} C_3H_2. \end{array}$$

Hence these species are usually included in gas-phase chemical networks with reaction rate accuracies of a factor 2 or better. We can thus use them to compare models with observations.

Figure 5 presents the results of the photochemical model for a few small hydrocarbon molecules and cations, namely C_2H, C_3H, C_3H_2, C_2H^+, and C_3H^+. From top to bottom, the figure shows the spatial profiles of the density, abundances relative to the number of hydrogen atoms, and the abundances relative to C_3H^+. The left column presents the profiles computed by the code, which samples the UV-illuminated gas on a finer spatial grid than the UV-shielded gas to correctly represent the steep physical and chemical gradients. The right column presents the profiles convolved with a Gaussian of 6″ full width at half maximum to facilitate the comparison with the abundances inferred

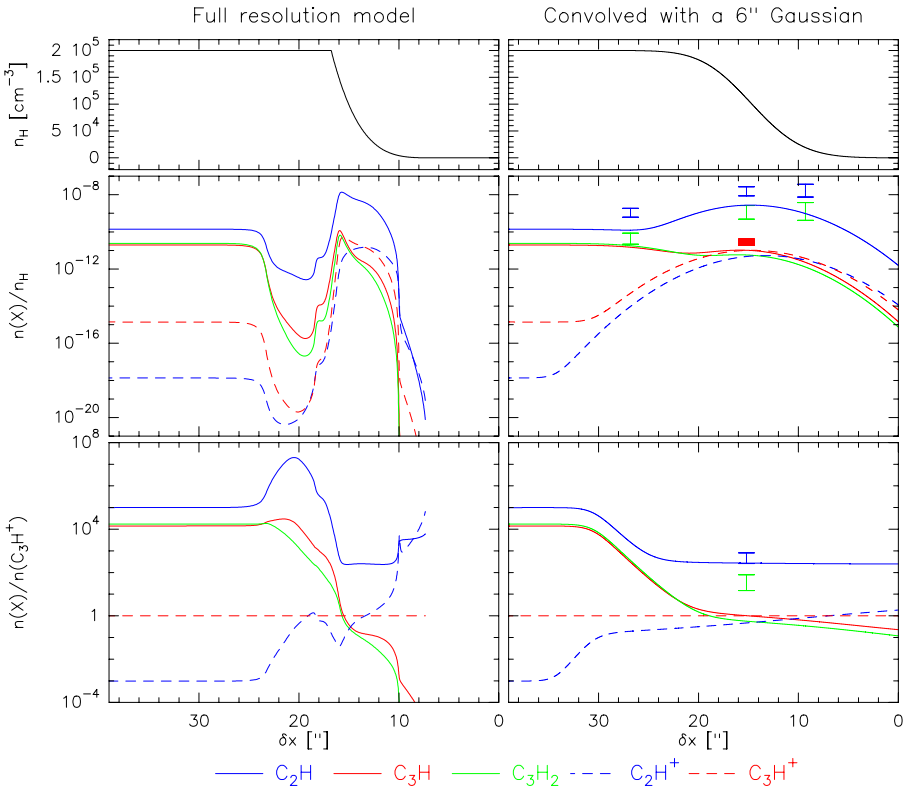

Fig. 5. Photochemical model of the Horsehead PDR displayed at the full resolution of the model (*left column*) and convolved with a Gaussian of 6″-FWHM (*right column*). *Top*: Horsehead density profile $n_{\rm H} = n({\rm H}) + 2n({\rm H_2})$. *Middle*: predicted abundance of selected small hydrocarbons molecules and cations. *Bottom*: abundances of the same hydrocarbons relative to the abundance of C_3H^+. The illuminating star is positioned at the right of the plots. The symbols present the measured range of possible abundances for C_2H (blue vertical segment), C_3H_2 (green vertical segment), and C_3H^+ (red filled rectangle), inferred at a typical resolution of 6″. The legend at the bottom of the figure presents the line coding for the curves: C_2H in plain blue, C_2H^+ in dashed blue, C_3H in plain red, C_3H^+ in dashed red, and C_3H_2 in green.

from PdBI observations at 6″ angular resolution. The measured abundances are displayed with vertical segments for C_2H, and c-C_3H_2, and with a filled rectangle for C_3H^+. Although the l-C_3H^+ abundance is only inferred from the IRAM-30 m single-dish telescope, we also show it here because we used a simple model of its emission based on the PdBI hydrocarbon data to correct for the beam dilution. Table 3 quantitatively compares the measured and modeled abundances at the PDR position ("IR peak" at $A_{\rm v} \sim 1$ mag), inside the molecular cloud at a position representative of the UV-shielded material "cloud" ($A_{\rm v} \sim 8$ mag), and closer to the H region (i.e., "IR edge" at $A_{\rm v} \sim 0.01$ mag).

We only consider the most stable isomers to compare the measured and modeled abundances. Table 4 indicates that the amount of C_3H_2 locked in the linear species is negligible, and that twice as much C_3H is locked in the cyclic species compared to the linear species. Moreover, Table 1 of Mebel et al. (2007) indicates that the cyclic form of C_3H_2 and C_3H are more stable than their linear form by 59.3 kJ mol^{-1} (or 0.61 eV), and 11 kJ mol^{-1} (or 0.11 eV), respectively. Finally, Savić et al. (2005) indicated that the cyclic form of C_3H^+ is less stable than the linear one by 220 kJ mol^{-1}, or 2.28 eV. Given the large difference in energies, we here assume that the linear form is the main product in the gas phase.

While C_2H has much brighter lines and a column density higher by two orders of magnitude compared to linear and cyclic C_3H, we have no hint of a detection of bright lines associated to C_2H^+. This is due to a combination of two effects. First, the spectroscopic structure of C_2H^+ (which has a $^3\Pi$ ground electronic state) is more complex than that of C_3H^+, implying that the emission is spread over more lines. The knowledge of the rotational spectrum of C_2H^+ would enable a deep search of this reactive molecular ion to check whether C_2H^+ is also present in the Horsehead PDR. Second, C_2H^+ is predicted to be less abundant than C_3H^+ (except when $A_{\rm v} \leq 0.1$ mag), because it is efficiently destroyed by H_2, independently of the temperature. In contrast, the detection of C_3H^+ at the warm PDR position corroborates that the destruction of C_3H^+ by H_2 is much less efficient there than in the cold-core region, i.e., the $C_3H^+ + H_2$ reaction is strongly dependent on the gas temperature (Savić & Gerlich 2005).

On one hand, the agreement between the interferometric abundances of C_2H and C_3H_2 and the modeled curves improved at the "cloud" position by up to four orders of magnitude compared to the models of Pety et al. (2005, see their Fig. 10). This is the result of the recent addition of the chemistry on the grain surface to the Meudon PDR code. Indeed, the modeled and predicted abundances of c-C_3H_2 are consistent, while the modeled abundance of C_2H is still one order of magnitude lower than the measured abundance (cf. Table 3). However, it is worth noting that the "cloud" position ($\delta x = 24.9''$, $\delta y = -5.3''$) does not fall, for historical reasons, on the dense core. Indeed, the C_2H emission presents a dip at the DCO^+ peak ($\delta x = 44.7''$, $\delta y = 16.5''$, blue cross in Fig. 2), while the c-C_3H_2 emission shows a bright filament there. These observational facts indicate that C_2H probably depletes at a higher rate onto grains than C_3H_2.

On the other hand, the model results did not change significantly in the UV-illuminated part (IR peak and IR edge). The measured abundances are typically one and two orders of magnitude higher than the modeled abundances for C_2H and C_3H_2. In contrast, the measured abundance of C_3H^+ is only about a factor 2 higher than the modeled abundance (cf. Table 3). If the assumptions used here are correct (the geometry of the l-C_3H^+ emission, and neglecting the amount of c-C_3H^+), this difference between the small hydrocarbon molecules and l-C_3H^+ would confirm that there is a non gas-phase chemical way in which small hydrocarbons are formed in UV-illuminated regions, e.g., the photo-erosion of PAHs (Pety et al. 2005). Interferometric observations of C_3H and C_3H^+ are needed to confirm this result. Indeed, Fig. 6 shows the spatial profile of

Table A.1. Gaussian fit results for the lines of small hydrocarbons detected toward the Horsehead PDR at RA = $5^h40^m53.936^s$, Dec = $-2°28'00''$ (J2000).

Species	Transition	Frequency MHz	Area mK km s^{-1}	Velocity km s^{-1}	Width km s^{-1}
C_2H	$N = 1–0, J = 3/2–1/2\ F = 1–1$	87 284.105	238 ± 3	10.675 ± 0.005	0.735 ± 0.013
	$N = 1–0, J = 3/2–1/2\ F = 2–1$	87 316.898	1943 ± 6	10.682 ± 0.001	0.815 ± 0.003
	$N = 1–0, J = 3/2–1/2\ F = 1–0$	87 328.585	1035 ± 4	10.675 ± 0.002	0.769 ± 0.004
	$N = 1–0, J = 1/2–1/2\ F = 1–1$	87 401.989	1103 ± 5	10.694 ± 0.002	0.785 ± 0.004
	$N = 1–0, J = 1/2–1/2\ F = 0–1$	87 407.165	489 ± 4	10.697 ± 0.003	0.749 ± 0.008
	$N = 1–0, J = 1/2–1/2\ F = 1–0$	87 446.470	262 ± 3	10.700 ± 0.004	0.745 ± 0.011
c-C_3H	$N = 2_{12}–1_{11}, J = 5/2–3/2\ F = 3–2$	91 494.231	106 ± 3	10.395 ± 0.010	0.691 ± 0.024
	$N = 2_{12}–1_{11}, J = 5/2–3/2\ F = 2–1$	91 497.525	59 ± 3	10.561 ± 0.012	0.594 ± 0.034
	$N = 2_{12}–1_{11}, J = 3/2–1/2\ F = 1–0$	91 692.752	32 ± 3	10.712 ± 0.036	0.887 ± 0.084
	$N = 2_{12}–1_{11}, J = 3/2–1/2\ F = 2–1$	91 699.471	74 ± 4	10.760 ± 0.020	0.858 ± 0.050
l-C_3H	$J = 9/2–7/2\ F = 5–4(f)$	97 995.166	44 ± 7	10.605 ± 0.051	0.647 ± 0.108
	$J = 9/2–7/2\ F = 4–3(f)$	97 995.913	45 ± 10	10.583 ± 0.092	0.848 ± 0.235
	$J = 9/2–7/2\ F = 5–4(e)$	98 011.611	41 ± 7	10.629 ± 0.046	0.599 ± 0.116
	$J = 9/2–7/2\ F = 4–3(e)$	98 012.524	35 ± 8	10.550 ± 0.075	0.651 ± 0.183
c-C_3H_2	$2_{02}–1_{11}$	82 093.542	242 ± 6	10.704 ± 0.009	0.741 ± 0.023
	$3_{12}–3_{03}$	82 966.200	68 ± 3	10.660 ± 0.012	0.618 ± 0.029
	$3_{22}–3_{13}$	84 727.696	14 ± 2	10.633 ± 0.028	0.344 ± 0.051
	$2_{12}–1_{01}$	85 338.893	748 ± 4	10.687 ± 0.002	0.767 ± 0.005
	$3_{03}–2_{12}$	117 151.191	507 ± 72	10.680 ± 0.051	0.715 ± 0.117
l-C_3H_2	$4_{14}–3_{13}$	82 395.090	107 ± 7	10.681 ± 0.020	0.720 ± 0.057
	$4_{04}–3_{03}$	83 165.256	43 ± 4	10.362 ± 0.029	0.647 ± 0.068
	$4_{13}–3_{12}$	83 933.700	93 ± 3	10.690 ± 0.010	0.689 ± 0.025
	$5_{15}–4_{14}$	102 992.379	81 ± 3	10.658 ± 0.012	0.657 ± 0.030
	$5_{33}–4_{32}$	103 914.354	27 ± 2	10.592 ± 0.023	0.538 ± 0.052
	$5_{05}–4_{04}$	103 952.926	34 ± 3	10.803 ± 0.030	0.652 ± 0.068
	$5_{14}–4_{13}$	104 915.583	58 ± 4	10.696 ± 0.025	0.703 ± 0.058
C_4H	$N = 9–8, J = 19/2–17/2$	85 634.004	198 ± 4	10.737 ± 0.007	0.689 ± 0.018
	$N = 9–8, J = 17/2–15/2$	85 672.579	168 ± 4	10.725 ± 0.007	0.663 ± 0.018
	$N = 10–9, J = 21/2–19/2$	95 150.388	204 ± 3	10.734 ± 0.004	0.682 ± 0.011
	$N = 10–9, J = 19/2–17/2$	95 188.946	177 ± 3	10.700 ± 0.005	0.665 ± 0.013
	$N = 11–10, J = 23/2–21/2$	104 666.565	202 ± 4	10.732 ± 0.007	0.714 ± 0.019
	$N = 11–10, J = 21/2–19/2$	104 705.106	177 ± 5	10.705 ± 0.011	0.728 ± 0.026
	$N = 12–11, J = 25/2–23/2$	114 182.512	162 ± 12	10.665 ± 0.021	0.582 ± 0.051
	$N = 12–11, J = 23/2–21/2$	114 221.040	186 ± 12	10.663 ± 0.022	0.719 ± 0.056

Notes. Only lines in the 3 mm band with an energy of the upper level lower than 100 K and a higher signal-to-noise ratio than 8 are shown.

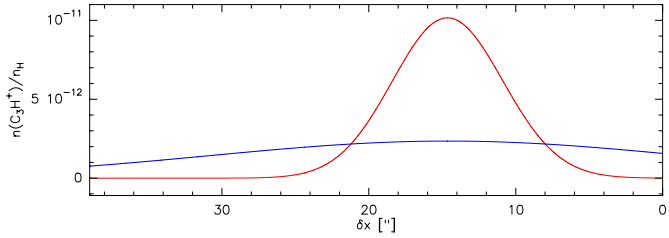

Fig. 6. Spatial profiles of the predicted abundance of C_3H^+ cation. The modeled abundance profile was convolved along the x-axis with a Gaussian of 6″-FWHM (red line), and 27″-FWHM (blue line).

the modeled C_3H^+ abundance convolved by convolution at 6″ and 27″. Clearly, only interferometric observations can provide the high angular resolution needed to resolve the actual structure of the C_3H^+ emission, and potentially detect a spatial shift with respect to the millimeter wave emission of other small hydrocarbons and to the infrared imaging of PAHs and dust grains.

6. Summary

We reported the first detection of l-C_3H^+ in the interstellar medium. Laboratory measurements of the l-C_3H^+ spectroscopy are needed to improve the spectroscopic characterization of this molecular ion. Interferometric imaging with either PdBI or ALMA is required to better constrain the small hydrocarbon chemistry.

Acknowledgements. This work was funded by grant ANR-09-BLAN-0231-01 from the French *Agence Nationale de la Recherche* as part of the SCHISM project. V.G. thanks the Chilean Government for support through the Becas Chile scholarship program. J.R.G. thanks the Spanish MICINN for his support through a Ramón y Cajal research contract and additional funding through grants AYA2009-07304 and CSD2009-00038. We thank H. S. Liszt for finding the neat acronym of this project, "Horsehead WHISPER".

Appendix A: Fit likelihood

We wish to know to which development order we can significantly fit the frequency model to the observed data. Assuming that all intensity channels are independent measures with Gaussian noise, the likelihood, $\mathcal{L}$, of the fit of the model to the data is given by

$$\mathcal{L} = \prod_{i=1}^{N} \left[\frac{1}{\sqrt{2\pi\sigma_i}} \exp\left(-\frac{[I_i^{\rm obs} - I_i^{\rm mod}(\theta)]^2}{2\sigma_i^2} \right) \right], \quad \text{(A.1)}$$

where i is the index over the N measured channel intensities, σ_i the noise of channel i, $I^{\rm obs}$ and $I^{\rm mod}$ the observed and modeled

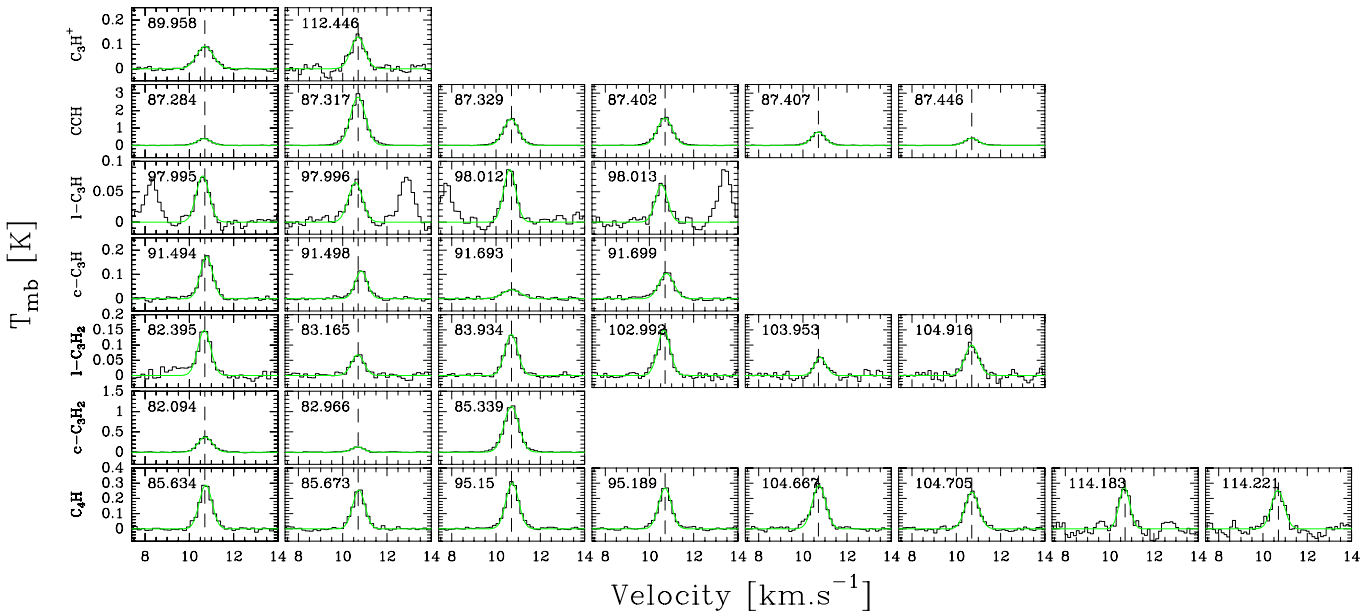

Fig. A.1. Hydrocarbon lines detected toward the Horsehead PDR at RA = $5^h40^m53.936^s$, Dec = $-2°28'00''$ (J2000). Only lines in the 3 mm band, whose energy of the upper level is lower than 100 K and which have a higher signal-to-noise ratio than 8, are shown. The green lines are Gaussian fits. The vertical dashed lines mark 10.7 km s^{-1}.

intensities, and θ the set of model parameters. Taking the logarithm yields $\ln(\mathcal{L}) = K - 0.5\chi^2$, where

$$K = -\frac{1}{2}N\ln(2\pi\sigma_i) \quad \text{and} \quad \chi^2 = \sum_{i=1}^{N}\frac{[I_i^{\rm obs} - I_i^{\rm mod}(\theta)]^2}{\sigma_i^2}.$$

K is a constant and χ^2 is the usual chi square measure of the fit quality. If we try to fit two models M_1 and M_2, which differs only by one parameter, to the same data, the comparison of the fits is said to have only one degree of freedom. The difference $\chi^2_{M_1} - \chi^2_{M_2} = 2\ln(\mathcal{L}_{M_2}/\mathcal{L}_{M_1})$ then follows the well known χ^2 distribution with one degree of freedom. In our case, the difference of χ^2 between the second and third order models is 9.2, which implies that the third-order model better reproduces the data than the second-order model with a probability ≥99.75%. In contrast, developing the centrifugal effect to the fourth order does not bring a significant improvement over the third order development. We therefore stopped the determination of the spectroscopic constants to the third order model.

References

Abergel, A., Teyssier, D., Bernard, J. P., et al. 2003, A&A, 410, 577
Cooper, D. L., & Murphy, S. C. 1988, ApJ, 333, 482
Fuente, A., Rodríguez-Franco, A., García-Burillo, S., Martín-Pintado, J., & Black, J. H. 2003, A&A, 406, 899
Gerin, M., Goicoechea, J. R., Pety, J., & Hily-Blant, P. 2009, A&A, 494, 977
Goicoechea, J. R., Pety, J., Gerin, M., et al. 2006, A&A, 456, 565
Goicoechea, J. R., Pety, J., Gerin, M., Hily-Blant, P., & Le Bourlot, J. 2009, A&A, 498, 771
Goldsmith, P. F., & Langer, W. D. 1999, ApJ, 517, 209
Guzmán, V., Pety, J., Gratier, P., et al. 2012a, A&A, 543, L1
Guzmán, V., Roueff, E., Gauss, J., et al. 2012b, A&A, in press, DOI: 10.1051/0004-6361/201220174
Ikuta, S. 1997, J. Chem. Phys., 106, 4536
Le Bourlot, J., Le Petit, F., Pinto, C., Roueff, E., & Roy, F. 2012, A&A, 541, A76
Le Petit, F., Nehmé, C., Le Bourlot, J., & Roueff, E. 2006, ApJS, 164, 506
Lucas, R., & Liszt, H. S. 2000, A&A, 358, 1069
Mangum, J. G., & Wootten, A. 1990, A&A, 239, 319
Maret, S., Hily-Blant, P., Pety, J., Bardeau, S., & Reynier, E. 2011, A&A, 526, A47
Mebel, A. M., Kislov, V. V., & Hayashi, M. 2007, J. Chem. Phys., 126, 204310
Müller, H. S. P., Thorwirth, S., Roth, D. A., & Winnewisser, G. 2001, A&A, 370, L49
Pety, J. 2005, in SF2A-2005: Semaine de l'Astrophysique Française, eds. F. Casoli, T. Contini, J. M. Hameury, & L. Pagani, 721
Pety, J., Teyssier, D., Fossé, D., et al. 2005, A&A, 435, 885
Pety, J., Goicoechea, J. R., Hily-Blant, P., Gerin, M., & Teyssier, D. 2007, A&A, 464, L41
Pickett, H. M., Poynter, R. L., Cohen, E. A., et al. 1998, J. Quant. Spec. Radiat. Transf., 60, 883
Radom, L., Hariharan, P. C., Pople, J. A., & Schleyer, P. R. 1976, J. Am. Chem. Soc., 98, 3436
Rimmer, P. B., Herbst, E., Morata, O., & Roueff, E. 2012, A&A, 537, A7
Savić, I., & Gerlich, D. 2005, Phys. Chemist. Chem. Phys. (Incorporating Faraday Transactions), 7, 1026
Savić, I., Schlemmer, S., & Gerlich, D. 2005, ApJ, 621, 1163
Teyssier, D., Fossé, D., Gerin, M., et al. 2004, A&A, 417, 135
Teyssier, D., Hily-Blant, P., Gerin, M., et al. 2005, in ESA SP 577, ed. A. Wilson, 423
Turner, B. E., Herbst, E., & Terzieva, R. 2000, ApJS, 126, 427
Wakelam, V., Smith, I. W. M., Herbst, E., et al. 2010, Space Sci. Rev., 156, 13
Wilson, S., & Green, S. 1980, ApJ, 240, 968
Wilson, S., & Green, S. 1982, ApJ, 253, 989
Woon, D. E., & Dunning, Jr., T. H. 1993, J. Chem. Phys., 98, 1358
Wootten, A., Bozyan, E. P., Garrett, D. B., Loren, R. B., & Snell, R. L. 1980, ApJ, 239, 844

Part II

Complex molecules

Chapter 5

H_2CO and CH_3OH

5.1 Introduction

H_2CO and CH_3OH are key species in the synthesis of more complex organic molecules, like amino acids and other prebiotic molecules (Bernstein et al. 2002; Muñoz Caro et al. 2002; Garrod et al. 2008), that could eventually end up in proto-planetary disks, and hence in new planetary systems. Indeed, H_2CO and CH_3OH can trigger the formation of more complex organic molecules, such as s dimethyl ether (CH_3OCH_3) and acetic acid (CH_3COOH), in the warm gas (Charnley et al. 1992). H_2CO and CH_3OH are also good tracers of the physical conditions, *i.e.* the gas density and temperature, in Galactic and extragalactic molecular clouds (Mangum & Wootten 1993; Leurini et al. 2004; Mangum et al. 2013). In addition, because H_2CO and CH_3OH are expected to form in the ices around dust grains, they could potentially be used to trace *snow lines* in protoplanetary disks, which is the distance from the central protostar at which ice can form, and hence where small icy bodies, like comets, and rocky planets can potentially form (Qi et al. 2013). To fully exploit all these properties, it is necessary to understand the dominant formation pathways of H_2CO and CH_3OH in the ISM.

Formaldehyde (H_2CO) was the first organic molecule discovered in the ISM (Snyder et al. 1969). One year later, methanol (CH_3OH) was detected toward the Galactic center (Ball et al. 1970). Owing to their large dipole moment (2.3 D and 1.7 D for H_2CO and CH_3OH, respectively), their rotational lines are easy to detect from ground-based observations. Therefore, since their discovery both species have been detected in a variety of environments, such as Galactic H II regions (e.g., Downes et al. 1980; Codella & Moscadelli 2000), protostars (e.g., Young et al. 2004; Maret et al. 2004; Jørgensen et al. 2005), PDRs (e.g., Leurini et al. 2010), starburst galaxies (e.g., Mangum et al. 2008; Meier & Turner 2005) and comets (e.g., Mumma & Charnley 2011, and references therein). They are also observed in shocked regions, caused by an impact of molecular outflows on the surrounding molecular clouds (e.g., Garay et al. 1998; Tafalla et al. 2010; Sakai et al. 2012; Codella et al. 2012). Observed typical gas-phase abundances relative to H_2 range from $\sim 10^{-7}$ in hot cores (e.g., Sutton et al. 1995; Ceccarelli et al. 2000) to $\sim 10^{-9}$ in cold dark clouds (e.g., Bergman et al. 2011).

Formaldehyde is a slightly asymmetric top molecule (like H_2O), and thus each rotational level is split by this asymmetry into two energy levels. The energy levels are designated by the total angular momentum quantum number J, the projection of J along the symmetry axis for a limiting prolate symmetric top K_a, and for a limiting oblate symmetric top K_c. The asymmetry of H_2CO is very small ($\kappa = -0.96$[1]), so it is structurally similar to a prolate

[1]The Ray's asymmetry parameter κ gives the closeness of a given molecule to the prolate ($\kappa = -1$) or oblate ($\kappa = 1$) limits, and is defined as $\kappa = \frac{2B-A-C}{A-C}$, where $A = \frac{1}{2I_a}$, $B = \frac{1}{2I_b}$ and $C = \frac{1}{2I_c}$

symmetric top molecule. Because it contains two identical hydrogen atoms, H_2CO exists in two different nuclear spin forms. When the hydrogen nuclei spin are parallel, the molecule is called ortho–H_2CO, and when the hydrogen nuclei spin are anti-parallel, the molecule is called para–H_2CO. For the ortho state, K_a is an odd number, while for the para state, K_a is an even number.

Methanol is also a slightly asymmetric rotor ($\kappa = -0.98$). It contains an hydroxyl group (OH), which can rotate around the methyl (CH_3) symmetry axis (hindered internal rotation). Due to the threefold symmetry of its hindering potential, CH_3OH also occurs in two symmetry states, A and E. The energy levels of each symmetry state, are characterized by the total angular momentum quantum number J, and its projection K along the molecular symmetry axis. Because radiative and collisional transitions between the two nuclear spin forms of H_2CO and CH_3OH are forbidden, ortho and para forms of H_2CO, as well as E- and A-type CH_3OH, should be treated as different species. Isomeric conversion can happen through proton exchange reactions, but the timescales are too long compared to the lifetime of the molecules (e.g., Tudorie et al. 2006).

5.2 Formation of H_2CO and CH_3OH

H_2CO can be formed both in the gas-phase and on the surface of dust grains. The relative efficiency of each of these routes will depend on the physical conditions of the medium. CH_3OH, on the other side, is thought to be formed entirely on the surfaces of dust grains. These different formation routes are discussed next.

5.2.1 Gas-phase chemistry

In the gas-phase, the formation of H_2CO and CH_3OH start with CH_3^+. This ion is the result of successive ion-neutral reactions that start with C^+ or CH^+,

$$C^+ + H_2 \rightarrow CH_2^+ \tag{5.1}$$
$$CH^+ + H_2 \rightarrow CH_2^+ + H \tag{5.2}$$
$$CH_2^+ + H_2 \rightarrow CH_3^+ + H. \tag{5.3}$$

CH_3^+ can react again with molecular hydrogen and form CH_5^+, which later recombines with electrons to form the methyl radical (CH_3). H_2CO will then result from the reaction between oxygen atoms and CH_3 (Federman & Allen 1991),

$$CH_3^+ + H_2 \rightarrow CH_5^+ \tag{5.4}$$
$$CH_5^+ + e^- \rightarrow CH_3 + H_2 \tag{5.5}$$
$$CH_3 + O \rightarrow H_2CO + H. \tag{5.6}$$

The methyl ion (CH_3^+) can also react with water to form protonated methanol ($CH_3OH_2^+$),

which will then recombine with electrons to form CH_3OH,

$$CH_3^+ + H_2O \rightarrow CH_3OH_2^+ + h\nu \tag{5.7}$$

$$CH_3OH_2^+ + e^- \rightarrow CH_3OH + H. \tag{5.8}$$

However, the radiative association between CH_3^+ and water is too slow to explain the observed abundances of $\sim 10^{-9}$ in cold dark clouds (Garrod et al. 2006). In addition, laboratory experiments have shown that the dissociative recombination of protonated methanol leading to methanol has a very low branching ratio, and the main products are by far H, CH_3 and OH (Geppert et al. 2006). Therefore, an additional formation mechanism is needed, such as formation on the surface of dust grains.

5.2.2 Grain surface chemistry

The mechanism to form H_2CO and CH_3OH on ices is thought to be the successive hydrogenation of CO,

$$CO + H \rightarrow HCO \tag{5.9}$$

$$HCO + H \rightarrow H_2CO \tag{5.10}$$

$$H_2CO + H \rightarrow CH_2OH \tag{5.11}$$

$$CH_2OH + H \rightarrow CH_3OH \tag{5.12}$$

(Tielens & Whittet 1997; Watanabe & Kouchi 2002). Laboratory experiments have succeeded to efficiently form both H_2CO and CH_3OH through this mechanism (Watanabe et al. 2004; Fuchs et al. 2009). Moreover, observations by the *Infrared Space Observatory (ISO)* and *Spitzer* have shown that dust grains are covered by ice mantles in the cold envelopes surrounding high-mass protostars (Gibb et al. 2000b, 2004), low-mass protostars (Boogert et al. 2008; Pontoppidan et al. 2008; Öberg et al. 2008; Bottinelli et al. 2010) and in isolated dense cores (Boogert et al. 2011). These studies revealed that the ice mantles consist mostly of H_2O, CO_2 and CO, with smaller amounts of CH_3OH, CH_4, NH_3 and H_2CO. HCO ice has not been detected in the interstellar medium (ISM), probably because its formation on the ices is slower than its subsequent hydrogenation to form H_2CO. Indeed, the reactions involving CO and H_2CO in this hydrogenation path have activation energy barriers (Fuchs et al. 2009).

Observations of ices in the envelopes of low-mass protostars show large variations of the CH_3OH ice abundance with respect to water ice (1%-30%; Boogert et al. 2008). In cold cores, a methanol abundance of 5%-12% relative to water has been found (Boogert et al. 2011). The variations in the CH_3OH ice abundance are caused by the different local physical conditions, and thus reflect the variations in the evolutionary stages of these sources (Cuppen et al. 2009). The abundance of H_2CO ice has been more difficult to determine because it has been detected in just a few sources and its stronger ice feature at 6 μm is blended with the one of HCOOH (Öberg et al. 2011). A relatively constant H_2CO ice abundance of $\sim 6\%$ relative to water is found in low-mass protostars (Gibb et al. 2004; Boogert et al. 2008).

5.2.3 Photo-desorption into the gas-phase

Once H_2CO and CH_3OH are formed on the surfaces of dust grains they can be released into the gas-phase either through thermal or non-thermal processes. Thermal processes dominate in regions where dust grains are warm. The sublimation temperatures of H_2CO and CH_3OH are $\sim$ 45 K and $\sim$ 80 K, respectively (Tielens & Allamandola 1987; Brown & Bolina 2007; Green et al. 2009). Hence, this is the dominant mechanism to release molecules into the gas-phase in hot cores, hot corinos and shocked regions (e.g., Jørgensen et al. 2005; Bisschop et al. 2007; Bottinelli et al. 2007; Codella et al. 2012), where the ices that were formed in the cold gas in the prestellar stage are completely sublimated into the gas-phase through thermal desorption and sputtering. This also happens in highly far-UV illuminated PDRs, like in the Orion bar (Leurini et al. 2010).

Non-thermal desorption by far-UV photons can also be efficient, as shown by laboratory experiments (Öberg et al. 2009a,b,c). The CH_3OH photodesorption yield found in these experiment is $\sim 10^{-3}$ molecules per incident UV photon, similar to other species like CO, CO_2 and H_2O. Photodesorption dominates in colder regions, either UV-shielded dense cores where secondary UV photons are produced by the interaction between cosmic rays and H_2 molecules (e.g., Caselli et al. 2012) or in low UV-field illumination photo-dissociation regions, where dust grains are too cold to sublimate their ices. This is the case of the Horsehead, where the combination of moderate radiation field ($\chi = 60$ relative to the Draine field; Draine 1978), and high density ($n_{\rm H} \sim 10^4 - 10^5$ cm^{-3}) implies low dust grain temperatures, from $T_{\rm dust} \sim 30$ K in the outer PDR to $T_{\rm dust} \sim 20$ K slightly deeper inside the cloud (Goicoechea et al. 2009a).

5.3 H_2CO and CH_3OH as tracers of physical properties

Because formaldehyde and methanol are slightly asymmetric rotors, they share many of the properties of the purely symmetric rotor molecules, such as NH_3, CH_3CN and CH_3CCH. One of the most powerful properties of symmetric rotors is that they are excellent probes of the kinetic temperature of the gas. The reason for this is that radiative selection rules dictate $\Delta K = 0$ for symmetric top molecules. This means that energy levels with different K values are populated by collisions. Therefore, line ratios from different $K-$ladders[2] are excellent tracers of the kinetic temperature of the gas. Slightly asymmetric rotors share this property with symmetric rotors and are thus good tracers of the kinetic temperature of the gas. In addition to these diagnostic property, H_2CO and CH_3OH are ubiquitous in the ISM and they have a rich spectrum at millimeter and sub-millimeter wavelengths. This is important because it is possible to observe several lines at the same time, removing uncertainties related to the calibration of the observations. Also, the energy of the upper levels of these transitions cover several hundreds of Kelvin, which is important to disentangle excitation effects. For all these reasons, H_2CO and CH_3OH are good tracers of the kinetic temperature, but also of the gas density and in a wide variety of environments, from cold ($T_{\rm kin} \sim 10$ K) cores to hot ($T_{\rm kin} > 200$ K) core sources near high-mass protostars.

[2] A $K-$ladder is a set of energy levels with the same $K-$values and varying $J-$values. In the same way, a $J-$ladder is a set of energy levels with the same $J-$values and varying $K-$values.

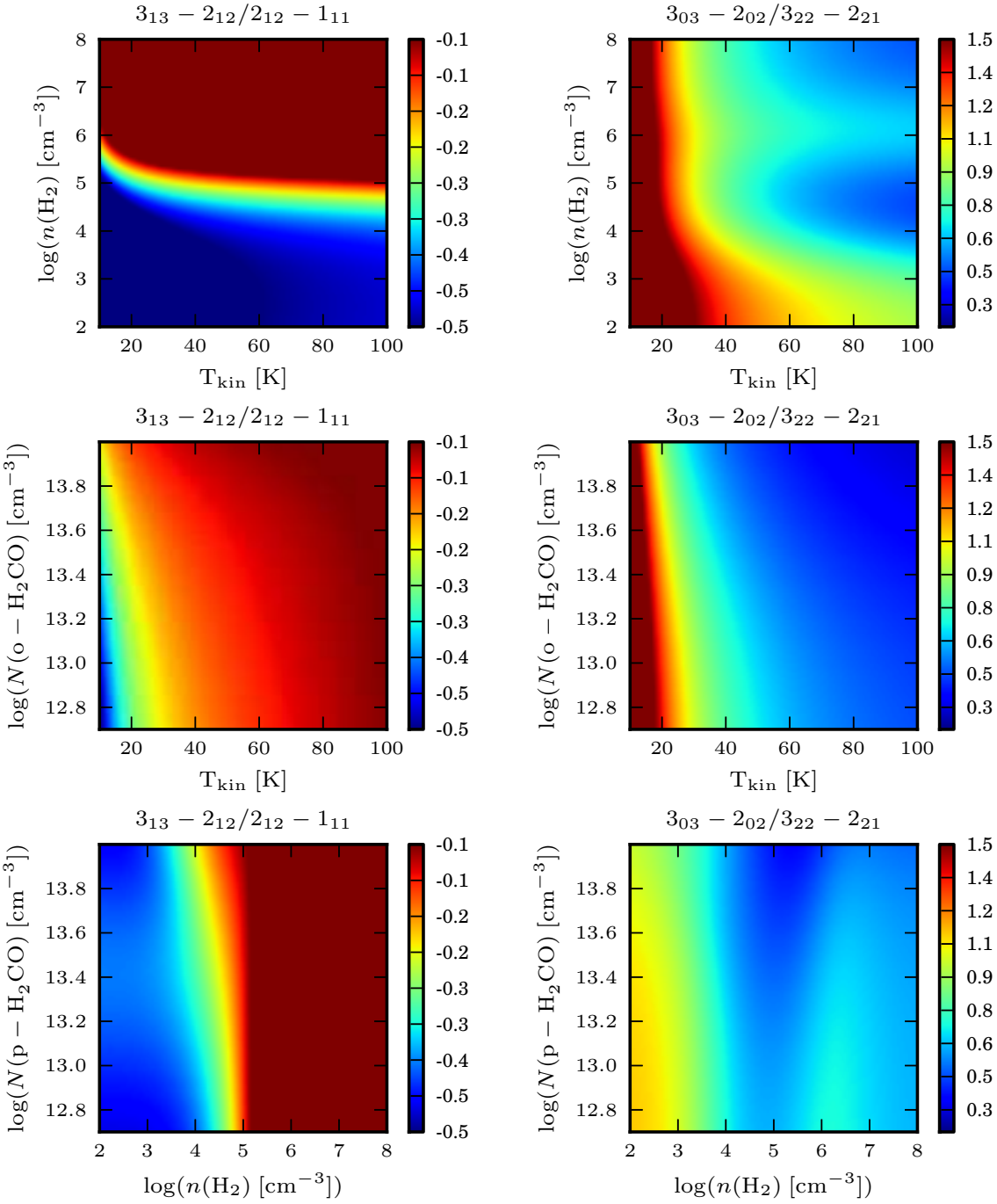

Figure 5.1: Line ratios (in logarithmic scale) predicted by RADEX for o – H_2CO (*left*) and p – H_2CO (*right*). *Upper:* Models for a fixed ortho and para H_2CO column density of 10^{12} cm^{-2}. *Middle:* Models for a fixed H_2 density of 10^5 cm^{-3}. *Bottom:* Models for a fixed kinetic temperature of 60 K.

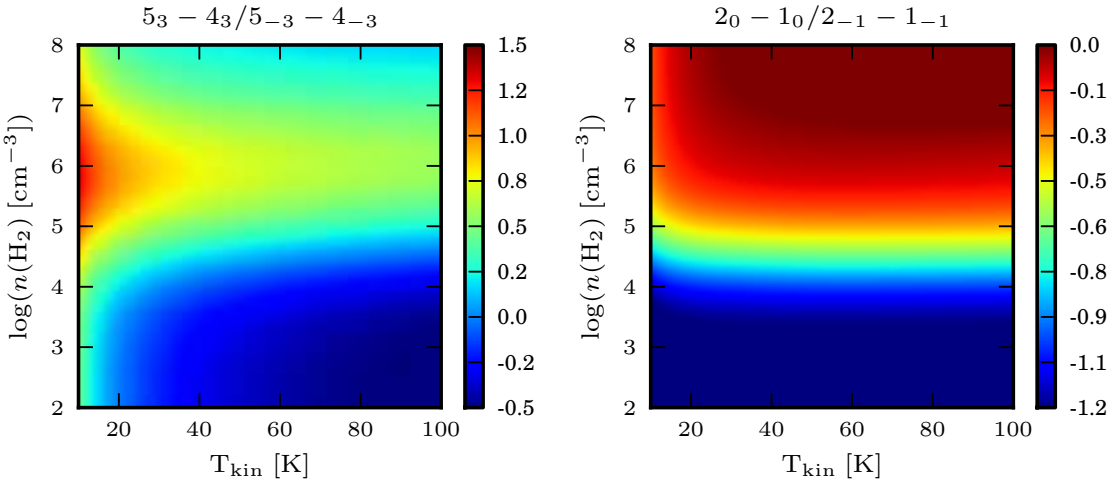

Figure 5.2: Line ratios (in logarithmic scale) predicted by RADEX for $CH_3OH - E$. Models for a fixed CH_3OH column density of 10^{12} cm^{-2}.

Mangum & Wootten (1993) performed a detailed analysis of the temperature and density tracing properties of H_2CO. They found that for $T_{kin} \lesssim 50$ K, several line ratios from the same $K-$ladders are good tracers of the kinetic temperature, while ratios from different $K-$ladders are good probes of the gas density. Figure 5.1 displays an example, with lines that are detected in the Horsehead. The line ratio of two $o - H_2CO$ (left panels) and two $p - H_2CO$ (right panels) lines is shown for a grid of models computed with RADEX (see Section 5.4.1.2 for a description of RADEX). In the upper panels of Fig. 5.1, the line ratios are shown as a function of kinetic temperature and H_2 density, for a fixed column density of H_2CO. In the middle panels the line ratios are shown as a function of kinetic temperature and H_2CO column density, for a fixed H_2 density. Finally, in the bottom panels the line ratios are shown as a function of H_2 density and H_2CO column density, for a fixed kinetic temperature. From these models, it is clear that the $3_{13} - 2_{12}/2_{12} - 1_{11}$ line ratio is a good density probe, while the $3_{03} - 2_{02}/3_{22} - 2_{21}$ line ratio is a better temperature probe for $T_{kin} \lesssim 30$ K. Note that the ortho lines arise from the same $K-$ladder, while the para lines arise from different $K-$ladders.

Leurini et al. (2004) studied the diagnostic properties of CH_3OH in dense molecular clouds, and later tested these properties with observations of high-mass star forming regions (Leurini et al. 2007). They found that the line ratios in the $J = 2 - 1$ and $J = 5 - 4$ ladders are mainly sensitive to the density, with a weak dependence on kinetic temperature. Line ratios in the $J = 7 - 6$ ladder show a dependence on both density and kinetic temperature. Therefore, when many lines are observed it is possible to determine both density and kinetic temperature. Fig. 5.2 displays two $CH_3OH - E$ line ratios as a function of kinetic temperature and density. We can see that the $2_0 - 1_0/2_{-1} - 1_{-1}$ line ratio is mainly sensitive to the gas density, while the $5_3 - 4_3/5_{-3} - 4_{-3}$ line ratio is sensitive to both density and temperature. Line ratios are not sensitive to the column density of the molecule. Therefore the integrated line intensities must be used to derive the beam-averaged column density.

5.4 Observations of H_2CO and CH_3OH in the Horsehead

We detected several millimeter lines of H_2CO (ortho and para) and CH_3OH (E and A types) toward the PDR and dense core positions. In order to study the spatial distribution of these molecules, we complemented these observations with single-dish ($\sim 18''$) and high-resolution ($\sim 6''$) interferometric maps of both species. These results are included in the publications Guzmán et al. (2011) and Guzman et al. (2013).

5.4.1 Determination of column densities

5.4.1.1 LTE analysis

First-order estimates of the beam-averaged column density and the excitation temperature can be found by means of the widely used rotational diagram analysis (Goldsmith & Langer 1999). To do this, we assume that the gas is under LTE, and therefore all excitation temperatures are the same, and the energy levels are populated following Boltzmann's law. We built rotational diagrams corrected for line-opacity effects through

$$\ln \frac{N_u^{\rm thin}}{g_u} + \ln C_\tau = \ln \frac{N}{Z} - \frac{E_u}{kT_{\rm rot}} \tag{5.13}$$

(see Appendix A), where N is the total column density of the molecule, g_u is the upper level degeneracy, E_u/k is the energy of the upper level in K, Z is the partition function at the rotational temperature $T_{\rm rot}$, $C_\tau = \frac{\tau}{1-e^{-\tau}} \leq 1$ is a line opacity correction factor, where τ is the opacity of the line, and $N_u^{\rm thin}$ is the column density of the upper level for an optically thin line when the source fills the beam. This last parameter is given by

$$N_u^{\rm thin} = \frac{8\pi k \nu^2 W}{hc^3 A_{ul}} \tag{5.14}$$

where k is the Boltzmann constant, ν is the line frequency, W is the integrated line intensity, h is the Planck constant, c is the speed of light and A_{ul} is the Einstein coefficient for spontaneous emission.

Figure 5.3 displays the rotational diagrams for H_2CO and CH_3OH for different line-opacities. The different symmetry species are treated as different species. The line-opacity of each transition is computed from the line-opacity of a reference transition (e.g., τ_2), as follows:

$$\frac{\tau_1}{\tau_2} = \frac{g_u^1}{g_u^2}\frac{A_{ul}^1}{A_{ul}^2}\left(\frac{\nu_2}{\nu_1}\right)^3 \left(\frac{e^{h\nu_1/kT_{\rm rot}}-1}{e^{h\nu_2/kT_{\rm rot}}-1}\right)\left(\frac{e^{-E_u^1/kT_{\rm rot}}}{e^{-E_u^2/kT_{\rm rot}}}\right) \tag{5.15}$$

where the sub-index and super-index indicate the reference transition (2 in this example) and the transition for which the opacity is computed (1 in this example), respectively. The observed intensities are corrected for line-opacities of 0, 1 and 5 for the lower-frequency transition of $o-H_2CO$, $p-H_2CO$, CH_3OH-E and CH_3OH-A that was observed. The ortho $2_{12}-2_{11}$ and para $2_{02}-1_{01}$ lines of the $H_2^{13}CO$ isotopologue were detected at the dense core position, from which an opacity in the range $1.6-1.9$ is derived for H_2CO. No isotopologues of CH_3OH were detected in either position. The effect of the opacity on the

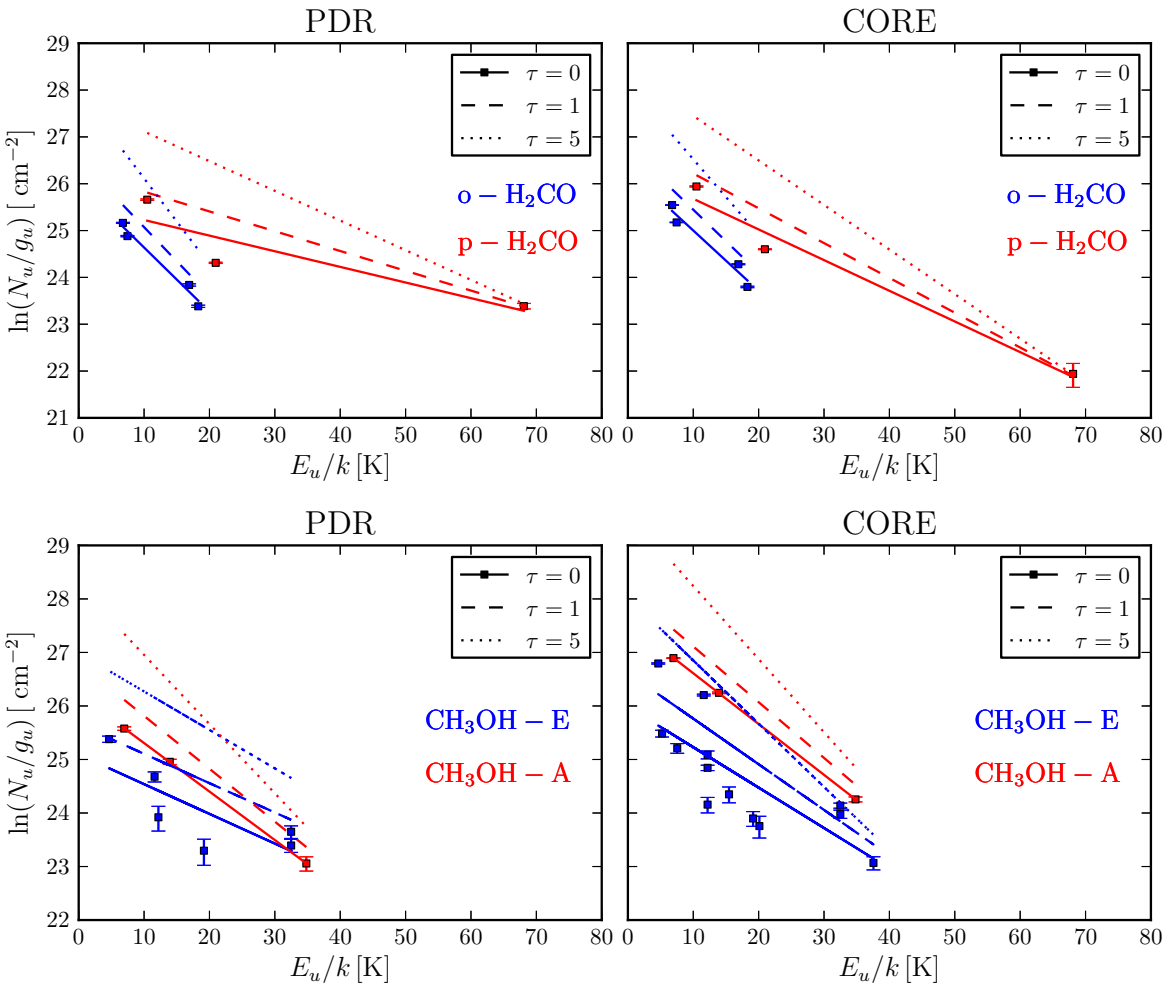

Figure 5.3: Rotational diagrams for the PDR (*left*) and dense core (*right*). The ortho and para H_2CO lines (*upper panels*) are treated as different species, as well as the E and A type CH_3OH (*lower panels*). The points correspond to the observations without line-opacity correction ($\tau = 0$). The observations corrected for line-opacity are not included in the figure to avoid confusion, but the fit of the line-opacity corrected observations are shown in dashed ($\tau = 1$) and dotted lines ($\tau = 5$).

rotational diagram is seen in Fig. 5.3 and the derived rotational temperatures and column densities are listed in Table 5.1. In short, at higher line-opacities the rotational temperature decreases and the inferred column density increases. Therefore, if one does not correct for line-opacity effects the column density can be underestimated, in this case by almost one order of magnitude.

The inferred rotational temperatures are different between the two symmetry species of H_2CO and CH_3OH. These temperatures are also lower than the kinetic temperature of the PDR ($T_{\rm kin} \sim 60$ K) and dense core ($T_{\rm kin} \sim 20$ K), which means they are sub-thermally excited. Sub-thermal emission is expected for transitions with high critical densities compared to the

Table 5.1: Rotational diagram results.

Species		PDR			CORE		
	τ	$T_{\rm rot}$ [K]	$Z(T_{\rm rot})$	N [cm^{-2}]	$T_{\rm rot}$ [K]	$Z(T_{\rm rot})$	N [cm^{-2}]
o $-$ H_2CO	0	7.3	33.7	6.6×10^{12}	7.8	35.2	9.2×10^{12}
	1	6.9	32.2	1.1×10^{13}	7.4	34.1	1.5×10^{13}
	5	5.4	27.6	3.8×10^{13}	6.2	30.0	5.0×10^{13}
p $-$ H_2CO	0	30.0	23.3	2.9×10^{12}	15.3	9.6	2.6×10^{12}
	1	23.7	16.7	4.2×10^{12}	13.5	8.3	4.3×10^{12}
	5	15.8	10.0	1.1×10^{13}	10.5	6.4	1.4×10^{13}
CH_3OH $-$ E	0	18.0	47.5	3.8×10^{12}	13.3	30.0	5.8×10^{12}
	1	18.3	48.4	6.7×10^{12}	11.7	25.0	9.1×10^{12}
	5	13.9	32.3	1.7×10^{13}	8.5	15.6	2.3×10^{13}
CH_3OH $-$ A	0	11.0	14.9	3.6×10^{12}	10.5	13.9	1.3×10^{13}
	1	10.1	13.1	5.7×10^{12}	9.6	12.1	2.0×10^{13}
	5	7.7	8.9	1.6×10^{13}	7.3	8.2	5.9×10^{13}

H_2 density. The critical density of a transition is defined as the density at which the sum of the spontaneous radiative de-excitation rates (A_{ul}) is equal to the sum of the collisional de-excitation rates (γ_{ul}) of a given level. Therefore, for a given collisional partner and kinetic temperature,

$$n_{cr}(J'_{K'_aK'_c}, T_{\rm kin}) = \frac{\sum_{J''_{K''_aK''_c}} A(J'_{K'_aK'_c} \rightarrow J''_{K''_aK''_c})}{\sum_{J''_{K''_aK''_c}} \gamma(J'_{K'_aK'_c} \rightarrow J''_{K''_aK''_c}, T_{\rm kin})} \tag{5.16}$$

In high-density environments or for molecules with small dipole moments like CO, collisions dominate the de-excitation ($\gamma_{ul} \gg A_{ul}$), the excitation temperature is the same as the kinetic temperature of the gas, and the gas is thus under LTE. The critical densities of the observed H_2CO and CH_3OH transitions are listed in Tables 4 and 3 in Guzmán et al. (2011) and Guzman et al. (2013) respectively. The observed lines of both species have high critical densities ($\sim 10^6$ cm^{-3} for H_2CO and $\sim 10^5$ cm^{-3} for CH_3OH), which is consistent with the low rotational temperatures derived above. It is also clear from Figure 5.3 that most of the observations are not well fitted by a straight line, *i.e.* by a single excitation temperature. This is especially true for CH_3OH $-$ E, for which more lines are detected. All this suggests that the gas is far from thermalization, and a non-LTE analysis must be done to determine the column densities.

5.4.1.2 Local non-LTE radiative transfer

When the gas is not in LTE, one has to explicitly solve the statistical equilibrium equations (including collisional and radiative rates) for each rotational level. The level populations are coupled to the radiation field (line and continuum photons), which also depends on the level populations at different positions of the cloud. The non-LTE excitation problem is thus a non-linear, nonlocal problem. One of the most widely used non-LTE approach is the escape

Table 5.2: Local non-LTE results.

Species	ν^a	PDR n_H 10^4 cm^{-3}	PDR T_{kin} K	PDR N 10^{12} cm^{-2}	CORE n_H 10^5 cm^{-3}	CORE T_{kin} K	CORE N 10^{12} cm^{-2}
o − H_2CO	1	6.0*	60*	12.1	1.0*	20.0*	22.7
p − H_2CO	1	6.0*	60*	5.3	1.0*	20.0*	7.5
				No electron excitation			
CH_3OH − E	3	10.1	39.6	2.7	0.4	38.4	9.5
	2	6.0*	59.2	2.5	1.0*	31.2	6.5
	2	7.0	60*	2.5	0.6	20.0*	8.6
CH_3OH − A	1	6.0*	59.2*	1.9	1.0*	31.2*	8.1
				With electron excitation[b]			
CH_3OH − E	3	5.4	65.3	2.7	-	-	-
	2	6.0*	62.0	2.7	-	-	-
	2	6.5	60*	2.6	-	-	-
CH_3OH − A	1	6.0*	62.0*	1.9	-	-	-

(*) Fixed parameters.
(^{a}) Number of free parameters.
(^{b}) For an electron abundance $n(e^-)/n(H_2) = 10^{-4}$ cm^{-3} at the PDR. At the dense core, $n(e^-)/n(H_2) = 10^{-9}$ cm^{-3}, which is negligible.

probability method. In this method the probability that a newly emitted photon escapes the cloud is given by the parameter β_ν, with $\beta = 1$ for $\tau = 0$ and $\beta < 1$ for $\tau > 0$. The value of the escape probability will depend on the cloud geometry and line opacity. In the large velocity gradient (LVG) approximation (also called the Sobolev method; Sobolev 1957), β_ν depends on the velocity gradient in the cloud. The idea is that the velocity differences across the cloud are much larger than the thermal line widths at each position. Therefore, a photon emitted at a given position in the cloud can only interact with molecules that are nearby. This approximation is thus local and does not take into account the global transport of photons in the cloud. Nevertheless, this method usually gives a reasonable answer to the problem unless the lines are very opaque.

RADEX is a radiative transfer numerical code (van der Tak et al. 2007) that uses the LVG approximation to compute the line intensities of a species for a given column density, kinetic temperature and density of H_2. It can be used for species for which the collisional coefficients have been computed. In order to compute the column density of H_2CO and CH_3OH we run grids of models for different gas densities, kinetic temperatures and column densities. The details on the collisional coefficients and energy levels included in the computations are given in Guzmán et al. (2011) and Guzman et al. (2013) for H_2CO and CH_3OH, respectively.

Formaldehyde: As we detected few lines of the ortho and para species, we ran models for different column densities but kept the density and kinetic temperature fixed to well-known values in the Horsehead ($n(H_2) \sim 6 \times 10^4$ cm^{-3} and $T_{kin} \sim 60$ K; $n(H_2) \sim 10^5$ cm^{-3} and

$T_{\rm kin} \sim 20$ K). The best fits results were found by computing the χ^2, defined as

$$\chi^2 = \sum_{1}^{N} \frac{(O_i - M_i)^2}{\sigma_i^2} \tag{5.17}$$

for each model. Here, O_i and M_i are the observed and modeled integrated line areas of each line, and σ_i are the associated errors to the observations. The results are given in Table 5.2. The derived column densities are consistent with the results found with the rotational diagram analysis for opacities of ~ 1 (see Table 5.1). The ortho-to-para ratio inferred at the dense core is the equilibrium value of 3, while at the PDR a lower value of 2 is derived.

Methanol: Because we detected several lines of $CH_3OH - E$ we ran a grid of models leaving all three parameters, $n(H_2), T_{\rm kin}$ and N, free. The inferred physical properties at the PDR and dense core are not consistent with the well-known gas density and kinetic temperature at these positions (see Table 5.2). We therefore run models leaving only one or two of the parameters free. The inferred $CH_3OH - E$ column densities are consistent within these different models, no matter the number of free parameters. We then investigated the importance of electrons in the excitation at the PDR position, where the electron fraction is high 10^{-4} relative to H_2 (Goicoechea et al. 2009b). In the dense core the electron fraction is much lower (10^{-9}), so electron excitation is negligible at this position. The inferred $CH_3OH - E$ column densities does not change when electron excitation is included. However, the inferred gas density and kinetic temperature are in much better agreement with the well-known physical conditions in the PDR. At the dense core, on the other hand, electron excitation cannot explain the low gas density inferred by the model. This suggests that the $CH_3OH - E$ emission does not arise from the dense core itself, but from the lower density gas around it. Further evidence supporting this scenario will be discussed in Section 5.4.2. For $CH_3OH - A$ only three lines were detected. Therefore, in order to compute its column density, the gas density and kinetic temperature were fixed to the best fit values found for $CH_3OH - E$. Figure 5.4 shows the 1, 2 and 3σ confidence levels for the PDR (red) and dense core (blue) for models including electron excitation.

Table 5.3: Column densities in [cm^{-2}].

Molecule	PDR	Dense core
RADEX		
$N(o - H_2CO)$	1.2×10^{13}	2.3×10^{13}
$N(p - H_2CO)$	5.3×10^{12}	7.5×10^{12}
Monte-Carlo code		
$N(o - H_2CO)$	7.2×10^{12}	9.6×10^{12}
$N(p - H_2CO)$	3.6×10^{12}	3.2×10^{12}

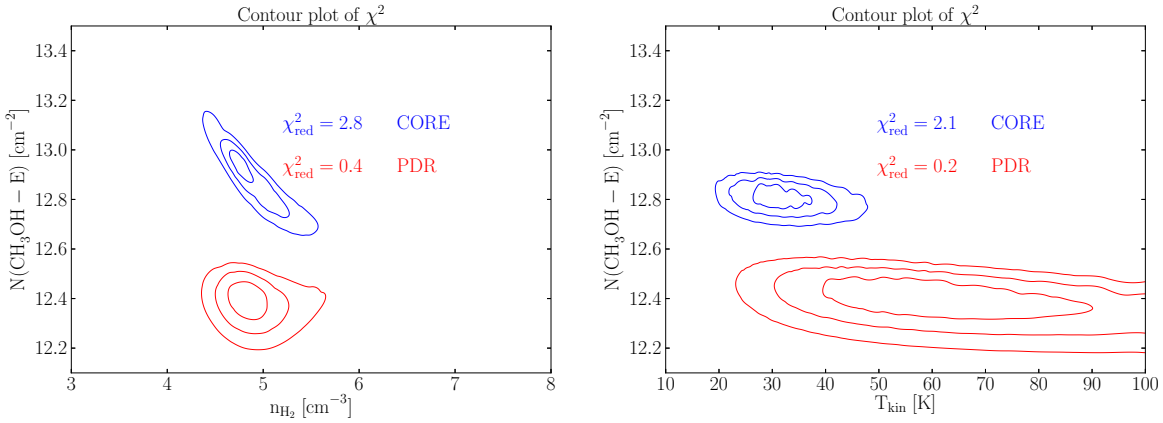

Figure 5.4: Contours of χ^2 for $CH_3OH - E$. (*Left:*) The kinetic temperature was kept constant to $T_{kin} = 60$ K for the PDR, and $T_{kin} = 20$ K for the dense core. (*Right:*) The H_2 density was kept constant to $n(H_2) = 6 \times 10^4$ cm^{-3} for the PDR, and $n(H_2) = 10^5$ cm^{-3} for the dense core. The red (PDR) and blue (core) contours indicate the 1, 2 and 3σ confidence levels for the models. The reduced χ^2, defined as $\chi^2 = \chi^2/(N-2)$ with N the number of observations, is shown for the best fit model at each position.

5.4.1.3 Nonlocal non-LTE radiative transfer

As mentioned in the last section, RADEX does not take into account the radiative coupling between different cloud positions that might affect the population of the energy levels. We therefore used a nonlocal non-LTE radiative Monte-Carlo code adapted to the Horsehead geometry to model the observed H_2CO line intensities. A description of the model can be found in the appendix of Goicoechea et al. (2006). The collisional coefficients and number of energy levels included are the same as the ones used for RADEX. The disadvantage of this model with respect to RADEX is that it can be much more time consuming, depending on the number of energy levels (and transitions) included. As methanol has a very rich spectrum, we did not use this model to compute its column density.

The observed H_2CO lines together with three models for different $o - H_2CO$ column densities are shown in Fig. 3 of Guzmán et al. (2011) and in Fig. 5 of Guzman et al. (2013). The column densities that best fit the observations are given in Table 5.3. The inferred H_2CO column densities with the Monte-Carlo code are ~ 2 times smaller than the values found with RADEX. This difference is not important when comparing the observed abundances with the model predictions. Both models result in an ortho-to-para ratio of 3 at the dense core position, and of 2 at the PDR position.

5.4.2 Results

The main results of this work are summarized next.

1. We detected several lines from ortho and para H_2CO, as well as from E- and A-type methanol, at the PDR and dense core positions in the Horsehead. H_2CO beam-averaged

abundances are similar in the PDR and dense core ($\simeq 2-3\times10^{-10}$). CH_3OH beam-averaged abundances are also similar at both positions ($\simeq 1-2.3\times10^{-10}$).

2. We detected HDCO and D_2CO in the dense core. We derive relative abundances of $[HDCO]/[H_2CO] = 0.11$ and $[D_2CO/H_2CO] = 0.04$.

3. The excitation and radiative transfer analysis of CH_3OH suggests that the methanol emission arises in a region with a gas density of $n(H_2) \sim 4\times10^4$ cm^{-3}, which is lower than the well-known gas density in the dense core ($n(H_2) \sim 10^5$ cm^{-3}). We find that when the electron abundance is high ($[e^-] > 10^{-4}$), the electron excitation is important to derive the physical conditions of the gas from methanol lines. The column density, on the other hand, is not sensitive to the inclusion of electron excitation.

4. We infer an equilibrium H_2CO ortho-to-para ratio of ~ 3 in the dense core, while in the PDR we find a non-equilibrium value of ~ 2. For CH_3OH, the inferred E/A ratio is close to one at both positions. The H_2CO/CH_3OH abundance ratio is 2.3 ± 0.4 in the PDR and 0.9 ± 0.1 in the dense core.

5. The high-angular resolution PdBI maps show that the emission of H_2CO and CH_3OH is extended, but some structure is present. Both H_2CO and CH_3OH lines are brighter in the inner and colder layers of the nebula. However, CH_3OH presents a dip in its emission at the dense core position, while H_2CO peaks at this position.

6. Pure gas-phase models predict H_2CO and CH_3OH abundances at the PDR position that are too low compared to the abundances inferred from the observations. The observations thus suggest that both species are mostly formed on the surface of dust grains, probably through the successive hydrogenation of CO ices as laboratory experiments have shown. The H_2CO and CH_3OH ices are subsequently released into the gas-phase through photodesorption. Thermal desorption is not efficient because dust grains are not warm enough ($T_{\rm dust} \simeq 20-30$ K).

7. At the dense core position, the H_2CO abundance inferred from the observations is well reproduced by a pure gas-phase model. However, the pure-gas phase model fails to reproduce the observed CH_3OH abundance by ~ 5 orders of magnitude at this position. Therefore, the observations suggest that at the dense core position, H_2CO is formed mainly on the gas-phase, while methanol is formed on the ices at the surface of dust grains and it is subsequently photodesorbed into the gas-phase.

The different formation routes for H_2CO at the PDR and dense core positions suggested by the models is strengthened by the different ortho-to-para ratios derived from the observations (result 4). At the dense core position, there are 3 observational results that suggest that H_2CO is formed in the gas-phase, while CH_3OH is formed through grain surface chemistry. First, methanol emission arises from a lower density gas than the dense core (result 3). Second, H_2CO and CH_3OH present a different spatial distribution at the dense core (result 5). If both species were formed through grain surface chemistry at this position, they would have a similar spatial distribution. Third, the H_2CO ortho-to-para ratio of ~ 3 we find for the

dense core is consistent with a gas-phase formation scenario (result 4). All this suggests that CH_3OH is present in an envelope around the dense core, while H_2CO is present in both the envelope and the dense core itself. This is consistent with the fact that the number of far-UV photons that can photodesorb species in the dense core is smaller than the number of far-UV photons available at the PDR position. Therefore photodesorption is inefficient in the dense core, and methanol remains depleted onto grains while H_2CO can still form in the gas phase.

A&A 534, A49 (2011)
DOI: 10.1051/0004-6361/201117257

Astronomy & Astrophysics

H_2CO in the Horsehead PDR: photo-desorption of dust grain ice mantles

V. Guzmán[1,2], J. Pety[2,1], J. R. Goicoechea[3], M. Gerin[1], and E. Roueff[4]

[1] LERMA – LRA, UMR 8112, Observatoire de Paris and École Normale Supérieure, 24 rue Lhomond, 75231 Paris, France
e-mail: [viviana.guzman;maryvonne.gerin]@lra.ens.fr
[2] IRAM, 300 rue de la Piscine, 38406 Grenoble Cedex, France
e-mail: pety@iram.fr
[3] Departamento de Astrofísica, Centro de Astrobiología, CSIC-INTA, Carretera de Ajalvir, Km 4, Torrejón de Ardoz, 28850 Madrid, Spain
e-mail: jr.goicoechea@cab.inta-csic.es
[4] LUTH UMR 8102, CNRS and Observatoire de Paris, Place J. Janssen, 92195 Meudon Cedex, France
e-mail: evelyne.roueff@obspm.fr

Received 13 May 2011 / Accepted 22 August 2011

ABSTRACT

Aims. For the first time we investigate the role of the grain surface chemistry in the Horsehead photo-dissociation region (PDR).
Methods. We performed deep observations of several H_2CO rotational lines toward the PDR and its associated dense-core in the Horsehead nebula, where the dust is cold ($T_{dust} \simeq 20-30$ K). We complemented these observations with a map of the p-H_2CO $3_{03}-2_{02}$ line at 218.2 GHz (with 12″ angular resolution). We determine the H_2CO abundances using a detailed radiative transfer analysis and compare these results with PDR models that include either pure gas-phase chemistry or both gas-phase and grain surface chemistry.
Results. The H_2CO abundances ($\simeq 2–3 \times 10^{-10}$) with respect to H-nuclei are similar in the PDR and dense-core. In the dense-core the pure gas-phase chemistry model reproduces the observed H_2CO abundance. Thus, surface processes do not contribute significantly to the gas-phase H_2CO abundance in the core. In contrast, the formation of H_2CO on the surface of dust grains and subsequent photo-desorption into the gas-phase are needed in the PDR to explain the observed gas-phase H_2CO abundance, because the gas-phase chemistry alone does not produce enough H_2CO. The assignments of different formation routes are strengthen by the different measured ortho-to-para ratio of H_2CO: the dense-core displays the equilibrium value (~3) while the PDR displays an out-of-equilibrium value (~2).
Conclusions. Photo-desorption of H_2CO ices is an efficient mechanism to release a significant amount of gas-phase H_2CO into the Horsehead PDR.

Key words. astrochemistry – ISM: clouds – ISM: molecules – ISM: individual objects: Horsehead nebula – radiative transfer – radio lines: ISM

1. Introduction

Photo-dissociation region (PDR) models are used to understand the evolution of the far-UV illuminated matter both in our Galaxy and in external galaxies. The spectacular instrumental improvements, which happen in radioastronomy with the advent of Herschel, ALMA and NOEMA, call for matching progresses in PDR modeling. In particular, the physics and chemistry of the dust grains and of the gas-phase are intricately intertwined. It is well known that the formation of ice grain mantles leads to the removal of chemical reservoirs like CO, O, and other abundant species from the gas phase, enabling new chemical routes to be opened and others to be closed. Despite their low temperature, the mantles are chemically active. Hydrogenation/deuteration reactions are known to be efficient, because hydrogen (or deuterium atoms) can migrate on the surfaces, but reactions with O, N, and C must also be considered. Complex molecules may therefore be formed before they are released into the gas phase. Moreover, the release of the products into the gas phase happens either through thermal processes (evaporation) or non-thermal ones (cosmic ray or far-UV photon-induced desorption). Recent photo-desorption experiments on water and CO ices show that this mechanism is much more efficient than previously thought (Öberg et al. 2009b,a; Muñoz Caro et al. 2010). These results led various groups to include photo-desorption into PDR models (see the results on H_2O and O_2 by Hollenbach et al. 2009; Walsh et al. 2010; Hassel et al. 2010). The availability of well-defined observations is essential here to distinguish between chemical assumptions about the significant grain surface processes, i.e., adsorption, desorption, and diffusion. It is now confirmed that some interstellar species are mostly formed in the gas-phase (CO for instance), others on grains (CH_3OH, Garrod et al. 2007), while the chemical routes for other complex species such as formaldehyde, are still debated because it is likely that solid and gas-phase processes are both needed.

Formaldehyde (H_2CO) was the first organic molecule discovered in the interstellar medium (Snyder et al. 1969). It is a relatively simple organic molecule that can be formed in the gas-phase and on the surface of dust grains. In the warm gas, H_2CO can trigger the formation of more complex organic molecules (Charnley et al. 1992). It is one of the most popular molecules used for studying the physical conditions of the gas in astrophysical sources. Indeed, it is a good probe of the temperature and density of the gas (Mangum & Wootten 1993). Owing to its

Table 1. Observation parameters for the maps shown in Fig. 1.

Molecule	Transition	Frequency GHz	Instrument	Beam arcsec	PA °	Vel. resol. km s^{-1}	Int. time hours	T_{sys} K (T_A^*)	Noise K (T_{mb})	Obs. date
	Continuum at 1.2 mm		30m/MAMBO	11.7 × 11.7	0	–	–	–	–	–
DCO^+	3–2	216.112582	30m/HERA	11.4 × 11.4	0	0.11	1.5/2.0[a]	230	0.10	2006 Mar.
p-H_2CO	3_{03}–2_{02}	218.222190	30m/HERA	11.9 × 11.9	0	0.05	2.1/3.4[a]	280	0.32	2008 Jan.
HCO	$1_{0,1}$ 3/2, 2–$0_{0,0}$ 1/2, 1	86.670760	PdBI/C&D	6.69 × 4.39	16	0.20	6.5[b]	150	0.09[c]	2006–2007

Notes. The projection center of all maps is $\alpha_{2000} = 05^h40^m54.27^s$, $\delta_{2000} = -02°28'00''$. [(a)] Two values are given for the integration time: the on-source time and the telescope time. [(b)] On-source time computed as if the source were always observed with six antennae. [(c)] The noise values quoted here are the noises at the mosaic phase center (mosaic noise is inhomogeneous because of the primary beam correction; it steeply increases at the mosaic edges).

Table 2. Observation parameters of the deep integrations of the o-H_2CO and p-H_2CO lines toward the PDR and the dense-core.

Position	Molecule	Transition	ν [GHz]	Line area K km s^{-1}	Instrument	F_{eff}	B_{eff}	Int. time hours	T_{peak} K (T_{mb})	rms K	S/N
	o-H_2CO	2_{12}–1_{11}	140.839	1.75 ± 0.02	30-m/C150	0.93	0.70	1.9	1.87	0.061	31
	p-H_2CO	2_{02}–1_{01}	145.603	1.32 ± 0.02	30-m/D150	0.93	0.69	1.9	1.61	0.047	34
	o-H_2CO	2_{11}–1_{10}	150.498	1.41 ± 0.02	30-m/C150	0.93	0.68	1.4	1.52	0.053	29
PDR	o-H_2CO	3_{13}–2_{12}	211.211	1.24 ± 0.03	30-m/B230	0.91	0.57	1.1	1.46	0.096	15
	p-H_2CO	3_{03}–2_{02}	218.222	0.77 ± 0.01	30-m/B230	0.91	0.55	3.9	1.11	0.052	21
	p-H_2CO	3_{22}–2_{21}	218.476	0.17 ± 0.01	30-m/B230	0.91	0.55	2.0	0.27	0.055	5
	o-H_2CO	3_{12}–2_{11}	225.698	0.84 ± 0.02	30-m/A230	0.91	0.54	6.5	1.12	0.079	14
	o-H_2CO	2_{12}–1_{11}	140.839	2.56 ± 0.01	30-m/C150	0.93	0.70	3.7	3.46	0.036	96
	p-H_2CO	2_{02}–1_{01}	145.603	1.75 ± 0.02	30-m/D150	0.93	0.69	1.9	2.62	0.044	60
	o-H_2CO	2_{11}–1_{10}	150.498	1.89 ± 0.01	30-m/C150	0.93	0.68	1.5	2.52	0.052	49
	o-H_2CO	3_{13}–2_{12}	211.211	1.93 ± 0.02	30-m/B230	0.91	0.57	2.0	3.02	0.065	47
	p-H_2CO	3_{03}–2_{02}	218.222	1.03 ± 0.01	30-m/B230	0.91	0.55	3.0	1.83	0.057	32
	p-H_2CO	3_{22}–2_{21}	218.476	0.04 ± 0.01	30-m/B230	0.91	0.55	4.5	0.06	0.037	2
Dense-core	o-H_2CO	3_{12}–2_{11}	225.698	1.27 ± 0.02	30-m/A230	0.91	0.54	8.4	1.96	0.073	27
	o-$H_2^{13}CO$	2_{12}–1_{11}	137.450	0.09 ± 0.02	30-m/D150	0.95	0.70	2.0	0.11	0.063	2
	p-$H_2^{13}CO$	2_{02}–1_{01}	141.984	0.10 ± 0.01	30-m/D150	0.95	0.70	1.5	0.11	0.060	2
	HDCO	2_{11}–1_{10}	134.285	0.13 ± 0.01	30-m/C150	0.94	0.71	2.0	0.32	0.042	8
	HDCO	3_{12}–2_{11}	201.341	0.05 ± 0.01	30-m/A230	0.91	0.59	3.5	0.13	0.032	4
	p-D_2CO	2_{12}–1_{11}	110.838	0.04 ± 0.01	30-m/A100	0.95	0.75	4.9	0.08	0.031	3
	o-D_2CO	4_{04}–3_{03}	231.410	0.04 ± 0.01	30-m/A230	0.91	0.53	4.5	0.09	0.068	1

large dipole moment (2.3 Debye), its rotational lines are easy to detect from ground-based observations. It is present in a variety of environments, such as Galactic HII regions (e.g., Downes et al. 1980), proto-stellar cores (e.g., Young et al. 2004; Maret et al. 2004), young stellar objects (e.g., Araya et al. 2007), PDRs (e.g., Leurini et al. 2010), starburst galaxies (e.g., Mangum et al. 2008) and comets (e.g., Snyder et al. 1989; Milam et al. 2006).

The Horsehead PDR is particularly well-suited to investigate grain surface chemistry in a UV irradiated environment. It is viewed nearly edge-on (Habart et al. 2005) at a distance of 400 pc (implying that 10″ correspond to 0.02 pc). Thus, it is possible to study the interaction of far-UV radiation with dense interstellar clouds and the transition from warm to cold gas in a PDR with a simple geometry, very close to the prototypical kind of source needed to serve as a reference to chemical models. Its relatively low UV illumination ($\chi = 60$ in Draine units, Draine 1978) and high density ($n_H \sim 10^4$–10^5 cm^{-3}) implies low dust grain temperatures, from $T_{dust} \sim 30$ K in the PDR to $T_{dust} \sim 20$ K deeper inside the cloud (Goicoechea et al. 2009a). The release of the grain mantle products into the gas phase is consequently dominated by photo-desorption, while regions with warmer dust (the Orion bar or the star-forming cores) provide mixed information on the thermal and non-thermal processes (e.g., Bisschop et al. 2007).

In this paper we present deep observations of several formaldehyde lines toward two particular positions in the Horsehead nebula: the PDR, corresponding to the peak of the HCO emission (Gerin et al. 2009), where the gas is warm ($T_{kin} \sim 60$ K); and the dense-core, a cold ($T_{kin} \leq 20$ K) condensation located less than 40″ away from the PDR edge, where HCO^+ is highly deuterated (Pety et al. 2007). We present the observations and data reduction in Sect. 2, while the results and abundances are given in Sect. 3. In Sect. 4 we present the H_2CO chemistry and PDR modeling. A discussion is given in Sect. 5 and we conclude in Sect. 6.

2. Observations and data reduction

Tables 1 and 2 summarize the observation parameters for the data obtained with the IRAM-30 m and PdBI telescopes. Figure 1 displays the p-H_2CO, HCO, DCO^+ and 1.2 mm continuum maps. The p-H_2CO line was mapped during 3.3 h of good winter weather (~1 mm of water vapor) using the first polarization (i.e. nine of the eighteen available pixels) of the IRAM-30m/HERA single-sideband multi-beam receiver. We used the frequency-switched, on-the-fly observing mode. We observed along and perpendicular to the direction of the exciting star in zigzags (i.e. ± the lambda and beta scanning direction). The multi-beam system was rotated by 9.6° with respect to the scanning direction. This ensured Nyquist sampling between the rows except at the edges of the map. The fully sampled part of the map covered a 150″ × 150″ portion of the sky. A detailed description

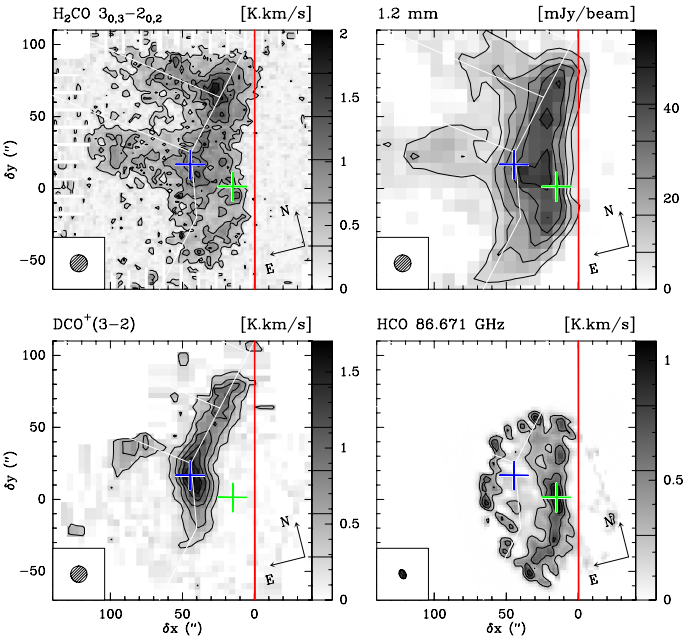

Fig. 1. Integrated intensity maps of the Horsehead edge. The intensities are expressed in the main-beam temperature scale. Maps were rotated by 14° counter-clockwise around the projection center, located at $(\delta x, \delta y) = (20'', 0'')$, to bring the exciting star direction in the horizontal direction and the horizontal zero was set at the PDR edge, delineated by the red vertical line. The crosses show the positions of the PDR (green) and the dense-core (blue), where deep integrations were performed at IRAM-30m (see Fig. 3). The spatial resolution is plotted in the bottom left corner. Values of contour levels are shown on each image lookup table. The emission of all lines is integrated between 10.1 and 11.1 km s^{-1}.

of the HCO, DCO^+ and 1.2 mm continuum observations and data reductions can be found in Gerin et al. (2009), Pety et al. (2007), and Hily-Blant et al. (2005).

We performed deep integrations of o-H_2CO and p-H_2CO low-energy rotational lines (see Figs. 2 and 3) centered on the PDR and the dense-core. To obtain these deep integration spectra, we used the position-switching observing mode. The on-off cycle duration was 1 min and the off-position offsets were (δ RA, δ Dec) = (−100″, 0″), i.e. the H region ionized by σOri and free of molecular emission. From our knowledge of the IRAM-30 m telescope we estimate the absolute position accuracy to be 3″.

The data processing was made with the GILDAS[1] softwares (Pety 2005). The IRAM-30m data were first calibrated to the T_A^* scale using the chopper-wheel method (Penzias & Burrus 1973), and finally converted to main-beam temperatures (T_{mb}) using the forward and main-beam efficiencies (F_{eff} and B_{eff}) displayed in Table 2. The resulting amplitude accuracy is ∼ 10%. Frequency-switched spectra were folded using the standard shift-and-add method before baseline subtraction. The resulting spectra were finally gridded through convolution with a Gaussian to obtain the maps.

3. Results

3.1. H_2CO spatial distribution

The 218.2 GHz p-H_2CO integrated line-intensity map is shown in Fig. 1 together with the 86.7 GHz HCO, 216.1 GHz DCO^+ integrated line-intensity maps and the 1.2 mm continuum-emission map. Formaldehyde emission is extended throughout the Horsehead with a relatively constant intensity. The H_2CO spatial distribution ressembles the 1.2 mm continuum emission: it follows the top of the famous Horsehead nebula from its front to its mane. It also delineates the throat of the Horsehead. The peak of the H_2CO emission spatially coincides with the peak of the DCO^+ emission, which arises from a cold dense-core. However, H_2CO emission is also clearly present along the PDR, which is traced by the HCO emission. The PDR and dense-core, namely the peaks of the HCO and DCO^+ emission are shown with green and blue crosses respectively. Gaussian fits of the H_2CO lines at the HCO peak result in broader line widths than at the DCO^+ peak. That the lines are broader in the PDR confirms that H_2CO lines toward the DCO^+ peak arise from the dense-core rather than from the illuminated surface of the cloud. There is a peak in the H_2CO emission toward the north-west region of the nebula, near the edge of the PDR, where two protostars have been identified (B33-1 and B33-28, Bowler et al. 2009). These protostars heat the dust around them, so it is likely that H_2CO has been evaporated from the grain ice mantles.

[1] See http://www.iram.fr/IRAMFR/GILDAS for more information about the GILDAS softwares.

Table 3. Spectroscopic parameters of the observed lines obtained from the CDMS data base (Müller et al. 2001).

Molecule	Transition	ν [GHz]	E_u [K]	A_{ul} [s^{-1}]	g_u
o-H_2CO	$2_{12}-1_{11}$	140.839	21.92	5.3×10^{-5}	15
p-H_2CO	$2_{02}-1_{01}$	145.603	10.48	7.8×10^{-5}	5
o-H_2CO	$2_{11}-1_{10}$	150.498	22.62	6.5×10^{-5}	15
o-H_2CO	$3_{13}-2_{12}$	211.211	32.06	2.3×10^{-4}	21
p-H_2CO	$3_{03}-2_{02}$	218.222	20.96	2.8×10^{-4}	7
p-H_2CO	$3_{22}-2_{21}$	218.476	68.09	1.6×10^{-4}	7
o-H_2CO	$3_{12}-2_{11}$	225.698	33.45	2.8×10^{-4}	21
o-$H_2^{13}CO$	$2_{12}-1_{11}$	137.450	10.51	4.9×10^{-5}	15
p-$H_2^{13}CO$	$2_{02}-1_{01}$	141.984	2.37	7.2×10^{-5}	5
HDCO	$2_{11}-1_{10}$	134.285	17.63	4.6×10^{-5}	5
HDCO	$3_{12}-2_{11}$	201.341	27.29	2.0×10^{-4}	7
o-D_2CO	$2_{12}-1_{11}$	110.838	13.37	2.6×10^{-5}	5
p-D_2CO	$4_{04}-3_{03}$	231.410	27.88	3.5×10^{-4}	18

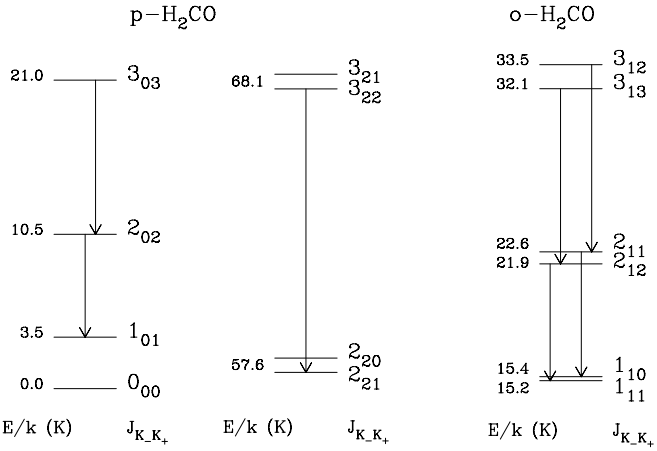

Fig. 2. Lower energy rotational levels of para- (*left*) and ortho-H_2CO (*right*). The energy above para ground-state is shown at the left of each level. The arrows indicate the transitions detected in the Horsehead.

3.2. H_2CO column density

We computed the column densities of H_2CO at the PDR and the dense-core positions. For this we first used the $H_2^{13}CO$ lines to

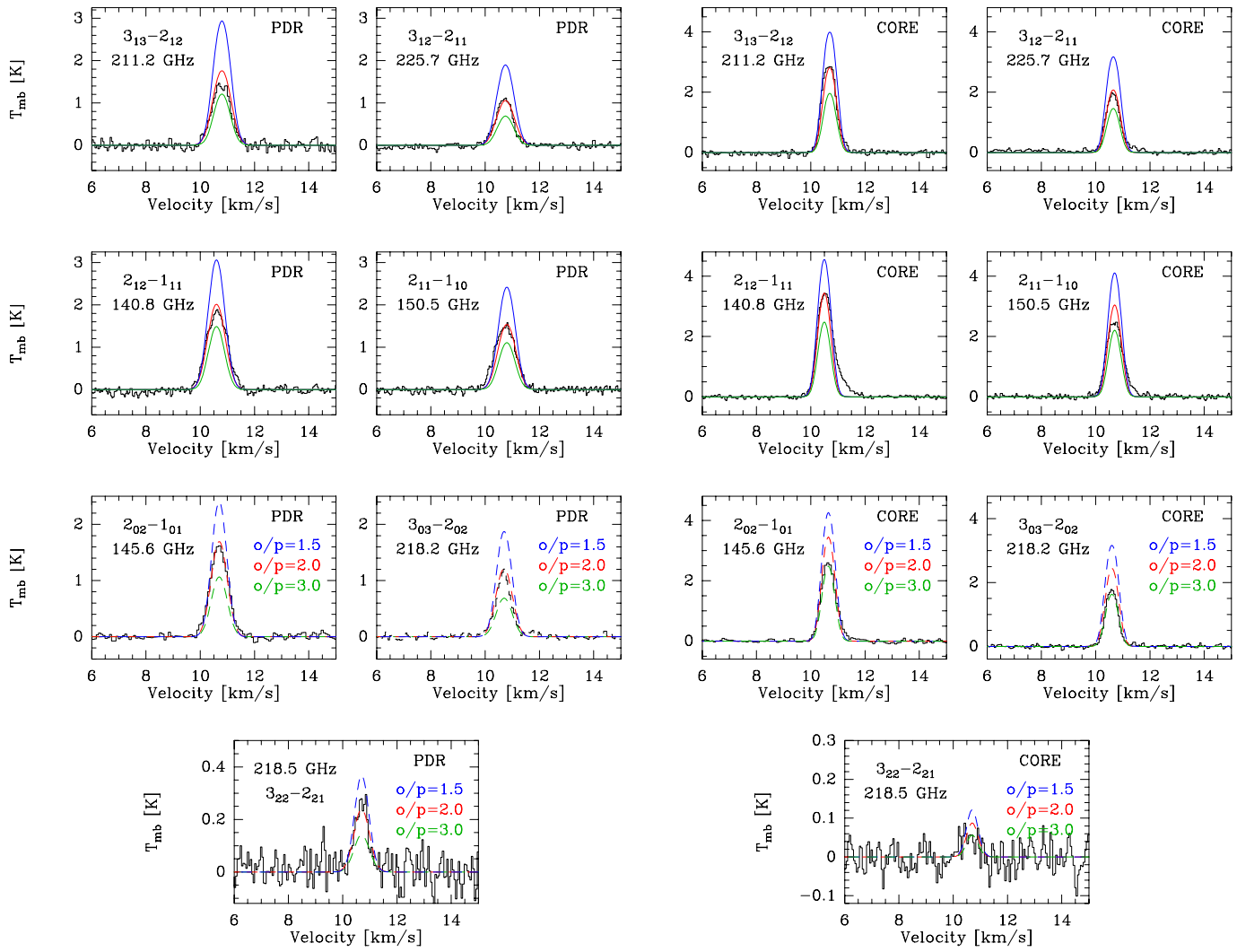

Fig. 3. Radiative transfer modeling of H_2CO lines for two positions toward the Horsehead. *Two left columns*: the PDR position (T_{kin} = 60 K, $n(H_2) = 6 \times 10^4$ cm^{-3}, N(o-H_2CO) = 7.2×10^{12} cm^{-2}) and *two right columns*: the dense-core position (T_{kin} = 20 K, $n(H_2) = 10^5$ cm^{-3}, N(o-H_2CO) = 9.6×10^{12} cm^{-2}). The *two top rows* display the ortho lines, for which we varied the column density around the best match (red curve) by a factor of 1.5 (blue curve) and 1/1.5 (green curve). The *two bottom rows* display the para lines, for which we kept the column density of the best match for o-H_2CO (red curves) constant and varied the ortho-to-para ratio of H_2CO: o/p = 1.5 (dashed blue), o/p = 2 (dashed red) and o/p = 3 (dashed green).

estimate the optical depth of the H_2CO lines. Then, we made a first estimate of the column densities and excitation temperatures using rotational diagrams. Finally, we used these first estimates as an input for a detailed nonlocal non-LTE excitation and radiative transfer analysis to compute the H_2CO abundances. The spectroscopic parameters for the detected transitions (shown in Fig. 2) are given in Table 3. We assumed that the emission is extended and fills the 30 m beam, as shown by the map of the 3_{03}–2_{02} transition (see Fig. 1).

3.2.1. Opacity of the H_2CO lines

We detected two transitions of the formaldehyde isotopologue $H_2^{13}CO$ in the dense-core position (see upper panels in Fig. 4). By comparing the flux between H_2CO and $H_2^{13}CO$ for the same transition it is possible to estimate the opacity of the H_2CO line, assuming that the $H_2^{13}CO$ line is optically thin, as follows:

$$\frac{F_{H_2CO}}{F_{H_2^{13}CO}} = \frac{[^{12}C]}{[^{13}C]}\beta \qquad (1)$$

where β is the escape probability function, which in the case of a homogeneous slab of gas (de Jong et al. 1980) is equal to

$$\beta = \frac{1 - \exp(-3\tau)}{3\tau}. \qquad (2)$$

The isotopic abundance ratio $^{12}C/^{13}C \simeq 60$ (Langer & Penzias 1990; Savage et al. 2002) is almost twice the line intensity ratio between formaldehyde and its isotopologue, and therefore the H_2CO lines have moderate opacities. From the observations we estimate $\tau_{2_{12}-2_{11}} \sim 1.6$ and $\tau_{2_{02}-1_{01}} \sim 1.9$ for H_2CO in the dense-core.

3.2.2. Rotational diagram analysis

First-order estimates of the beam-averaged column densities and the rotational temperatures can be found by means of the widely used rotational diagram analysis (Goldsmith & Langer 1999). To do this, we assume that the gas is under LTE, and therefore all excitation temperatures are the same, and the energy levels

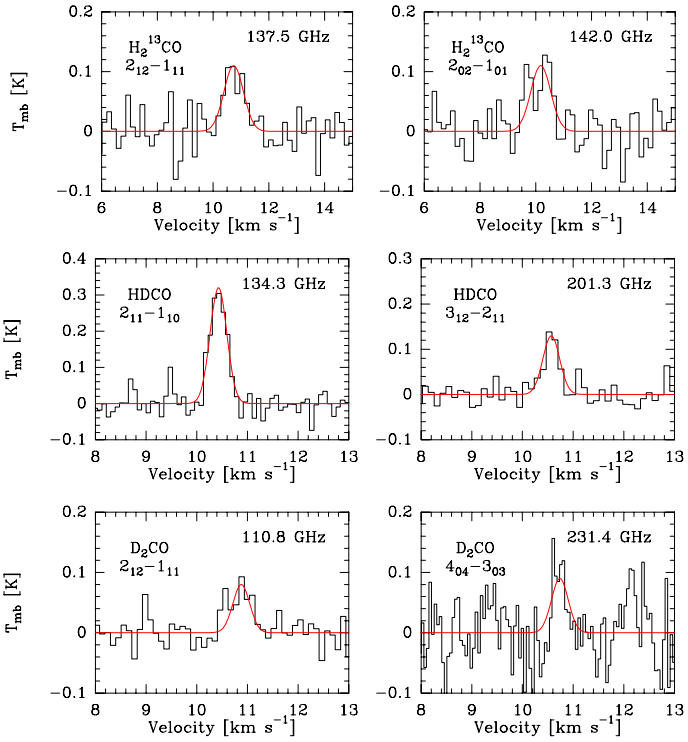

Fig. 4. $H_2^{13}CO$ and deuterated H_2CO lines detected toward the dense-core. Gaussian fits are shown with red lines. For HDCO and D_2CO the line width was fixed to the width of the HDCO ($2_{11}-1_{10}$) line, because it has the best signal-to-noise ratio.

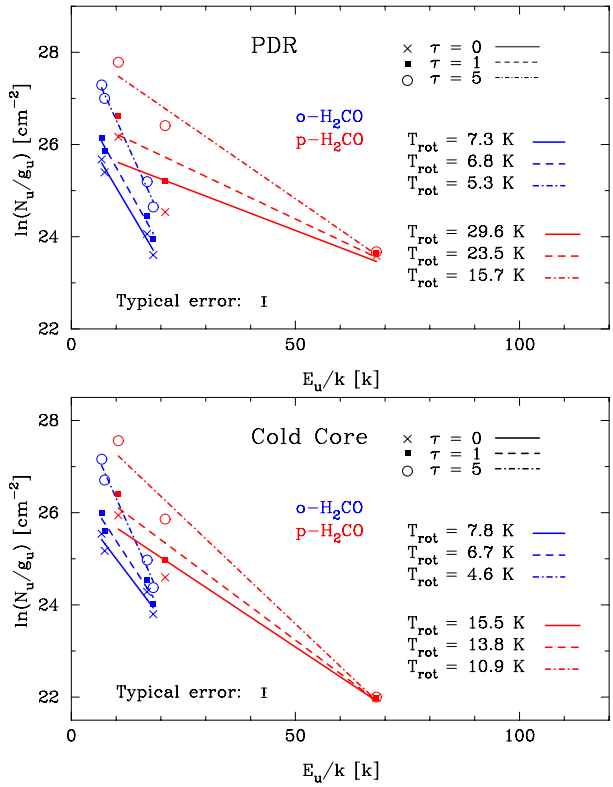

Fig. 5. H_2CO rotational diagrams corrected for line-opacity effects at the PDR and dense-core position. Rotational temperatures are shown for each considered opacity.

are populated following Boltzmann's law. We built rotational diagrams corrected for line-opacity effects through

$$\ln \frac{N_u^{thin}}{g_u} + \ln C_\tau = \ln \frac{N}{Z} - \frac{E_u}{kT_{rot}}, \quad (3)$$

where N is the total column density of the molecule, g_u is the level degeneracy, E_u/k is the energy of the upper level in K, Z is the partition function at the rotational temperature T_{rot}, $C_\tau = \frac{\tau}{1-e^{-\tau}} \leq 1$ is a line-opacity correction factor, where τ is the opacity of the line, and N_u^{thin} is the column density of the upper level for an optically thin line when the source fills the beam. This last parameter is given by

$$N_u^{thin} = \frac{8\pi k \nu^2 W}{hc^3 A_{ul}}, \quad (4)$$

where k is the Boltzmann constant, ν is the line frequency, W is the integrated line intensity, h is the Planck constant, c is the speed of light and A_{ul} is the Einstein coefficient for spontaneous emission.

Ortho- and para forms of H_2CO are treated as different species because radiative transitions between them are forbidden. Resulting rotational diagrams are shown in Fig. 5 for three different o-H_2CO ($2_{12}-1_{11}$) and p-H_2CO ($2_{02}-1_{01}$) line-opacities (τ = 0, 1 and 5). We find column densities of $N \sim 10^{12}-10^{13}$ cm^{-2}, depending on the opacity. We infer very different rotational temperatures for o-H_2CO ($T_{rot} \sim 4-8$ K) and p-H_2CO ($T_{rot} \sim 10-30$ K), which are also lower than the well-known conditions in the PDR ($T_{kin} \sim 60$ K) and in the dense-core ($T_{kin} \sim 20$ K). This suggests that the gas is far from thermalization, and therefore we used these column densities and rotational temperatures as an input for a more complex analysis to derive the H_2CO column densities.

Table 4. H_2CO critical densities (cm^{-3}) for three different colliding partners computed for T_{kin} = 60 K.

$J_{K_aK_c}$	p-H_2	o-H_2	He
2_{02}	7.2×10^5	3.6×10^5	1.3×10^6
3_{03}	1.6×10^6	9.9×10^5	4.2×10^6
3_{22}	5.8×10^5	4.7×10^5	2.5×10^6
2_{12}	3.7×10^5	2.5×10^5	8.1×10^5
2_{11}	4.3×10^5	2.2×10^5	8.7×10^5
3_{13}	9.7×10^5	7.0×10^5	2.3×10^6
3_{12}	1.3×10^6	7.9×10^5	3.2×10^6

3.2.3. Radiative transfer models

The critical density of a given collisional partner corresponds to the density at which the sum of spontaneous radiative de-excitation rates is equal to the sum of collisional de-excitation rates (γ) of a given level

$$n_{cr}(J_{K_aK_c}, T_{kin}) = \frac{\sum_{J'_{K'_aK'_c}} A(J_{K_aK_c} \rightarrow J'_{K'_aK'_c})}{\sum_{J'_{K'_aK'_c}} \gamma(J_{K_aK_c} \rightarrow J'_{K'_aK'_c}, T_{kin})}. \quad (5)$$

Formaldehyde lines have high critical densities ($\sim10^6$ cm^{-3}, see Table 4) compared to the H_2 density in the Horsehead ($\sim10^4-10^5$ cm^{-3}). Because we expect subthermal emission ($T_{ex} \ll T_{kin}$) for transitions with high critical densities compared to the H_2 density, we used a nonlocal non-LTE radiative transfer code adapted to the Horsehead geometry to model the observed H_2CO line intensities (Goicoechea et al. 2006). We used a nonlocal code to take into account the radiative coupling between different cloud positions that might affect the population of the energy levels. The code is able to predict the line

Table 5. Column densities and abundances.

	Molecule	PDR	Dense-core
Column densities [cm^{-2}]	N_H	3.8×10^{22}	6.4×10^{22}
	N(o-H_2CO)	7.2×10^{12}	9.6×10^{12}
	N(p-H_2CO)	3.6×10^{12}	3.2×10^{12}
	N(HCO)[a]	3.2×10^{13}	$<4.6 \times 10^{12}$
	N(HDCO)[b]	–	1.6×10^{12}
	N(o-D_2CO)[b]	–	5.1×10^{11}
	N(p-D_2CO)[b]	–	5.1×10^{11}
Abundances [X] = $\frac{N(X)}{(N(H)+2\,N(H_2))}$	[o-H_2CO]	1.9×10^{-10}	1.5×10^{-10}
	[p-H_2CO]	9.5×10^{-11}	5.0×10^{-11}
	[HCO]	8.4×10^{-10}	$<7.2 \times 10^{-11}$
	[HDCO]	–	2.5×10^{-11}
	[D_2CO]	–	1.6×10^{-11}

Notes. [a] Gerin et al. (2009). [b] For T_{ex} = 6 K (LTE).

profiles. It takes into account line trapping, collisional excitation and radiative excitation by absorption of cosmic microwave background and dust continuum photons. We included 40 rotational levels for o-H_2CO and 41 rotational levels for p-H_2CO, where the maximum energy level lies at ~285 K for both species. We considered o-H_2, p-H_2 and He as collision partners with the following collisional excitation rates:

- collisional rates of o-H_2CO and p-H_2CO with He are taken from Green (1991);
- collisional rates of o-H_2CO with o-H_2 and p-H_2 from Troscompt et al. (2009) for the first 10 energy levels, i.e. $E_u \leq 50$ K. We complemented these data with He collision rates of Green (1991) scaled to H_2. Following the new H_2CO–H_2 collisional rate calculations, we scaled the H_2CO–He rates by a factor 2.5 instead of the usual ~1.4 mass factor (A. Faure, priv. comm.);
- collisional rates of p-H_2CO with o-H_2 and p-H_2 from Troscompt et al. (to be submitted).

Results are presented in Fig. 3 for three different column densities. Best matches (see Table 5) are for column densities of N(o-H_2CO) = 7.2×10^{12} cm^{-2} and N(p-H_2CO) = 3.6×10^{12} cm^{-2} in the PDR position, and N(o-H_2CO) = 9.6×10^{12} cm^{-2} and N(p-H_2CO) = 3.2×10^{12} cm^{-2} in the dense-core position. In the excitation- and radiative transfer models we adopt an H_2 ortho-to-para ratio of 3 (high-temperature limit), although it is likely that the ortho-to-para ratio is lower in the Horsehead (e.g., Habart et al. 2011). Indeed, the H_2CO column densities are not sensitive to the change of the H_2 ortho-to-para ratio for the physical conditions of the Horsehead (see Appendix A).

3.3. H_2CO ortho-to-para ratio

The ratio between the column densities of o-H_2CO and p-H_2CO provides information about the formation of the molecule, because the characteristic conversion time from one symmetry state to the other is longer than the H_2CO lifetime (Tudorie et al. 2006). When the molecule forms in the gas-phase, a ratio of 3 is expected, which corresponds to the statistical weight ratio between the ground states of the ortho- and para species. A ratio lower than 3 is expected when the molecule is formed on the surface of cold ($T_{dust} \lesssim 20$ K) dust grains (Kahane et al. 1984; Dickens & Irvine 1999). From the derived column densities we infer H_2CO ortho-to-para ratios of ~2 in the PDR and of ~3 in the dense-core. This suggests that in the dense-core H_2CO is mainly formed in the gas-phase, whereas in the PDR H_2CO is formed on the surface of dust grains. Dickens & Irvine (1999) measured H_2CO ortho-to-para ratios between 1.5 and 2 toward star-forming cores with outflows, and ratios near 3 toward three quiescent cores. Jørgensen et al. (2005) also found an ortho-to-para ratio of 1.6 in the envelopes around low-mass protostars.

3.4. HDCO and D_2CO column densities

We detected HDCO and D_2CO in the dense-core (see two bottom rows in Fig. 4), and we estimated their abundances assuming LTE. For T_{ex} = 6 K we obtain N(HDCO) = 1.6×10^{12} cm^{-2}, $N(D_2CO) = 5.1 \times 10^{11}$ cm^{-2} and a D_2CO ortho-to-para ratio of 1, which translates into relative abundances or fractionation levels [HDCO]/[H_2CO] = 0.11 and [D_2CO]/[H_2CO] = 0.04 for the inferred formaldehyde column densities in the dense-core.

Deuterium fractionation can occur in the gas-phase by means of ion-molecule reactions, where D is transferred from HD to other species. High abundances of deuterated molecules compared to the elemental D/H abundance (~1.5×10^{-5}, Linsky et al. 2006) have been observed in different astrophysical environments, from cold dense cores and hot molecular cores even to PDRs. Pety et al. (2007) found high deuteration ([DCO^+]/[HCO^+] > 0.02) in the Horsehead dense-core. A pure gas-phase chemical model was able to reproduce the observed fractionation level of HCO^+ for $T_{kin} \leq 20$ K. Parise et al. (2009) found high fractionation levels for DCN and HDCO toward the Orion Bar PDR ([XD]/[XH] ~ 0.01). They found that these ratios are consistent with pure gas-phase chemistry models where the gas is warm (>50 K), so the deuterium chemistry is driven mainly by CH_2D^+, as opposed to colder regions ($\lesssim$20 K) like the Horsehead dense-core, where H_2D^+ is the main actor. Owing to the low temperature in the core it is likely that a non-negligible fraction of CO is frozen on the dust grains, enhancing the deuterium fractionation.

Another way to form deuterated molecules in cold environments is trough D addition or H-D substitution reactions on the surface of dust grains (Hidaka et al. 2009). In the Horsehead core though, desorption from the grain mantles is not efficient in releasing products into the gas-phase (see Sect. 4). It is then more likely that the gas-phase HDCO and D_2CO molecules detected here are formed in the gas-phase. Nevertheless, there can still be a considerable amount of deuterated H_2CO trapped in the ices around dust grains.

4. H_2CO chemistry

We used a one-dimensional, steady-state photochemical model (Le Bourlot et al. 1993; Le Petit et al. 2006) to study the H_2CO chemistry in the Horsehead. The physical conditions have already been constrained by our previous observational studies and we keep the same assumptions for the density profile (displayed in the upper panel of Fig. 6), radiation field (χ = 60 in Draine units), elemental gas-phase abundances (see Table 6 in Goicoechea et al. 2009b) and cosmic ray ionization rate ($\zeta = 5 \times 10^{-17}$ s^{-1}).

Unlike other organic molecules like methanol, which can only be efficiently formed on the surface of grains (Tielens & Whittet 1997; Woon 2002; Cuppen et al. 2009), formaldehyde can be formed in both the gas-phase and on the surface of grains. Next, we investigate these two different scenarios.

4.1. Pure gas-phase chemistry models

We used the *Ohio State University (osu)* pure gas-phase chemical network upgraded to photochemical studies. We included the

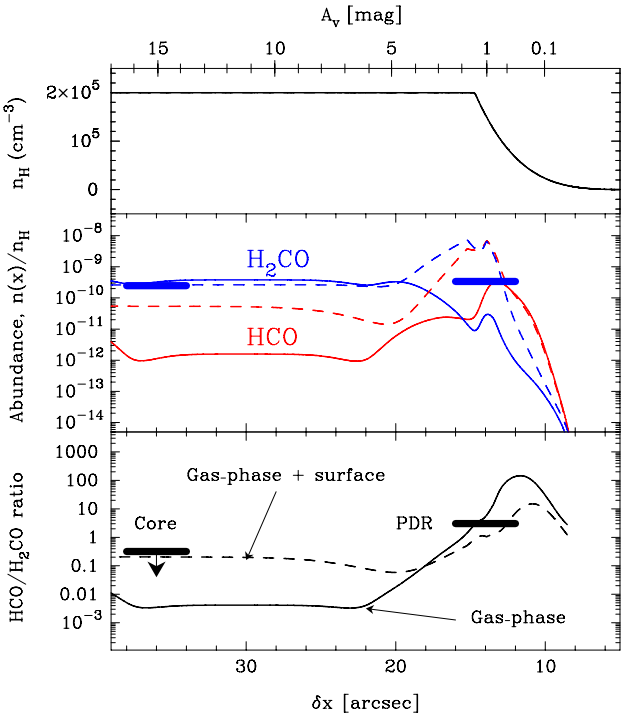

Fig. 6. Photochemical model of the Horsehead PDR. *Upper panel*: PDR density profile ($n_H = n(H) + 2n(H_2)$ in cm^{-3}). *Middle panel*: predicted abundance (relative to n_H) of H_2CO (blue) and HCO (red). *Lower panel*: predicted HCO/H_2CO abundance ratio. In the two bottom panels, models shown as solid lines include pure gas-phase chemistry and models shown as dashed lines include gas-phase as well as grain surface chemistry. The horizontal bars show the measured H_2CO abundances and abundance ratios.

photo-dissociation of HCO and of H_2CO (leading to CO and H_2) with rates of $1.1\times10^{-9}\exp(-0.8A_V)$ and $10^{-9}\exp(-1.74A_V)$ s^{-1}, respectively (van Dishoeck 1988). We also included the H_2CO photo-dissociation channel that leads to HCO and H (see e.g., Yin et al. 2007; Troe 2007) with the same rate of the one that leads to CO and H_2, and the atomic oxygen reaction with the methylene radical (CH_2) to explain the high abundance of HCO in the PDR (Gerin et al. 2009).

The predicted HCO and H_2CO abundance profiles and the HCO/H_2CO abundance ratio are shown as solid lines in Fig. 6 (middle and lower panel, respectively). The formation of H_2CO in the PDR and dense-core is dominated by reactions between oxygen atoms and the methyl radical (CH_3). The destruction of H_2CO in the PDR is dominated by photo-dissociation, while it is dominated by reactions with ions in the dense-core. The pure-gas phase model satisfactorily reproduces the observed H_2CO abundance in the dense-core ($\delta x \sim 35''$) but it predicts an abundance in the PDR ($\delta x \sim 15''$) that is at least one order of magnitude lower than the observed value.

4.2. Grain chemistry models

We considered the surface chemistry reactions introduced by Stantcheva et al. (2002), which include the following sequence of hydrogen addition reactions on CO to form formaldehyde and methanol

$$\mathrm{CO} \underset{\mathrm{H}}{\rightarrow} \mathrm{HCO} \underset{\mathrm{H}}{\rightarrow} \mathrm{H_2CO} \underset{\mathrm{H}}{\rightarrow} \mathrm{H_3CO} \underset{\mathrm{H}}{\rightarrow} \mathrm{CH_3OH}.$$

We also introduce water formation via hydrogenation reactions of O, OH until H_2O.

Adsorption, desorption and diffusive reactions were introduced in the Meudon PDR code in the rate equations approach. The corresponding implementation will be described in a specific paper (Le Bourlot et al., to be submitted) and we simply mention the main processes included in the present study. We distinguish between mantle molecules, which may accumulate in several layers (e.g., H_2O, H_2CO, CH_3OH), and light species (e.g., H, H_2), which stay on the external layer. Photo-desorption can be an efficient mechanism to release molecules to the gas phase in regions exposed to strong radiation fields, as shown recently in laboratory studies (Öberg et al. 2009b,a; Muñoz Caro et al. 2010). Thermal desorption is also introduced. It critically depends on the desorption barrier values, which are somewhat uncertain. Diffusive reactions occur on grain surfaces and the diffusion barriers are assumed to be 1/3 of the desorption energy values. Photodesorption efficiencies have been measured in the laboratory for CO, CO_2, H_2O and CH_3OH. These experiments have shown that all common ices have photodesorption yields of a few 10^{-3} molecules per incident UV photon (Öberg et al. 2007, 2009a,b,c). Therefore, we also take a photo-desorption efficiency of 10^{-3} for those species that have not been studied in the laboratory. We assume in addition that for formaldehyde the two branching ratios toward H_2CO and HCO+H channels are identical, i.e. 5×10^{-4}. Given the high density in the dense-core, the grains are assumed to be strongly coupled to the gas in the inner region, so that their temperatures become equal to 20 K in the dark region, whereas the illuminated dust grains reach temperature values of about 30 K.

The predicted HCO and H_2CO abundances are shown as dashed lines in Fig. 6. This model reproduces the observed H_2CO abundance in the dense-core and predicts a similar abundance as the pure gas-phase model. This way, formation on grain surfaces does not contribute significantly to the observed gas-phase H_2CO abundance in the dense-core. This is because of the low photo-desorption rates in the core caused by the shielding from the external UV field. On the other hand, the H_2CO abundance can increase by up to three orders of magnitude in the illuminated part of the cloud ($A_V \lesssim 4$) when including the grain surface reactions. The H_2CO abundance now even peaks in the PDR, while it peaked in the dense-core in the pure gas-phase model. The model predicts a H_2CO abundance peak in the PDR that is higher than the observed abundance averaged over the 30 m (~16″). This limited resolution prevents us from resolving the predicted abundance peak. Interferometric observations are needed to prove the existence of this peak in the PDR.

5. Discussion

H_2CO has been detected in a variety of different astrophysical environments, with a wide range of gas temperatures and densities. It has been detected in diffuse clouds with high abundances (~10^{-9}), observed in absorption against bright HII regions (e.g., Liszt & Lucas 1995; Liszt et al. 2006). It is not well understood how H_2CO can be formed and survive in such harsh environments, because gas-phase process cannot compete with the photo-dissociation and dust grain temperatures are too high for molecules to freeze on their surfaces. Roueff et al. (2006) detected absorption lines of H_2CO at 3.6 μm toward the high-mass protostar W33A, and estimated an H_2CO abundance of ~10^{-7} where the gas has a temperature of ~100 K. Recently, Bergman et al. (2011) found H_2CO abundances ~5×10^{-9} in the ρ Ophiuchi A cloud core. Abundances of H_2CO and other more complex molecules toward hot cores and protostars are high. In these regions the gas is dense and hot, so the dust grains also

have high temperatures (>100 K). Therefore, the ice mantles, formed in the cold pre-stellar phase, are completely evaporated. Once these molecules are in the gas-phase, they trigger an active chemistry in the hot gas, forming even more complex molecules (Charnley et al. 1992).

H_2CO has also been observed in other PDRs. Leurini et al. (2010) detected H_2CO in the Orion Bar PDR toward both the clump ($n_H \sim 10^6$ cm^{-3}) and the inter-clump ($n_H \sim 10^4$ cm^{-3}) gas components. They found higher H_2CO abundances ($\sim 10^{-9}$–10^{-7}) than the ones inferred in this work for the Horsehead ($\sim 10^{-10}$). Molecules trapped in the ice mantles can be thermally desorbed when the dust grains are warm enough. The dust temperature at which a significant amount of H_2CO evaporates can be estimated by equating the flux of desorbing molecules from the ices to the flux of adsorbing molecules from the gas (see Eq. (5) in Hollenbach et al. 2009). Taking an H_2CO desorption energy of 2050 K (Garrod & Herbst 2006), we obtain an evaporation temperature of ~41 K. In the Orion Bar the dust grains have temperatures of $T_{dust} > 55$–70 K, so molecules can be desorbed from the icy mantles both thermally and non-thermally. But in the Horsehead PDR dust grains are colder ($T_{dust} \sim 20$–30 K), therefore molecules can only be desorbed non-thermally. Hence, the main desorption mechanism in the PDR is photo-desorption. In this respect, the Horsehead PDR offers a cleaner environment to isolate the role of FUV photo-desorption of ice mantles. In the Horsehead dense-core dust grains are also cold (~20 K), but photo-desorption is not efficient because the dust is shielded from the external UV field. Cosmic rays can desorb molecules from the ice mantles, but this contribution is not significant because the desorption rates are too low compared to the H_2CO formation rates in the gas-phase. Both the measured H_2CO abundance and ortho-to-para ratio agree with the scenario in which H_2CO in the dense-core is formed in the gas phase with no significant contribution from grain surface chemistry.

We have shown that photo-desorption is an efficient mechanism to form gas-phase H_2CO in the Horsehead PDR. But, to understand the importance of grain surface chemistry over gas-phase chemistry in the formation of complex organic molecules, a similar analysis of other molecules, such as CH_3OH and CH_2CO, is needed. In particular, CH_3OH is one of final products in the CO hydrogenation pathway on grain surfaces. It can also form H_2CO when it is photo-dissociated. Therefore, their gas-phase abundance ratios will help us to constrain their dominant formation mechanism and the relative contributions of gas-phase and grain surface chemistry. Similar studies in different environments will also bring additional information about the relative efficiencies of the different desorption mechanisms.

6. Summary and conclusions

We have presented deep observations of H_2CO lines toward the Horsehead PDR and a shielded condensation less than 40″ away from the PDR edge. We complemented these observations with a p-H_2CO emission map. H_2CO emission is extended throughout the Horsehead with a relatively constant intensity and resembles the 1.2 mm dust continuum emission. H_2CO beam-averaged abundances are similar ($\simeq 2$–3×10^{-10}) in the PDR and dense-core positions. We infer an equilibrium H_2CO ortho-to-para ratio of ~3 in the dense-core, while in the PDR we find a non-equilibrium value of ~2.

For the first time we investigated the role of grain surface chemistry in our PDR models of the Horsehead. Pure gas-phase and grain surface chemistry models give similar results of the H_2CO abundance in the dense-core, both consistent with the observations. This way, the observed gas-phase H_2CO in the core is formed mainly trough gas-phase reactions, with no significant contribution from surface process. In contrast, photo-desorption of H_2CO ices from dust grains is needed to explain the observed H_2CO gas-phase abundance in the PDR, because gas-phase chemistry alone does not produce enough H_2CO. These different formation routes are consistent with the inferred H_2CO ortho-to-para ratios. Thus, photo-desorption is an efficient mechanism to produce complex organic molecules in the PDR. Because the chemistries of H_2CO and CH_3OH are closely linked, we will continue this investigation in a next paper by studying the chemistry of CH_3OH in detail.

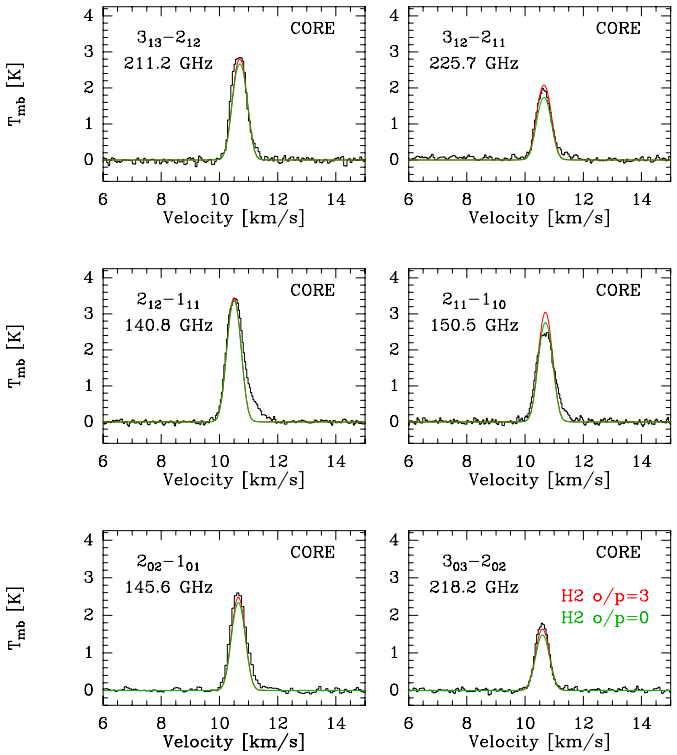

Fig. A.1. Radiative-transfer modeling of H_2CO lines for the core position in the Horsehead. The two top rows display the ortho lines and the bottom row displays the para lines. The best-match models are given in colors ($T_{kin} = 20$ K, $n(H_2) = 10^5$ cm^{-3}, N(o-H_2CO) = 9.6×10^{12} cm^{-2}, N(p-H_2CO) = 3.2×10^{12} cm^{-2}), taking a H_2 ortho-to-para ratio of 3 (red lines) and of 0 (green lines).

Acknowledgements. We thank A. Faure and N. Troscompt for sending us the p-H_2CO – o-H_2 and p-H_2CO – p-H_2 collisional rates prior to publication. We thank the referee for a careful reading of the manuscript and interesting comments. V.G. thanks support from the Chilean Government through the Becas Chile scholarship program. This work was also funded by grant ANR-09-BLAN-0231-01 from the French *Agence Nationale de la Recherche* as part of the SCHISM project. J.R.G. thanks the Spanish MICINN for funding support through grants AYA2009-07304 and CSD2009-00038. J.R.G. is supported by a Ramón y Cajal research contract from the Spanish MICINN and co-financed by the European Social Fund.

Appendix A: H_2 ortho-to-para ratio

We investigated the influence of the H_2 ortho-to-para ratio adopted in the excitation and radiative transfer models. In Fig. A.1 we show the best-match models for the H_2CO lines toward the core position in the Horsehead assuming two different values for the H_2 ortho-to-para ratio. We show models for an H_2

ortho-to-para ratio of 3 in red (high temperature limit), and we show models for the extreme case where the H_2 ortho-to-para ratio is 0 in green (low temperature limit). The difference between the models is less than 10%, which is within the observational uncertainties and therefore not significant.

References

Araya, E., Hofner, P., Goss, W. M., et al. 2007, ApJS, 170, 152
Bergman, P., Parise, B., Liseau, R., & Larsson, B. 2011, A&A, 527, A39
Bisschop, S. E., Jørgensen, J. K., van Dishoeck, E. F., & de Wachter, E. B. M. 2007, A&A, 465, 913
Bowler, B. P., Waller, W. H., Megeath, S. T., Patten, B. M., & Tamura, M. 2009, AJ, 137, 3685
Charnley, S. B., Tielens, A. G. G. M., & Millar, T. J. 1992, ApJ, 399, L71
Cuppen, H. M., van Dishoeck, E. F., Herbst, E., & Tielens, A. G. G. M. 2009, A&A, 508, 275
de Jong, T., Boland, W., & Dalgarno, A. 1980, A&A, 91, 68
Dickens, J. E., & Irvine, W. M. 1999, ApJ, 518, 733
Downes, D., Wilson, T. L., Bieging, J., & Wink, J. 1980, A&AS, 40, 379
Draine, B. T. 1978, ApJS, 36, 595
Garrod, R. T., & Herbst, E. 2006, A&A, 457, 927
Garrod, R. T., Wakelam, V., & Herbst, E. 2007, A&A, 467, 1103
Gerin, M., Goicoechea, J. R., Pety, J., & Hily-Blant, P. 2009, A&A, 494, 977
Goicoechea, J. R., Pety, J., Gerin, M., et al. 2006, A&A, 456, 565
Goicoechea, J. R., Compiègne, M., & Habart, E. 2009a, ApJ, 699, L165
Goicoechea, J. R., Pety, J., Gerin, M., Hily-Blant, P., & Le Bourlot, J. 2009b, A&A, 498, 771
Goldsmith, P. F., & Langer, W. D. 1999, ApJ, 517, 209
Green, S. 1991, ApJS, 76, 979
Habart, E., Abergel, A., Walmsley, C. M., Teyssier, D., & Pety, J. 2005, A&A, 437, 177
Habart, E., Abergel, A., Boulanger, F., et al. 2011, A&A, 527, A122
Hassel, G. E., Herbst, E., & Bergin, E. A. 2010, A&A, 515, A66
Hidaka, H., Watanabe, M., Kouchi, A., & Watanabe, N. 2009, ApJ, 702, 291
Hily-Blant, P., Teyssier, D., Philipp, S., & Güsten, R. 2005, A&A, 440, 909
Hollenbach, D., Kaufman, M. J., Bergin, E. A., & Melnick, G. J. 2009, ApJ, 690, 1497
Jørgensen, J. K., Schöier, F. L., & van Dishoeck, E. F. 2005, A&A, 437, 501
Kahane, C., Lucas, R., Frerking, M. A., Langer, W. D., & Encrenaz, P. 1984, A&A, 137, 211
Langer, W. D., & Penzias, A. A. 1990, ApJ, 357, 477
Le Bourlot, J., Pineau Des Forets, G., Roueff, E., & Flower, D. R. 1993, A&A, 267, 233
Le Petit, F., Nehmé, C., Le Bourlot, J., & Roueff, E. 2006, ApJS, 164, 506
Leurini, S., Parise, B., Schilke, P., Pety, J., & Rolffs, R. 2010, A&A, 511, A82
Linsky, J. L., Draine, B. T., Moos, H. W., et al. 2006, ApJ, 647, 1106
Liszt, H., & Lucas, R. 1995, A&A, 299, 847
Liszt, H. S., Lucas, R., & Pety, J. 2006, A&A, 448, 253
Mangum, J. G., & Wootten, A. 1993, ApJS, 89, 123
Mangum, J. G., Darling, J., Menten, K. M., & Henkel, C. 2008, ApJ, 673, 832
Maret, S., Ceccarelli, C., Caux, E., et al. 2004, A&A, 416, 577
Milam, S. N., Remijan, A. J., Womack, M., et al. 2006, ApJ, 649, 1169
Muñoz Caro, G. M., Jiménez-Escobar, A., Martín-Gago, J. Á., et al. 2010, A&A, 522, A108
Müller, H. S. P., Thorwirth, S., Roth, D. A., & Winnewisser, G. 2001, A&A, 370, L49
Öberg, K. I., Fuchs, G. W., Awad, Z., et al. 2007, ApJ, 662, L23
Öberg, K. I., Garrod, R. T., van Dishoeck, E. F., & Linnartz, H. 2009a, A&A, 504, 891
Öberg, K. I., Linnartz, H., Visser, R., & van Dishoeck, E. F. 2009b, ApJ, 693, 1209
Öberg, K. I., van Dishoeck, E. F., & Linnartz, H. 2009c, A&A, 496, 281
Parise, B., Leurini, S., Schilke, P., et al. 2009, A&A, 508, 737
Penzias, A. A., & Burrus, C. A. 1973, ARA&A, 11, 51
Pety, J. 2005, in SF2A-2005: Semaine de l'Astrophysique Francaise, ed. F. Casoli, T. Contini, J. M. Hameury, & L. Pagani, 721
Pety, J., Goicoechea, J. R., Hily-Blant, P., Gerin, M., & Teyssier, D. 2007, A&A, 464, L41
Roueff, E., Dartois, E., Geballe, T. R., & Gerin, M. 2006, A&A, 447, 963
Savage, C., Apponi, A. J., Ziurys, L. M., & Wyckoff, S. 2002, ApJ, 578, 211
Snyder, L. E., Buhl, D., Zuckerman, B., & Palmer, P. 1969, Phys. Rev. Lett., 22, 679
Snyder, L. E., Palmer, P., & de Pater, I. 1989, AJ, 97, 246
Stantcheva, T., Shematovich, V. I., & Herbst, E. 2002, A&A, 391, 1069
Tielens, A. G. G. M., & Whittet, D. C. B. 1997, in IAU Symp. 178, ed. E. F. van Dishoeck, 45
Troe, J. 2007, J. Phys. Chem. A, 111, 3868
Troscompt, N., Faure, A., Wiesenfeld, L., Ceccarelli, C., & Valiron, P. 2009, A&A, 493, 687
Tudorie, M., Cacciani, P., Cosléou, J., et al. 2006, A&A, 453, 755
van Dishoeck, E. F. 1988, in Rate Coefficients in Astrochemistry, Proceedings of a Conference held in UMIST, Manchester, United Kingdom, September 21–24, 1987. ed. T. J. Millar, & D. A. Williams (Dordrecht, Boston: Kluwer Academic Publishers), 49
Walsh, C., Millar, T. J., & Nomura, H. 2010, ApJ, 722, 1607
Woon, D. E. 2002, ApJ, 569, 541
Yin, H.-M., Rowling, S. J., Büll, A., & Kable, S. H. 2007, J. Chem. Phys., 127, 064302
Young, K. E., Lee, J., Evans, II, N. J., Goldsmith, P. F., & Doty, S. D. 2004, ApJ, 614, 252

A&A 560, A73 (2013)
DOI: 10.1051/0004-6361/201322460

Astronomy & Astrophysics

The IRAM-30 m line survey of the Horsehead PDR

IV. Comparative chemistry of H_2CO and CH_3OH⋆,⋆⋆

V. V. Guzmán[1], J. R. Goicoechea[2], J. Pety[1,3], P. Gratier[1], M. Gerin[3], E. Roueff[4], F. Le Petit[4], J. Le Bourlot[4], and A. Faure[5]

[1] Institut de Radioastronomie Millimétrique (IRAM), 300 rue de la Piscine, 38406 Saint-Martin-d'Hères, France
e-mail: [guzman;pety;gratier]@iram.fr
[2] Departamento de Astrofísica, Centro de Astrobiología, CSIC-INTA, Carretera de Ajalvir, Km 4. Torrejón de Ardoz, 28850 Madrid, Spain
e-mail: jr.goicoechea@cab.inta-csic.es
[3] LERMA – LRA, UMR 8112, Observatoire de Paris and École Normale Supérieure, 24 rue Lhomond, 75231 Paris, France
e-mail: maryvonne.gerin@lra.ens.fr
[4] LUTH UMR 8102, CNRS and Observatoire de Paris, Place J. Janssen, 92195 Meudon Cedex, France
e-mail: [evelyne.roueff;franck.lepetit;jacques.lebourlot]@obspm.fr
[5] UJF-Grenoble 1/CNRS-INSU, Institut de Planétologie et d'Astrophysique de Grenoble (IPAG) UMR 5274, 38041 Grenoble, France
e-mail: alexandre.faure@obs.ujf-grenoble.fr

Received 7 August 2013 / Accepted 21 October 2013

ABSTRACT

Context. Theoretical models and laboratory experiments show that CH_3OH is efficiently formed on cold grain surfaces through the successive hydrogenation of CO, forming HCO and H_2CO as intermediate species. In cold cores and low UV-field illumination photodissociation regions (PDRs) the ices can be released into the gas-phase through nonthermal processes such as photodesorption, which considerably increases their gas-phase abundances.
Aims. We investigate the dominant formation mechanism of H_2CO and CH_3OH in the Horsehead PDR and its associated dense core.
Methods. We performed deep integrations of several H_2CO and CH_3OH lines at two positions in the Horsehead, namely the PDR and dense core, with the IRAM-30 m telescope. In addition, we observed one H_2CO higher-frequency line with the CSO telescope at both positions. We determined the H_2CO and CH_3OH column densities and abundances from the single-dish observations complemented with IRAM-PdBI high-angular resolution maps (6″) of both species. We compared the observed abundances with PDR models including either pure gas-phase chemistry or both gas-phase and grain surface chemistry.
Results. We derived CH_3OH abundances relative to total number of hydrogen atoms of $\sim 1.2 \times 10^{-10}$ and $\sim 2.3 \times 10^{-10}$ in the PDR and dense-core positions, respectively. These abundances are similar to the inferred H_2CO abundance in both positions ($\sim 2 \times 10^{-10}$). We find an abundance ratio H_2CO/CH_3OH of ∼2 in the PDR and ∼1 in the dense core. Pure gas-phase models cannot reproduce the observed abundances of either H_2CO or CH_3OH at the PDR position. The two species are therefore formed on the surface of dust grains and are subsequently photodesorbed into the gas-phase at this position. At the dense core, on the other hand, photodesorption of ices is needed to explain the observed abundance of CH_3OH, while a pure gas-phase model can reproduce the observed H_2CO abundance. The high-resolution observations show that CH_3OH is depleted onto grains at the dense core. CH_3OH is thus present in an envelope around this position, while H_2CO is present in both the envelope and the dense core itself.
Conclusions. Photodesorption is an efficient mechanism to release complex molecules in low-FUV-illuminated PDRs, where thermal desorption of ice mantles is ineffective.

Key words. astrochemistry – ISM: clouds – ISM: molecules – photon-dominated region (PDR) – radiative transfer – radio lines: ISM

1. Introduction

Formaldehyde (H_2CO) and methanol (CH_3OH) are key species in the synthesis of more complex organic molecules, such as amino acids and other prebiotic molecules (Bernstein et al. 2002; Muñoz Caro et al. 2002; Garrod et al. 2008), that might finally arrive in proto-planetary disks, and hence in new planetary systems. It is therefore of great interest to understand how these molecules are formed. Both species have been detected in a wide range of interstellar environments, with typical gas-phase abundances relative to H_2 of $\sim 10^{-7}$ in hot cores (e.g., Sutton et al. 1995; Ceccarelli et al. 2000) and $\sim 10^{-9}$ in cold dark clouds (e.g., Bergman et al. 2011). They are also observed in shocked regions, caused by an impact of molecular outflows on the surrounding molecular clouds (e.g., Sakai et al. 2012; Codella et al. 2012; Tafalla et al. 2010). Because they are slightly asymmetric rotors, H_2CO and CH_3OH are good tracers of the physical conditions in Galactic and extragalactic molecular clouds (Mangum & Wootten 1993; Leurini et al. 2004; Mangum et al. 2013).

Unlike H_2CO, which can be formed both in the gas-phase and on the surface of dust grains, CH_3OH is thought to be formed entirely on the surfaces of dust grains, because classical

⋆ Based on observations obtained with the IRAM Plateau de Bure interferometer and 30 m telescope. IRAM is supported by INSU/CNRS (France), MPG (Germany), and IGN (Spain).
⋆⋆ The reduced datacubes (FITS files) are only available at the CDS via anonymous ftp to cdsarc.u-strasbg.fr (130.79.128.5) or via http://cdsarc.u-strasbg.fr/viz-bin/qcat?J/A+A/560/A73

Table 1. Observation parameters for the 30 m maps shown in Fig. 3.

Molecule	Transition	Frequency GHz	Instrument	Mode	Beam arcsec	Vel. resol. km s^{-1}	Int. time hours	T_{sys} K (T_A^*)	Noise K (T_{mb})	Reference
Continuum at 1.2 mm			30 m/MAMBO	–	11.7 × 11.7	–	–	–	–	Hily-Blant et al. (2005)
DCO^+	3–2	216.112582	30 m/HERA	FSW	11.4 × 11.4	0.11	1.5/2.0[a]	230	0.10	Pety et al. (2007)
p – H_2CO	3_{03}–2_{02}	218.222190	30 m/HERA	PSW	11.9 × 11.9	0.05	2.1/3.4[a]	280	0.32	Guzmán et al. (2011)
p – H_2CO	2_{02}–1_{01}	145.602949	30 m/EMIR	PSW	17.8 × 17.8	0.20	7.4/12.9[a]	208	0.17	This work
CH_3OH – E	3_{-1}–2_{-1}	145.097370	30 m/EMIR	PSW	17.9 × 17.9	0.20	7.4/12.9[a]	208	0.108[b]	This work
			30 m/C150	FSW	17.9 × 17.9	0.20	2.6/3.2[a]	163	0.108[b]	This work
CH_3OH – A	3_0–2_0	145.103152	30 m/EMIR	PSW	17.9 × 17.9	0.20	7.4/12.9[a]	208	0.095[b]	This work
			30 m/C150	FSW	17.9 × 17.9	0.20	2.6/3.2[a]	263	0.095[b]	This work

Notes. The projection center of the maps is $\alpha_{2000} = 05^h40^m54.27^s$, $\delta_{2000} = -02°28'00''$. [(a)] Two values are given for the integration time: the on-source time and the telescope time. [(b)] The noise value is computed on the final maps that combine the data from both observing runs (2007 and 2012).

ion-neutral chemistry in the gas-phase alone cannot account for the observed CH_3OH abundances (Garrod et al. 2006; Geppert et al. 2006). The mechanism to form CH_3OH on ices is thought to be the successive hydrogenation of CO, forming H_2CO as an intermediate product,

$$CO \xrightarrow[H]{E_b} HCO \underset{H}{\rightarrow} H_2CO \xrightarrow[H]{E_b} CH_2OH, CH_3O \underset{H}{\rightarrow} CH_3OH, \quad (1)$$

where E_b are activation energy barries (Tielens & Whittet 1997; Watanabe & Kouchi 2002). Indeed, laboratory experiments have succeeded to efficiently form both H_2CO and CH_3OH through this mechanism (Watanabe et al. 2004; Fuchs et al. 2009). Moreover, observations by the Infrared Space Observatory (ISO) and *Spitzer* have shown that dust grains are covered by ice mantles in the cold envelopes surrounding high-mass protostars (Gibb et al. 2000, 2004), low-mass protostars (Boogert et al. 2008; Pontoppidan et al. 2008; Öberg et al. 2008; Bottinelli et al. 2010), and in isolated dense cores (Boogert et al. 2011). These studies revealed that the ice mantles consist mostly of H_2O, CO_2 and CO, with smaller amounts of CH_3OH, CH_4, NH_3, and H_2CO. HCO ice has not been detected in the interstellar medium (ISM), probably because its formation on the ices is slower than its subsequent hydrogenation to form H_2CO. Indeed, the reactions starting with CO and H_2CO in the hydrogenation path (1) have activation energy barriers (Fuchs et al. 2009).

Once these species are formed on the ices, they can be desorbed into the gas-phase either through thermal or nonthermal processes. Thermal desorption dominates in regions where dust grains reach temperatures of at least 45 K for formaldehyde (Tielens & Allamandola 1987) and 80 K for methanol (Brown & Bolina 2007; Green et al. 2009). This occurs in hot cores and hot corinos (e.g., Jørgensen et al. 2005; Bisschop et al. 2007; Bottinelli et al. 2007), but also in highly far-ultraviolet (FUV) illuminated photo-dissociation regions (PDRs), such as the Orion bar (Leurini et al. 2010). Nonthermal desorption by FUV photons can also be efficient, as shown by laboratory experiments (Öberg et al. 2009b,c). Nonthermal desorption dominates in colder regions, either UV-shielded dense cores where secondary UV photons are produced by the interaction between cosmic rays and H_2 molecules (e.g., Caselli et al. 2012), or in low-UV-field illumination photo-dissociation regions, where dust grains are too cold to sublimate their ices. This is the case of the Horsehead, where the combination of a moderate-radiation field ($\chi = 60$ relative to the Draine field; Draine 1978), and high density ($n_H \sim 10^4$–10^5 cm^{-3}) implies low dust grain temperatures, from $T_{dust} \sim 30$ K in the outer PDR to $T_{dust} \sim 20$ K slightly deeper inside the cloud (Goicoechea et al. 2009a). Guzmán et al. (2011) compared single-dish observations of H_2CO with PDR models including grain-surface chemistry. They showed that the observed H_2CO abundance in the UV-illuminated edge of the Horsehead nebula can only be explained by the formation of H_2CO on the grains followed by its photo-desorption into the gas-phase. Pure gas-phase chemistry was enough to explain the H_2CO abundance in the colder and UV-shielded gas. The assignments of different formation routes were strengthened by the different measured ortho-to-para ratio of H_2CO: the dense core displays an equilibrium value of ~3, while the PDR displays an out-of-equilibrium value of ~2. The PDR model predicted that H_2CO will be one order of magnitude more abundant in the PDR than the IRAM-30 m beam-averaged measurements.

To further constrain the chemistry of complex organic molecules and investigate the high abundance in the PDR position predicted by the model, we here present high-resolution interferometric maps of H_2CO and CH_3OH in addition to single-dish deep integrations of the low-lying rotational lines of CH_3OH toward two particular positions in the Horsehead: the warm PDR and its associated cold dense core. The observations and data reduction are presented in Sect. 2. The resulting single-dish and interferometric data are described in Sect. 3. In Sect. 4, we compute the CH_3OH column densities and abundances. We compare these results with PDR models in Sect. 5. A discussion is presented in Sect. 6. We summarize and conclude in Sect. 7.

2. Observations and data reduction

In this section, we describe the observations and data reduction of the newly acquired H_2CO and CH_3OH data. A detailed description of the HCO, 218.222 GHz H_2CO, DCO^+, and 1.2 mm continuum observations and data reduction can be found in Gerin et al. (2009), Guzmán et al. (2011), Pety et al. (2007), and Hily-Blant et al. (2005), respectively. Tables 1–3 summarize the observation parameters of the data obtained with the IRAM-30 m, PdBI, and CSO telescopes.

2.1. PdBI maps

We used the Plateau de Bure Interferometer (PdBI) to obtain 6″ resolution maps of the emission of the H_2CO 2_{02}–1_{01} line at 146.603 GHz, the CH_3OH – E 3_{-1}–2_{-1} line at 145.097 GHz, and the CH_3OH – A 3_0–2_0 line at 145.103 GHz. These observations were carried out in August and October 2011 with five

Table 2. Observation parameters for the PdBI maps shown in Fig. 4.

Molecule	Transition	Frequency GHz	Instrument	Beam arcsec	PA °	Vel. resol. km s^{-1}	Int. time hours	T_{sys} K (T_A^*)	Noise mK (T_{mb})	Reference
HCO	1_{01} 3/2, 2–0_{00} 1/2, 1	86.670760	PdBI/C&D	6.7 × 4.4	16	0.20	6.5[a]	150	90[b]	Gerin et al. (2009)
p – H_2CO	2_{02}–1_{01}	145.602949	PdBI/C&D	6.1 × 5.6	166	0.20	5.3/19[a]	145	244	This work
CH_3OH – E	3_{-1}–2_{-1}	145.097370	PdBI/C&D	6.1 × 5.6	166	0.20	5.3/19[a]	145	116	This work
CH_3OH – A	3_0–2_0	145.103152	PdBI/C&D	6.1 × 5.6	166	0.20	5.3/19[a]	145	127	This work

Notes. The projection center of the maps is $\alpha_{2000} = 05^h40^m54.27^s$, $\delta_{2000} = -02°28'00''$. [(a)] Two values are given for the integration time: the on-source time (as if the source were always observed with 6 antennae) and the telescope time. [(b)] The noise values quoted here are the noises at the mosaic phase center (mosaic noise is inhomogeneous due to primary-beam correction; it steeply increases at the mosaic edges).

Table 3. Observation parameters of the deep integrations of the CH_3OH lines detected with the 30 m and the H_2CO line detected with the CSO toward the PDR and the dense core.

Position	Molecule	Transition	ν GHz	Line area mK km s^{-1}	Velocity km s^{-1}	*FWHM* km s^{-1}	T_{peak} mK	rms mK	*S/N*
PDR	CH_3OH – E	5_{-1}–4_0	84.521	29.1 ± 3.1	10.64 ± 0.05	0.98 ± 0.14	27.9	4.7	6
	CH_3OH – E	2_{-1}–1_{-1}	96.739	74.1 ± 4.3	10.73 ± 0.02	0.56 ± 0.04	125.0	9.4	13
	CH_3OH – E	2_0–1_0	96.745	22.3 ± 4.7	10.68 ± 0.05	0.63 ± 0.21	33.2	7.5	4
	CH_3OH – E	3_0–2_0	145.094	26.9 ± 6.5	10.77 ± 0.05	0.42 ± 0.11	59.8	21.7	3
	CH_3OH – E	3_{-1}–2_{-1}	145.097	98.4 ± 9.0	10.54 ± 0.02	0.51 ± 0.06	180.8	21.5	8
	CH_3OH – E	5_{-1}–4_{-1}	241.767	81.0 ± 8.8	10.66 ± 0.04	0.85 ± 0.11	89.5	13.1	7
	CH_3OH – A	2_0–1_0	96.741	120.3 ± 3.9	10.73 ± 0.01	0.61 ± 0.02	186.6	7.7	24
	CH_3OH – A	3_0–2_0	145.103	145.7 ± 7.0	10.66 ± 0.01	0.51 ± 0.03	266.2	19.4	14
	CH_3OH – A	5_0–4_0	241.791	59.5 ± 7.3	10.81 ± 0.03	0.48 ± 0.08	117.1	12.5	9
	o-H_2CO	4_{13}–3_{12}	300.837	204.1 ± 39.0	10.75 ± 0.07	0.68 ± 0.16	281.1	60.8	5
Core	CH_3OH – E	5_{-1}–4_0	84.521	43.8 ± 3.0	10.64 ± 0.02	0.65 ± 0.05	63.3	6.4	10
	CH_3OH – E	2_{-1}–1_{-1}	96.739	304.4 ± 3.5	10.65 ± 0.00	0.57 ± 0.01	497.5	7.9	63
	CH_3OH – E	2_0–1_0	96.745	57.6 ± 2.7	10.66 ± 0.01	0.50 ± 0.03	107.6	5.7	19
	CH_3OH – E	2_1–1_1	96.755	11.0 ± 3.0	10.56 ± 0.05	0.41 ± 0.14	25.0	7.0	3
	CH_3OH – E	0_0–1_{-1}	108.894	74.4 ± 4.6	10.63 ± 0.01	0.46 ± 0.03	151.8	13.5	11
	CH_3OH – E	3_0–2_0	145.094	50.4 ± 6.9	10.48 ± 0.02	0.31 ± 0.05	154.5	24.3	6
	CH_3OH – E	3_{-1}–2_{-1}	145.097	449.7 ± 7.5	10.48 ± 0.00	0.52 ± 0.01	819.8	21.6	38
	CH_3OH – E	3_1–2_1	145.132	<12	–	0.5[a]	–	22.0	–
	CH_3OH – E	1_0–1_{-1}	157.271	122.3 ± 11.0	10.66 ± 0.03	0.56 ± 0.05	206.9	34.8	6
	CH_3OH – E	2_0–2_{-1}	157.276	69.5 ± 9.7	10.64 ± 0.03	0.42 ± 0.07	154.0	28.1	5
	CH_3OH – E	1_1–0_0	213.427	42.8 ± 6.4	10.64 ± 0.04	0.46 ± 0.07	87.5	12.2	7
	CH_3OH – E	4_2–3_1	218.440	47.4 ± 5.6	10.62 ± 0.04	0.62 ± 0.08	71.5	9.2	8
	CH_3OH – E	5_{-1}–4_{-1}	241.767	170.8 ± 7.9	10.57 ± 0.01	0.52 ± 0.03	311.5	15.3	20
	CH_3OH – E	2_0–1_{-1}	254.015	59.6 ± 4.3	10.53 ± 0.02	0.44 ± 0.03	126.5	7.9	16
	CH_3OH – E	2_1–1_0	261.806	43.3 ± 7.3	10.56 ± 0.03	0.29 ± 0.14	141.1	22.5	6
	CH_3OH – A	2_0–1_0	96.741	448.5 ± 3.9	10.65 ± 0.00	0.58 ± 0.01	725.6	8.1	89
	CH_3OH – A	3_0–2_0	145.103	527.2 ± 8.0	10.56 ± 0.00	0.52 ± 0.01	949.5	21.3	45
	CH_3OH – A	5_0–4_0	241.791	200.2 ± 8.9	10.67 ± 0.01	0.47 ± 0.02	398.4	16.2	25
	o-H_2CO	4_{13}–3_{12}	300.837	211.1 ± 33.0	10.78 ± 0.05	0.62 ± 0.10	320.8	56.4	6

Notes. All temperatures are given in the main-beam temperature scale. [(a)] Fixed to compute the upper limit in the line area.

antennas in the D configuration and six antennas in the C configuration. The baseline lengths ranged between 24 and 176 m. We observed a 19-field mosaic in a hexagonal pattern covering an almost circular field-of-view of 80″ in diameter. The observations used about 19 h of telescope time. The on-source time scaled to a six antenna array is 5.3 h after filtering out low-quality visibilities. Two correlator windows of 20 MHz (yielding a spectral resolution of 39 kHz) were concatenated to cover both CH_3OH lines. Another 20 MHz window was centered on the targeted H_2CO line. During the observations, the typical precipitable water vapor amounted to 6 mm and the typical system temperature was 145 K. The median noise level achieved over the mosaic is 0.24 K and 0.12 K (T_{mb}, in channels of 0.2 km s^{-1} width) for H_2CO and CH_3OH, respectively.

We used the standard algorithms implemented in the GILDAS[1]/CLIC software to calibrate the PdBI data. The radio-frequency bandpass was calibrated by observing the bright quasar 3C 454.3. Phase and amplitude temporal variations where calibrated by fitting spline polynomials through regular mesurements of two nearby quasars (0420−014 and 0528+134). The PdBI secondary flux calibrator MWC 349 was observed once

[1] See http://www.iram.fr/IRAMFR/GILDAS for more information about the GILDAS softwares (Pety 2005).

during every track, which allowed us to derive the flux scale of the interferometric data. The absolute flux accuracy is ∼10%.

2.2. 30 m maps

A multiplicative interferometer filters out the low spatial frequencies, that is, spatially extended emission. We therefore observed the same region with the IRAM-30 m single-dish telescope to recover the low spatial frequency (short- and zero-spacing) information filtered out by the PdBI. The H_2CO $2_{02}-1_{01}$ (145.603 GHz) line was observed simultaneously with the CH_3OH-E $3_{-1}-2_{-1}$ (145.097 GHz) and CH_3OH-A 3_0-2_0 (145.103 GHz) lines during ∼13 h of average summer weather in August and September 2012. We used the two polarizations of the EMIR receivers and the FTS backends at 49 kHz spectral resolution. We used the position-switching, on-the-fly observing mode. The off-position offsets were (δRA, δDec) = (100″, 0″), that is, the H region ionized by σOri and free of molecular emission. We completed the observations of the 146.097 GHz and 146.103 GHz CH_3OH lines with older but higher-quality observations obtained in January 2007. We used one polarization of the C150 receiver and one 20 MHz window of the VESPA correlator, yielding a spectral resolution of 20 kHz. In this case, we used the frequency-switched, on-the-fly observing mode, with a frequency throw of 7.9 MHz. In both observations, we observed along and perpendicular to the direction of the exciting star in zigzags (i.e., ± the lambda and beta scanning direction). From our knowledge of the IRAM-30 m telescope, we estimate the absolute position accuracy to be 3″.

The IRAM-30 m data were processed with the GILDAS/CLASS software. The data were first calibrated to the T_A^* scale using the chopper-wheel method (Penzias & Burrus 1973). The mixer tuning tables were incorrect for the frequency tuned in 2012. This basically turned the single sideband mixers into double-sideband ones. Because the actual rejection was unknown, we were unable to recompute an accurate T_A^* scale. Instead, we fixed the 2012 T_A^* scale according to the 2007 scale, which was correct. To do this, we correlated the 2007 and 2012 CH_3OH data sets, which allowed us to determine the multiplicative factors needed to fix the 2012 data (1.9 and 2.4 for the vertical and horizontal polarizations, respectively). We applied the same factors for the H_2CO data that were acquired with the same tuning. The data were converted to main-beam temperatures (T_{mb}) using the forward and main-beam efficiencies (F_{eff} and B_{eff}). The resulting amplitude accuracy is 10%. We then computed the experimental noise by subtracting a zeroth-order baseline from every spectra. A systematic comparison of this noise value with the theoretical noise computed from the system temperature, the integration time, and the channel width allowed us to filter out outlier spectra. The spectra where then gridded to a data cube through a convolution with a Gaussian kernel. Finally, we fitted another baseline of order 3 through each spectra of the cube.

2.3. Joint imaging and deconvolving of the interferometric and single-dish data

Following Rodriguez-Fernandez et al. (2008), the GILDAS/MAPPING software and the single-dish map from the IRAM-30 m were used to create the short-spacing visibilities not sampled by the Plateau de Bure interferometer. In short, the maps were deconvolved from the IRAM-30 m beam in the Fourier plane before multiplication by the PdBI primary beam in the image plane. After a last Fourier transform, pseudo-visibilities were sampled between 0 and 15 m (the diameter of the PdBI antenna). These visibilities were then merged with the interferometric observations. Each mosaic field was imaged and a dirty mosaic was built by combining these fields in the following best way in terms of signal-to-noise ratio (Pety & Rodríguez-Fernández 2010). The resulting data cubes were then scaled from Jy/beam to T_{mb} temperature scale using the synthesized beam size (see Table 2).

2.4. Deep pointed integrations with the 30 m

These observations are part of the Horsehead WHISPER project (Wideband High-resolution Iram-30 m Surveys at two Positions with Emir Receivers, PI: J. Pety), a complete and unbiased line survey at 1, 2, and 3 mm, carried out with the IRAM-30 m telescope. Two positions were observed: 1) the HCO peak, which is characteristic of the photo-dissociation region at the surface of the Horsehead nebula (Gerin et al. 2009); and 2) the DCO^+ peak, which belongs to a cold condensation located less than 40″ away from the PDR edge, where HCO^+ and other species are highly deuterated (Pety et al. 2007). Hereafter we refer to these two positions as the PDR and dense core, respectively. The combination of the new EMIR receivers at the IRAM-30 m telescope and the Fourier transform spectrometers (FTS) yields a spectral survey with unprecedented combination of bandwidth (36 GHz at 3 mm, 25 GHz at 2 mm and 76 GHz at 1 mm), spectral resolution (49 kHz at 3 and 2 mm; and 195 kHz at 1 mm), and sensitivity (median noise 8.1 mK, 18.5 mK and 8.3 mK, respectively). A detailed presentation of the observing strategy and data reduction process will be given in a forthcoming paper. In short, all frequencies were observed with two different frequency tunings and the Horsehead PDR and dense-core positions were alternatively observed every 15 min in position-switching mode with a common fixed off-position. This observing strategy allows us to remove potential ghost lines that are incompletely rejected from a strong line in the image sideband (the typical rejection of the EMIR sideband-separating mixers is only 13dB).

2.5. Deep pointed integrations with the CSO

We also report the detection of a new H_2CO line in the Horsehead. The H_2CO $4_{13}-3_{12}$ at line at 300.836 GHz was observed at the Caltech Submillimeter Observatory (CSO) telescope in October 2012. We used the Barney receiver and the FFTS2 backends at 269 kHz spectral resolution. We used the position-switching mode with the same off-position as was used in the 30 m observations, that is, (δRA, δDec) = (100″, 0″). The data were processed with the GILDAS/CLASS software. A fourth-order baseline was fit and subtracted from the spectra. The data were converted to T_{mb} using a beam efficiency of 0.68 measured towards Jupiter.

3. Observational results

3.1. Deep pointed integrations

Figure 1 presents the CH_3OH lines detected in the Horsehead. A diagram with the lower-energy rotational levels of E- and A-type methanol is shown in Fig. 2, with color arrows indicating the detected lines. We detected 9 and 16 lines at the PDR and dense-core positions, respectively. Of these lines, at each position, three arise from A-type methanol and the rest arise from E-type methanol. The brightest CH_3OH lines are those arising from A-type symmetry species. All lines are brighter in

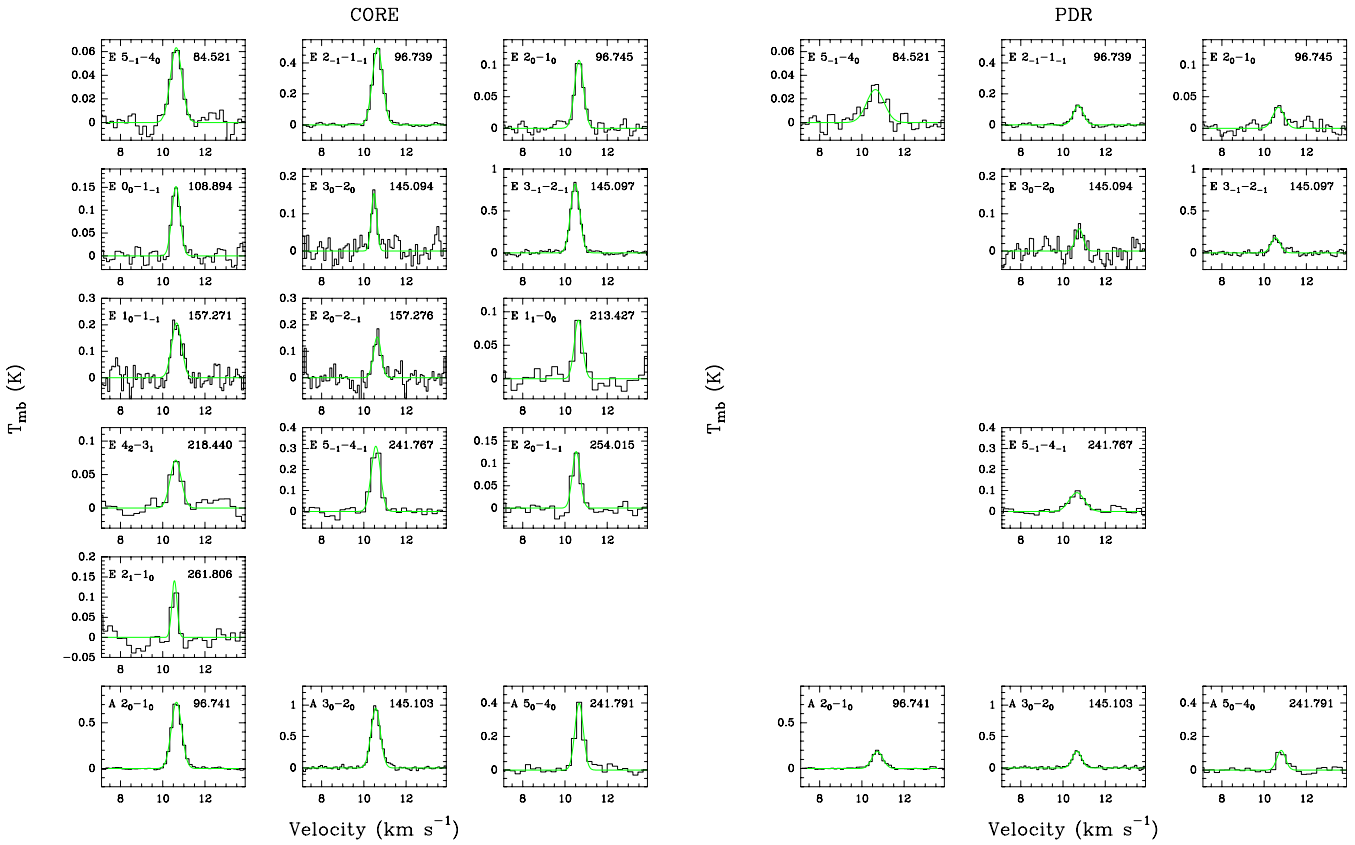

Fig. 1. Detected CH_3OH lines toward the dense-core (*left*) and PDR (*right*) positions. The green curves are Gaussian fits. The line frequency in GHz is given in each box. For each line, the same scale is used at both positions to facilitate the comparison.

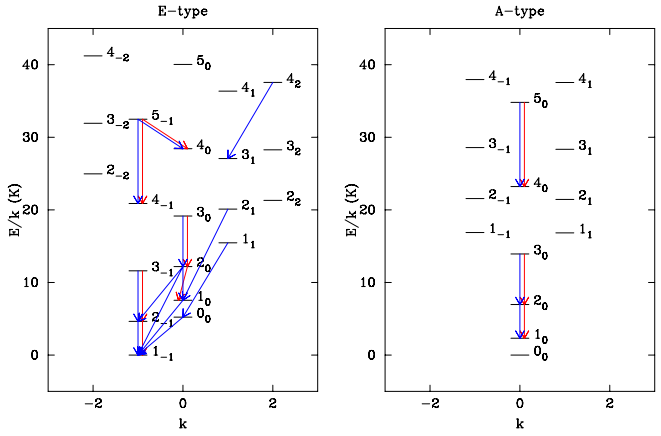

Fig. 2. Lower-energy rotational levels of CH_3OH – E (*left*) and CH_3OH – A (*right*). The arrows indicate the lines detected in the PDR (red) and the core (blue).

the dense core than in the PDR. The same behavior was found for H_2CO (Guzmán et al. 2011). Gaussian fits of the CH_3OH lines at the PDR in general result in broader line widths than at the dense core, although a few lines have similar linewidths toward both positions.

3.2. 30m maps

Figure 3 displays the single-dish maps of the 1.2 mm dust continuum emission and the line-integrated emission of the $DCO^+(3-2)$ (216 GHz) line, the p – H_2CO 3_{03}–2_{02} (218 GHz) and 2_{02}–1_{01} (146 GHz) lines, the CH_3OH – E 3_{-1}–2_{-1} (146 GHz) line, and the CH_3OH – A 3_0–2_0 (146 GHz) line. The formaldehyde and methanol emission to first order resembles the dust continuum spatial distribution. It first follows the photo-dissociation front, that is, the top of the Horsehead nebula from its front to its mane. It then forms two filaments almost perpendicular to the photo-dissociation front, one of them delineating the Horsehead throat. The E- and A-type methanol emission shows similar spatial distributions.

In contrast to the DCO^+ emission, which delineates a narrow filament, formaldehyde and methanol emission is extended. The impression that the formaldehyde emission is slightly more extended than the methanol emission is an artifact related to the different signal-to-noise ratio of these maps. Indeed, the 146 GHz E-type methanol map has by far the lowest signal-to-noise ratio. The highest signal-to-noise ratio map (i.e., the 146 GHz formaldehyde one) thus indicates that both formaldehyde and methanol emit in the PDR region (green cross).

Although the methanol emission in general correlates well with the formaldehyde emission, there are a few differences. First, formaldehyde peaks on the right side (closest to the photo-dissociation front) of the dense core as traced by the DCO^+ emission, while methanol peaks on its left side. Second, the 146 GHz formaldehyde line peaks at the DCO^+ emission peak (blue cross), where the gas is cold ($T_{kin} \simeq 20$ K) and dense ($n_H \sim 10^5$ cm^{-3}), while CH_3OH presents a local minimum at the same position.

3.3. PdBI maps

Figure 4 displays the HCO $1_{01}3/2,2$–$0_{00}1/2,1$ (86.670 GHz), H_2CO 2_{02}–1_{01} (145.602 GHz), CH_3OH – E 3_{-1}–2_{-1} (145.097 GHz), and CH_3OH – A 3_0–2_0 (145.103 GHz) integrated intensity maps obtained with the PdBI. In contrast

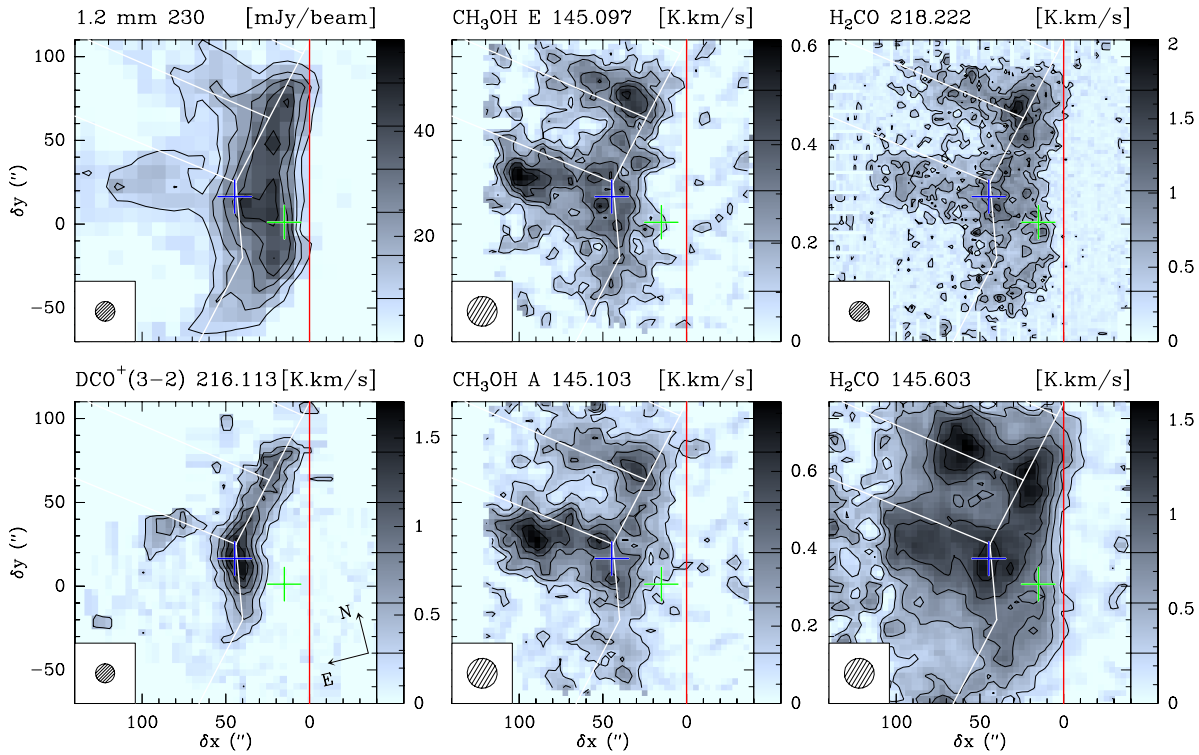

Fig. 3. IRAM-30 m maps of the Horsehead edge. Maps were rotated by 14° counterclockwise around the projection center, located at $(\delta x, \delta y) = (20'', 0'')$, to bring the exciting star direction in the horizontal direction, and the horizontal zero was set at the PDR edge, delineated by the red vertical line. The crosses show the positions of the PDR (green) and the dense core (blue), where deep integrations were performed at IRAM-30 m. The white lines delineate the arc-like structure of the DCO^+ emission. The spatial resolution is plotted in the bottom-left corner. Values of contour levels are shown in the respective image lookup table. The emission of all lines is integrated between 10.1 and 11.1 km s^{-1}.

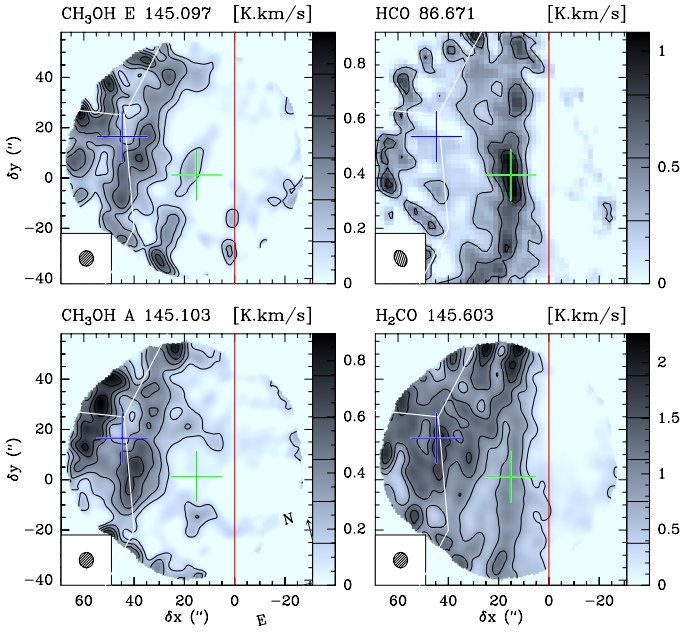

Fig. 4. IRAM-PdBI maps of the Horsehead edge. The field of view is smaller than in Fig. 3. The angular resolution is 6.″7 × 4.″4 for HCO and 6.″1×5.″6 for H_2CO and CH_3OH. All other descriptions are identical to Fig. 3.

to the case of HCO, which peaks in the PDR, the H_2CO and CH_3OH lines are brighter in the more UV-shielded layers of the nebula. However, the filament traced by the HCO emission is clearly seen in the H_2CO map at the PDR edge. The exact spatial distribution of the CH_3OH emission near the PDR position is difficult to infer due to the low signal-to-noise ratio at this position.

The minimum seen in the methanol 30 m maps near the dense-core position (blue cross) is present in both methanol lines and is preserved in the higher angular resolution map. On the other hand, H_2CO, which was observed simultaneously with CH_3OH, peaks at the dense core. This suggests that 1) the methanol gap is real and not an artifact of the deconvolution; and 2) methanol and formaldehyde emission show opposite behavior at the DCO^+ peak.

In contrast with HCO data, the maps of H_2CO and CH_3OH emission obtained with the PdBI only data (i.e., without the short-spacings from the IRAM-30 m telescope) looks like noise with a typical noise level of 0.15 K. Indeed, the spectra extracted from the hybrid synthesis (PdBI + 30 m) cube at the position of the dense core and of the PDR have an integrated area compatible, within the noise level, with the 30 m spectra at the same positions. This implies that the beam dilution of the single-dish observations of H_2CO and CH_3OH is marginal. We therefore used the higher signal-to-noise ratio 30 m spectra to infer the column densities at the PDR and dense-core positions.

4. Column densities and abundances

4.1. H_2CO

Figure 5 shows the new o-H_2CO $4_{13}-3_{12}$ line detected in the Horsehead. Guzmán et al. (2011) reported the detection of four o-H_2CO lines at lower frequencies. They used a nonlocal excitation and radiative transfer model from Goicoechea et al. (2006) adapted to the Horsehead geometry to model the observed H_2CO line intensities. The parameters they used are $T_{\rm kin}$ = 60 K and $n(H_2) = 6 \times 10^4$ cm^{-3} at the PDR position

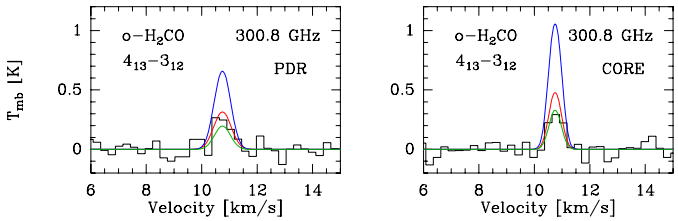

Fig. 5. New o-H_2CO line detected toward the PDR (*left*) and dense-core (*right*) positions. The three color lines plot the radiative-transfer models from Guzmán et al. (2011), where the column density was varied around the best match (red curve) by a factor of 1.5 (blue curve) and 1/1.5 (green curve). The column density used for the best fit is given in Table 6. The line frequency in GHz is given in each box.

Table 4. Critical densities[a] (cm^{-3}) for the CH_3OH lines detected in this work with p-H_2 and o-H_2 as colliding partners computed for two kinetic temperatures.

		T_{kin} = 20 K		T_{kin} = 60 K	
Type	J_K	p-H_2	o-H_2	p-H_2	o-H_2
E	5_{-1}	2.47×10^5	1.91×10^5	2.52×10^5	2.08×10^5
	2_{-1}	2.81×10^4	2.33×10^4	2.66×10^4	2.33×10^4
	2_0	3.28×10^5	1.52×10^5	3.59×10^5	1.55×10^5
	0_0	–	1.58×10^5	–	2.16×10^5
	3_0	4.13×10^5	2.88×10^5	4.40×10^5	2.83×10^5
	3_{-1}	7.05×10^4	6.88×10^4	6.88×10^4	6.83×10^4
	1_0	3.73×10^5	1.11×10^5	3.75×10^5	1.14×10^5
	1_1	2.70×10^6	2.62×10^5	3.83×10^6	2.83×10^5
	4_2	3.58×10^5	1.87×10^5	3.50×10^5	1.94×10^5
	2_1	6.75×10^5	2.88×10^5	7.19×10^5	2.83×10^5
A	5_{-1}	2.28×10^5	2.06×10^5	2.45×10^5	2.20×10^5
	2_{-1}	6.70×10^4	6.56×10^4	7.04×10^4	7.35×10^4
	2_0	2.86×10^4	2.29×10^4	2.96×10^4	2.58×10^4

Notes. [a] Computed as $n_{cr}(J'_{K'_aK'_c}, T_{kin}) = \frac{\sum_{J''_{K''_aK''_c}} A(J'_{K'_aK'_c}\rightarrow J''_{K''_aK''_c})}{\sum_{J''_{K''_aK''_c}} \gamma(J'_{K'_aK'_c}\rightarrow J''_{K''_aK''_c}, T_{kin})}$.

and T_{kin} = 20 K and $n(H_2) = 10^5$ cm^{-3} at the dense-core position. The column density that best reproduced the observations is given in Table 6 and the modeled line profile is shown in red in Fig. 5. The line profiles for two other models are also shown. The new detected H_2CO line agrees with the predictions of our previous model and thus corroborates the H_2CO column density derived by Guzmán et al. (2011).

4.2. CH_3OH

Typical densities in the Horsehead ($n_H = 10^4$–10^5 cm^{-3}) are lower than the critical densities of the observed transitions of methanol (see Table 4). We therefore expect the lines to be subthermally excited ($T_{ex} \ll T_{kin}$), and a non-LTE approach is needed to compute the CH_3OH column densities. E and A symmetries of CH_3OH were treated as different species because radiative transitions between them occur on timescales too long compared with the lifetime of the molecules. We did not correct for beam-dilution factors because the interferometric maps indicate that beam dilution is marginal for these molecules. The spectroscopic parameters for the detected transitions are given in Table 5.

We performed non-LTE radiative-transfer modeling using the RADEX LVG model (van der Tak et al. 2007), which computes the line intensities of a species for a given column density, kinetic temperature, and density of H_2. We included 100 rotational levels for CH_3OH – E and CH_3OH – A, where the highest energy level lies at ∼155 cm^{-1} for both species. We considered p-H_2 and o-H_2 as collision partners with collisional excitation rates from Rabli & Flower (2010). An H_2 ortho-to-para ratio of 3 (high-temperature limit) was assumed in the models. Lower H_2 ortho-to-para ratios were also tested, and we found that the difference is negligible. We also investigated the importance of electrons in the excitation at the PDR. The electron fraction is 10^{-4} relative to H_2 in the PDR position, while in the dense core the electron fraction is $\sim10^{-9}$ (Goicoechea et al. 2009b). We computed the CH_3OH – E–electron and CH_3OH – A–electron collisional coefficients within the dipolar Born approximation (e.g., Itikawa 1971). Owing to the relatively large dipole of methanol (1.7 D), dipole-allowed cross sections are expected to be dominant and mostly determined by the long-range electron-dipole interaction. Thus, for the water molecule, which has a similar dipole (1.8 D), Faure et al. (2004) have shown that the Born approximation is accurate down to typically 1 eV. At lower energy, short-range forces can become important, and these effects were found to reduce the low-energy cross-sections by up to a factor of ∼1.5. In the case of methanol, the Born treatment probably overestimates the rotational cross-sections by a factor of 2–3, as suggested by the measurements of the total elastic cross-section (see Vinodkumar et al. 2013, and references therein). In the Born approximation, cross-sections are proportional to line strengths and the square of the dipole and therefore strictly obey the dipolar selection rule. In this work, line strengths and dipoles were taken from the JPL catalog (Pickett et al. 1998). Excitation cross-sections were computed in the energy range 0.1 meV–1 eV and rate coefficients were deduced in the range 10–1000 K, for the lowest 256 levels of CH_3OH – A (1853 transitions) and the lowest 256 levels of CH_3OH – E (2324 transitions).

We first constrained the column density of CH_3OH – E because we detected more lines of this species. The density profile across the PDR in the Horsehead is well constrained (Habart et al. 2005). Several efforts have been made to compute the thermal profile, but it remains less well constrained than the density. We therefore decided to fix the H_2 density and vary the temperature in our models. For this, we ran grids of models for kinetic

Table 5. Spectroscopic parameters of the detected lines obtained from the CDMS data base (Müller et al. 2001).

Molecule	Transition	ν [GHz]	E_u [K]	A_{ul} [s^{-1}]	g_u
CH_3OH – E	5_{-1}–4_0	84.521	40.4	2.0×10^{-6}	11
CH_3OH – E	2_{-1}–1_{-1}	96.739	12.5	3.0×10^{-6}	5
CH_3OH – E	2_0–1_0	96.745	20.1	3.0×10^{-6}	5
CH_3OH – E	0_0–1_{-1}	108.894	13.1	1.5×10^{-5}	1
CH_3OH – E	3_0–2_0	145.094	27.1	1.2×10^{-5}	7
CH_3OH – E	3_{-1}–2_{-1}	145.097	19.5	1.1×10^{-5}	7
CH_3OH – E	1_0–1_{-1}	157.271	15.4	2.2×10^{-5}	3
CH_3OH – E	2_0–2_{-1}	157.276	20.1	2.2×10^{-5}	5
CH_3OH – E	1_1–0_0	213.427	23.4	3.4×10^{-5}	3
CH_3OH – E	4_2–3_1	218.440	45.5	4.7×10^{-5}	9
CH_3OH – E	5_{-1}–4_{-1}	241.767	40.4	5.8×10^{-5}	11
CH_3OH – E	2_0–1_{-1}	254.015	20.1	1.9×10^{-5}	5
CH_3OH – E	2_1–1_0	261.806	28.0	5.6×10^{-5}	5
CH_3OH – A	2_0–1_0	96.741	7.0	3.0×10^{-6}	5
CH_3OH – A	3_0–2_0	145.103	13.9	1.2×10^{-5}	7
CH_3OH – A	5_0–4_0	241.791	34.8	6.0×10^{-5}	11

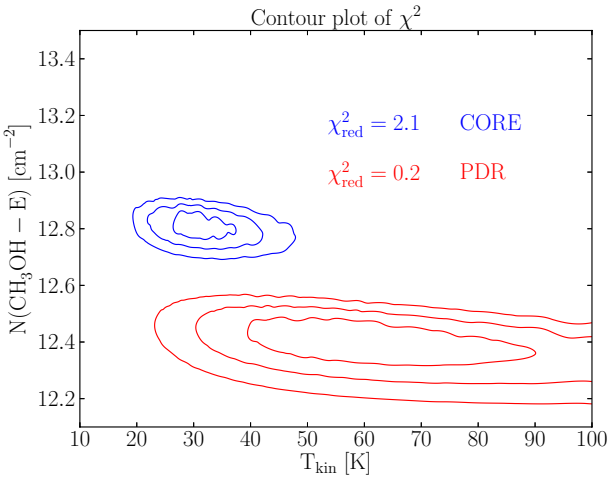

Fig. 6. χ^2 as a function of N(CH_3OH – E) and T_{kin} for the PDR (red) and dense-core (blue) positions. The H_2 density was kept constant to $n(H_2) = 6 \times 10^4$ cm^{-3} (PDR) and $n(H_2) = 1 \times 10^5$ cm^{-3} (dense core). The contours indicate the 1, 2, and 3σ confidence levels for the models. The reduced χ^2, defined as $\chi^2_{red} = \chi^2/(N-2)$, is shown for the best-fit model at each position.

temperatures of 10–100 K and CH_3OH – E column densities between 10^{11} and 10^{15} cm^{-2}. The density of H_2 was kept constant to the well-known values of $n_H = 6 \times 10^4$ cm^{-3} in the PDR and $n_H = 1 \times 10^5$ cm^{-3} in the dense core. Then, the χ^2 was computed[2] at each point of the grid to determine the best-fit parameters. Figure 6 shows the 1, 2, and 3σ confidence levels for the PDR (red) and dense core (blue) for models without electron excitation. The best fits are for kinetic temperatures of 60 K (PDR) and 30 K (core), which agrees well with previous determinations. The CH_3OH – E column densities are well constrained. The best fits are for CH_3OH – E column densities of $(2.7 \pm 0.5) \times 10^{12}$ cm^{-2} and $(6.5 \pm 0.8) \times 10^{12}$ cm^{-2} for the PDR and dense core, respectively. We also ran models for a fixed kinetic temperature instead of a fixed gas density. These models resulted in similar CH_3OH column densities, but in a H_2 gas density of $n_H = 6 \times 10^4$ cm^{-3} at the dense-core position, which is lower than expected ($n_H \sim 10^5$ cm^{-3}).

We found that the change in the CH_3OH – E column density is negligible in these models when we included the electron excitation. However, for a grid of models with the three parameters (T_{kin}, n_H and $N(CH_3OH)$) free and no electron excitation, we found a low kinetic temperature ($T_{kin} = 40$ K) and a high density ($n_H = 10^5$) at the PDR. When we included the electron excitation, on the other hand, we obtained $T_{kin} \sim 65$ K and $n_H \sim 5 \times 10^4$ cm^{-3}, which agrees much better with previous estimates. The inferred CH_3OH column density is the same for both models ($N = 2.7 \times 10^{12}$ cm^{-2}). Hence, collisions with electrons are not important for determining the CH_3OH column density, but they are important for determining the kinetic temperature and density of the gas. The electron excitation was found to be important for determining the column density of CH_3CN in the PDR (Gratier et al. 2013).

The determination of the CH_3OH – A column density is more difficult because only three lines were detected, which provides fewer constrains to the model. We therefore fixed the kinetic temperature to the best-fit values found for CH_3OH – E, in addition to keeping the density of H_2 constant, and ran models varying the column density only. The best fits are obtained for CH_3OH – A column densities of $(2.0 \pm 0.3) \times 10^{12}$ cm^{-2} and $(8.1 \pm 1.0) \times 10^{12}$ cm^{-2} for the PDR and dense core, respectively.

[2] $\chi^2 = \sum_1^N \frac{(\text{Observation} - \text{Model})^2}{\sigma^2}$, with N the number of detected lines.

Table 6. Column densities and abundances.

	Molecule	PDR	Dense core
Column density [cm^{-2}]	N_H	3.8×10^{22}	6.4×10^{22}
	N(HCO)[a]	3.2×10^{13}	$<4.6 \times 10^{12}$
	N(o-H_2CO)[b]	7.2×10^{12}	9.6×10^{12}
	N(p – H_2CO)[b]	3.6×10^{12}	3.2×10^{12}
	N(CH_3OH – E)	2.7×10^{12}	6.5×10^{12}
	N(CH_3OH – A)	2.0×10^{12}	8.1×10^{12}
Abundances $\frac{N(X)}{(N(H)+2\,N(H_2))}$	[HCO]	8.4×10^{-10}	$<7.2 \times 10^{-11}$
	[o-H_2CO]	1.9×10^{-10}	1.5×10^{-10}
	[p – H_2CO]	9.5×10^{-11}	5.0×10^{-11}
	[CH_3OH – E]	7.0×10^{-11}	1.0×10^{-10}
	[CH_3OH – A]	5.3×10^{-11}	1.3×10^{-10}
	H_2CO/CH_3OH[c]	2.3 ± 0.4	0.9 ± 0.1

Notes. [(a)] Gerin et al. (2009). [(b)] Guzmán et al. (2011). [(c)] We estimated an error of ~15% for the H_2CO column density (similar to CH_3OH) in computing the error in the ratio.

Table 6 summarizes the derived column densities and abundances relative to the total number of atomic hydrogen atoms for HCO, H_2CO, and CH_3OH. The E/A methanol ratio is 1.3 ± 0.3 and 0.8 ± 0.1 for the PDR and dense core, respectively. The total CH_3OH abundance is similar in the PDR and dense core, being only a factor ~ 1.9 larger in the dense core. Similar abundances were also found for H_2CO in both positions. The H_2CO/CH_3OH abundance ratio is $\sim 2.3 \pm 0.4$ in the PDR and $\sim 0.9 \pm 0.1$ in the dense core.

4.3. Deuterated CH_3OH

Guzmán et al. (2011) detected single and doubly deuterated formaldehyde in the Horsehead and derived [HDCO]/[H_2CO] = 0.11 and [D_2CO]/[H_2CO] = 0.04 in the dense core. We now searched for deuterated methanol at this position. We did not detect transitions from deuterated methanol, but we computed an upper limit for the CH_2DOH column density toward the dense core. The low-energy transitions $2_K - 2_K$ of CH_2DOH lie at 89 GHz. The rms noise at this frequency is 6.43 mK with 0.17 km s^{-1} spectral resolution. Assuming a linewidth of 0.5 km s^{-1}, we obtain an upper limit for the integrated line intensity of 6 mK km s^{-1}. This translates into a 1σ upper limit for the column density of 1.4×10^{12} cm^{-2} and a fractionation ratio [CH_2DOH/CH_3OH] $\leq$ 0.26 at the dense-core position. Assuming that methanol has fractionation levels similar to those of H_2CO, we conclude that our data are not sensitive enough to detect lines from deuterated methanol molecules. For reference, singly, doubly, and even triply deuterated methanol species such as CH_2DOH, CHD_2OH, and CD_3OH have been detected toward low-mass protostars with abundance ratios of 37–65% (CH_2DOH), 20% (CHD_2OH), and 1.4% (CD_3OH) compared to their non-deuterated isotopologue (Parise et al. 2004, 2006).

5. Comparison with models

In this section we study the HCO, H_2CO, and CH_3OH chemistry in the Horsehead. We used an updated version of the one-dimensional, steady-state photochemical model (Le Petit et al. 2006) used in the study of H_2CO by Guzmán et al. (2011). We

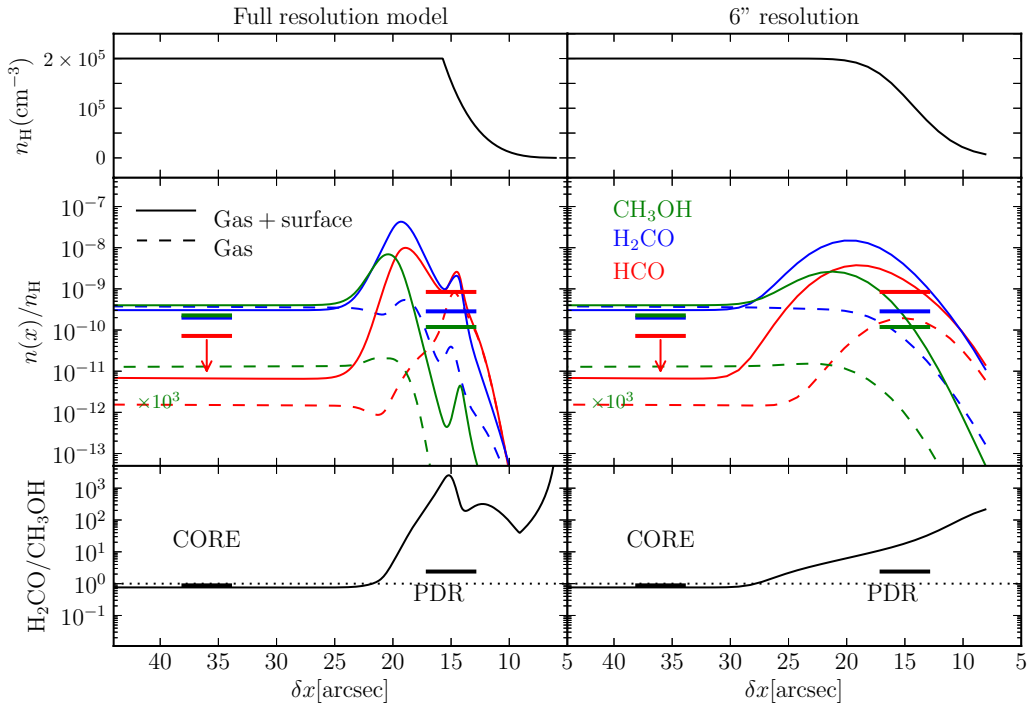

Fig. 7. Photochemical model of the Horsehead PDR. The *left column* shows the full-resolution model and the *right column* shows the model convolved with a Gaussian of 6″ FWHM. *Upper panel*: PDR density profile ($n_H = n(H) + 2n(H_2)$ in cm^{-3}). *Middle panel*: predicted abundance (relative to n_H) of HCO (red), H_2CO (blue) and CH_3OH (green). *Lower panel*: predicted H_2CO/CH_3OH abundance ratio. Models shown as dashed lines include pure gas-phase chemistry and models shown as solid lines include both gas-phase and grain surface chemistry. The CH_3OH abundance predicted by the pure gas-phase model has been multiplied by 10^3 in the *middle panel* so that it could fit in the figure.

include the density profile displayed in the upper panel of Fig. 7, a radiation field $\chi = 60$ (relative to the Draine field; Draine 1978), the elemental gas-phase abundances from Goicoechea et al. (2009b; see their Table 5), and a cosmic-ray ionization rate $\zeta = 5 \times 10^{-17}$ s^{-1} per H_2 molecule.

We compare the results of a pure gas-phase chemical network with one that also includes grain surface reactions. Figure 7 displays the results for the photochemical models. The left column presents the results computed by the code, which samples the UV-illuminated gas on a finer spatial grid than the UV-shielded gas to correctly represent the steep physical and chemical gradients. The right column presents the results convolved with a Gaussian of 6″ (FWHM) to facilitate the comparison with the abundances inferred from the PdBI observations at 6″ angular resolution. The predicted H_2CO and CH_3OH abundance profiles are shown in the middle panel. The H_2CO/CH_3OH abundance ratio is shown in the lower panel. The horizontal bars show the results inferred from observations. Results for the pure gas-phase model are shown as dashed lines and results for the model including grain surface chemistry are shown as solid lines.

5.1. Pure gas-phase models

We used a modified version of the pure gas-phase chemical network of the Ohio State University (OSU). Our network includes the photodissociation of HCO and of H_2CO (leading to CO and H_2), and the atomic oxygen reaction with the methylene radical (CH_2) to explain the high abundance of HCO in the PDR (Gerin et al. 2009). The H_2CO photodissociation channel that leads to HCO + H is also included.

As previously shown by Guzmán et al. (2011), the pure-gas phase model satisfactorily reproduces the observed H_2CO abundance in the dense core ($\delta x \sim 35''$), but it underestimates the abundance in the PDR ($\delta x \sim 15''$) by at least one order of magnitude. In this model the formation of H_2CO is dominated by reactions between oxygen atoms and the methyl radical (CH_3) in both the PDR and dense core. The destruction of H_2CO in the PDR is dominated by reactions with S^+ and by photodissociation, while it is dominated by reactions with ions (mainly H_3O^+, HCO^+ and S^+) in the dense core.

In the gas phase, methanol is mainly produced by the dissociative recombination of $CH_3OH_2^+$, which is formed by reactions between CH_3^+ and water. It is now well established that this reaction is not efficient enough to explain the observed CH_3OH abundances (Garrod et al. 2006; Geppert et al. 2006). Indeed, the pure gas-phase model underestimates the CH_3OH abundance by ~5 orders of magnitude in both the PDR and dense core. Note that the CH_3OH abundance predicted by the pure gas-phase model has been multiplied by 1000 in Fig. 7.

5.2. Grain surface chemistry models

We included the reactions on the surface of dust grains to the gas-phase chemical network described in Sect. 5.1. A detailed description of the implementation of grain surface chemistry in the Meudon PDR code will be given in a subsequent paper (Le Bourlot et al., in prep.). The model includes the adsorption, desorption, and diffusive reactions on grains, where the sequence to form formaldehyde and methanol is the one shown in the hydrogenation path (1). We also introduce water formation via hydrogenation reactions of O, OH until H_2O. The hydrogenation of formaldehyde can lead to CH_3O and/or CH_2OH. Gas-phase methoxy radical (CH_3O) was recently detected in the cold dense core B1-b (Cernicharo et al. 2012). We do not distinguish between these two isomers, that is, CH_3O and CH_2OH, in our network. The energy barriers associated with the H + CO (200 K)

and H + H_2CO (300 K) reactions have been modified with respect to Guzmán et al. (2011). As shown by laboratory studies (Öberg et al. 2009b,a; Muñoz Caro et al. 2010), photodesorption can be an efficient mechanism to release molecules into the gas phase in regions exposed to radiation fields. We included photodesorption yields of 10^{-3} and 2×10^{-4} molecules per incident UV photon, for H_2CO and CH_3OH, respectively. These values are close to those measured in the laboratory for CO, CO_2, H_2O, and CH_3OH (Öberg et al. 2007, 2009a–c). Photodesorption of adsorbed CH_3OH can produce both methanol and formaldehyde in the gas-phase with a 50/50 branching ratio. This channel was not included in the model of Guzmán et al. (2011), where photodesorption of adsorbed CH_3OH produced only gas-phase methanol. We checked that the use of steady-state chemistry in the model is a valid assumption for the physical conditions prevailing in the Horsehead PDR and dense core. Indeed, the formation and destruction timescales of H_2CO and CH_3OH are <30 yr and <5000 yr at the PDR and dense core, respectively, while the estimated age of the Horsehead is $\sim 5 \times 10^5$ yr (Pound et al. 2003).

The new results are shown as solid lines in Fig. 7. The dust temperatures in this model are 20 K. The model predicts two abundance peaks at the edge of the nebula ($\delta x \sim 15$ and $\delta x \sim 20$), with CH_3OH peaking deeper inside the cloud than HCO and H_2CO, and an abundance plateau at the inner layers of the cloud. This way, HCO and H_2CO dominate at the outer layers of the cloud, while CH_3OH dominates in the inner layers. At the dense-core position ($\delta x \sim 35''$), the modeled H_2CO abundance is similar to the one predicted by the pure gas-phase model. The CH_3OH abundance, on the other hand, increases by ~5 orders of magnitude with respect to the pure gas-phase model. The observed H_2CO and CH_3OH abundances in the dense core are well reproduced by the model that includes both gas-phase and grain surface chemistry. In the PDR, this model also agrees well with the observed HCO and CH_3OH abundances, but the predicted H_2CO abundance is higher than observed.

In this model, CH_3OH is produced by photodesorption of CH_3OH ices everywhere in the cloud. At the dense core, the FUV photons that photodesorb the CH_3OH ices are secondary photons produced by the interaction between cosmic rays and H_2 molecules. Gas-phase CH_3OH is mainly destroyed by photodissociation in the PDR and by freeze-out in the dense core. H_2CO is produced mainly by direct photodesorption of H_2CO ices in the PDR position. In the model of Guzmán et al. (2011), we found that the dominant formation path for H_2CO in the dense core was the gas-phase route that involved CH_3 and O. With this new model, we find that at the dense core H_2CO is produced mainly by photodissociation of CH_3OH ices. This difference is the result of the several modifications made to the model, of which the most important is the inclusion of the channel that leads to H_2CO in the photodesorption of CH_3OH ice. H_2CO is mainly destroyed by photodissociation in the PDR and by reactions with ions (mainly N_2H^+ and H_3^+) in the dense core[3].

[3] We first ran models assuming the solar sulfur abundance (S/H = 1.38×10^{-5}). With this S abundance and including the grain surface chemistry, the destruction of H_2CO is dominated by reactions with S^+ in both the PDR and dense core. We then ran models using a lower sulfur abundance (S/H = 3.5×10^{-6}), which reproduces the observed CS and HCS^+ abundances (Goicoechea et al. 2006). In this model, which is the one adopted in this paper, S^+ is not important in the destruction of H_2CO. As a result, the predicted H_2CO abundance at the dense core is three times higher in the low-S abundance model and the agreement between model and observations is better. We conclude that a sulfur abundance of S/H = 3.5×10^{-6} can reproduce the observed abundance of CS, HCS^+, and H_2CO.

It is important to remember that models that include complex grain surface processes use numerous physical parameters, such as the adsorption energy, diffusion energy of absorbed species, the activation energy of the different hydrogenation reactions, and the desorption yield, which have large uncertainties. The results predicted by these models are highly dependent on the values used for these parameters. Providing observational results is crucial to constrain these parameters and benchmark the models.

6. Discussion

6.1. Observational evidence of different H_2CO formation mechanisms

The observations suggest that H_2CO is formed on the surface of dust grains at the PDR and is mostly formed in the gas-phase at the dense core. First, we found a different ortho-to-para ratio in each position: an equilibrium value of 3 was found at the dense core, while a lower out-of-equilibrium value of 2 was found at the PDR. Second, if H_2CO is formed on the grains, its spatial distribution is expected to resemble the spatial distribution of CH_3OH. However, the high-resolution PdBI maps show that the CH_3OH emission presents a minimum at the dense-core position, while H_2CO peaks at this position. The easiest interpretation is that 1) the photodesorption of both H_2CO and CH_3OH is inefficient at the dense core, therefore the ices remain depleted onto grains; and that 2) H_2CO is formed in the gas phase at this position. Indeed, the pure gas-phase model reproduces the H_2CO abundance at the dense core well. Moreover, fewer photons can photodesorb species at the dense core than are available at the PDR position. This way, gas-phase CH_3OH is present in an envelope around the dense core, while H_2CO is present in both the envelope and the dense core itself. This is consistent with the lower gas-density inferred from the radiative-transfer analysis of CH_3OH at the dense-core position.

Depletion of CH_3OH has also been observed in other dense cores. Tafalla et al. (2006) found that CH_3OH shows a dip in its emission at the center of the dense cores L1498 and L1517B. They concluded that the drop in emission corresponds to a real drop in column density, suggesting that CH_3OH freeze out onto grains at the center of these dense cores.

6.2. Comparison with other environments

H_2CO and CH_3OH have been detected in the Orion Bar, which is a more extreme case of a PDR (higher χ, $T_{\rm kin}$ and $T_{\rm dust}$). Leurini et al. (2010) estimated an abundance ratio H_2CO/CH_3OH = 14–1400 in the interclump medium ($n_{\rm H} \sim 10^4$ cm^{-3}) and H_2CO/CH_3OH = 0.9–2.5 in the denser clumps ($n_{\rm H} \sim 10^6$ cm^{-3}). Despite the large uncertainties and the fact that the clumpy medium was not resolved, they concluded that the abundance of methanol relative to formaldehyde decreases by at least one order of magnitude in the interclump medium in comparison to the dense clumps. Unlike the situation at the Orion Bar, we only found a small difference in the H_2CO/CH_3OH abundance ratio between the PDR and dense core in the Horsehead (H_2CO/CH_3OH is only twice as high in the PDR). This is probably due to the difference in the radiation field between the two sources ($\chi \simeq 10^4$ in the Orion Bar; χ = 60 in the Horsehead). Hence, photodissociation of CH_3OH (which produces H_2CO) is more efficient in the Orion Bar, especially in the interclump medium, and the ratio of H_2CO/CH_3OH is thus higher. The H_2CO/CH_3OH abundance ratio we derive in the Horshead (0.9–2.3) is very similar to the one found in the dense clumps of the Orion Bar. These clumps are more protected from

the FUV photons and thus resemble more closely the conditions prevailing in the Horsehead. Indeed, $\chi/n \sim 100/10^4$ in the Horsehead, which is similar to the ratio found in the dense clumps of the Orion Bar ($\chi/n \sim 10^4/10^6$).

Maret et al. (2004, 2005) measured the formaldehyde and methanol abundances toward a sample of low-mass protostars. From these studies, an abundance ratio H_2CO/CH_3OH = 0.7–4.3 was found for the hot-corino region. In the low-mass starless cores, L1498 and L1517B, Tafalla et al. (2006) found H_2CO/CH_3OH = 1.1–2.2. These values are similar to the abundance ratio derived in the Horsehead. A lower abundance ratio was found in hot cores (H_2CO/CH_3OH = 0.13–0.28; Bisschop et al. 2007), and an even lower ratio was found in shocked gas in Galactic center clouds ($H_2CO/CH_3OH \sim 0.01$; Requena-Torres et al. 2006). In the diffuse medium, H_2CO is widely detected (e.g., Liszt et al. 2006), but methanol has not been detected, although it has been searched for by Liszt et al. (2008). They derived an upper limit for the CH_3OH column density, which translates into a lower limit for the abundance ratio of $H_2CO/CH_3OH \geq 12$.

6.3. Thermal and nonthermal desorption

In hot cores, hot corinos, and shocked regions the ices that were formed in the cold gas in the prestellar stage are completely sublimated into the gas-phase through thermal desorption and sputtering. The observed H_2CO and CH_3OH gas-phase abundances in these regions should therefore resemble the original ice composition. Observations of ices in the envelopes of low-mass protostars show strong variations of the CH_3OH ice abundance with respect to water ice (1%–30%; Boogert et al. 2008). In cold cores, a methanol ice abundance of 5%–12% relative to water has been found (Boogert et al. 2011). The variations in the CH_3OH ice abundance are caused by the different local physical conditions and thus reflect the variations in the evolutionary stages of these sources (Cuppen et al. 2009). The abundance of H_2CO ice has been more difficult to determine because it has been detected in just a few sources, and its stronger ice feature at 6 μm is blended with that of HCOOH (Öberg et al. 2011). A relatively constant H_2CO ice abundance of ~6% relative to water was found in low-mass protostars (Gibb et al. 2004; Boogert et al. 2008). This value seems to be independent of the CH_3OH ice abundance. From these detections, an ice abundance ratio $H_2CO/CH_3OH \simeq 0.2–6.0$ is obtained in low-mass protostars, which is consistent with the gas-phase abundance ratio found in hot corinos by Maret et al. (2004, 2005).

In cold cores and low-UV illumination PDRs, the ices are released through nonthermal processes, such as photodesorption. The H_2CO/CH_3OH ratio will therefore depend on the dust temperature and on the number of UV photons that will desorb the ices into the gas-phase. The CH_3OH photodesorption yield has been previously found to be $\sim 10^{-3}$ molecules per incident UV photon, similar to other species such as CO, CO_2, and H_2O (Öberg et al. 2009a–c). Although the CH_3OH photodesorption yield is uncertain, the one adopted in our model gives a CH_3OH abundance that is consistent with the observations. As discussed in Sect. 5.2, the predictions of chemical models including grain surface chemistry are highly dependent on the different physical parameters. Future laboratory studies, using different ice mixtures (similar to those observed in the ISM), will help to better understand the nonthermal desorption of ices into the gas phase and will hopefully provide precise values for the photodesorption yields and other parameters needed in the models.

7. Summary and conclusions

We have presented deep observations of CH_3OH lines toward the Horsehead PDR and its associated dense core, together with single-dish and interferometric observations of H_2CO and CH_3OH. In general, formaldehyde and methanol emission is extended, although there are a few differences. The CH_3OH emission presents a minimum at the dense-core position that is also seen in the lower angular resolution 30 m map, while H_2CO peaks at this position. From the high-resolution maps, we concluded that beam dilution of the single-dish deep integrations is marginal. This is in contrast with the model prediction of an abundance peak at the PDR position. We therefore confirm the H_2CO abundances inferred by Guzmán et al. (2011) and derived a similar CH_3OH abundance with respect to H ($\sim 10^{-10}$) in the PDR and dense-core position that is also similar to the observed abundance of H_2CO. We found that collisions with electrons are not important in determining the CH_3OH column density when the physical conditions of the gas are known. However, to determine the kinetic temperature and density of the gas, electron excitation should be taken into account. The inferred methanol E/A ratio is close to one in both the PDR and the dense-core position. The H_2CO/CH_3OH abundance ratio is 2.3 ± 0.4 in the PDR and 0.9 ± 0.1 in the dense core.

At the PDR, observations suggest that both H_2CO and CH_3OH are formed on the surface of dust grains and are subsequently released into the gas phase through photodesorption. Indeed, pure gas-phase chemical models predict H_2CO and CH_3OH abundances that are too low compared with what is inferred from the observations. At the dense core, on the other hand, the dominant formation mechanism differs for H_2CO and CH_3OH. H_2CO is mostly formed in the gas phase, while CH_3OH is formed on the grains. Indeed, a pure gas-phase model can reproduce the observed H_2CO abundance at this position, while it fails by ~5 orders of magnitude for CH_3OH. Moreover, the high-resolution PdBI maps show that CH_3OH is present in an envelope around the dense core, while H_2CO is present in both the envelope and the dense core itself. The result of different H_2CO formation mechanisms in the PDR and dense core are strengthened by the different ortho-to-para ratio inferred from the observations (o/p $\sim$ 2 in the PDR and the equilibrium value o/p ~ 3 in the dense core).

Acknowledgements. We thank the IRAM PdBI and 30 m staff for their support during the observations. We thank Simon Radford for his help during the CSO observations and data reduction. VG thanks support from the Chilean Government through the Becas Chile scholarship program. This work was also funded by grant ANR-09-BLAN-0231-01 from the French *Agence Nationale de la Recherche* as part of the SCHISM project. J.R.G. thanks the Spanish MINECO for funding support from grants AYA2012-32032, AYA2009-07304 and CSD2009-00038. J.R.G. is supported by a Ramón y Cajal research contract.

References

Bergman, P., Parise, B., Liseau, R., & Larsson, B. 2011, A&A, 527, A39
Bernstein, M. P., Dworkin, J. P., Sandford, S. A., Cooper, G. W., & Allamandola, L. J. 2002, Nature, 416, 401
Bisschop, S. E., Jørgensen, J. K., van Dishoeck, E. F., & de Wachter, E. B. M. 2007, A&A, 465, 913
Boogert, A. C. A., Pontoppidan, K. M., Knez, C., et al. 2008, ApJ, 678, 985
Boogert, A. C. A., Huard, T. L., Cook, A. M., et al. 2011, ApJ, 729, 92
Bottinelli, S., Ceccarelli, C., Williams, J. P., & Lefloch, B. 2007, A&A, 463, 601
Bottinelli, S., Boogert, A. C. A., Bouwman, J., et al. 2010, ApJ, 718, 1100
Brown, W. A., & Bolina, A. S. 2007, MNRAS, 374, 1006
Caselli, P., Keto, E., Bergin, E. A., et al. 2012, ApJ, 759, L37
Ceccarelli, C., Loinard, L., Castets, A., Tielens, A. G. G. M., & Caux, E. 2000, A&A, 357, L9
Cernicharo, J., Marcelino, N., Roueff, E., et al. 2012, ApJ, 759, L43

Codella, C., Ceccarelli, C., Lefloch, B., et al. 2012, ApJ, 757, L9
Cuppen, H. M., van Dishoeck, E. F., Herbst, E., & Tielens, A. G. G. M. 2009, A&A, 508, 275
Draine, B. T. 1978, ApJS, 36, 595
Faure, A., Gorfinkiel, J. D., & Tennyson, J. 2004, MNRAS, 347, 323
Fuchs, G. W., Cuppen, H. M., Ioppolo, S., et al. 2009, A&A, 505, 629
Garrod, R., Park, I. H., Caselli, P., & Herbst, E. 2006, Faraday Discuss., 133, 51
Garrod, R. T., Weaver, S. L. W., & Herbst, E. 2008, ApJ, 682, 283
Geppert, W. D., Hamberg, M., Thomas, R. D., et al. 2006, Faraday Discuss., 133, 177
Gerin, M., Goicoechea, J. R., Pety, J., & Hily-Blant, P. 2009, A&A, 494, 977
Gibb, E. L., Whittet, D. C. B., Schutte, W. A., et al. 2000, ApJ, 536, 347
Gibb, E. L., Whittet, D. C. B., Boogert, A. C. A., & Tielens, A. G. G. M. 2004, ApJS, 151, 35
Goicoechea, J. R., Pety, J., Gerin, M., et al. 2006, A&A, 456, 565
Goicoechea, J. R., Compiègne, M., & Habart, E. 2009a, ApJ, 699, L165
Goicoechea, J. R., Pety, J., Gerin, M., Hily-Blant, P., & Le Bourlot, J. 2009b, A&A, 498, 771
Gratier, P., Pety, J., Guzmán, V., et al. 2013, A&A, 557, A101
Green, S. D., Bolina, A. S., Chen, R., et al. 2009, MNRAS, 398, 357
Guzmán, V., Pety, J., Goicoechea, J. R., Gerin, M., & Roueff, E. 2011, A&A, 534, A49
Habart, E., Abergel, A., Walmsley, C. M., Teyssier, D., & Pety, J. 2005, A&A, 437, 177
Hily-Blant, P., Teyssier, D., Philipp, S., & Güsten, R. 2005, A&A, 440, 909
Itikawa, Y. 1971, J. Phys. Soc. Jpn., 30, 835
Jørgensen, J. K., Schöier, F. L., & van Dishoeck, E. F. 2005, A&A, 437, 501
Le Petit, F., Nehmé, C., Le Bourlot, J., & Roueff, E. 2006, ApJS, 164, 506
Leurini, S., Schilke, P., Menten, K. M., et al. 2004, A&A, 422, 573
Leurini, S., Parise, B., Schilke, P., Pety, J., & Rolffs, R. 2010, A&A, 511, A82
Liszt, H. S., Lucas, R., & Pety, J. 2006, A&A, 448, 253
Liszt, H. S., Pety, J., & Lucas, R. 2008, A&A, 486, 493
Mangum, J. G., & Wootten, A. 1993, ApJS, 89, 123
Mangum, J. G., Darling, J., Henkel, C., & Menten, K. M. 2013, ApJ, 766, 108
Maret, S., Ceccarelli, C., Caux, E., et al. 2004, A&A, 416, 577
Maret, S., Ceccarelli, C., Tielens, A. G. G. M., et al. 2005, A&A, 442, 527
Muñoz Caro, G. M., Meierhenrich, U. J., Schutte, W. A., et al. 2002, Nature, 416, 403
Muñoz Caro, G. M., Jiménez-Escobar, A., Martín-Gago, J. Á., et al. 2010, A&A, 522, A108
Müller, H. S. P., Thorwirth, S., Roth, D. A., & Winnewisser, G. 2001, A&A, 370, L49
Öberg, K. I., Fuchs, G. W., Awad, Z., et al. 2007, ApJ, 662, L23
Öberg, K. I., Boogert, A. C. A., Pontoppidan, K. M., et al. 2008, ApJ, 678, 1032
Öberg, K. I., Garrod, R. T., van Dishoeck, E. F., & Linnartz, H. 2009a, A&A, 504, 891
Öberg, K. I., Linnartz, H., Visser, R., & van Dishoeck, E. F. 2009b, ApJ, 693, 1209
Öberg, K. I., van Dishoeck, E. F., & Linnartz, H. 2009c, A&A, 496, 281
Öberg, K. I., Boogert, A. C. A., Pontoppidan, K. M., et al. 2011, ApJ, 740, 109
Parise, B., Castets, A., Herbst, E., et al. 2004, A&A, 416, 159
Parise, B., Ceccarelli, C., Tielens, A. G. G. M., et al. 2006, A&A, 453, 949
Penzias, A. A., & Burrus, C. A. 1973, ARA&A, 11, 51
Pety, J. 2005, in SF2A-2005: Semaine de l'Astrophysique Française, eds. F. Casoli, T. Contini, J. M. Hameury, & L. Pagani, 721
Pety, J., & Rodríguez-Fernández, N. 2010, A&A, 517, A12
Pety, J., Goicoechea, J. R., Hily-Blant, P., Gerin, M., & Teyssier, D. 2007, A&A, 464, L41
Pickett, H. M., Poynter, R. L., Cohen, E. A., et al. 1998, J. Quant. Spec. Rad. Transf., 60, 883
Pontoppidan, K. M., Boogert, A. C. A., Fraser, H. J., et al. 2008, ApJ, 678, 1005
Pound, M. W., Reipurth, B., & Bally, J. 2003, AJ, 125, 2108
Rabli, D., & Flower, D. R. 2010, MNRAS, 406, 95
Requena-Torres, M. A., Martín-Pintado, J., Rodríguez-Franco, A., et al. 2006, A&A, 455, 971
Rodriguez-Fernandez, N., Pety, J., & Gueth, F. 2008, Single-dish observation and processing to produce the short-spacing information for a millimeter interferometer, Tech. Rep., IRAM Memo 2008-2
Sakai, N., Ceccarelli, C., Bottinelli, S., Sakai, T., & Yamamoto, S. 2012, ApJ, 754, 70
Sutton, E. C., Peng, R., Danchi, W. C., et al. 1995, ApJS, 97, 455
Tafalla, M., Santiago-García, J., Myers, P. C., et al. 2006, A&A, 455, 577
Tafalla, M., Santiago-García, J., Hacar, A., & Bachiller, R. 2010, A&A, 522, A91
Tielens, A. G. G. M., & Allamandola, L. J. 1987, in Interstellar Processes, eds. D. J. Hollenbach, & H. A. Thronson, Jr., Astrophys. Space Sci. Lib., 134, 397
Tielens, A. G. G. M., & Whittet, D. C. B. 1997, in IAU Symp. 178, ed. E. F. van Dishoeck, 45
van der Tak, F. F. S., Black, J. H., Schöier, F. L., Jansen, D. J., & van Dishoeck, E. F. 2007, A&A, 468, 627
Vinodkumar, M., Limbachiya, C., Barot, A., & Mason, N. 2013, Phys. Rev. A, 87, 012702
Watanabe, N., & Kouchi, A. 2002, ApJ, 571, L173
Watanabe, N., Nagaoka, A., Shiraki, T., & Kouchi, A. 2004, ApJ, 616, 638

Chapter 6

CH_3CN, CH_3NC and HC_3N

Of the $\sim$ 180 molecules detected in the ISM so far, nearly 20% of them contain nitrogen. Nitriles are particularly important for pre-biotic chemistry, as they are believed to be parent molecules of many of the amino acids (e.g., Hudson et al. 2008). The complex nitriles, methyl cyanide (CH_3CN) and cyanoacetylene (HC_3N), are the simplest of the organic nitriles found in the ISM. CH_3CN was first detected in the ISM by Solomon et al. (1971) towards the massive star forming regions Sagittarius A and B. Since then, CH_3CN has been detected in numerous different environments, such as comets (e.g., Remijan et al. 2008), hot-corino sources (e.g., Cazaux et al. 2003), hot-core sources (e.g., Bottinelli et al. 2004a; Araya et al. 2005; Purcell et al. 2006), ultracompact H II regions (Ginard et al. 2012) and in shocked gas (Codella et al. 2009). CH_3CN has also been detected in the nearby galaxies M82 and NGC 253 (Mauersberger et al. 1991). The methyl cyanide isomer, CH_3NC was first tentatively detected towards Sgr B2(OH) by Cernicharo et al. (1988). Its presence in the ISM was confirmed several years after when it was observed toward the high-mass star-forming region Sgr B2(N) (Remijan et al. 2005). HC_3N was detected for the first time towards Sagittarius B (Turner 1971). Since then, it has been detected in dense molecular clouds (Schloerb et al. 1983; Li & Goldsmith 2012), circumstellar envelopes (e.g., Pardo et al. 2004), comets (e.g., Bockelée-Morvan et al. 2000), hot cores (de Vicente et al. 2000) and in several nearby galaxies Lindberg et al. (2011).

CH_3CN is a prolate symmetric top, whose rotational energy levels are described by the total angular momentum, J, and its projection along the molecular symmetry axis, K. As described in the previous Chapter, selection rules dictate $\Delta K = 0$ for symmetric rotors, which means that different K–ladders are populated only trough collisions. In addition, a set of transitions from the same $J + 1 \rightarrow J$ levels but different K–ladders occur in a relatively narrow frequency range. These set of lines can therefore be observed simultaneously in a single setup, removing calibration uncertainties from the observations. For these reasons, CH_3CN is considered to be a good *thermometer* of the gas. Purcell et al. (2006) detected 3 mm lines of CH_3CN towards 58 candidate hot molecular cores on a sample of 82 methanol maser-selected star-forming regions. They detected CH_3CN in isolated methanol maser sites and found that CH_3CN is more prevalent and brighter when an ultracompact H II region is present. The inferred CH_3CN abundance cannot be accounted for by current gas-phase chemical models.

HC_3N is a linear molecule and the simplest carbon chain containing nitrogen, called cyanopolyyne molecules ($HC_{2n+1}N$; $n = 1, 2, 3$,etc). It is commonly used as a density probe in both galactic (e.g., Wyrowski et al. 2003) and extragalactic sources (e.g., Mauersberger et al. 1990). It has been proposed to be a good tracer of hot core regions, because it has several vibrational states in the range 300-1000 K, which are only excited if the gas is dense

and warm (de Vicente et al. 2000).

6.1 Formation of CH_3CN

6.1.1 Gas-phase chemistry

In the gas-phase, CH_3CN and CH_3NC are thought to be formed mainly by the radiative association of CH_3^+ and HCN/HNC

$$CH_3^+ + \text{HCN/HNC} \xrightarrow{k_1} H_4C_2N^+ + h\nu \tag{6.1}$$

followed by the dissociative recombination with electrons

$$H_4C_2N^+ + e^- \xrightarrow{k_2, k_2^t} CH_3CN/CH_3NC + H \tag{6.2}$$

(Huntress & Mitchell 1979; Bates 1983; Leung et al. 1984). In this last reaction, k_2 is the dissociation rate that leads to CH_3CN, while k_2^t is the total dissociation rate leading to CH_3CN, CH_3NC, and possibly other products. Another gas-phase formation route for CH_3CN is the radiative association of the CN and CH_3 radicals (Charnley et al. 1992). The main destruction path for CH_3CN in PDRs is photodissociation

$$CH_3CN + h\nu \xrightarrow{k_3} CH_3 + CN. \tag{6.3}$$

6.1.2 Grain surface chemistry

The large CH_3CN abundances found in hot cores (up to $\sim 10^{-7}$; Herbst & van Dishoeck 2009) cannot be explained by means of pure gas-phase chemistry (e.g., Olmi et al. 1996; Hatchell et al. 1998). Mackay (1999) proposed that these high abundances could be explained if the gas-phase precursors, CH_3^+ and HCN, are produced from evaporated methanol and ammonia ices, respectively.

CH_3CN could also be directly produced on the surface of dust grains, through reactions between CH_3 and CN (Garrod et al. 2008), and be released into the gas-phase through thermal or non-thermal desorption. Another possibility is that CH_3CN is produced by the photo-processing of ices. Danger et al. (2011) have studied the formation of CH_3CN by the UV photolysis of ethylamine ($CH_3CH_2NH_2$) ices. They determined that CH_3CN could be formed at 20 K with a yield of 4%.

However, CH_3CN ices have not been detected in the ISM so far. Observations with ISO suggest upper limits for the CH_3CN ice abundance of less than 10^{-6} relative to hydrogen nuclei (Gibb et al. 2000a; Herbst & van Dishoeck 2009).

6.2 Nitriles in the Horsehead nebula

We systematically searched for lines of CH_3CN, HC_3N, C_3N and some of their isomers in the Horsehead WHISPER line survey, with the aim of constraining the chemistry of nitriles.

6.2.1 Results

The main results of the work published in Gratier et al. (2013) are summarized next.

1. We detected the $J = 5 - 4$, $J = 6 - 5$, $J = 7 - 6$ and $J = 8 - 7$ ($K = 0, 1, 2, 3$ ladders for all lines) lines of CH_3CN towards the PDR. Only the $J = 5 - 4, K = 0, 1, 2, 3$ and $J = 6 - 5, K = 0, 1$ lines are detected towards the dense core. Due to the narrow linewidths ($0.6 - 0.8$ km s^{-1}) in the Horsehead, we are able to resolve the hyperfine splitting in the $J = 5 - 4, K = 2$, $J = 5 - 4, K = 3$ and $J = 6 - 5, K = 3$ lines.

2. We report the first clear detection at millimeter wavelengths of 3 CH_3NC lines towards the PDR position. The detected lines are the $J = 5 - 4, K = 0, 1, 3$. None of them are detected towards the dense core. The weighted average CH_3NC/CH_3CN integrated intensity ratio is 0.15 ± 0.02 at the PDR position.

3. We detected 4 HC_3N lines at both the PDR and dense core. These are the $J = 9 - 8$, $J = 10 - 9$, $J = 11 - 10$ and $J = 12 - 11$.

4. We detected 6 lines of C_3N at the PDR position.

5. CH_3CN and CH_3NC lines are brighter in the PDR than in the dense core. In contrast, HC_3N lines are slightly brighter in the dense core than in the PDR.

6. We used excitation and radiative transfer models to compute the column densities, and studied the importance of electron excitation for CH_3CN. We find that including the electron excitation reduced the derived CH_3CN column density by 40% at the PDR position. The inferred CH_3CN abundances are 2.5×10^{-10} in the PDR and 7.9×10^{-12} in the dense core. Therefore, CH_3CN is 30 times more abundant in the PDR than in the dense core. This result is surprising as CH_3CN is expected to be efficiently photo-dissociated in UV-illuminated regions. However, it is in agreement with the findings of Purcell et al. (2006), which show enhanced CH_3CN abundances towards ultracompact H II regions. In contrast to CH_3CN, HC_3N has a similar abundance in both positions ($\sim 8 \times 10^{-12}$).

7. As no collisional coefficients are available for CH_3NC, we used the same ones as for CH_3CN, and derive a CH_3NC/CH_3CN abundance ratio of 0.15 ± 0.12 in the PDR, and < 0.15 in the dense core. For C_3N, we assumed LTE and derive an abundance of 5×10^{-11} in the PDR and $< 1.5 \times 10^{-11}$ in the dense core.

8. A pure gas-phase chemical model predicts a CH_3CN abundance that is at least a few thousands times lower than what is inferred from the observations. We thus propose that the CH_3CN gas-phase abundance is enhanced when dust grain ice mantles are destroyed, by photo-desorption or thermal evaporation in PDRs, and by sputtering in shocks.

A&A 557, A101 (2013)
DOI: 10.1051/0004-6361/201321031

Astronomy & Astrophysics

The IRAM-30 m line survey of the Horsehead PDR

III. High abundance of complex (iso-)nitrile molecules in UV-illuminated gas⋆,⋆⋆

P. Gratier[1], J. Pety[1,2], V. Guzmán[1], M. Gerin[2], J. R. Goicoechea[3], E. Roueff[4], and A. Faure[5]

[1] Institut de Radioastronomie Millimétrique, 300 rue de la Piscine, 38406 Saint Martin d'Hères, France
e-mail: [gratier;pety]@iram.fr
[2] LERMA, UMR 8112, CNRS and Observatoire de Paris, 61 avenue de l'Observatoire, 75014 Paris, France
[3] Centro de Astrobiología, CSIC-INTA, Carretera de Ajalvir, Km 4, Torrejón de Ardoz, 28850 Madrid, Spain
[4] LUTH UMR 8102, CNRS and Observatoire de Paris, Place J. Janssen, 92195 Meudon Cedex, France
[5] UJF-Grenoble 1/CNRS-INSU, Institut de Planétologie et d'Astrophysique de Grenoble (IPAG) UMR 5274, 38041 Grenoble, France

Received 2 January 2013 / Accepted 7 May 2013

ABSTRACT

Context. Complex (iso-)nitrile molecules, such as CH_3CN and HC_3N, are relatively easily detected in our Galaxy and in other galaxies.
Aims. We aim at constraining their chemistry through observations of two positions in the Horsehead edge: the photo-dissociation region (PDR) and the dense, cold, and UV-shielded core just behind it.
Methods. We systematically searched for lines of CH_3CN, HC_3N, C_3N, and some of their isomers in our sensitive unbiased line survey at 3, 2, and 1 mm. We stacked the lines of C_3N to improve the detectability of this species. We derived column densities and abundances through Bayesian analysis using a large velocity gradient radiative transfer model.
Results. We report the first clear detection of CH_3NC at millimeter wavelength. We detected 17 lines of CH_3CN at the PDR and 6 at the dense core position, and we resolved its hyperfine structure for 3 lines. We detected 4 lines of HC_3N, and C_3N is clearly detected at the PDR position. We computed new electron collisional rate coefficients for CH_3CN, and we found that including electron excitation reduces the derived column density by 40% at the PDR position, where the electron density is 1–5 cm^{-3}. While CH_3CN is 30 times more abundant in the PDR (2.5×10^{-10}) than in the dense core (8×10^{-12}), HC_3N has similar abundance at both positions (8×10^{-12}). The isomeric ratio CH_3NC/CH_3CN is 0.15 ± 0.02.
Conclusions. The significant amount of complex (iso-)nitrile molecule in the UV illuminated gas is puzzling as the photodissociation is expected to be efficient. This is all the more surprising in the case of CH_3CN, which is 30 times more abundant in the PDR than in the dense core. In this case, pure gas phase chemistry cannot reproduce the amount of CH_3CN observed in the UV-illuminated gas. We propose that CH_3CN gas phase abundance is enhanced when ice mantles of grains are destroyed through photo-desorption or thermal-evaporation in PDRs, and through sputtering in shocks.

Key words. astrochemistry – ISM: clouds – ISM: molecules – ISM: individual objects: Horsehead – radiative transfer

1. Introduction

Complex nitriles like CH_3CN and HC_3N are easily detected in (massive) star-forming regions (Araya et al. 2005; Bottinelli et al. 2004; Purcell et al. 2006). CH_3CN and HC_3N were detected in the Mon R2 ultracompact H region (Ginard et al. 2012). Mauersberger et al. (1991) reported the first detection of CH_3CN in M 82 and NGC 253. Lindberg et al. (2011) detected HC_3N in 13 local universe galaxies. These molecules are often used to constrain the physical conditions of the host gas. In particular, CH_3CN is thought to be a good thermometer because it exhibits sets of metastable transitions, which are only coupled through collisions, but not radiatively (Guesten et al. 1985).

Moreover, CH_3CN is easily detected towards hot molecular cores (Olmi et al. 1996a,b; Hatchell et al. 1998; Purcell et al. 2006). In particular, Purcell et al. (2006) detect 3 mm lines of CH_3CN in 58 candidate hot molecular cores on a sample of 83 methanol maser-selected star-forming regions. They detect CH_3CN in isolated methanol maser sites and find that CH_3CN is more prevalent and brighter when an ultracompact H region is present, independent of the distance to the source. The inferred CH_3CN abundances are higher than can be accounted for by current pure gas phase chemical modeling (e.g. Olmi et al. 1996b; Hatchell et al. 1998). Mackay (1999) proposed that the CH_3CN abundance could be explained if the abundances of the gas phase precursors of CH_3CN, i.e. CH_3^+ and HCN, are enhanced by evaporation from grain ices and by further photo-processing of methanol and ammonia.

The mane of the Horsehead nebula is an ideal source to test the excitation and chemistry of nitriles. Indeed, it is viewed nearly edge-on (Abergel et al. 2003) at a distance of 400 pc (implying that 10″ correspond to 0.02 pc). It has a steep density gradient, from $n_H \sim 100\,cm^{-3}$ in the UV illuminated outer layers rising to $n_H \sim 2 \times 10^5\,cm^{-3}$ in less than 10″ (Habart et al. 2005). Gerin et al. (2009) show that the HCO emission delineates the UV illuminated edge of the nebula. Less than 40″ away from the HCO peak emission where the gas is warm ($T_{kin} \sim 60$ K), there

⋆ Based on observations obtained with the IRAM-30 m telescope. IRAM is supported by INSU/CNRS (France), MPG (Germany), and IGN (Spain).
⋆⋆ Appendices are available in electronic form at http://www.aanda.org

Table 1. Dipole moments for the observed species.

Species	Dipole moment (Debye)	Reference
CH_3CN	3.93	Gadhi et al. (1995)
CH_3NC	3.89	Cernicharo et al. (1988)
HC_3N	3.73	Deleon & Muenter (1985)
HC_2NC	2.93	Krüger et al. (1991)
C_3N	2.85	McCarthy et al. (1995)

is a UV-shielded, dense, and cold condensation ($T_{\rm kin} \leq 20$ K), where HCO^+ is highly deuterated (Pety et al. 2007). For simplicity, the HCO and DCO^+ emission peaks are hereafter referred to as the PDR and dense core positions. The moderate illumination ($\chi \sim 60$ Abergel et al. 2003; Draine 1978) translates into dust temperatures low enough that thermal evaporation of complex molecules is negligible. In the Horsehead nebula one can thus isolate photo-desorption effects for complex molecules like formaldehyde, which can form on the grain ice mantles before being photo-desorbed into gas phase, as was shown by Guzmán et al. (2011).

In this work, we report the detection of CH_3CN, CH_3NC, HC_3N, and C_3N in the PDR and/or the dense core positions of the Horsehead edge. Determining the isomeric abundance ratio is an important tool for constraining the chemical routes to form the molecules. Indeed, the observed column density ratios often differ significantly from the ones expected by the energies of the molecules at thermodynamic equilibrium. One such example related to the CH_3CN/CH_3NC ratio is the ratio between HNC and HCN which is found in the interstellar medium to be close to 1 (Sarrasin et al. 2010; Mendes et al. 2012), even though HNC is less stable than HCN by 0.5 eV. This gives constraints on the mechanisms of formation and destruction of these species. We thus also searched for emission of CH_3NC and HC_2NC. Table 1 shows that all these species have similar dipole moments.

Section 2 presents the observations and the spectroscopy of the observed molecules. Section 3 summarizes the observed line properties. Section 4 explains how the column densities are computed and it presents the inferred abundances. The implications of these results for the chemistry of CH_3CN and HC_3N are discussed in Sect. 5. Appendix A summarizes the line properties (integrated intensity, line width, systemic velocity) for observed lines and derived upper limits for undetected lines. Appendix B details the Bayesian approach used to infer the abundances from the line brightnesses. Finally, Appendix C discusses the shortcoming of the rotational diagram method in the subthermal excitation conditions found in the PDR position. Larger versions of Figs. 3 and 4 are presented in Appendix D.

2. Observations and spectroscopy

After a short description of the Horsehead WHISPER unbiased line survey, this section presents the spectroscopy of the different molecules studied here, including their hyperfine structure.

2.1. Horsehead WHISPER: an unbiased line survey

The data[1] presented in this paper are extracted from the Horsehead Wideband High-resolution Iram-30 m Surveys at two Positions with Emir Receivers (WHISPER project, PI: J. Pety), an unbiased line survey of the 3, 2 and 1 mm band, which is currently completed with the IRAM-30 m telescope. This project was observed in 2011 and 2012. Two positions are observed: 1) the HCO peak that is characteristics of the photo-dissociation region at the surface of the Horsehead nebula (Gerin et al. 2009); and 2) the DCO^+ peak that belongs to the nearby cold dense core at high visual extinction (Pety et al. 2007). The combination of the new EMIR receivers and the Fourier Transform Spectrometers yield a spectral survey with unprecedented bandwidth (36 GHz at 3 mm, 34 GHz at 2 mm, and 76 GHz at 1 mm), spectral resolution (49 kHz at 3 and 2 mm and 195 kHz at 1 mm, this corresponds a velocity resolution between 0.1 and 0.3 km s^{-1}), and sensitivity (median noises of 8.0 mK, 18.5 mK, and 8.3 mK respectively). This allowed us to detect ~150 lines from ~30 species and their isotopologues. Each sky frequency was observed with two different frequency tunings. The Horsehead PDR and dense core positions (see Fig. 1) were alternatively observed every 15 minutes in position switching mode with a common fixed off position (offset: $-100''$, $0''$ from RA = $05^h40^m54.27^s$, Dec = $-02°28'00''$). The total observing time amounted to one hour per frequency setup and position. This observing strategy allows us to remove potential ghost lines resulting from the incomplete attenuation of strong spectral features in the image side band (the typical rejection of the EMIR sideband separating mixers is 13dB or a factor 20). A detailed presentation of the observing strategy and data reduction process will be given in another paper. Table 2 summarizes the beamwidths and noise levels for the frequency ranges of the survey corresponding to the lines discussed in this paper.

Table 2. Observation parameters for the observed lines.

Molecule	Transition	Frequency (GHz)	HPBW ($''$)	rms (mK [$T_{\rm mb}$])
CH_3CN	$J = 5$–4 $K = 0, 4^\dagger$	91.972	26.9	5.8
	$J = 6$–5 $K = 0, 5^\dagger$	110.356	22.4	9.8
	$J = 7$–6 $K = 0, 6^\dagger$	128.734	19.2	21.8
	$J = 8$–7 $K = 0, 7^\dagger$	147.105	16.8	20.9
CH_3NC	$J = 5$–4 $K = 0, 4^\dagger$	100.508	24.6	8.2
HC_3N	$J = 9$–$8^\dagger$	81.881	30.2	19.1
	$J = 10$–9	90.979	27.2	5.4
	$J = 11$–10	100.076	24.7	8.7
	$J = 12$–11	109.173	22.7	11.0
HC_2NC	$J = 9$–8	89.419	27.7	5.4
	$J = 10$–9	99.354	24.9	7.1
	$J = 11$–10	109.289	22.6	9.3
HNC_3	$J = 9$–8	84.028	29.4	6.0
	$J = 10$–9	93.364	26.5	5.0
	$J = 11$–10	102.700	24.1	8.1
	$J = 12$–11	112.036	22.1	10.7
C_3N	$N = 9$–$8^\dagger$	89.054	27.8	6.3
	$N = 10$–$9^\dagger$	98.949	25.0	8.3
	$N = 11$–$10^\dagger$	108.843	22.7	11.4

Notes. $^{(\dagger)}$ The quoted frequencies are characteristic values for the multiplet frequencies. The exact frequencies for each line are given in Tables A.1 to A.6.

2.2. CH_3CN and CH_3NC: two symmetric top species

2.2.1. Energy diagrams

Figure 2 displays the CH_3CN energy diagram. The CH_3NC energy diagram has a similar structure. Indeed, as prolate

[1] Published WHISPER data are available on the project website: http://www.iram.fr/~horsehead/

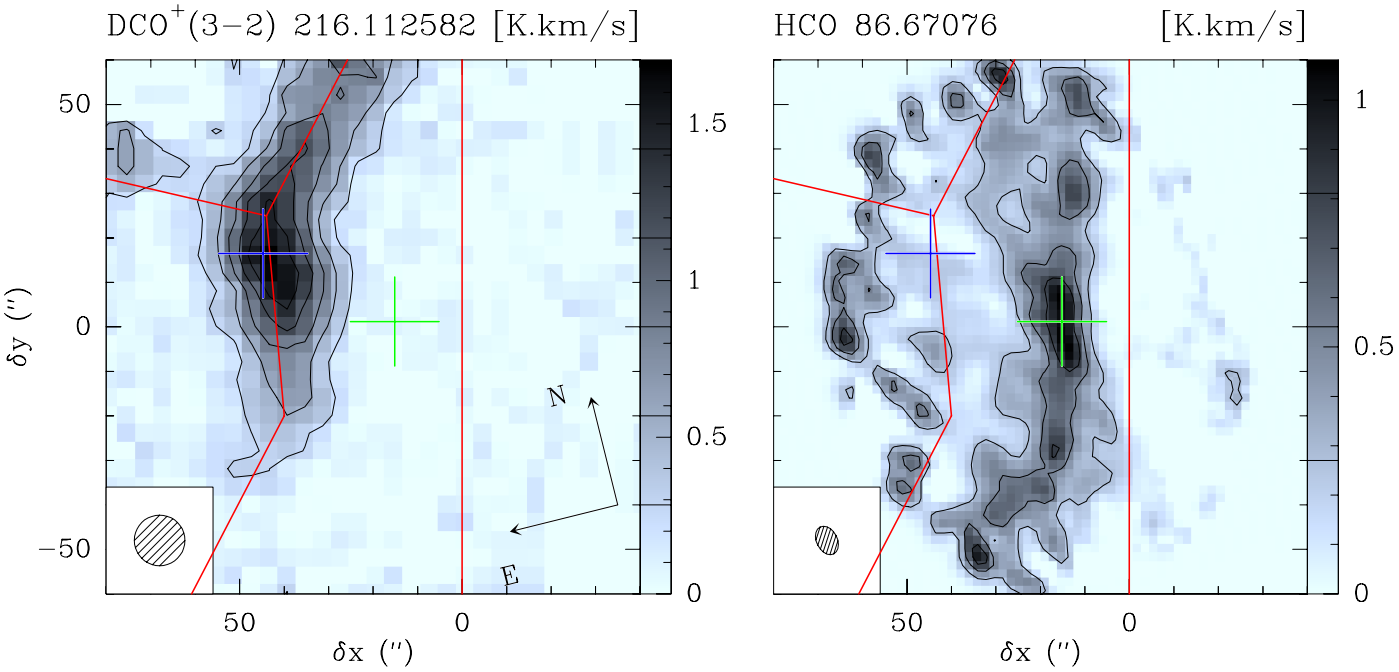

Fig. 1. Overview of the Horsehead mane photodissociation region showing the two observed positions. *Left*: DCO^+ map (Pety et al. 2007), *right*: HCO emission map (Gerin et al. 2009). In both maps, The HCO emission peak (PDR position) at RA = $05^h40^m53.9^s$, Dec = −02°28′00″ is shown with a green cross, and the DCO^+ emission peak (dense core position) at RA = $05^h40^m55.7^s$, Dec = −02°28′22″ with a blue one. The maps have been rotated 14 degree anti clockwise around the position RA = $05^h40^m54.27^s$, Dec = −02°28′00″ and shifted 20″ to the east to align the PDR front (vertical red line) with the horizontal 0 offset of the map.

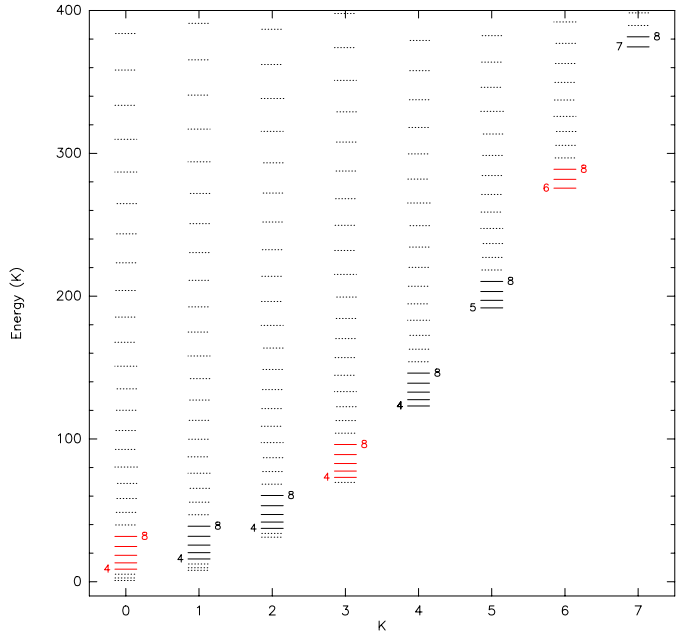

Fig. 2. CH_3CN energy diagram of levels which contribute to the $J = 5 \rightarrow 4$, $J = 6 \rightarrow 5$, $J = 7 \rightarrow 6$, and $J = 8 \rightarrow 7$ transitions in the 3 and 2 mm frequency ranges, i.e. for K levels from 0 to 7 and J levels from 4 to 8, other levels are displayed in dotted line. The E ($K = 3n \pm 1$) and A ($K = 3n$) states are displayed in black and red, respectively.

symmetric top molecules, their rotational energy ($E_{J,K}$) is derived (Gordy & Cook 1984) from the moments of inertia and angular momentum through

$$\frac{E_{J,K}}{h} = B_e J(J+1) + (A_e - B_e)K^2 - D_K K^4 - D_J J^2(J+1)^2 - D_{J,K} J(J+1)K^2,$$

where 1) the J and K quantum numbers describe respectively the total angular momentum and its projection along the molecule symmetry axis; 2) A_e and B_e are the rotational constants, characteristics of the moments of inertia along and perpendicular to the symmetry axes; and 3) the D_J, D_K and $D_{J,K}$ are the centrifugal stretching constants. As a symmetric top, the degeneracy on the symmetry axis is removed, giving a splitting of each rotational J level into doubly degenerate K components, with $K = 0, \ldots, J$ (except when $K = 0$).

2.2.2. Transitions

Using the rules for allowed rotational transitions (Gordy & Cook 1984)

$$\Delta K = 0 \text{ and } \Delta J = \pm 1, \quad (1)$$

the frequencies of a (J,K) transition can then be derived as

$$\nu_{(J+1 \rightarrow J, K \rightarrow K)} = 2B_e(J+1) - 4D_J(J+1)^3 - 2D_{J,K}(J+1)K^2.$$

A set of ($J + 1 \rightarrow J$, K = const.) lines is named a J-ladder, and a set of (J = const., $K + 1 \rightarrow K$) lines is named a K-ladder.

For a given J, the probed energy range is mainly determined by $(A_e - B_e)K^2$ (a first order effect), while the frequencies are separated by $2D_{J,K}(J+1)K^2$ (a second order effect due to the centrifugal distortion). Hence, each J-ladder can be observed simultaneously in a relatively narrow frequency band, while they probe a wide range of energies, typically from 10 to a few 100 K. This is why the excitation of symmetric top molecules are good thermometers when the lines are thermalized.

2.3. HC_3N, HC_2NC, HNC_3 and C_3N: four rigid rotors

HC_3N, HC_2NC and HNC_3 are linear species with a $^1\Sigma^+$ electronic state. Their spectroscopy is thus much simpler than

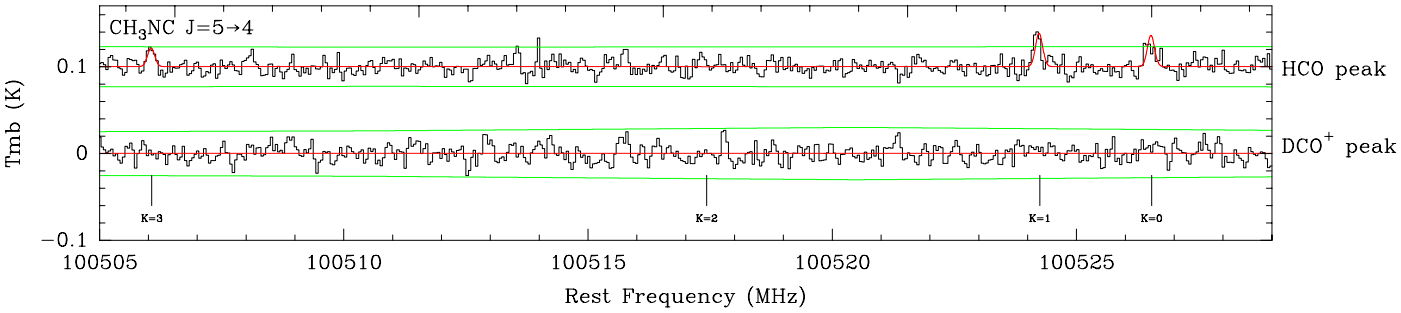

Fig. 3. Spectrum of the CH_3NC 3 mm detected lines at the HCO peak (i.e., the PDR position, top spectrum) and the DCO^+ peak (i.e., inside the cold dense core, bottom spectrum), the spectrum towards the HCO peak has been shifted vertically by 0.1 K for clarity. The panel displays the K set of lines for the given ΔJ set of lines. The frequencies corresponding to each transitions are displayed as vertical bars. The best fit model is overplotted in red. The green horizontal lines display the $\pm 3\sigma$ significance levels.

the symmetric top ones. Their rotational spectrum is well described by the rigid rotor approximation with lines separated by 9.1 GHz, 9.9 GHz, 9.3 GHz respectively. HC_2NC and HNC_3 are isomers of HC_3N, which can also be described as rigid rotors. C_3N has a more complex $^2\Sigma$ ground state electronic structure, which exhibits doublets of nearby frequencies.

2.4. Hyperfine splitting

All of the observed N species exhibit a hyperfine structure, although that of the ^{15}N species are not resolved due to the small magnetic dipole coupling term. The NC isomers have lower hyperfine splitting values than the CN isomers. This comes from the fact that the electric field gradient, which creates the hyperfine splitting through interaction with the nuclear electric quadrupole moment of ^{14}N, is stronger for outermost N positions. This is well known for HCN and HNC (see Bechtel et al. 2006).

As the Horsehead PDR is seen edge-on, the lines are narrow with typical full width at half maximum values of 0.6−0.8 km s^{-1}. This enables us to resolve the hyperfine splitting when it is large enough. In the case of symmetric top molecules, the hyperfine splitting increases with increasing K levels and decreasing J level. In practice, the hyperfine splitting is resolved only for the ($J = 5 \rightarrow 4$, $K = 2$), ($J = 5 \rightarrow 4$, $K = 3$), and ($J = 6 \rightarrow 5$, $K = 3$) lines of CH_3CN in our observations (see Fig. 4).

We wish to estimate the correct integrated intensities for each ($\Delta J, K$) line even though hyperfine components can be blended. To do this, we fitted together multiple Gaussian profiles over all of the hyperfine levels for each ($\Delta J = 1, K = $ cst) transition. In this global fit, we fixed 1) the relative intensities of the hyperfine levels to the optically thin values and 2) the frequency offsets of all the lines to the CDMS catalog values (Müller et al. 2005). There remains $J + 2$ free parameters, namely a global linewidth, a global velocity shift and a multiplicative amplitude factor for each of the hyperfine set of lines in the ($\Delta J = 1, K = $ const.), with $K = 0, ..., J - 1$. The integrated intensity of each ($\Delta J, K$) transition is then obtained by summing the integrated intensities of the individual Gaussian functions fitted to the hyperfine structure. This method is only correct for optically thin lines. Section 4.2.1 shows that this is case for the spectral lines we analyze in this paper.

3. Observational results

3.1. First clear detection of CH_3NC in the millimeter domain

Figure 3 shows the 3 lines of CH_3NC detected in the Horsehead PDR. They belong to the 5 lines of the $J = 5-4$ K-ladder of CH_3NC. None of them were detected in the UV-shielded dense core. As the hyperfine splitting is not resolved for any of these lines, we simultaneously fitted a single Gaussian profile at each frequency found in the JPL database (Pickett et al. 1998). Moreover, we required a common linewidth for the different lines. The fit results are displayed in Table A.1. The line intensity modeling carried out in Sect. 4 predicts line intensities for the other CH_3NC lines in the 1, 2 and 3 mm bands well below our detection limit.

This is the first clear detection of this molecule in the millimeter domain. A detection of the $J = 1-0$ line of CH_3NC at centimeter wavelengths (i.e., 20.1 GHz) has been reported by Irvine & Schloerb (1984) in TMC-1 and Remijan et al. (2005) in SgrB2. At millimeter wavelengths, Cernicharo et al. (1988) reported a tentative detection of the $J = 4-3$, $J = 5-4$ and $J = 7-6$ lines in SgrB2 but the large linewidths (20 km s^{-1} FWHM) and contamination from numerous other lines prevented a robust identification.

3.2. CH_3CN lines are brighter in the PDR than in the dense core

In our line survey, four $J+1 \rightarrow J$ K-ladders are detected: the $J = 5 \rightarrow 4$, $J = 6 \rightarrow 5$ K-ladders in the 3 mm atmospheric window at 91.9 GHz and 110.3 GHz respectively and, the $J = 7 \rightarrow 6$ and $J = 8 \rightarrow 7$ K-ladders in the 2 mm window at 128.7 GHz and 147.1 GHz. Figure 4 displays the 17 and 6 detected lines at the PDR and dense core positions, respectively. Lines from the additional 5 $J + 1 \rightarrow J$ K-ladders (from $J = 11-10$ to $J = 15-14$), whose wavelengths lie at 1mm, remain undetected in our survey. The corresponding noise levels for these undetected lines are 15–30 mK per 200 kHz channel.

The derived line properties are synthesized in Table A.2. Not only are there many more detected lines of CH_3CN in the PDR than in the dense core, but the detected lines are also brighter in the less dense, UV-illuminated PDR position. Moreover, when the lines are detected in both environment, they systematically show a narrower linewidth in the PDR than in the core.

3.3. CH_3NC/CH_3CN isomeric line ratios

The value of the ratios of the CH_3NC/CH_3CN integrated intensities for the $J = 5-4$ K-ladder are given in Table 3 for both the PDR and dense core positions. The weighted average line ratio is 0.15 ± 0.02 at the PDR position. The individual ratios exhibit a small scatter around this value.

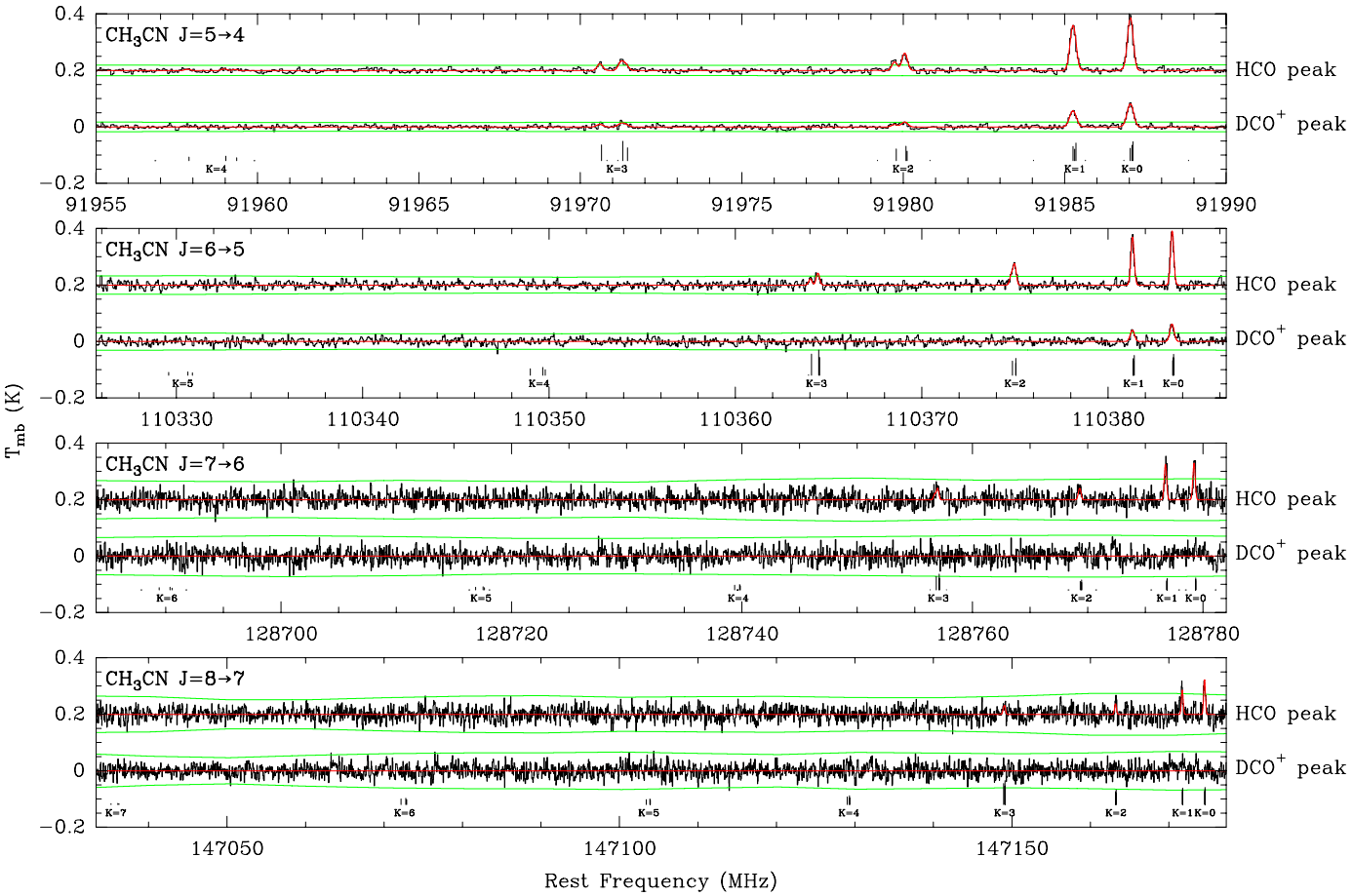

Fig. 4. Spectrum of the CH_3CN 3 mm and 2 mm detected lines at the HCO peak (i.e., the PDR position, top spectrum of each panel) and the DCO^+ peak (i.e., inside the cold dense core, bottom spectrum of each panel), each spectrum towards the HCO peak has been shifted vertically by 0.2 K for clarity. The panel displays the K set of lines for a given ΔJ set of lines. The frequencies corresponding to each transitions are displayed as vertical bars, whose heights indicate their relative hyperfine intensities in the optically thin regime applicable to these observations. The best fit model is overplotted in red. The green horizontal lines display the $\pm 3\sigma$ significance levels.

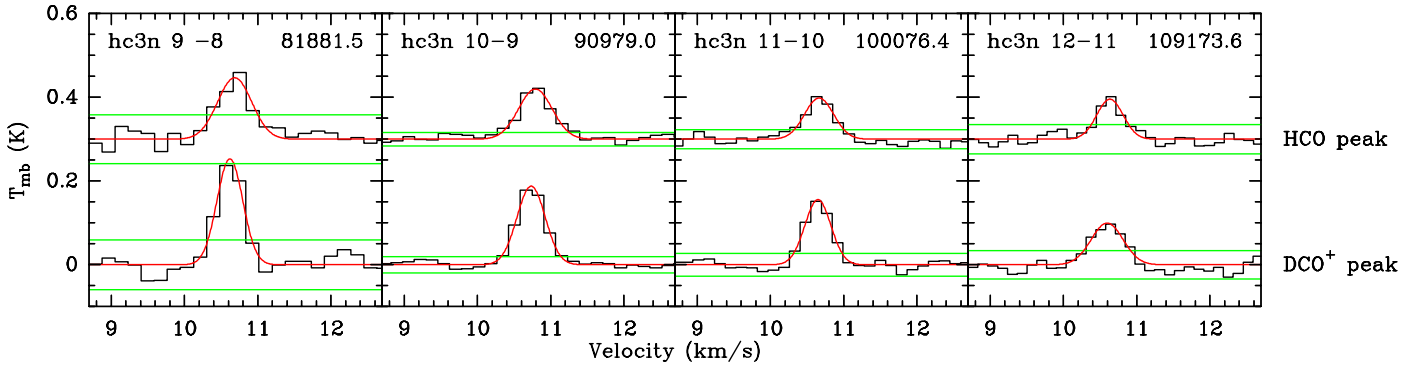

Fig. 5. Spectrum of the HC_3N 3 mm lines at the HCO peak (i.e., the PDR position, top spectrum of each panel) and the DCO^+ peak (i.e., inside the cold dense core, bottom spectrum of each panel), each spectrum towards the HCO peak has been shifted vertically by 0.3 K for clarity.

3.4. HC_3N lines have similar brigthnesses in the PDR and the dense core

Four HC_3N lines lie in the 3 mm, 2 in the 2 mm and 8 in the 1 mm band we have observed. All four 3 mm lines of HC_3N are detected at both observed positions, no detection were obtained at 2 and 1 mm. Independent Gaussian profiles were fitted for each detected line. Figure 5 displays the HC_3N lines, which are detected in our survey and Table A.3 summarizes the fit results. In contrast with the results for CH_3CN, HC_3N lines are slightly more luminous in the UV-shielded dense core.

HC_2NC has three lines in the 3 mm band. None of these are detected in any of the two observed positions. HNC_3 has four lines in the 3 mm band, none of them are detected. Table A.5 gives the derived upper limits for both species. Stacking with the method presented in Sect. 3.5 did not reveal any detection. For reference, HC_2NC and HNC_3 have both been detected in dark

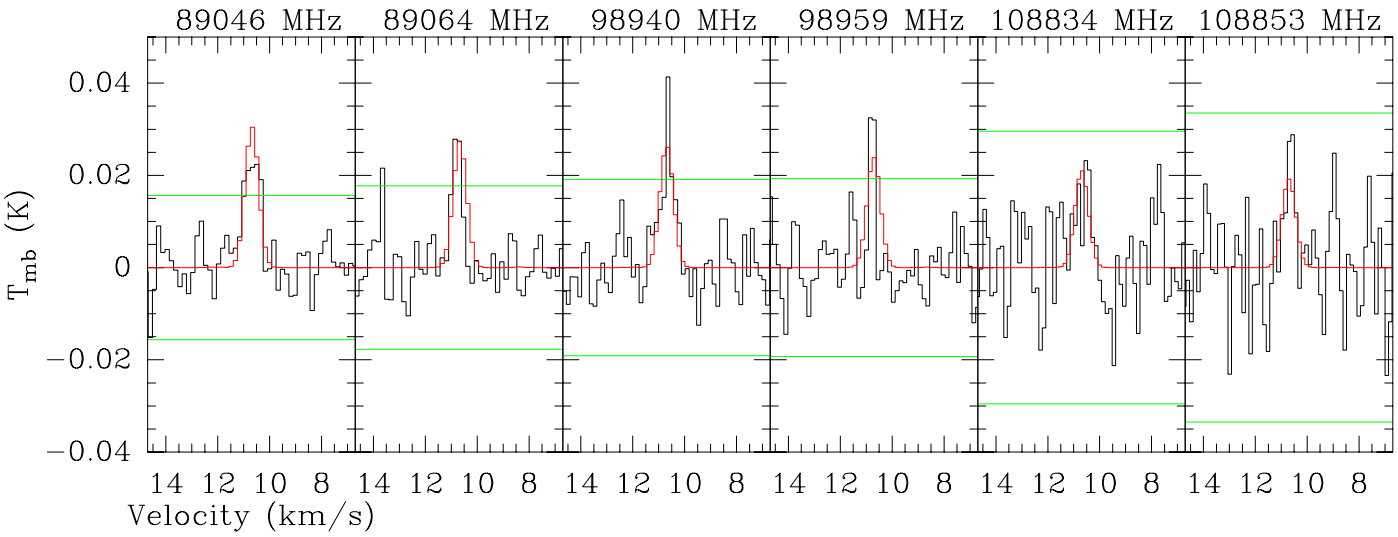

Fig. 6. Observed spectra (*black line*) of the three 3 mm C_3N doublets at the PDR peak. The green horizontal lines are the $\pm 3\sigma$ levels. The red spectrum is the LTE model for a $6'' \times 50''$ filament centered at the PDR positions, a 10 K excitation temperature, and a column density of 2×10^{12} cm^{-2}.

Table 3. CH_3NC/CH_3CN line ratio for different K levels of $J = 5{-}4$.

Line	HCO peak	DCO^+ peak
$K = 0$	0.12 ± 0.02	<0.17
$K = 1$	0.16 ± 0.02	<0.24
$K = 2$	<0.14	<0.57
$K = 3$	0.23 ± 0.05	<0.54
$K = 4$	<1	<1.2

clouds (Kawaguchi et al. 1992a,b), while only HC_2NC has been detected in circumstellar envelopes (Gensheimer 1997).

3.5. C_3N is twice as bright in the PDR than in the dense core

Because of its $^2\Sigma$ ground state electronic structure, and of the hyperfine splitting due to the Nitrogen atom, the energy radiated by C_3N is spread over a large number of lines. This implies that individual lines of C_3N are less easily detected than, e.g., that of CH_3CN in the same conditions of noise. We thus have coadded the spectral regions where individual lines from C_3N were expected to show up. This method can be applied to any species expected to present a rich spectrum with numerous weak spectral lines of similar intensity.

Using the list of transitions observable in our survey from public catalogs, we averaged the intensities of each potential line after 1) aligning each spectral window to the same LSR velocity, and 2) resampling each line spectrum to the same velocity resolution. In this process, we reject all partss of the original spectrum which could be contaminated by a line from another already detected species. We first tried a simple noise-weighted average, i.e.,

$$S(v) = \frac{\sum_i \frac{T_i(v)}{\sigma_i^2}}{\sum_i \frac{1}{\sigma_i^2}}, \tag{2}$$

where v is the velocity, $T_i(v)$, and σ_i the brightness temperature and noise of the ith transition, and $S(v)$ the stacked spectra. This is however a too simple approach because the searched species have complex hyperfine structures with expected line intensities which vary over several orders of magnitude. Hence, the signal can easily be drowned in noise. It is thus important to also weight the different lines according to their expected integrated intensities, W_i,

$$S(v) = \frac{\sum_i \frac{W_i}{\sigma_i^2} T_i(v)}{\sum_i \frac{W_i}{\sigma_i^2}} = \frac{\sum_i \frac{w_i}{\sigma_i^2} T_i(v)}{\sum_i \frac{w_i}{\sigma_i^2}} \quad \text{with} \quad w_i = \frac{W_i}{\Sigma W_i}. \tag{3}$$

The relative integrated intensities, w_i, are computed with a simple local thermodynamic equilibrium (LTE) approach. In the optically thin regime, only the excitation temperature fixes the w_i, because the normalization cancels the contribution of the total column density.

We explored a range of excitation temperatures and we kept the stacked spectra corresponding to the highest derived peak temperature. This strategy was checked against a spectrum simulated with a LTE code, assuming a typical excitation temperature of 10 K, consistent with our previous studies of complex molecules in the Horsehead edge, which showed that they are subthermally excited (Guzmán et al. 2011; Pety et al. 2012). The proposed strategy recovered the right excitation temperature.

There are 7+4+3 C_3N doublets in the 1, 2, and 3 mm bands, each one split by hyperfine interaction into a total of 211 lines. Observationally, this results into six marginal detections (i.e., a peak signal-to-noise ratio (S/N) lower or close to 3) at the PDR position (see Fig. 6).

Figure 7 shows 1) the distribution of C_3N line brightnesses modeled assuming optically thin LTE emission with $T_{ex} = 10$ K, and 2) the C_3N spectra obtained by stacking the 383 mm lines at the PDR and dense core position. The contributions from all 173 lines at 1 mm and 2 mm is negligible in our case, as none of them are brighter than 20% of the brightest 3 mm band line. Including the 1 mm and 2 mm lines would have reduced the spectral resolution of the stacked spectrum as individual spectra must first be resampled to the coarsest velocity resolution (0.282 km s^{-1}).

C_3N is twice as bright in the PDR than in the dense core. The brightest C_3N line corresponds to a telescope half primary beam width of 27.7″, the proportion of the line intensity observed towards the dense core that arises from beam pickup from the PDR position is less than 8%. The remaining emission could

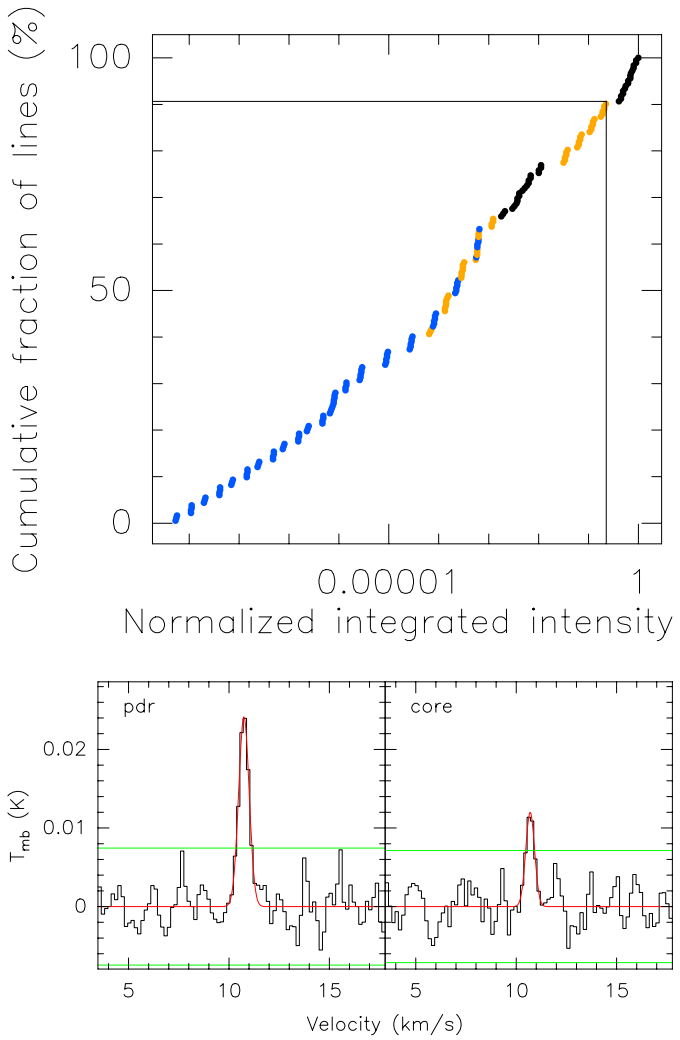

Fig. 7. *Top*: cumulative distribution function of computed integrated intensities for C_3N in the optically thin LTE regime with T_{ex} = 10 K, and normalized to the intensity of the brightest line. Only 10% of all the 1, 2 and 3 mm lines have intensities brighter than a fifth of the brightest line. The transitions are color coded by bands, black: 3mm, orange: 2 mm, blue: 1 mm. *Bottom* C_3N spectra resulting from the stacking of 38 individual lines at 3 mm. The stacked spectra are shown both for the PDR and dense core positions. The red curve is a gaussian fit to the stacked spectra, the green lines are $\pm 3\sigma$ levels.

arise in the lower density skin of the dense core, already detected in HCO (Gerin et al. 2009) and CF^+ (Guzmán et al. 2012a,b).

4. Column densities and abundances

4.1. Tools

4.1.1. Local thermodynamic equilibrium vs. escape probability radiative transfer

Detailed excitation and radiative transfer calculations are needed to estimate the line intensities of interstellar species from the source physical properties (gas density, temperature and source size) and the species column density. The inverse problem of deriving physical conditions and column densities for observed line intensities needs assumptions. For instance, the rotation diagram analysis can be used when the populations of the energy levels are in LTE (see Goldsmith & Langer 1999, for a detailed description of non LTE and optical thickness effects on the rotational diagram method). The critical densities for the methylcyanide lines are typically 10^5–10^6 cm^{-3}, while the typical gas density and temperatures are 6×10^4 cm^{-3} and 60 K in the Horsehead PDR, and 1×10^5 cm^{-3} and 25 K in the dense core.

The lines detected in the Horsehead are thus subthermally excited. In this case, both collisional and radiative (de)excitation must be taken into account. For instance, escape probability methods (Sobolev 1960; Castor 1970; Goldreich & Kwan 1974) correctly treat the radiative transfer micro-physics. However, they suppose the presence of a large velocity gradient so that photons escape their local environment, i.e., radiative transfer is only local. RADEX (van der Tak et al. 2007) is one such method. We use it here and we compare the results with those obtained in LTE.

4.1.2. Hydrogen vs. electron excitation

In order to correctly treat the micro-physics, radiative transfer methods need collisional (de)excitation coefficients as inputs. In general, only collisions with the most abundant gas species, i.e. ortho and para H_2 and helium, are taken into account. However, excitation by electrons are expected to play a significant role when the electron fraction reaches $[e^-] = n_e/n_{H_2} \sim 10^{-5}$–$10^{-4}$. The importance of the collisional exception with these two families of partners are similar when $n_eC_e \sim n_{H_2}C_{H_2}$. While collisional coefficients with neutral are typically 10^{-11}–10^{-10} cm^3 s^{-1}, those with electrons are around 10^{-6}. Goicoechea et al. (2009) determined an electron fraction of 10^{-4} at the PDR position, implying that electrons contribute significantly to the excitation. In contrast, the same study derived an electron fraction of a few 10^{-9} in the dense core, where the electron excitation is thus negligible.

We have computed the CH_3CN-e^- and HC_3N-e^- collisional coefficients within the dipolar Born approximation (e.g. Itikawa 1971). Owing to the large dipole of both species (3.73 D for HC_3N and 3.92 D for CH_3CN), dipole-allowed cross sections are indeed expected to be dominant and entirely determined by the long-range electron-dipole interaction (see e.g. Faure et al. 2007). In this approximation, cross sections are proportional to line strengths (and the square of the dipole) and therefore strictly obey the dipolar selection rule (see Eq. (1)). Line strengths and dipoles were taken from the CDMS catalog (Müller et al. 2005). Excitation cross sections were computed in the energy range 0.1 meV–1 eV and rate coefficients were deduced in the range 10–1000 K, for the lowest 251 levels of CH_3CN (238 transitions) and the lowest 31 levels of HC_3N (30 transitions). The CH_3CN–e^- and HC_3N–e^- collisional rates are available online through the BASECOL[2] database.

4.1.3. Beam dilution

Beam dilution arises when the source does not fill the beam. In our observations, the half primary beam width of the IRAM-30 m varies from 30″ at the low end of the 3 mm band to 10″ at the high end of 1 mm band. Moreover, a PDR lies by definition at the interface between fully ionized and molecular gas. Previous PDR modeling of the Horsehead edge implies that the physical and chemical typical angular scales ranges from 1 to 50″. It thus is likely that the beam dilution will affect the line luminosities and then the derivation of column densities. Beam dilution can be more easily disentangled from excitation effects when several lines of different energy levels and critical densities

[2] http://basecol.obspm.fr

Table 4. Quantitative informations of the distribution functions used as priors in the Bayesian fitting.

Parameter	Type	HCO peak	DCO^+ peak
$\log_{10} n_{H_2}$	normal	4.8 ± 0.2^a	5.0 ± 0.2^a
T_K	normal	60 ± 10^b	25 ± 10^c
$\log_{10} N$	uniform	[9, 17]	[9, 17]
beam dilution	uniform	[0, 1]	[0, 1]

References. [(a)] Habart et al. (2005); [(b)] Pety et al. (2005); [(c)] Goicoechea et al. (2006).

Table 5. Beam dilution for CH_3CN determined from the radiative transfer modeling.

Species	Line	Resolution ($''$)	Dilution (2σ confidence interval) PDR	dense core
CH_3CN	$J = 5$–4	26.9	[0.19–0.31]	[0.65–1.00]
	$J = 6$–5	22.4	[0.31–0.45]	[0.52–0.88]
	$J = 7$–6	19.2	[0.49–0.63]	–
	$J = 8$–7	16.8	[0.82–1.00]	–

happen at close by frequencies so that the beam dilution is identical for these lines. However, we cannot derive source properties below the lowest measured angular resolution without an a priori analytical model of the source spatial distribution. The derived column densities are thus beam-averaged to the lowest observed angular resolution i.e. 16.8″ for CH_3CN and 22.7″ for HC_3N. A beam dilution factor is applied to transistions corresponding to a larger beam. The derived column densities will then be lower limits, because lower beam filling factors translate to higher column densities.

4.1.4. The Bayesian framework

In the case of subthermal excitation and optically thin lines, the main parameters controlling the line intensities (gas density, column density, temperature, beam dilution) cannot be independently retrieved without additional information. As stated in Sect. 1, our previous studies of the Horsehead edge implies a knowledge of the H_2 gas density and the gas temperature for each observed position.

We wish to combine these previously known information about the source with the observed line shapes in order to determine robust estimates of the column densities. The formulation of the inverse problem in the Bayesian framework is the best way to reach our goal. The principles of Bayesian inference can be found in (Press et al. 1992; Feigelson & Jogesh Babu 2012), and a technical description is available in Appendix B. In short, the information on the source physical properties is taken into account by defining informative priors, i.e. peaked distributions of the parameters. In our case, we use standard normal and lognormal distributions respectively for the temperature and density parameters. Lognormal laws allow us to span several orders of magnitude for, e.g. the density.

We have no a priori information for the column densities and the beam dilution. In the Bayesian framework, we used "uninformative" distributions (named Jeffreys prior), i.e. uniform distributions in a given plausible parameter range. RADEX has hard coded limits of 5 and 25 for $\log_{10} N$. It is safe to use a smaller interval for the considered species in the Horsehead case. The chosen statistical law for the column density was thus taken as a uniform distribution of the logarithm of the column density with 9 and 17 as boundaries. For the beam dilution, we chose a uniform distribution between 0 and 1. Table 4 summarizes the quantitative information characterizing the used distributions.

4.2. Derived results

4.2.1. CH_3CN abundance, beam dilution and line opacities

We used the collisional coefficients from Green (1986). These coefficients were computed for collisions with He and scaled to H_2. They are computed for 251 levels (31 375 coefficients) with upper level energies up to 1150 K. We restricted our computation to the first 185 levels (16 650 coefficients) up to upper level energies of 580 K in order to limit the computation time. We then checked that using the full set of coefficients for the best fit parameters yields the same integrated intensities.

The main remaining uncertainty is the quality of the used collisional rate as the potential energy surface and the dynamical method employed by Green (1986) were approximate. The rate coefficients of Green (1986), computed for Helium in the infinite sudden order (IOS) approximation, and then scaled by a factor $\sqrt{\mu_{CH_3CN-H_2}/\mu_{CH_3CN-He}} = 1.38$ to obtain the value for H_2 are expected to be lower than the actual H_2 rate coefficients by up to an order of magnitude. We thus checked the sensitivity of these results to the variation of the collisional rate coefficients by multiplying them by one order of magnitude. The absolute abundances varies by less than a factor 3 and the abundance ratio between the PDR and the dense core positions varies by at most 50%. Both results are thus robust.

As the hyperfine structure of some CH_3CN lines were resolved, there are two independent ways to measure the line opacities. The first one explicitly fits the hyperfine structure using the GILDAS HFS fitting method[3]. In our observations, the ($J = 5$–$4, K = 2$) set of hyperfine lines at the PDR position features the best compromise between signal-to-noise ratio and separation of the hyperfine components to enable a meaningful fit. The derived opacity is $\tau = 1.3 \pm 1.1$. The low opacity of CH_3CN is consistent with the non-detection of $^{13}CH_3CN$ and $CH_3^{13}CN$. The second method is based on opacities modeled by RADEX. For the same line, the derived opacity is 0.22 ± 0.05. None of the lines modeled by RADEX have opacities higher than 0.6 (see Fig. B.2). Given the large uncertainties of the HFS method in the estimate of the line opacities, this value is not taken into account in the analysis. Nevertheless, from the radiative transfer analysis, we derive that the CH_3CN lines are optically thin.

The beam filling factors for CH_3CN are summarized in Table 5. At the PDR position, the beam dilution factors are compatible with a source structure that is small (<10″) in only one dimension. In the dense core, only the two lower frequency lines are detected and the beam dilutions have similar values, larger than 0.5, implying the emission is more extended than at the PDR position.

The best fit results, which take the excitation by collision with electrons into account, are summarized in Table 6. The associated CH_3CN column densities for the PDR and core positions, are $N_{CH_3CN} = (6–15) \times 10^{12}$ cm^{-2} and $N_{CH_3CN} = (3–8) \times 10^{11}$ cm^{-2}, respectively these values correspond to the smallest observed beam for each molecule. This translates into abundances of $(2–4) \times 10^{-10}$ for the HCO peak and $(5–12) \times 10^{-12}$

[3] The HFS fitting method is described in the documentation of the GILDAS/CLASS software at http://www.iram.fr/IRAMFR/GILDAS

Table 6. Best fit parameters for the radiative transfer modeling.

Position	Species	Smallest observed beam ($''$)	$\log_{10} N_{H_{tot}}$ (cm^{-2})	$[e^-] = n_e/n_{H_2}$	T_K (K)	$\log_{10} n_{H_2}$ (cm^{-3})	$\log_{10} N$ (cm^{-2})	$\log_{10} X^a$
HCO peak	CH_3CN	16.8	22.6	0	43 ± 1	4.3 ± 0.1	13.2 ± 0.2	-9.4 ± 0.2
	CH_3CN	16.8	22.6	10^{-4}	45 ± 2	4.3 ± 0.3	13.0 ± 0.2	-9.6 ± 0.2
	HC_3N	22.7	22.6	0	60 ± 11	4.7 ± 0.2	11.5 ± 0.1	-11.1 ± 0.1
	HC_3N	22.7	22.6	10^{-4}	58 ± 11	4.6 ± 0.2	11.4 ± 0.1	-11.2 ± 0.1
DCO^+ peak	CH_3CN	16.8	22.8	0	33 ± 3	5.0 ± 0.2	11.7 ± 0.2	-11.1 ± 0.2
	HC_3N	22.7	22.8	0	30 ± 6	4.8 ± 0.2	11.7 ± 0.2	-11.1 ± 0.2

Notes. The left hand side of the table corresponds to fixed parameters, and the right hand side to computed values. $^{(a)}$ $X = \frac{N(X)}{N(H)+2N(H_2)}$.

for the DCO^+ peak. CH_3CN *is therefore 30 times more abundant in the PDR than in the dense core.*

4.2.2. CH_3NC abundances and CH_3NC/CH_3CN isomeric ratio

Only 3 CH_3NC lines are detected at the HCO peak and none at the DCO^+ peak. Including the beam dilution factors, more than 3 unknowns must be constrained forbidding a complete modeling of the physical parameters of the source without additional a priori assumptions. In addition to the same prior on the gas density and temperature as for CH_3CN, we assumed that the two molecules are cospatial, which translates into identical beam dilutions. In addition, we do not know about any computation of the CH_3NC collisional coefficients. We thus used the CH_3CN ones.

With these hypotheses, we derived a column density of $N_{CH_3NC} = (6\text{–}25) \times 10^{11}$ cm^{-2} at the PDR position and $N_{CH_3NC} \leq 5 \times 10^{11}$ cm^{-2} as the 2 sigma upper limit in the dense core.

The CH_3NC/CH_3CN abundance ratio is 0.15 ± 0.02 and <0.15 at the PDR and the dense core position, respectively. This value is similar to the ratio of the integrated intensities. This points towards optically thin lines.

4.2.3. HC_3N and HC_2NC abundances and isomeric ratio

We used the collisional coefficients computed by Wernli et al. (2007) for para-H_2 and Faure et al. (in prep.) for ortho-H_2. The derived critical densities for collisions of HC_3N with H_2 are 4×10^5–1×10^6 cm^{-3}. In this modeling, we used the standard RADEX prescription, i.e. the determination of the ortho-H_2/para-H_2 from the gas kinetic temperature (0.01 and 0.52 for $T_{kin} = 25$ and 60 K, respectively).

However, we checked that using a fixed ortho-H_2/para-H_2 ratio of 3 does not influence the results above the derived uncertainties.

For HC_3N, all 4 lines were detected at 3 mm at both positions, while neither the 2 lines at 2 mm nor the 8 lines at 1 mm were detected. The derived column densities and abundances of HC_3N are similar at the PDR and dense core positions with values of $(1\text{–}5) \times 10^{11}$ cm^{-2} and $(5\text{–}12) \times 10^{-12}$, respectively.

For HC_2NC, none of the millimetric lines were detected in either of the observed positions. Assuming the same priors on the gas temperature and density and cospatial emission of HC_2NC and HC_3N, the derived 2 sigma upper limits of the column densities of HC_2NC are $N_{HC_2NC} \leq 2 \times 10^{10}$ cm^{-2} at both position positions.

Since the opacities of all observed lines are low for HC_3N, the abundance ratio is similar to the observed intensity ratio.

Table 7. Column density and abundances for C_3N.

Position	Column density (cm^{-2})	Abundance
PDR	$(2 \pm 1) \times 10^{12}$	$(5 \pm 2.5) \times 10^{-11}$
Core	$<1 \times 10^{12}$	$<1.5 \times 10^{-11}$

The 2 sigma upper limit for the HC_2NC/HC_3N abundance ratio thus is 0.1.

4.2.4. C_3N abundance

Three doublets of C_3N are marginally detected at the PDR position in the 3 mm band. As the collision rates for C_3N are not available, we used the `CLASS/WEEDS` (Maret et al. 2011) LTE engine to model these lines. Based on previous experience (Guzmán et al. 2012a; Pety et al. 2012), we used an excitation temperature of 10 K, and a source structure corresponding to a $6'' \times 50''$ filament centered on the PDR position. This yields a column density of $(2 \pm 1) \times 10^{12}$ cm^{-3} at the PDR position, i.e., an abundance of $(5 \pm 2.5) \times 10^{-11}$. No individual line of C_3N is detected at the dense core position, even though stacking yields a 5σ detection. We thus report an 2σ upper limit on the column density at the dense core position of 1×10^{12} cm^{-3}, i.e., a 2σ upper limit on the abundance of 1.5×10^{-11}.

4.3. Comments

4.3.1. H_2H_2 vs. electron excitation

Table 6 compare the best fit parameters obtained either without electron excitation or with a fixed electron fraction of 10^{-4} as derived for the PDR position by Goicoechea et al. (2009). Including electron excitation reduces the derived column density by 40% for CH_3CN, but by less than the uncertainty on the column density (i.e., ≤25%) for HC_3N. This difference between the two molecules is due to a higher critical densities of CH_3CN lines (~10^6 cm^{-3}) compared to those of HC_3N (~10^5 cm^{-3}).

4.3.2. Shortcomings of rotational diagrams in the case of CH_3CN

CH_3CN is a relatively complex species. It is often assumed to exist only in dense environments where it is thermalized. In such environments, rotational diagrams (Goldsmith & Langer 1999) are then the tool of choice to derive the column density of CH_3CN. However, we find that CH_3CN is brighter and much more abundant in UV-illuminated relatively low density gas than in the UV-shielded dense core. In Appendix C, we discuss the

use of rotational diagrams in the case of moderately subthermal excitation such as in the PDR position. The determination of the column density through the use of a rotational diagram would have been underestimated by a factor 6 to 33, depending on the observed K-ladder, at the PDR position compared to the escape probability computations. The density being higher at the dense core position, the rotational diagram yield the same column density as the escape probability method.

5. Discussion

Even when taking the excitation by electrons into account, which is significant in the UV-illuminated gas, CH_3CN is 30 times more abundant in the PDR (2.5×10^{-10}) than in the UV-shielded dense core (8×10^{-12}). In contrast, HC_3N has similar abundance at both positions (8×10^{-12}), while C_3N is only abundant in the PDR (5×10^{-11}). In this section, we discuss the chemistry of CH_3CN and the values of the isomeric ratios.

5.1. CH_3CN and CH_3NC chemistry

The major gas phase route to CH_3CN and CH_3NC is thought to be a radiative association (Huntress & Mitchell 1979; Bates 1983; Leung et al. 1984)

$$CH_3^+ + HCN/HNC \rightleftharpoons C_2H_4N^{+\star} \rightarrow C_2H_4N^+ + h\nu, \quad (4)$$

with a reaction constant k_{ra}, followed by the ion-electron dissociative recombination reaction

$$C_2H_4N^+ + e^- \rightarrow CH_3CN/CH_3NC + H. \quad (5)$$

The main destruction route in presence of UV illumination is

$$CH_3CN + h\nu \rightarrow CH_3 + CN. \quad (6)$$

In this simplified view, the abundance of CH_3CN is given by

$$\frac{d[CH_3CN]}{dt} = k_e\, n_e\, [C_2H_4N^+] - \chi\, \kappa_{diss}\, [CH_3CN], \quad (7)$$

where the rate of the dissociative recombination to CH_3CN (Vigren et al. 2008)

$$k_e = 1.5 \times 10^{-7} \left(\frac{T}{300}\right)^{-0.5} \text{cm}^3\,\text{s}^{-1}, \quad (8)$$

the photodissociation rate (van Dishoeck et al. 2006) is

$$\kappa_{diss} = 1.56 \times 10^{-9}\,\text{s}^{-1}\ \exp(-\gamma A_v) \quad \text{with} \quad \gamma = 1.95, \quad (9)$$

and χ is the UV illumination at the PDR edge. The abundance of $C_2H_4N^+$ is given by

$$\frac{d[C_2H_4N^+]}{dt} = k_{ra}\, n_{CH_3^+}\, [HCN] - k_e^{tot}\, n_e\, [C_2H_4N^+], \quad (10)$$

where the value of the radiative association rate is typically $2 \times 10^{-8}\,\text{cm}^{-3}\,\text{s}^{-1}$ at 50 K (Bates 1983), and k_e^{tot} is the total rate of the dissociative recombination to CH_3CN, CH_3NC, and possibly other products. The steady-state solution is

$$[CH_3CN] = \frac{k_e}{k_e^{tot}} \frac{k_{ra}\, n_{CH_3^+}\, [HCN]}{\chi\, \kappa_{diss}}. \quad (11)$$

The UV illumination for the Horsehead PDR is $\chi \sim 60$ (Abergel et al. 2003; Draine 1978). Using the known density profile, we derive a visual extinction of $A_v \sim 2$ mag (see Fig. 4 Guzmán et al. 2012a). At the PDR position, the (pure gas phase) Meudon PDR code indicates that [HCN] $\sim 10^{-9}$, and $n_{CH_3^+} \sim 10^{-5}\,\text{cm}^{-3}$. With these normalizing factors, we deduce

$$[CH_3CN] = 10^{-13} \left[\frac{k_e}{k_e^{tot}} \frac{k_{ra}}{2 \times 10^{-8}} \frac{n_{CH_3^+}\, [HCN]}{10^{-14}} \frac{1.21}{\chi\, \exp(-\gamma A_v)}\right]. \quad (12)$$

So the predicted abundance of CH_3CN is $\sim 10^{-13}$ at the PDR position. This is an upper limit as $k_e \leq k_e^{tot}$. As the measured abundance of CH_3CN is ~2400 times larger than this predicted abundance, this route does not seem efficient enough to produce the observed amount of CH_3CN at the PDR position.

A potential alternative to pure gas phase chemistry is the formation of CH_3CN on ices through ice photo-processing followed by photo-desorption in the UV-illuminated part of the Horsehead edge. Danger et al. (2011) have studied the formation of CH_3CN by the UV photolysis of ethylamine ($CH_3CH_3NH_2$) ices. They determined that methyl cyanide could be formed at 20 K with a yield of 4%. Photo-desorption of small molecules like H_2CO (Guzmán et al. 2011; Noble et al. 2012) is efficient even at low grain temperatures (20 K) where thermal desorption is absent. Larger molecules created on the ices have higher photo-desorption thresholds and would stay on the grains.

CH_3CN has also been observed in shocks (e.g. L1157-B1 Arce et al. 2008; Codella et al. 2009). In this case, sputtering of grains by impacting gas evaporates the CH_3CN formed in ices. However, high abundances of CH_3CN is not a specific tracer of shock, as shown by the example of the Horsehead PDR.

5.2. Isomeric ratios

5.2.1. CH_3NC/CH_3CN

Defrees et al. (1985) argued that the CH_3NC/CH_3CN isomeric ratio depends on the isomerisation equilibrium which happens when the $C_2H_4N^{+\star}$ unstable molecule or "complex" radiatively loses its energy, provided that the dissociative recombination does not modify the molecule backbone. From consideration on the energies of the different isomers of $C_2H_4N^+$, they deduced an CH_3NC/CH_3CN isomeric ratio in the 0.1–0.4 range, i.e. very different from the typical HCN/HNC isomeric ratio value of 1 found in the interstellar medium (Sarrasin et al. 2010; Mendes et al. 2012).

From their tentative detection of the $J = 4 \rightarrow 3$, $J = 5 \rightarrow 4$, and $J = 7 \rightarrow 6$ lines of CH_3NC in Sgr B2, Cernicharo et al. (1988) found a CH_3NC/CH_3CN abundance ratio of ≃0.05. Also in Sgr B2, Remijan et al. (2005) deduced an even smaller CH_3NC/CH_3CN abundance ratio of 0.02 ± 0.02 from their detection of the CH_3CN and CH_3NC $J = 1 \rightarrow 0$ lines. The value we derive for this abundance ratio in the Horsehead PDR is 0.15 ± 0.02, i.e. 2–5 times higher than these previous results. Our value falls directly in the range (0.1–0.4) predicted by Defrees et al. (1985).

5.2.2. HC_2NC/HC_3N

HC_2NC was first detected in TMC-1 by Kawaguchi et al. (1992a), they find a HC_2NC/HC_3N abundance ratio of 0.02–0.05. In CRL618 (a circumstellar envelope affected by strong UV fields from the central star) Pardo & Cernicharo (2007) derive an abundance ratio of 0.025–0.03. Our derived upper limit for this abundance ratio is compatible with these results.

6. Summary

While CH_3CN is a complex nitrile molecule (more than 6 atoms), its lines are brighter in the PDR than in the dense core. Its linewidths are also narrower in the PDR than in the dense core. Due to the lower density at the PDR position, the lines are subthermally excited, implying that a rotational diagram analysis underestimates the column density by a factor 6−33 depending on the observed K-ladder. In other words, bright CH_3CN lines do not necessarily imply high densities ($n_H \gtrsim 10^6$ cm^{-3}) and LTE.

Large velocity gradient radiative transfer methods implies that CH_3CN is 30 times more abundant in the UV illuminated gas than in the UV shielded dense core. The overabundance of CH_3CN in the PDR compared to the dense core position is surprising because the photodissociation of this complex molecule is expected to be efficient. A simple pure gas phase chemical model underestimates the abundance of CH_3CN in the PDR by a factor of at least a few thousand. We propose that CH_3CN gas phase abundance is enhanced when ice mantles of grains are destroyed (photo-desorption or thermal-evaporation in PDRs, sputtering in shocks).

We also report the first clear detection of 4 CH_3NC lines in the millimeter bands at the PDR position. The CH_3NC/CH_3CN isomeric ratio of 0.15 is compatible with the theoretical range of 0.1−0.4 from Defrees et al. (1985).

In sharp contrast to CH_3CN and its isomer, HC_3N lines are stronger in the dense core than in the PDR. The HC_3N abundance is similar at both positions. No lines of its isomer HC_2NC were detected in either position. The pure gas phase chemistry of HC_3N is more complex than the CH_3CN one, requiring a detail chemical modeling to understand these results.

Acknowledgements. This work has been funded by the grant ANR-09-BLAN-0231-01 from the French *Agence Nationale de la Recherche* as part of the SCHISM project (http://schism.ens.fr/). J.R.G. thanks the Spanish MINECO for funding support through grants AYA2009-07304 and CSD2009-00038. J.R.G. is supported by a Ramón y Cajal research contract from the MINECO. V.G. acknowledges support from the Chilean Government through the Becas Chile scholarship program.

References

Abergel, A., Teyssier, D., Bernard, J. P., et al. 2003, A&A, 410, 577
Araya, E., Hofner, P., Kurtz, S., Bronfman, L., & DeDeo, S. 2005, ApJS, 157, 279
Arce, H. G., Santiago-García, J., Jørgensen, J. K., Tafalla, M., & Bachiller, R. 2008, ApJ, 681, L21
Bates, D. R. 1983, ApJ, 270, 564
Bauer, A., & Bogey, M. 1970, C. R. Acad. Sc. Ser. B, 271, 892
Bechtel, H. A., Steeves, A. H., & Field, R. W. 2006, ApJ, 649, L53
Bottinelli, S., Ceccarelli, C., Lefloch, B., et al. 2004, ApJ, 615, 354
Castor, J. I. 1970, MNRAS, 149, 111
Cernicharo, J., Kahane, C., Guelin, M., & Gomez-Gonzalez, J. 1988, A&A, 189, L1
Codella, C., Benedettini, M., Beltrán, M. T., et al. 2009, A&A, 507, L25
Danger, G., Bossa, J.-B., de Marcellus, P., et al. 2011, A&A, 525, A30
Defrees, D. J., McLean, A. D., & Herbst, E. 1985, ApJ, 293, 236
Deleon, R. L., & Muenter, J. S. 1985, J. Chem. Phys., 82, 1702
Draine, B. T. 1978, ApJS, 36, 595
Faure, A., Varambhia, H. N., Stoecklin, T., & Tennyson, J. 2007, MNRAS, 382, 840
Feigelson, E. D., & Jogesh Babu, G. 2012, Modern Statistical Methods for Astronomy (Cambridge: Cambridge University Press)
Foreman-Mackey, D., Hogg, D. W., Lang, D., & Goodman, J. 2013, PASP, 125, 306
Gadhi, J., Lahrouni, A., Legrand, J., & Demaison, J. 1995, J. Chim. Phys., 92, 1984
Gensheimer, P. D. 1997, ApJ, 479, L75
Gerin, M., Goicoechea, J. R., Pety, J., & Hily-Blant, P. 2009, A&A, 494, 977
Ginard, D., González-García, M., Fuente, A., et al. 2012, A&A, 543, A27
Goicoechea, J. R., Pety, J., Gerin, M., et al. 2006, A&A, 456, 565
Goicoechea, J. R., Pety, J., Gerin, M., Hily-Blant, P., & Le Bourlot, J. 2009, A&A, 498, 771
Goldreich, P., & Kwan, J. 1974, ApJ, 189, 441
Goldsmith, P. F., & Langer, W. D. 1999, ApJ, 517, 209
Goodman, J., & Weare, J. 2010, Commun. Appl. Math. Comput. Sci., 5
Gordy, W., & Cook, R. 1984, Microwave molecular spectra, Techniques of chemistry (Wiley)
Gottlieb, C. A., Gottlieb, E. W., Thaddeus, P., & Kawamura, H. 1983, ApJ, 275, 916
Green, S. 1986, ApJ, 309, 331
Guarnieri, A., Hinze, R., Krüger, M., & Zerbe-Foese, H. 1992, J. Mol. Spect. 156, 39
Guesten, R., Walmsley, C. M., Ungerechts, H., & Churchwell, E. 1985, A&A, 142, 381
Guzmán, V., Pety, J., Goicoechea, J. R., Gerin, M., & Roueff, E. 2011, A&A, 534, A49
Guzmán, V., Pety, J., Gratier, P., et al. 2012a, A&A, 543, L1
Guzmán, V., Roueff, E., Gauss, J., et al. 2012b, A&A, 548, A94
Habart, E., Abergel, A., Walmsley, C. M., Teyssier, D., & Pety, J. 2005, A&A, 437, 177
Hatchell, J., Thompson, M. A., Millar, T. J., & MacDonald, G. H. 1998, A&A, 133, 29
Hirahara, Y., Ohshima, Y., & Endo, Y. 1993, ApJ, 403, L83
Huntress, Jr., W. T., & Mitchell, G. F. 1979, ApJ, 231, 456
Irvine, W. M., & Schloerb, F. P. 1984, ApJ, 282, 516
Itikawa, Y. 1971, J. Phys. Soc. Japan, 30, 835
Kawaguchi, K., Ohishi, M., Ishikawa, S.-I., & Kaifu, N. 1992a, ApJ, 386, L51
Kawaguchi, K., Takano, S., Ohishi, M., et al. 1992b, ApJ, 396, L49
Krüger, M., Dreizler, H., Preugschat, D., & Lentz, D. 1991, Angewandte Chemie International Edition in English, 30, 1644
Leung, C. M., Herbst, E., & Huebner, W. F. 1984, ApJS, 56, 231
Lindberg, J. E., Aalto, S., Costagliola, F., et al. 2011, A&A, 527, A150
Mackay, D. D. S. 1999, MNRAS, 304, 61
Maret, S., Hily-Blant, P., Pety, J., Bardeau, S., & Reynier, E. 2011, A&A, 526, A47
Mauersberger, R., Henkel, C., Walmsley, C. M., Sage, L. J., & Wiklind, T. 1991, A&A, 247, 307
McCarthy, M. C., Gottlieb, C. A., Thaddeus, P., Horn, M., & Botschwina, P. 1995, J. Chem. Phys., 103, 7820
Mendes, M. B., Buhr, H., Berg, M. H., et al. 2012, ApJ, 746, L8
Müller, H. S. P., Schlöder, F., Stutzki, J., & Winnewisser, G. 2005, J. Mol. Struct., 742, 215
Müller, H. S. P., Drouin, B. J., & Pearson, J. C. 2009, A&A, 506, 1487
Noble, J. A., Theule, P., Mispelaer, F., et al. 2012, A&A, 543, A5
Olmi, L., Cesaroni, R., Neri, R., & Walmsley, C. M. 1996a, A&A, 315, 565
Olmi, L., Cesaroni, R., & Walmsley, C. M. 1996b, A&A, 307, 599
Pardo, J. R., & Cernicharo, J. 2007, ApJ, 654, 978
Pety, J., Teyssier, D., Fossé, D., et al. 2005, A&A, 435, 885
Pety, J., Goicoechea, J. R., Hily-Blant, P., Gerin, M., & Teyssier, D. 2007, A&A, 464, L41
Pety, J., Gratier, P., Guzmán, V., et al. 2012, A&A, 548, A68
Pickett, H. M., Poynter, R. L., Cohen, E. A., et al. 1998, J. Quant. Spec. Radiat. Transf., 60, 883
Press, W. H., Teukolsky, S. A., Vetterling, W. T., & Flannery, B. P. 1992, Numerical recipes in FORTRAN. The art of scientific computing
Purcell, C. R., Balasubramanyam, R., Burton, M. G., et al. 2006, MNRAS, 367, 553
Remijan, A. J., Hollis, J. M., Lovas, F. J., Plusquellic, D. F., & Jewell, P. R. 2005, ApJ, 632, 333
Sarrasin, E., Abdallah, D. B., Wernli, M., et al. 2010, MNRAS, 404, 518
Schöier, F. L., van der Tak, F. F. S., van Dishoeck, E. F., & Black, J. H. 2005, A&A, 432, 369
Sobolev, V. V. 1960, Moving envelopes of stars (Harvard University Press)
Thorwirth, S., Müller, H. S. P., & Winnewisser, G. 2000, J. Mol. Spectrosc., 204, 133
van der Tak, F. F. S., Black, J. H., Schöier, F. L., Jansen, D. J., & van Dishoeck, E. F. 2007, A&A, 468, 627
van Dishoeck, E. F., Jonkheid, B., & van Hemert, M. C. 2006, Faraday Discuss., 133, 231
Vigren, E., Kaminska, M., Hamberg, M., et al. 2008, Phys. Chem. Chem. Phys., 10, 4014
Wernli, M., Wiesenfeld, L., Faure, A., & Valiron, P. 2007, A&A, 464, 1147

Pages 12 to 19 are available in the electronic edition of the journal at http://www.aanda.org

Appendix A: Observational tables

This section gathers the observational fit obtained for all the lines studied in this paper. The line parameters are taken from the CDMS (Müller et al. 2005) for CH_3CN, HC_3N and C_3N, and from the JPL (Pickett et al. 1998) for CH_3NC, HC_2NC and HNC_3. Original spectroscopic data come from Müller et al. (2009) for CH_3CN, Thorwirth et al. (2000) for HC_3N, Gottlieb et al. (1983) for C_3N, Bauer & Bogey (1970) for CH_3NC, Guarnieri et al. (1992) for HC_2NC, and Hirahara et al. (1993) for HNC_3. The accuracy is excellent for CH_3CN, HC_3N, HC_2NC and C_3N and moderate for CH_3NC (~0.09 MHz or 0.27 km s^{-1} at 100 GHz), and HNC_3 (~0.12 MHz or 0.42 km s^{-1} at 84 GHz).

Table A.1. Line properties for CH_3NC in Tmb.

Line	Frequency (GHz)	E_u (K)	g_u	A_u (s^{-1})	I (mK[T_{mb}] km s^{-1})		V_{LSR} (km s^{-1})		ΔV (km s^{-1})	
					HCO peak	DCO^+ peak	HCO peak	DCO^+ peak	HCO peak	DCO^+ peak
J = 5–4 K = 4	100.490163	127.4	22	2.92(−5)	<9	<12	10.71 ± 0.026	...	0.50 ± 0.06	...
J = 5–4 K = 3	100.506072	78.0	44	5.20(−5)	12.1 ± 2.5	<12				
J = 5–4 K = 2	100.517433	42.7	22	6.83(−5)	<9	<12				
J = 5–4 K = 1	100.524249	21.5	22	7.81(−5)	20.1 ± 2.3	<12				
J = 5–4 K = 0	100.526541	14.5	22	8.13(−5)	16.5 ± 2.4	<12				

Notes. Upper limits at the 95% (2 sigma) level assuming a 0.7 km s^{-1} FWHM.

Table A.2. Observed line properties for CH_3CN.

Line	Frequency (GHz)	E_u (K)	g_u	A_u (s^{-1})	I (mK[T_{mb}] km s^{-1})		V_{LSR} (km s^{-1})		ΔV (km s^{-1})	
					HCO peak	DCO^+ peak	HCO peak	DCO^+ peak	HCO peak	DCO^+ peak
J = 5–4 K = 4	91.958726	127.5	22	2.30(−5)	9.0 ± 6.8	<10	10.72 ± 0.02	10.72 ± 0.02	0.64 ± 0.01	0.74 ± 0.03
J = 5–4 K = 3	91.971130	77.5	44	4.10(−5)	52.3 ± 3.3	22.1 ± 3.5				
J = 5–4 K = 2	91.979994	41.8	22	5.30(−5)	65.8 ± 2.9	20.7 ± 3.1				
J = 5–4 K = 1	91.985314	20.4	22	6.10(−5)	125.7 ± 2.1	49.7 ± 2.6				
J = 5–4 K = 0	91.987088	13.2	22	6.30(−5)	140.1 ± 2.3	68.7 ± 2.4				
J = 6–5 K = 5	110.330345	197.1	26	3.40(−5)	<12	<16	10.70 ± 0.02	10.72 ± 0.03	0.55 ± 0.02	0.71 ± 0.07
J = 6–5 K = 4	110.349470	132.8	26	6.20(−5)	<12	<16				
J = 6–5 K = 3	110.364354	82.8	52	8.30(−5)	38.4 ± 4.4	<16				
J = 6–5 K = 2	110.374989	47.1	26	9.90(−5)	60.8 ± 3.9	<16				
J = 6–5 K = 1	110.381372	25.7	26	1.08(−4)	106.4 ± 3.8	29.4 ± 3.9				
J = 6–5 K = 0	110.383500	18.5	26	1.11(−4)	116.7 ± 3.8	47.7 ± 4.6				
J = 7–6 K = 6	128.690111	281.8	120	4.70(−5)	<28	<34	10.69 ± 0.02	...	0.58 ± 0.01	...
J = 7–6 K = 5	128.717359	203.3	60	8.70(−5)	<28	<34		...		...
J = 7–6 K = 4	128.739669	139.0	60	1.20(−4)	<28	<34		...		...
J = 7–6 K = 3	128.757030	89.0	120	1.46(−4)	37.2 ± 9.2	<34		...		...
J = 7–6 K = 2	128.769436	53.3	60	1.64(−4)	26.9 ± 8.2	<34		...		...
J = 7–6 K = 1	128.776882	31.9	60	1.75(−4)	78.4 ± 5.5	<34		...		...
J = 7–6 K = 0	128.779364	24.7	60	1.78(−4)	81.4 ± 5.7	<34		...		...
J = 8–7 K = 7	147.035835	381.6	34	6.30(−5)	<24	<31	10.66 ± 0.02	...	0.54 ± 0.05	...
J = 8–7 K = 6	147.072602	288.8	68	1.17(−4)	<24	<31		...		...
J = 8–7 K = 5	147.103738	210.3	34	1.63(−4)	<24	<31		...		...
J = 8–7 K = 4	147.129230	146.1	34	2.01(−4)	<24	<31		...		...
J = 8–7 K = 3	147.149068	96.1	68	2.31(−4)	21.1 ± 7.9	<31		...		...
J = 8–7 K = 2	147.163244	60.4	34	2.52(−4)	23.2 ± 6.6	<31		...		...
J = 8–7 K = 1	147.171752	38.9	34	2.64(−4)	50.5 ± 6.8	<31		...		...
J = 8–7 K = 0	147.174588	31.8	34	2.69(−4)	70.8 ± 6.1	<31		...		...

Notes. Upper limits at the 95% (2 sigma) level assuming a 0.7 km s^{-1} FWHM.

Table A.3. Line properties for HC_3N in Tmb.

Line	Frequency (GHz)	E_u (K)	g_u	A_u (s^{-1})	I (mK[T_{mb}] km s^{-1})		V_{LSR} (km s^{-1})		ΔV (km s^{-1})	
					HCO peak	DCO^+ peak	HCO peak	DCO^+ peak	HCO peak	DCO^+ peak
J = 9–8	81.881468	19.7	17	4.2(−5)	86.9 ± 8.3	113.7 ± 7.0	10.69 ± 0.026	10.62 ± 0.014	0.562 ± 0.066	0.440 ± 0.030
J = 10–9	90.979023	24.0	19	5.8(−5)	65.6 ± 4.0	95.3 ± 3.2	10.78 ± 0.013	10.73 ± 0.008	0.474 ± 0.037	0.456 ± 0.017
J = 11–10	100.076392	28.8	21	7.8(−5)	49.6 ± 3.3	69.8 ± 4.0	10.66 ± 0.016	10.65 ± 0.012	0.474 ± 0.038	0.419 ± 0.027
J = 12–11	109.173634	34.1	23	1.0(−4)	43.2 ± 4.5	55.1 ± 4.1	10.64 ± 0.021	10.60 ± 0.019	0.429 ± 0.059	0.514 ± 0.040

Table A.4. Stacked line properties for C_3N.

Position	V_{LSR} (km s^{-1})	ΔV (km s^{-1})	S/N
HCO peak	10.73 ± 0.02	0.629 ± 0.055	10.0
DCO^+ peak	10.69 ± 0.04	0.547 ± 0.094	5.1

Notes. Upper limits at the 95% (2 sigma) level assuming a 0.7 km s^{-1} FWHM

Table A.5. Line properties for HC_2NC in Tmb.

Line	Frequency (GHz)	E_u (K)	g_u	A_u (s^{-1})	I (mK[T_{mb}] km s^{-1})		V_{LSR} (km s^{-1})		ΔV (km s^{-1})	
					HCO peak	DCO^+ peak	HCO peak	DCO^+ peak	HCO peak	DCO^+ peak
J = 9–8	89.419300	21.5	17	3.4(–5)	<9	<9	…	…	…	…
J = 10–9	99.354250	26.2	19	4.7(–5)	<11	<11	…	…	…	…
J = 11–10	109.289095	31.5	21	6.2(–5)	<13	<13	…	…	…	…

Notes. Upper limits at the 95% (2 sigma) level assuming a 0.7 km s^{-1} FWHM.

Table A.6. Line properties for HNC_3 in Tmb.

Line	Frequency (GHz)	E_u (K)	g_u	A_u (s^{-1})	I (mK[T_{mb}] km s^{-1})		V_{LSR} (km s^{-1})		ΔV (km s^{-1})	
					HCO peak	DCO^+ peak	HCO peak	DCO^+ peak	HCO peak	DCO^+ peak
J = 9–8	84.028469	20.2	17	1.0(–4)	<9	<9	…	…	…	…
J = 10–9	93.364537	24.6	19	1.4(–4)	<9	<9	…	…	…	…
J = 11–10	102.700471	29.6	21	1.9(–4)	<12	<11	…	…	…	…
J = 11–10	112.036255	35.0	23	2.5(–4)	<16	<16	…	…	…	…

Notes. Upper limits at the 95% (2 sigma) level assuming a 0.7 km s^{-1} FWHM

Appendix B: Bayesian radiative transfer modeling

The inputs of the RADEX code are the kinetic temperature (T_K), the volume density of the collisional partner[4] (n_{H_2}) and the column density of the computed species (N). Given a set of energy levels and the radiative and collisional transitions linking them (both from the LAMBDA database Schöier et al. 2005), the LVG code computes for each line, its opacity, excitation temperature and flux assuming a Gaussian profile of a given fixed linewidth. We combined this LVG model with a Bayesian fitting method to determine the optimal physical parameters of the source. We assume that the observation uncertainties are centered Gaussians. The observed data D is thus represented by a set of N integrated intensity and its associated measurement uncertainty, $D = \{I_i, \sigma_i\}_{i=1..N}$.

With the hypothesis of independent Gaussian centered noise, the likelihood of having observing the data D given the model parameters $\boldsymbol{\theta} = \{\theta_i\}$ is given by

$$L(D|\boldsymbol{\theta}) = \prod_{i=1}^{N} \left[\frac{1}{\sqrt{2\pi\sigma_i}} \exp\left(-\frac{[I_i^{\rm obs} - I_i^{\rm mod}(\boldsymbol{\theta})]^2}{2\sigma_i^2} \right) \right], \quad \text{(B.1)}$$

where i is an index over the N channels. Taking the logarithm, the equation becomes

$$\ln L(D|\boldsymbol{\theta}) = -\frac{1}{2} \sum_{i=1}^{N} \ln(2\pi\sigma_i) - \sum_{i=1}^{N} \frac{[I_i^{\rm obs} - I_i^{\rm mod}(\boldsymbol{\theta})]^2}{2\sigma_i^2}, \quad \text{(B.2)}$$

where $I^{\rm mod}$ are derived from the parameters $\boldsymbol{\theta}$ through the RADEX model. In the Bayesian framework, the posterior

[4] We neglect the influence of the He collisional partner.

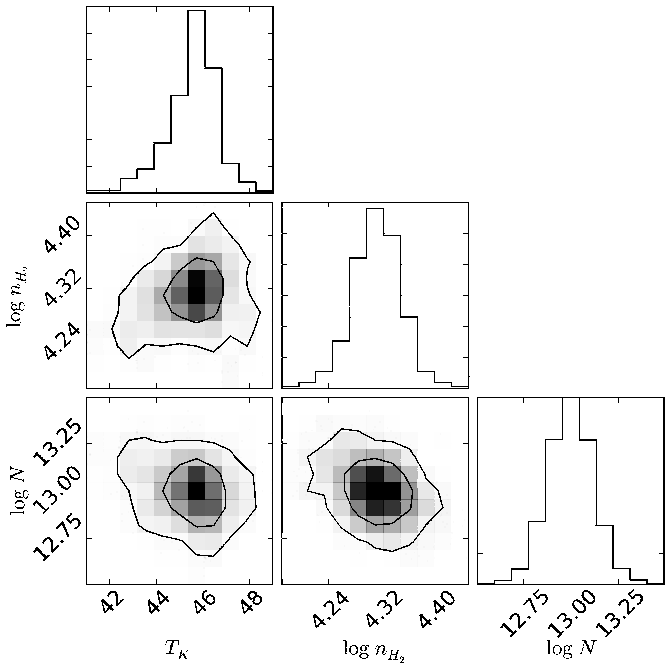

Fig. B.1. Distributions of the posterior probability for three parameters, i.e. gas density (n_{H_2}), kinetic temperature (T_K) and CH_3CN column density (N), at the PDR position. Along the diagonal, the one dimensional probability distribution functions are integrations of the two dimension probability distribution functions displayed below. The color coding of the two dimensional histograms runs from 0% (white) to 100% of the peak value(black). The contours correspond to 68% (1σ) and 95% (2σ) of cumulated posterior probability.

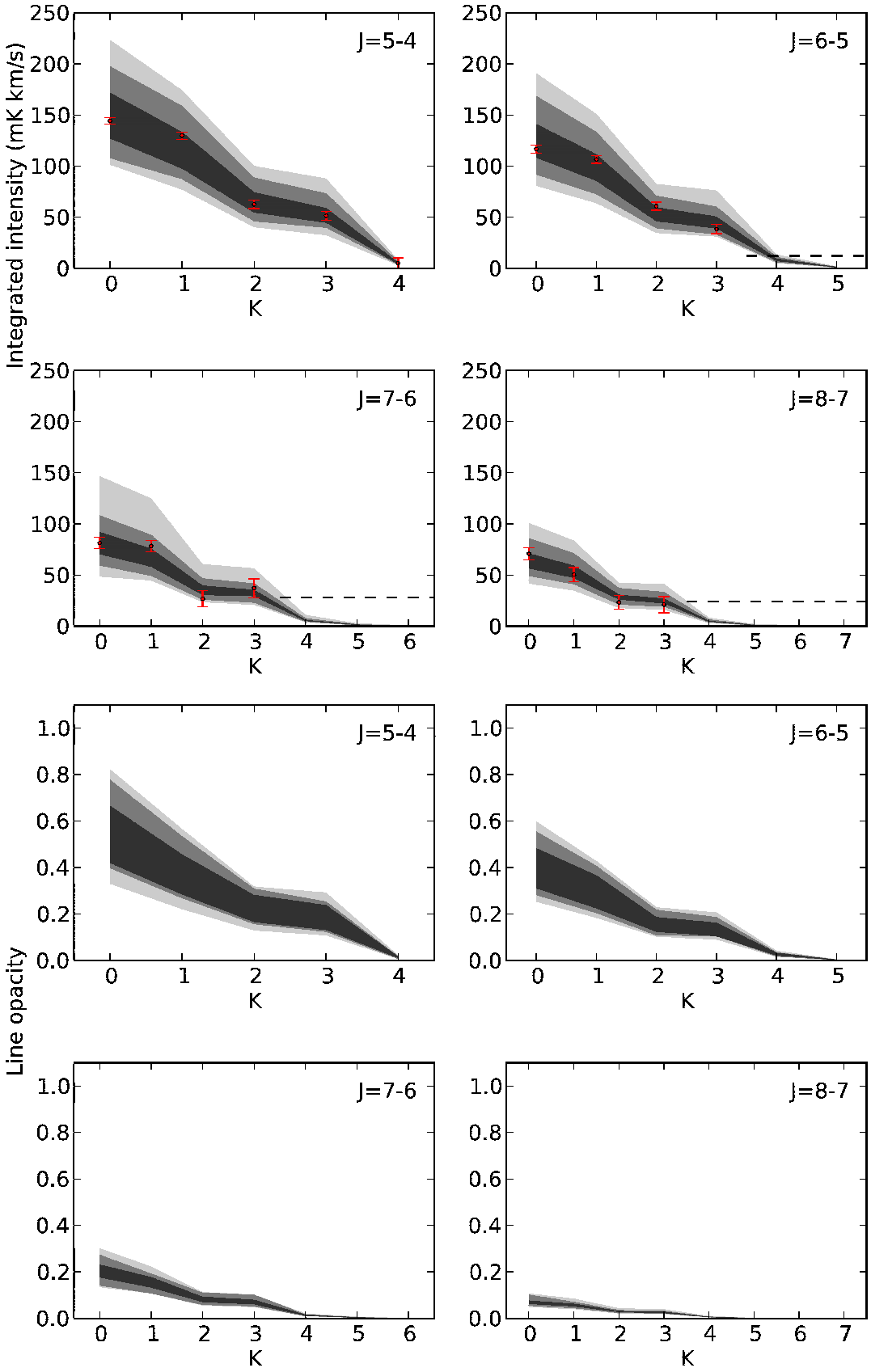

Fig. B.2. Distribution of modeled integrated intensities (*top 4 panels*) and line opacities (*bottom 4 panels*) as a function of the K number. Each panel presents the results for a different $(J+1 \rightarrow J)$ K-ladder. The 3 different gray levels corresponds to 3 different uncertainty intervals, i.e., 68% (1σ), 95% (2σ), and 99.9% (3σ) from dark to light gray. For the 4 *top panels*, the observed line intensities with their 1σ uncertainty intervals are plotted as red segments The dashed horizontal black line displays the 2σ upper limits for the undetected lines.

probability distribution of the parameters $p(\boldsymbol{\theta}|D)$ is obtained through the Bayes rule

$$p(\boldsymbol{\theta}|D) \propto L(D|\boldsymbol{\theta})p(\boldsymbol{\theta}), \tag{B.3}$$

where $p(\boldsymbol{\theta})$ is the prior probability distribution of the θ parameter. Through the use of informative prior distribution of the model parameters, it is possible to break model degeneracies. The posterior probability function can have a complicated surface with more than one maxima, in order to identify the best set of parameters (i.e., the posterior probability function around the global maxima) numerous tools have been developed. We use a Markov Chain Monte Carlo (MCMC) method for sampling the posterior probability function, specifically `emcee` (Foreman-Mackey et al. 2013), a MCMC Python implementation using the affine-invariant ensemble sampler presented in Goodman & Weare (2010). This sampling method enables us to have the posterior probability distribution as an equilibrium-sampling distribution. With the set of sampling values of the parameters it is then possible to compute marginalized one dimension probability distribution functions for each individual parameters. A central tendency (i.e. mean, median or histogram maximum) gives the most probable a posteriori parameter value and a confidence interval can be directly computed from the probability distribution of the parameters.

As an example, Figs. B.1 and B.2 shows the results of the modeling of the CH_3CN emission at the PDR position. Figure B.1 shows 2d posterior distributions of the model parameters. The marginalized 1d probability distribution functions of each parameter, which are displayed along the diagonal, are integrated over all the other parameter axes. Figure B.2 gathers the 1d probability distribution functions of the RADEX results: 1) the integrated intensity; and 2) the line opacity as a function of the K number for different $(J + 1 \rightarrow J)$ K-ladder.

Appendix C: Shortcomings of rotational diagrams in the case of CH_3CN

In this section, we quantify the error made when using rotational diagrams to derive column densities and abundances in moderately sub thermal excitation regimes such as those found in the PDR position ($\sim 6 \times 10^4$ cm^{-3}). We built the rotational diagrams assuming that the line emission is optically thin, i.e. we did not correct the measured column densities of the upper levels for opacity. Figures C.1 and C.2 shows the results. Two points stand out. First, the rotational temperatures derived from a fit of all the lines are lower than the kinetic temperature. However, the derived temperatures gets closer to the kinetic temperature when fitting the transitions with different J levels separately (one fit per panel in Figs. C.1 and C.2). This comes from the fact that different K-levels at constant J are not radiatively coupled (cf. Eq. (1)).

When fitting all the lines simultaneously, the rotational diagram derived column densities are underestimated by a factor 20 compared to the LVG derived ones for the PDR and a factor 2.5 for the dense core. When the K-ladders are fitted independently, the column densities increase when the associated J level decreases. Indeed, the high J levels are more difficult to thermalize because their critical densities are higher. As a consequence, the derived column densities is more and more underestimated as J increases. In the Horsehead PDR case, the column density derived from the rotational diagram for the lowest J level (5–4) is still six times lower than the column density derived by the escape probability radiative transfer modeling. In contrast, the rotational diagram and the RADEX methods yields the same column density at the dense core position. This is expected as the CH_3CN level population will be closer to thermal equilibrium in the higher density core.

Three different situations happen when using the rotational diagram method to determine the column density of CH_3CN and/or the gas kinetic temperature.

1. When the level populations follow an LTE distribution (e.g. the gas density is higher than a few 10^5 cm^{-3} for the J = 5–4 K-ladder) both the gas kinetic temperature and the CH_3CN column density can be derived accurately. This approximately corresponds to the case of the dense core position in our study.
2. When the excitation is slightly subthermal (e.g. the gas density is in the range $(4–8) \times 10^4$ cm^{-3} for the J = 5–4 K-ladder), the gas kinetic temperature can be obtained by fitting only the corresponding K-ladder lines that are close to thermalization. However, the column density will be underestimated. This corresponds to the case of the PDR position in our study.
3. When the excitation is strongly subthermal (e.g. the gas density is lower than 4×10^4 cm^{-3} for the J = 5–4 K-ladder), both the gas kinetic temperature and the CH_3CN are underestimated. It is then necessary to study the excitation with more advanced methods like escape probability methods.

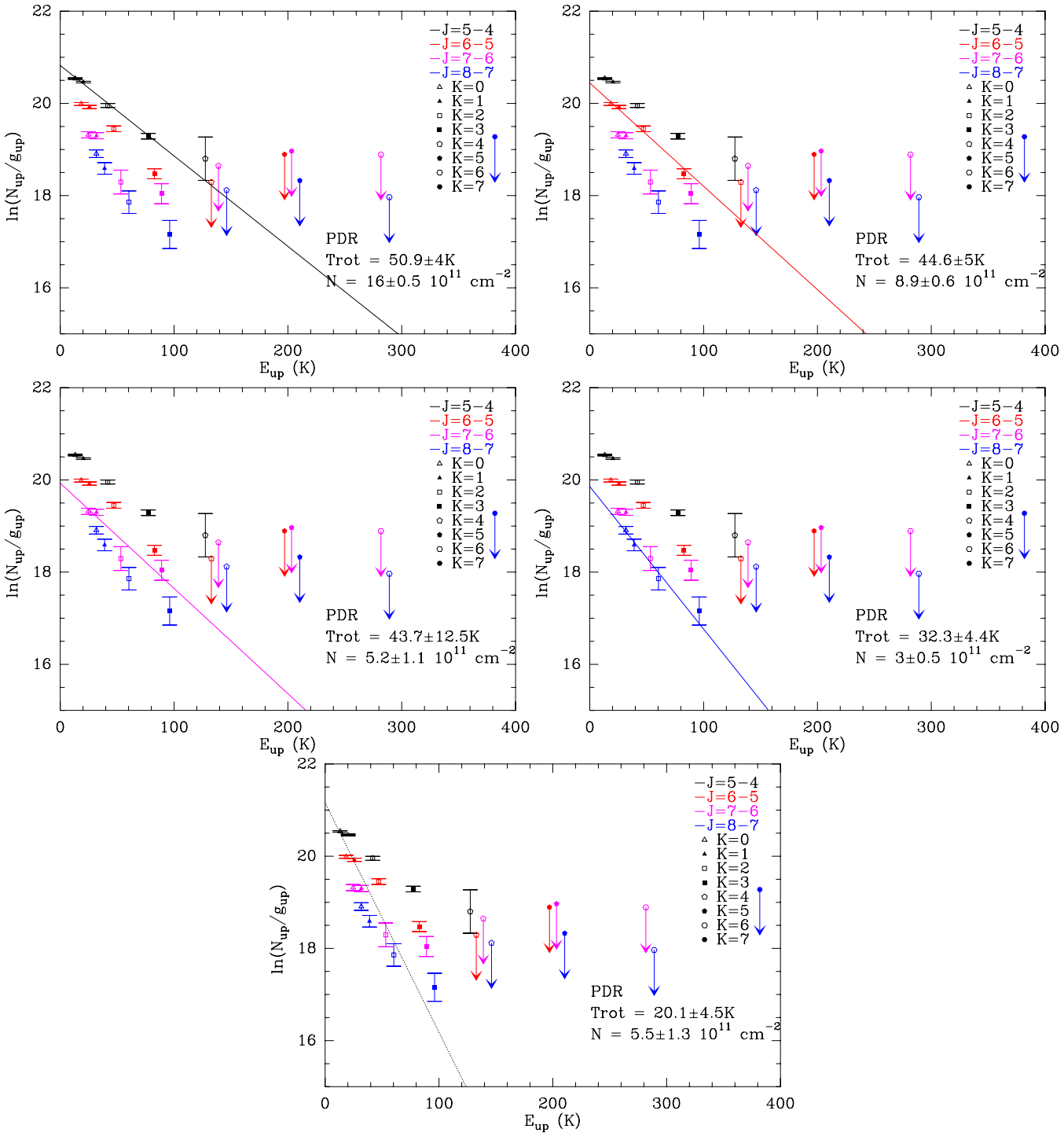

Fig. C.1. Rotational diagrams for CH_3CN at the HCO peak, in each of the 4 *top panels*, the solid lines correspond to fits restricted to to observed K transitions for a given $J-J-1$ set, the fitted line is of the same color as the fitted points. The final panel shows, in a dotted line, the result of fitting all lines simultaneously. *Each panel* shows the rotational temperature and column density derived from the fit.

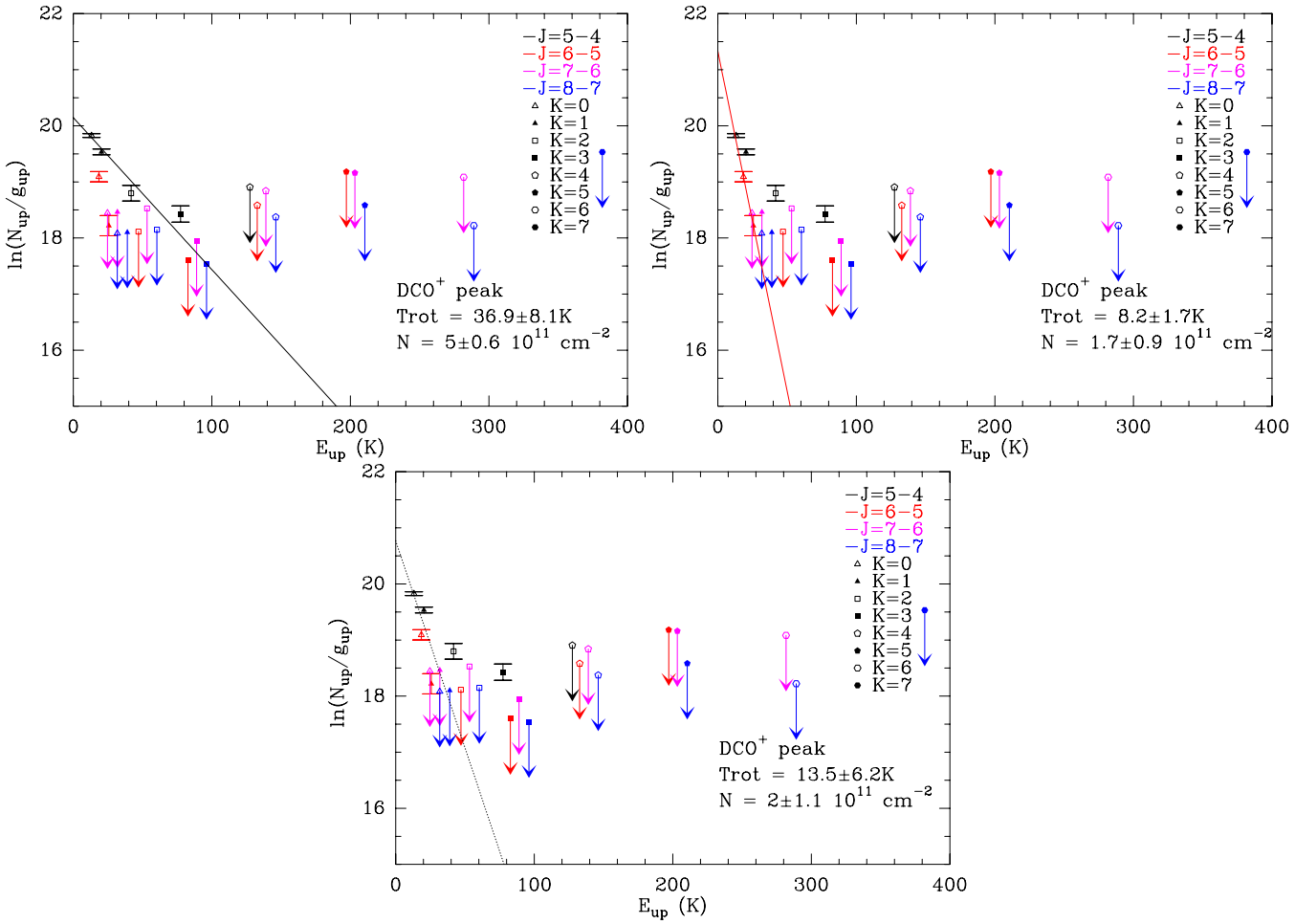

Fig. C.2. Same as Fig. C.1 for the dense core.

Appendix D: Methyl cyanide and isocyanide spectra

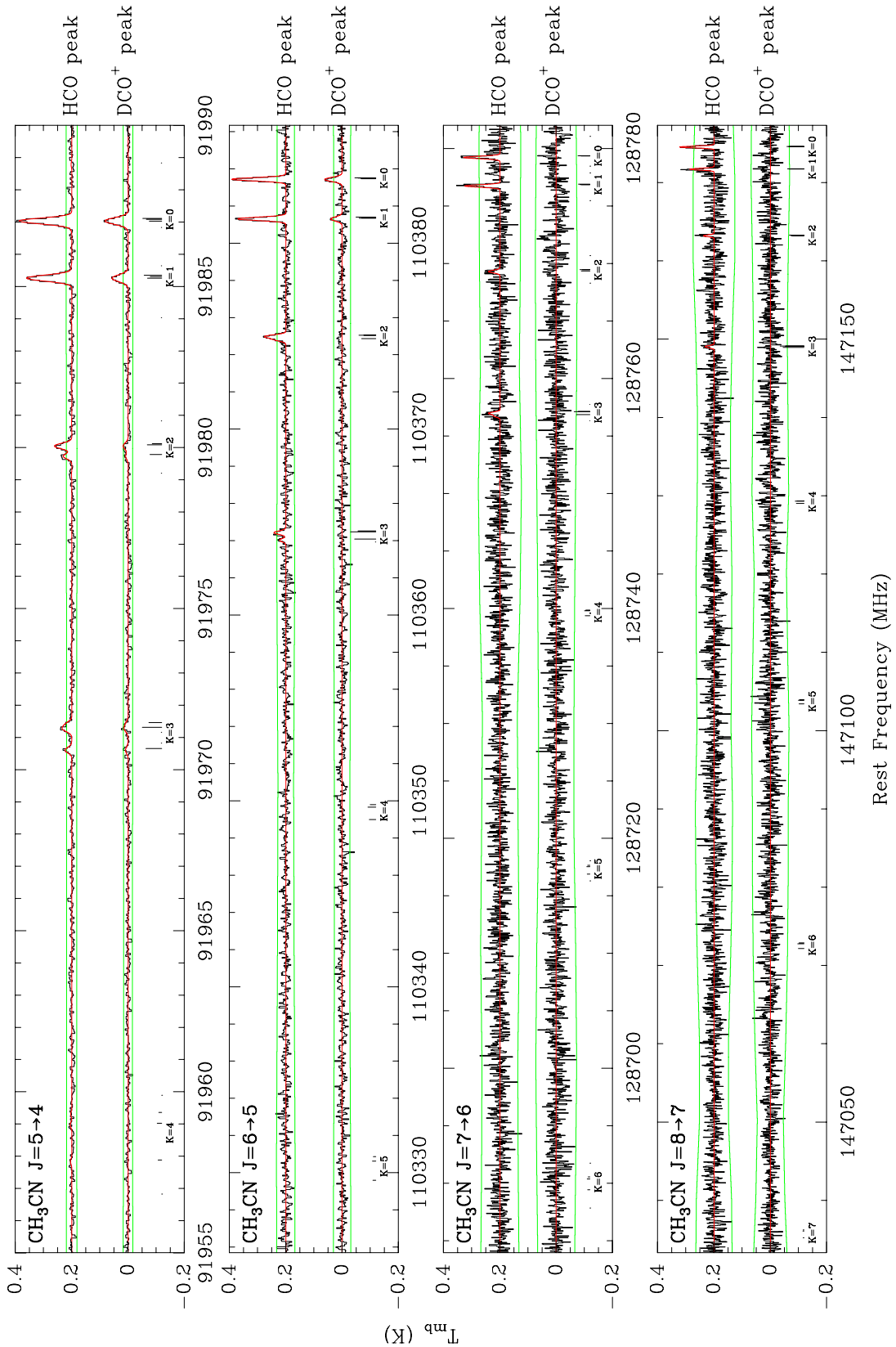

Fig. D.1. Spectrum of the CH_3CN 3 mm and 2 mm detected lines at the HCO peak (i.e., the PDR position, top spectrum of *each panel*) and the DCO^+ peak (i.e., inside the cold dense core, bottom spectrum of each panel), each spectrum towards the HCO peak has been shifted vertically by 0.2 K for clarity. The panel displays the K set of lines for a given ΔJ set of lines. The frequencies corresponding to each transitions are displayed as vertical bars, whose heights indicate their relative hyperfine intensities in the optically thin regime applicable to these observations. The best fit model is overplotted in red. The green horizontal lines display the $\pm 3\sigma$ significance levels.

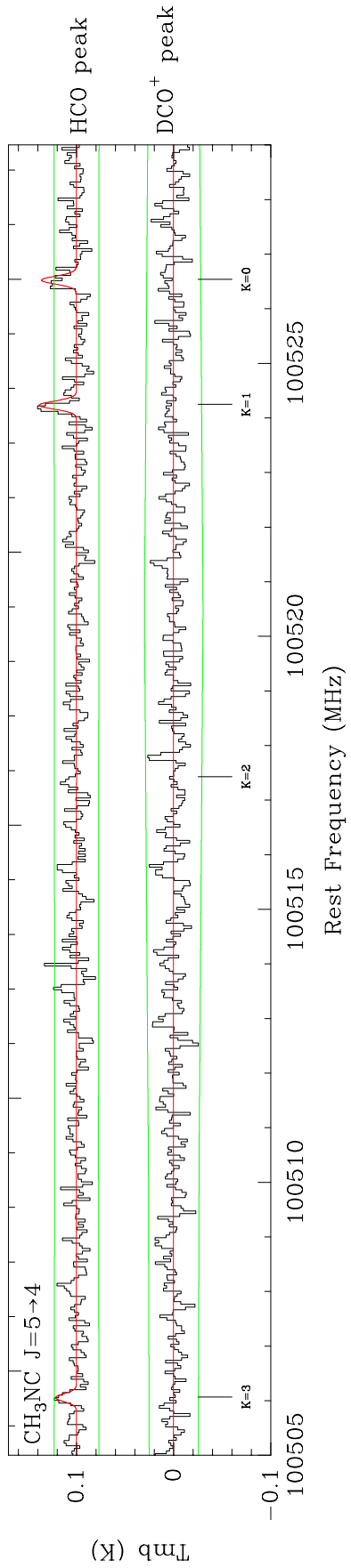

Fig. D.2. Spectrum of the CH_3NC 3mm detected lines at the HCO peak (i.e., the PDR position, top spectrum) and the DCO^+ peak (i.e., inside the cold dense core, bottom spectrum), the spectrum towards the HCO peak has been shifted vertically by 0.1 K for clarity. The panel displays the K set of lines for the given ΔJ set of lines. The frequencies corresponding to each transitions are displayed as vertical bars. The best fit model is overplotted in red. The green horizontal lines display the $\pm 3\sigma$ significance levels.

Chapter 7

HCOOH, CH_2CO, CH_3CO and CH_3CCH

7.1 Introduction

Nowadays, it is believed that the simplest prebiotic molecules, such as glycine (NH_2CH_2COOH), have an interstellar origin (e.g. Garrod 2013; Elsila et al. 2007). Indeed, numerous amino acids, which are the building blocks of proteins, have been found in meteorites (e.g., Glavin et al. 2013). In addition, glycine, which is the simplest amino acid, has been detected in samples returned by NASA's Stardust spacecraft from comet Wild 2 (Elsila et al. 2009). Glycine or other more complex amino acids have not been detected in the ISM yet. The most complex molecules detected in the ISM so far, are glycolaldehyde ($CH_2(OH)CHO$, Hollis et al. 2000), acetamide (CH_3CONH_2, Hollis et al. 2006), aminoacetonitrile (NH_2CH_2CN, Belloche et al. 2008a), and the ethyl formate (C_2H_5OCHO, Belloche et al. 2009). This shows the high degree of chemical complexity that can be reached in the ISM.

Complex organic molecules, such as methanol (CH_3OH), ketene (CH_2CO), acetaldehyde (CH_3CHO), formic acid (HCOOH), formamide (NH_2CHO), propyne (CH_3CCH), methyl formate ($HCOOCH_3$), and dimethyl ether (CH_3OCH_3), are widely observed in hot cores of high-mass protostars (e.g., Cummins et al. 1986; Blake et al. 1987; Bisschop et al. 2007), and also in hot-corinos of low-mass protostars (e.g., van Dishoeck et al. 1995; Cazaux et al. 2003). The complex molecules observed in protostars have been classified in three different generations by Herbst & van Dishoeck (2009), depending on their formation mechanism. The zeroth generation species form through grain surface processes in the cold (< 20 K) pre-stellar stage (e.g., H_2CO and CH_3OH). First generation species form from surface reactions between photodissociated products of the zeroth generation species in the warm-up ($20 - 100$ K) period. Finally, second generations species form in the hot (> 100 K) gas from the evaporated zeroth and first generation species in the so called hot-core phase. Although it is clear that grain surface processes play an important role in the formation of complex molecules, the exact formation mechanism of most complex molecules is still debated.

Bisschop et al. (2007) observed several complex molecules towards seven high-mass protostars, and classified them as cold (T$<$ 100 K) and hot (T$>$ 100 K) molecules based on their rotational temperatures. The hot molecules include H_2CO, CH_3OH, HNCO, CH_3CN, $HCOOCH_3$ and CH_3OCH_3, while the cold molecules include HCOOH, CH_2CO, CH_3CHO, and CH_3CCH. The cold molecules are expected to be present in the colder envelope around the hot-core. Öberg et al. (2013) studied the spatial distribution of complex molecules around a high-mass protostar and found that CH_2CO, CH_3CHO and CH_3CCH are indeed abundant in the cold envelope. They classified them as zeroth order molecules because their formation

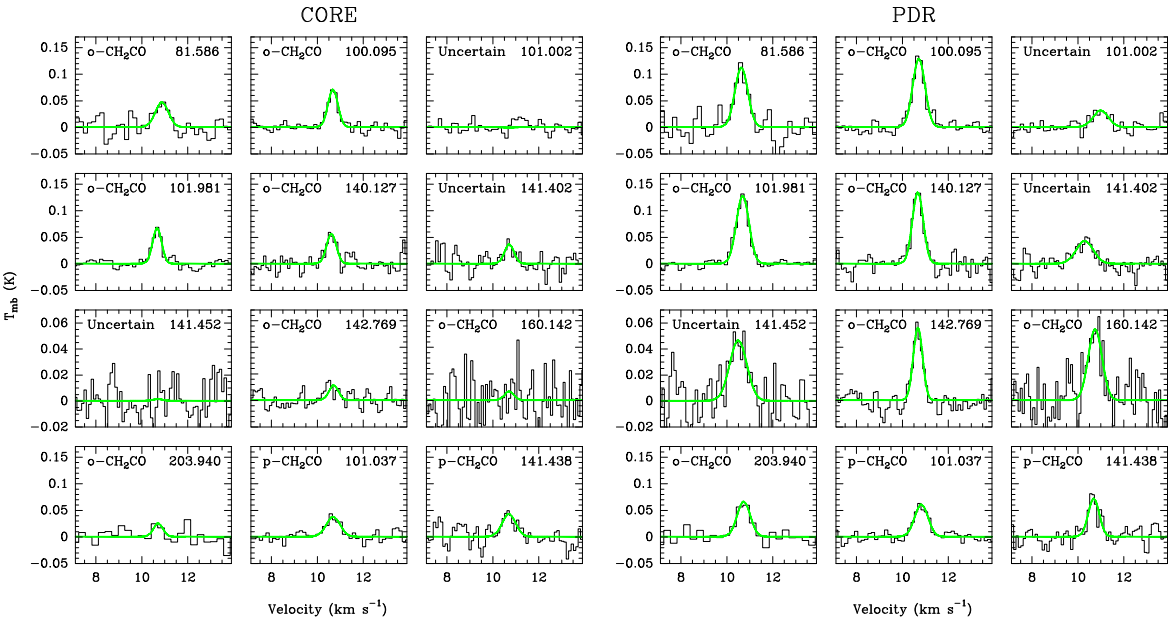

Figure 7.1: CH_2CO lines detected towards the PDR (*left*) and dense core (*right*). The green lines are Gaussian fits. For each line, the same scale is used at both positions to ease the comparison.

must require very little heat.

Complex organic molecules are not unique tracers of hot cores or hot corinos. They are also present in the cold UV-shielded gas. Bacmann et al. (2012) detected CH_3OCH_3, CH_3OCHO, CH_2CO and CH_3CHO in a cold ($\sim$ 10 K) prestellar core. These observations challenged the current formation scenario of complex molecules on dust grains, because the diffusion reactions that lead to the formation of species are not efficient on dust grains with temperatures of $\sim$ 10 K. CH_3CHO and CH_2CO have also been detected in the dark cloud TMC-1 (Matthews et al. 1985; Irvine et al. 1989). CH_2CO and CH_3CHO have also been detected in a $z = 0.89$ spiral galaxy located in front of the quasar PKS1830-211 (Muller et al. 2011).

Complex molecules have been detected in several environments including cold dense cores and protostellar sources. Here, we present the first detection of complex molecules in a PDR.

7.2 Observations

Within the WHISPER line survey, several lines of HCOOH, CH_2CO, CH_3CHO and CH_3CCH are detected. These are presented in Figs. 7.1, 7.2, 7.3 and 7.4. The spectroscopic parameters and gaussian fit results of the detected lines are listed at the end of this chapter in Tables 7.2, 7.3, 7.4 and 7.5. The spectroscopic parameters are taken from the CDMS (Müller et al. 2001) and JPL (Pickett et al. 1998) data bases.

Several bright ($> 5\sigma$) lines of ketene and acetaldehyde are detected. The formic acid and propyne present several but fainter ($2\sigma - 5\sigma$) lines towards the PDR and dense core

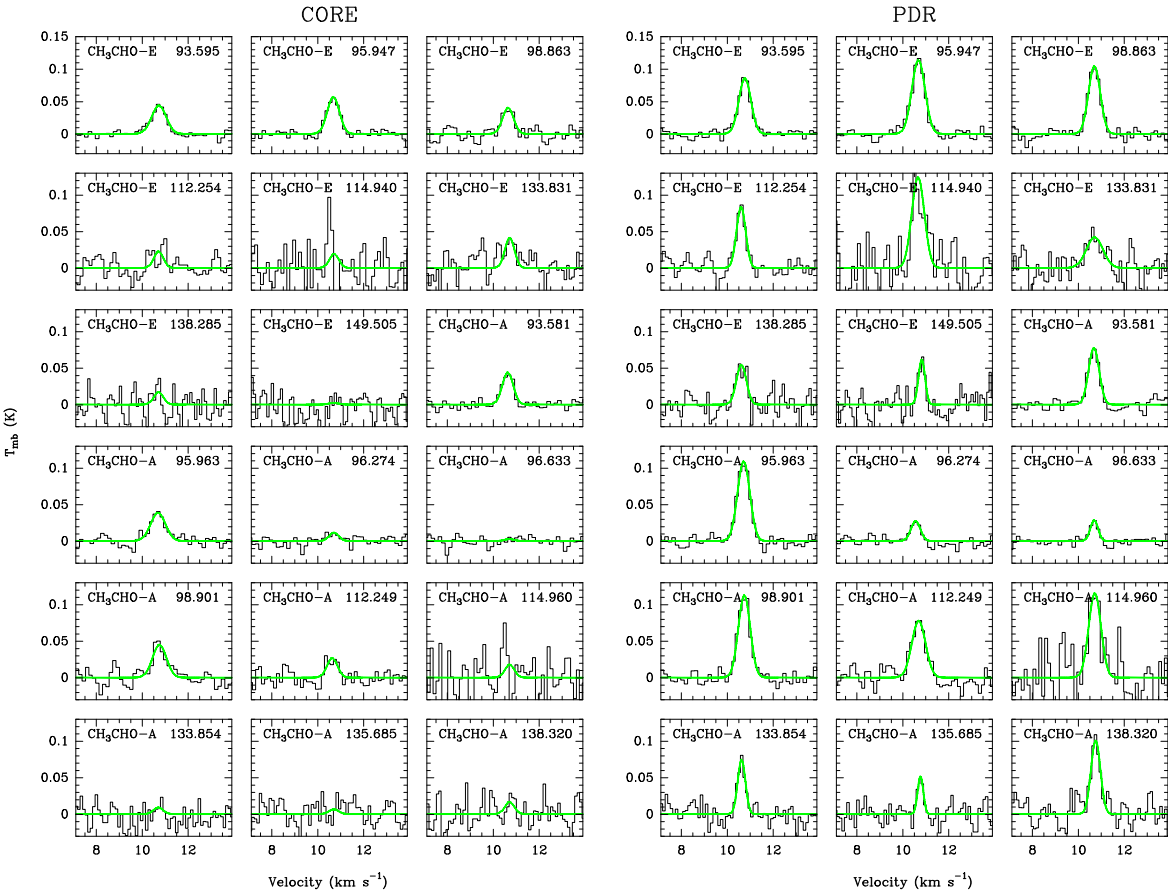

Figure 7.2: CH_3CHO lines detected towards the PDR (*left*) and dense core (*right*). The green lines are Gaussian fits. For each line, the same scale is used at both positions to ease the comparison.

positions. In order to confirm the correct identification of these molecules, we have modeled the spectrum of each species assuming LTE and optically thin emission, and checked that there are no predicted lines missing in the line survey.

Both ortho and para forms of CH_2CO are detected, as well as both E and A forms of CH_3CHO and CH_3CCH. All the lines detected of the formic acid correspond to the trans isomer. CH_2CO, CH_3CHO lines are brigher towards the PDR position than towards the dense core, while HCOOH and CH_3CCH lines have similar brightness in both positions.

7.3 Rotational temperatures and column densities

The beam-averaged column density of each molecule was estimated using rotational diagrams. The detected lines cover a sufficiently large energy range to derive a rotational temperature. The resulting rotational diagrams are shown in Fig. 7.5. The inferred rotational temperatures and column densities are summarized in Table 7.1. The partition function was computed independently for ortho and para nuclear spin forms (for ketene), and for E and A symmetry

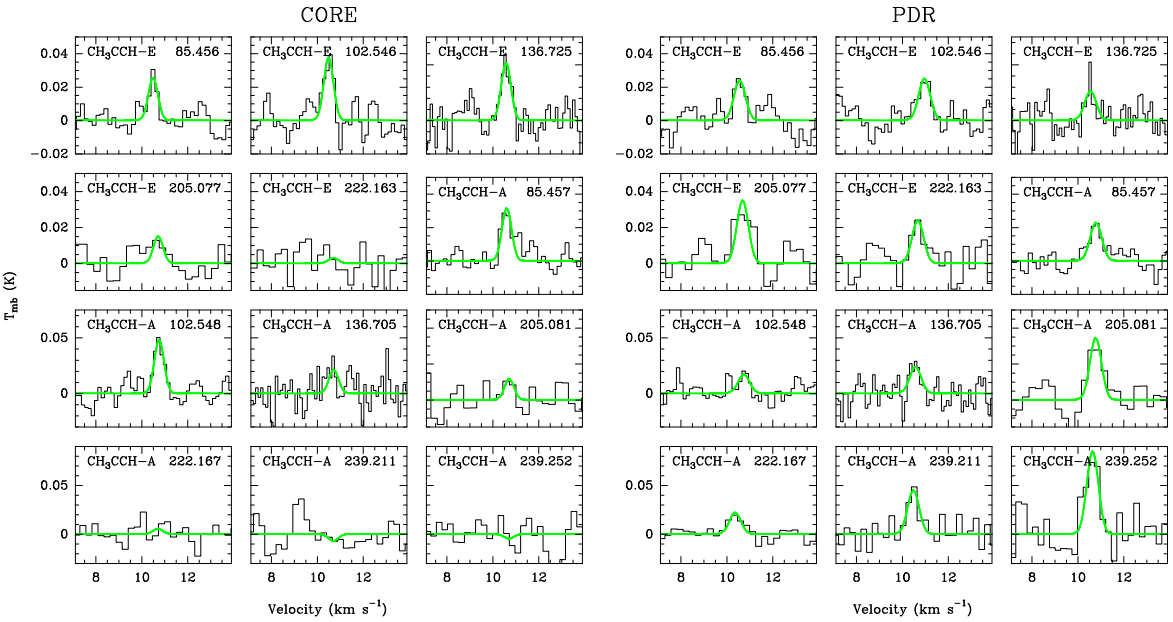

Figure 7.3: CH_3CCH lines detected towards the PDR (*left*) and dense core (*right*). The green lines are Gaussian fits. For each line, the same scale is used at both positions to ease the comparison.

forms (for CH_3CHO), by direct summation over the energy levels (see Appendix A).

7.3.1 Ketene

The ortho and para symmetries of CH_2CO were treated as different species. When including all the o $-$ CH_2CO and p $-$ CH_2CO lines detected in the PDR, the fit results in rotational temperatures of 154 K and 120 K for o $-$ CH_2CO and p $-$ CH_2CO, respectively. These temperatures are much larger than the kinetic temperature at the PDR ($\sim$60 K). When the three lines of CH_2CO with energies above 80 K that are detected at the PDR (gray points in Fig. 7.5) are not considered in the rotational diagrams, the derived rotational temperatures decrease to 18 K for both ortho and para species. This temperature agrees much better with the expected sub-thermal excitation in the Horsehead, and also with the derived rotational temperatures at the dense core. The enhanced emission of the three lines with $E_u > 80$ K could be the result of an excitation effect. However, these lines are broader (0.8 km s^{-1}) than the other CH_2CO lines and than other species detected in the Horsehead PDR (the typical linewidth is 0.6 km s^{-1}). In addition, the velocity of these three lines differs by 0.2 km s^{-1} from the systemic velocity of 10.7 km s^{-1} found for most species in the Horsehead. Cummins et al. (1986) detected several o $-$ CH_2CO lines toward Sgr B2, including the $5_{33} - 4_{32}$ at 101.002 GHz, which is one of the three lines detected in the Horsehead with $E_u > 80$ K. They also obtained a large rotational temperature, which led them to remove this line from the fit and consider the identification as uncertain. At the dense core position in the Horsehead, the derived rotational temperature for o $-$ CH_2CO is $\sim$ 14 K. Only two lines of p $-$ CH_2CO are detected at the dense core, resulting in a rotational temperature of $\sim$ 20 K. Ketene is

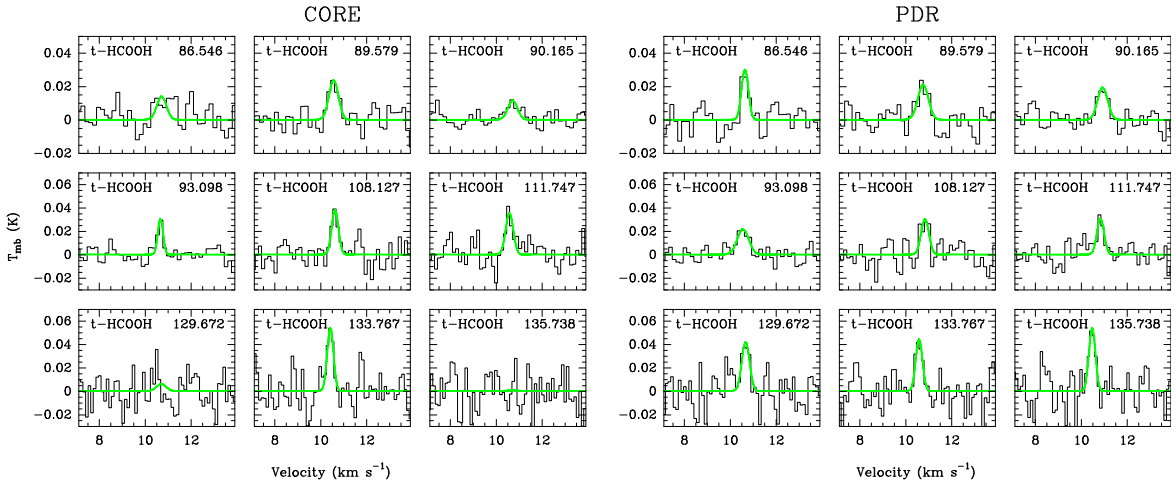

Figure 7.4: HCOOH lines detected towards the PDR (*left*) and dense core (*right*). The green lines are Gaussian fits. For each line, the same scale is used at both positions to ease the comparison.

~ 3 times more abundant in the PDR than in the dense core, with abundances of 1.5×10^{-10} (PDR) and 4.9×10^{-11} (core). The ortho-to-para ratio is poorly constrained, resulting in $o/p = 7.1 \pm 4.2$ (PDR) and $o/p = 5.7 \pm 3.9$ (dense core).

7.3.2 Acetaldehyde

The E and A symmetries of CH_3CHO were also treated as different species. Acetaldehyde has a large dipole moment (2.7 Debye) compared to methanol (1.7 Debye). Since the critical density is proportional to μ^2, sub-thermal effects are important for CH_3CHO (Bisschop et al. 2007). Indeed, the derived rotational temperatures for CH_3CHO ($6 - 10$ K) are the lowest ones of all the molecules discussed here. The derived column density of CH_3CHO is ~ 3 times larger in the PDR than in the dense core. The inferred E/A ratio is $\sim 0.3 \pm 0.1$ (PDR) and $\sim 0.2 \pm 0.2$ (core), *i.e.*, much lower than unity in both positions.

Figure 7.6 displays the averaged E and A CH_3CHO lines at 93.6 GHz. The CH_3CHO emission clearly peaks at the PDR position, delineating the edge of the Horsehead nebula. The CH_3CHO emission resembles the HCO emission at the 30m telescope angular resolution of $30''$, which is concentrated in a narrow structure peaking at the PDR. Higher-angular resolution ($6''$) observations by Gerin et al. (2009) showed that the HCO emission traces a filament of $\sim 12''$ width. The similarities between the emission of HCO and CH_3CHO thus suggest that CH_3CHO also arises from a narrow filament that peaks at the PDR position. Assuming a filament of $12''$ centered at the PDR, we estimate that $\sim 10\%$ of the CH_3CHO emission detected at the dense core corresponds to beam pick-up from the PDR due to the large beam at 93 GHz ($27''$). The remaining emission towards the core line of sight could arise from the cloud surface, as was found for CS(Goicoechea et al. 2006) and HCOGerin et al. (2009).

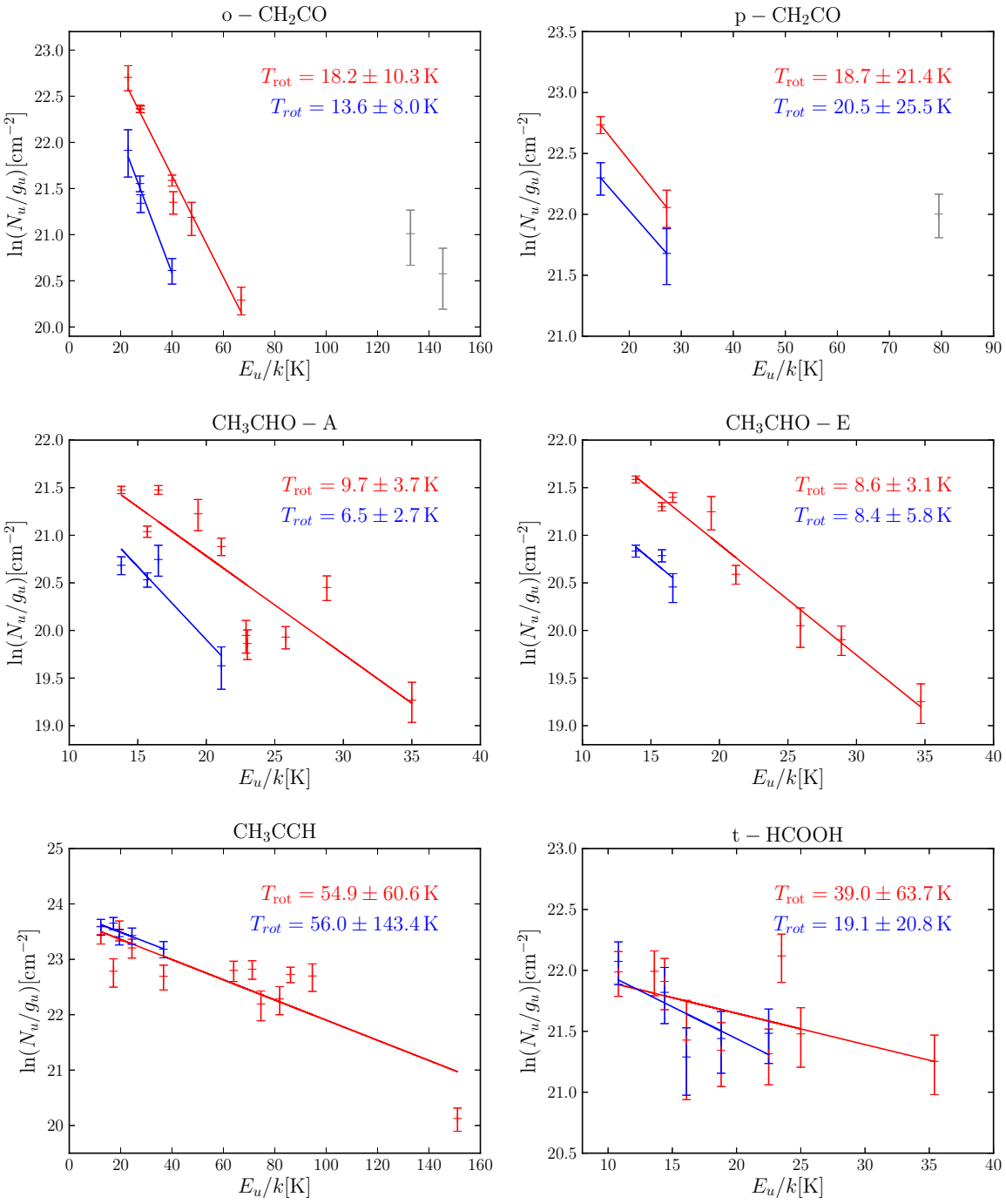

Figure 7.5: Rotational diagrams for the PDR (red) and dense core (blue).

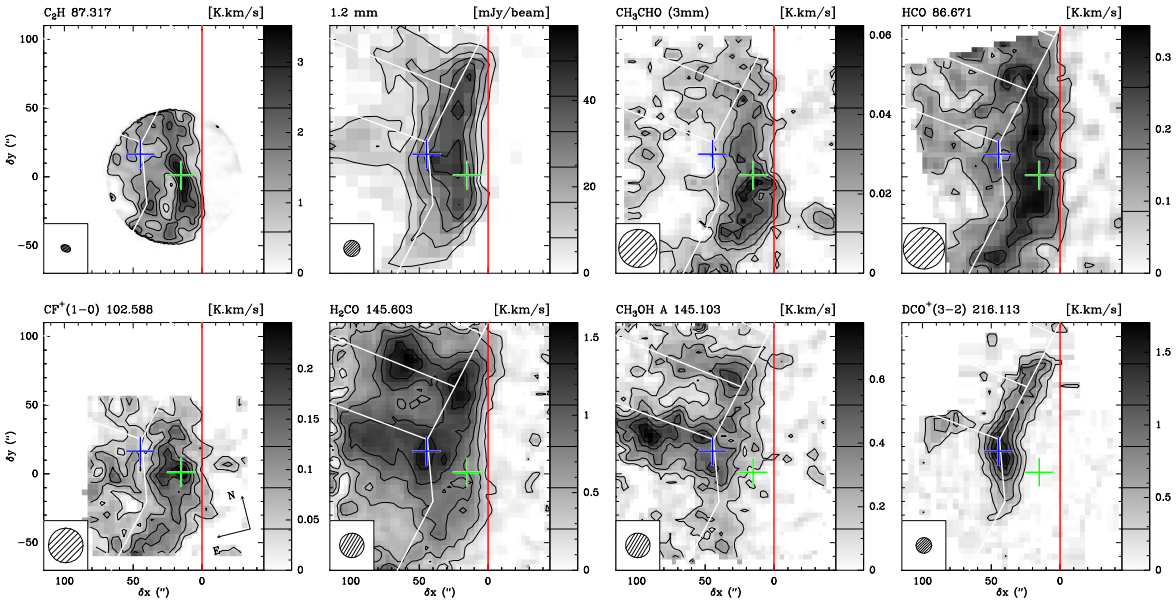

Figure 7.6: IRAM-30m and PdBI maps of the Horsehead edge. Maps were rotated by 14° counter-clockwise around the projection center, located at $(\delta x, \delta y) = (20'', 0'')$, to bring the exciting star direction in the horizontal direction. The horizontal zero, marked by the red vertical line, delineates the PDR edge. The crosses show the positions of the PDR (green) and the dense core (blue), where deep integrations were performed in the Horsehead WHISPER line survey (PI: J.Pety). The white lines delineate the arc-like structure of the DCO^+ emission. The spatial resolution is plotted in the bottom-left corner. Values of contour levels are shown in the respective image lookup table. The emission of all lines is integrated between 10.1 and 11.1 $\mathrm{km\,s^{-1}}$

7.3.3 Propyne

If $CH_3CCH - E$ and $CH_3CCH - A$ are treated as different species, the derived rotational temperatures at the PDR are ∼70 K and ∼53 K for E and A symmetries, respectively. At the dense core, a rotational temperature of ∼ 70 K is inferred for the E symmetry. A rotational temperature cannot be inferred for $CH_3CCH - A$ at the dense core because the two lines that are detected are faint. The two symmetries are therefore considered as the same species, resulting in a rotational temperature of ∼55 K and a total column density for the E- and A-type CH_3CCH of $\sim 2 \times 10^{13}$ $\mathrm{cm^{-2}}$ at both the PDR and dense core position. The inferred column density at the PDR position does not change when the E and A symmetries are separated.

7.3.4 Formic acid

The data in the rotational diagram of HCOOH present a large scatter because all the detected lines are weak and therefore have a larger uncertainty than the lines of the other complex molecules. The rotational temperature is poorly constrained. The inferred abundances of $\sim 5 \times 10^{-11}$ (PDR) and $\sim 1 \times 10^{-11}$ (core) are thus also uncertain and should be considered

Table 7.1: Column densities and abundances.

Molecule	PDR	Dense core
	Column densities [cm^{-2}]	
N_H	3.8×10^{22}	6.4×10^{22}
$N(CH_3OH - E)$	2.7×10^{12}	6.5×10^{12}
$N(CH_3OH - A)$	2.0×10^{12}	8.1×10^{12}
$N(t - HCOOH)$	$(2.0 \pm 0.6) \times 10^{12}$	$(8.7 \pm 3.8) \times 10^{11}$
$N(o - CH_2CO)$	$(2.3 \pm 0.6) \times 10^{12}$	$(9.5 \pm 3.5) \times 10^{11}$
$N(p - CH_2CO)$	$(6.9 \pm 3.4) \times 10^{11}$	$(4.7 \pm 2.3) \times 10^{11}$
$N(CH_3CHO - E)$	$(5.2 \pm 1.8) \times 10^{11}$	$(2.5 \pm 2.2) \times 10^{11}$
$N(CH_3CHO - A)$	$(2.0 \pm 0.7) \times 10^{12}$	$(1.2 \pm 0.7) \times 10^{12}$
$N(CH_3CCH)$	$(1.7 \pm 0.4) \times 10^{13}$	$(2.0 \pm 0.7) \times 10^{13}$
	Abundances $N(X)/(N(H) + 2\ N(H_2))$	
$[CH_3OH - E]$	7.0×10^{-11}	1.0×10^{-10}
$[CH_3OH - A]$	5.3×10^{-11}	1.3×10^{-10}
$[t - HCOOH]$	$(5.3 \pm 1.6) \times 10^{-11}$	$(1.4 \pm 0.6) \times 10^{-11}$
$[o - CH_2CO]$	$(6.1 \pm 1.5) \times 10^{-11}$	$(1.5 \pm 0.5) \times 10^{-11}$
$[p - CH_2CO]$	$(1.8 \pm 0.9) \times 10^{-11}$	$(7.3 \pm 0.4) \times 10^{-12}$
$[CH_3CHO - E]$	$(1.4 \pm 0.5) \times 10^{-11}$	$(3.9 \pm 3.4) \times 10^{-12}$
$[CH_3CHO - A]$	$(5.3 \pm 1.8) \times 10^{-11}$	$(1.9 \pm 1.1) \times 10^{-11}$
$[CH_3CCH]$	$(4.5 \pm 1.1) \times 10^{-10}$	$(3.1 \pm 1.1) \times 10^{-10}$

as an order of magnitude estimate. Deeper integration times are needed to better constrain the HCOOH abundance.

7.4 Discussion and conclusions

Ketene and acetaldehyde are thought to form on the surface of dust grains. Indeed, CH_3CHO has been proposed as a candidate for the 7.41 μm absorption feature observed toward high-mass protostars (Schutte et al. 1999). Ketene and acetaldehyde are thought to form together on the ices through C and H atom additions to CO (Herbst & van Dishoeck 2009). The expected sequence is

$$CO \xrightarrow{H} HCO \xrightarrow{C} HCCO \xrightarrow{H} CH_2CO \xrightarrow{2H} CH_3CHO. \quad (7.1)$$

Ketene can also be formed from reactions between C_2H_2 and O in irradiated H_2O-rich and CO_2-rich ices, as shown by recent laboratory experiments (Hudson & Loeffler 2013). Laboratory experiments also show that reactions between C_2H_4 and O can produce acetaldehyde and its isomer, ethylene oxide (CH_2OCH_2) (Ward & Price 2011). CH_2CO and CH_3CHO could also be formed in the gas-phase, through ion-molecule and neutral-neutral reactions. Indeed, gas-phase models predict abundances that are comparable to those measured in some of the high-mass protostars observed by Bisschop et al. (2007).

The exact formation path of HCOOH on ices is unclear, though HCOOH ices have been observed in star-forming regions (Keane et al. 2001). Several formation paths on grain surfaces have been proposed in the past. It could form from the addition of H and O atoms to CO or to CO_2(Tielens & Hagen 1982). Garrod et al. (2006) proposed that HCOOH could form through reactions between HCO and OH. More recently, Ioppolo et al. (2011) have studied the hydrogenation of the HO-CO complex in the laboratory and showed it is an efficient formation route to HCOOH.

The abundances derived in the Horsehead PDR for HCOOH, CH_2CO, and CH_3CHO, are $3-4$ times larger toward the PDR than toward the dense core. The case of CH_3CN is even more extreme as it is ~ 30 times more abundant in the PDR than in the dense core(Gratier et al. 2013). CH_3CCH is only 1.5 times more abundant in the PDR than in the dense core. In contrast, methanol is ~ 2 times *less* abundant in the PDR than in the dense core. When comparing the abundances of the different molecules, we found that CH_3CCH is one order of magnitude more abundant ($3-4\times10^{-10}$) than CH_2CO and CH_3CHO ($2-7\times10^{-11}$). Contrary to the other complex molecules, which present [X]/[CH_3OH] ratios lower than 1, CH_3CCH is ~ 4 times more abundant than methanol in the PDR, and ~ 1.3 times more abundant than methanol in the dense core. Öberg et al. (2013) also found large CH_3CCH abundances (~ 1 relative to methanol) toward the high-mass protostar NGC 7538 IRS9. They found the CH_3CCH/CH_3OH abundance ratio to be significantly different to what models including grain surface processes predict, which suggests that an important cold formation pathway is missing for CH_3CCH.

Fig. 7.7 shows a comparison between the abundances derived in the Horsehead and those derived toward the hot corino sources from Bisschop et al. (2007) and toward the prestellar core L1689B(Bacmann et al. 2012). CH_3OH is several orders of magnitude more abundant toward the hot core sources than in the Horsehead. The abundances of the other complex molecules with respect to H_2 vary over ~ 1 order of magnitude between the different hot core sources, and are comparable to the abundances derived in the Horsehead. The abundances with respect to CH_3OH are also shown in the right panel of Fig. 7.7. In this case, the abundances of complex molecules are ~ 3 orders of magnitude larger in the Horsehead than in the hot cores. However, this could be a consequence of methanol and the other complex molecules tracing different regions in the hot core sources. Methanol probably traces the hot ($T_{\rm kin} > 100$ K) gas where species have evaporated from the grains, while the other complex molecules trace the colder envelope around the protostars, where the ices have not completely evaporated but can be photodesorbed.

The fact that we only detect cold molecules (HCOOH, CH_2CO, CH_3CHO and CH_3CCH) and none of the hot molecules (e.g., CH_3OCH_3 and $HCOOCH_3$), is in agreement with the idea that the cold molecules are zeroth or first generation species formed on the cold grain surfaces and trace the warm/cold envelope around protostars, because their formation probably requires little energy. In the Horsehead, the enhanced abundances toward the PDR compared to the dense core (for HCOOH, CH_2CO, and CH_3CHO), suggests that their formation is more efficient in the presence of far-UV photons. The similarities between the HCO and CH_3CHO emission maps also suggests that the CH_3CHO abundance at the PDR could be even higher than estimated here, if the emission arises from a narrow filament like HCO. This could be the result of an efficient photodesorption in the PDR, due to the larger

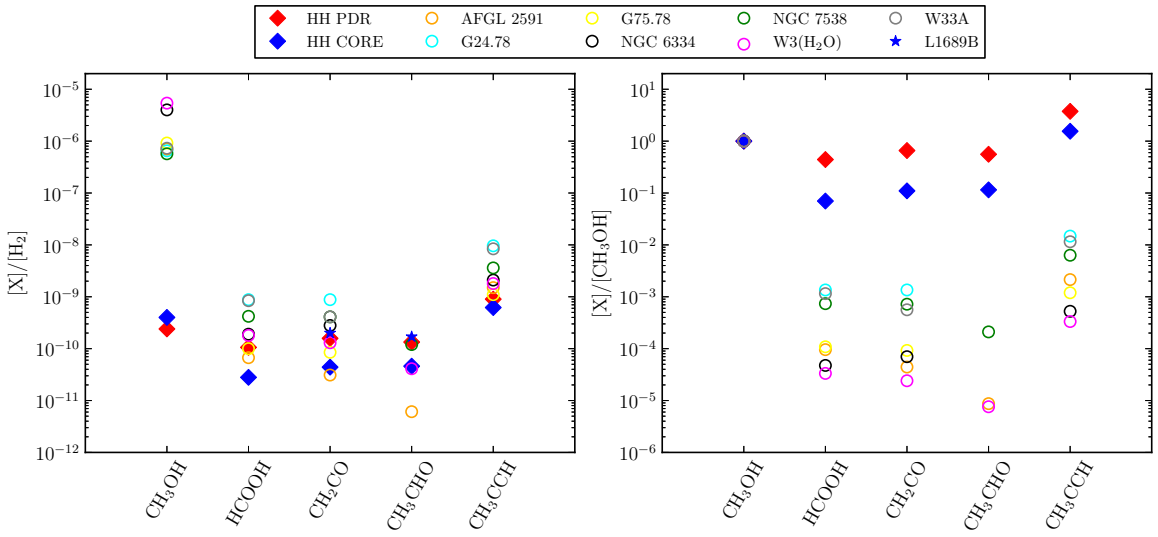

Figure 7.7: Abundances with respect to H_2 (*left*) and with respect to CH_3OH (*right*) towards the hot core sources from Bisschop et al. (2007) (*open circles*), the cold prestellar core from Bacmann et al. (2012) (*blue star*) and the Horsehead PDR and dense core (*red and blue diamonds*).

radiation field compared to the dense core, which is consistent with the much lower than unity E/A ratio (statistical value) we infer from the observations. But it could also indicate that the formation on the grains itself is more efficient in the PDR, due to a better mobility of the molecules in ice mantles. Indeed, recent laboratories experiments have shown that the diffusion of molecules is active at $T_{\rm dust} \gtrsim 30$ K, allowing reactions to proceed faster when the ices are warmed by far-UV photons(Vinogradoff et al. 2013; Mispelaer et al. 2013). Dust temperatures in the Horsehead PDR range from $T_{\rm dust} \sim 30$ K in the PDR to $T_{\rm dust} \sim 20$ K in the dense core(Goicoechea et al. 2009a).

Complex molecules are usually considered as hot-core tracers. The detection of these molecules in other environments, such as prestellar cores (Bacmann et al. 2012) and now in PDRs, suggests that they can also form in the cold gas and in UV-irradiated warm gas. We have shown that complex molecules can survive in the presence of FUV radiation, and their formation could even be enhanced due to the radiation. This opens the possibility of detecting complex molecules in other FUV-illuminated regions, such as protoplanetary disks, in the future.

Table 7.2: Observation parameters of the deep integrations of the HCOOH lines detected towards the PDR and dense core.

Molecule	Transition	ν GHz	E_u K	A_{ul} s^{-1}	g_u	Line area mK km s^{-1}	Velocity km s^{-1}	FWHM km s^{-1}	T_{peak} mK	RMS mK	S/N
					PDR						
t − HCOOH	$4_{14} - 3_{13}$	86.546	13.6	6.0×10^{-6}	9	14.3±2.5	10.63	0.41	32.6	6.0	5
t − HCOOH	$4_{04} - 3_{03}$	89.579	10.8	7.0×10^{-6}	9	13.9±2.6	10.74	0.58	22.6	5.8	4
t − HCOOH	$4_{22} - 3_{21}$	90.165	23.5	6.0×10^{-6}	9	10.2±2.2	10.91	0.51	18.7	5.4	3
t − HCOOH	$4_{13} - 3_{12}$	93.098	14.4	8.0×10^{-6}	9	10.8±2.4	10.54	0.51	19.7	6.0	3
t − HCOOH	$5_{15} - 4_{14}$	108.127	18.8	1.3×10^{-5}	11	11.3±2.9	10.83	0.38	27.7	9.8	3
t − HCOOH	$5_{05} - 4_{04}$	111.747	16.1	1.4×10^{-5}	11	13.2±5.1	10.82	0.41	30.0	9.3	3
t − HCOOH	$6_{16} - 5_{15}$	129.672	25.0	2.2×10^{-5}	13	17.8±4.1	10.66	0.40	42.1	13.2	3
t − HCOOH	$6_{06} - 5_{05}$	133.767	22.5	2.5×10^{-5}	13	17.1±3.9	10.57	0.36	45.2	14.1	3
t − HCOOH	$6_{24} - 5_{23}$	135.738	35.4	2.3×10^{-5}	13	16.1±3.5	10.46	0.30	49.9	13.9	4
					CORE						
t − HCOOH	$4_{04} - 3_{03}$	89.579	10.8	7.0×10^{-6}	9	17.2±2.8	10.56	0.59	27.4	6.2	4
t − HCOOH	$4_{13} - 3_{12}$	93.098	14.4	8.0×10^{-6}	9	11.4±2.6	10.64	0.34	31.4	6.5	5
t − HCOOH	$5_{15} - 4_{14}$	108.127	18.8	1.3×10^{-5}	11	16.3±3.5	10.61	0.38	40.1	9.9	4
t − HCOOH	$5_{05} - 4_{04}$	111.747	16.1	1.4×10^{-5}	11	11.5±3.1	10.54	0.30	36.3	9.0	4
t − HCOOH	$6_{06} - 5_{05}$	133.767	22.5	2.5×10^{-5}	13	26.2±5.6	10.39	0.44	55.9	13.5	4

Note: All temperatures are given in the main beam temperature scale.

Table 7.3: Observation parameters of the deep integrations of the CH_2CO lines detected towards the PDR and dense core.

Molecule	Transition	ν GHz	E_u K	A_{ul} s^{-1}	g_u	Line area mK km s^{-1}	Velocity km s^{-1}	FWHM km s^{-1}	T_{peak} mK	RMS mK	S/N
				PDR							
o − CH_2CO	$4_{13} - 3_{12}$	81.586	22.9	5.0×10^{-6}	27	83.1±10.7	10.62	0.69	113.4	19.8	6
o − CH_2CO	$5_{15} - 4_{14}$	100.095	27.5	1.0×10^{-5}	33	87.9± 3.6	10.70	0.64	128.7	7.4	17
o − CH_2CO	$5_{14} - 4_{13}$	101.981	27.8	1.1×10^{-5}	33	89.0± 3.2	10.67	0.65	127.7	7.1	18
o − CH_2CO	$7_{17} - 6_{16}$	140.127	40.0	2.9×10^{-5}	45	77.9± 4.7	10.66	0.55	133.0	12.4	11
o − CH_2CO	$7_{16} - 6_{15}$	142.769	40.5	3.1×10^{-5}	45	68.4± 8.1	10.66	0.47	135.3	25.6	5
o − CH_2CO	$8_{18} - 7_{17}$	160.142	47.6	4.5×10^{-5}	51	102.7±13.5	10.74	0.72	134.2	35.7	4
o − CH_2CO	$10_{19} - 9_{18}$	203.940	66.9	9.3×10^{-5}	63	45.9± 7.0	10.72	0.67	64.8	10.6	6
p − CH_2CO	$5_{05} - 4_{04}$	101.037	14.5	1.1×10^{-5}	11	45.3± 3.1	10.81	0.70	60.8	6.8	9
p − CH_2CO	$7_{07} - 6_{06}$	141.438	27.2	3.1×10^{-5}	15	42.9± 6.7	10.67	0.56	71.6	17.9	4
o − CH_2CO[c]	$5_{33} - 4_{32}$[a]	101.002	132.8	7.0×10^{-6}	33	31.0± 4.5	10.98	0.87	33.6	8.5	4
o − CH_2CO[c]	$7_{35} - 6_{34}$[b]	141.402	145.4	2.5×10^{-5}	45	50.2± 8.0	10.28	1.03	45.9	16.9	3
o − CH_2CO[c]	$7_{25} - 6_{24}$	141.452	79.5	2.8×10^{-5}	15	39.1± 6.9	10.48	0.83	44.4	15.7	3
				CORE							
o − CH_2CO	$4_{13} - 3_{12}$	81.586	22.9	5.0×10^{-6}	27	34.3±8.6	10.86	0.69	47.0	17.8	3
o − CH_2CO	$5_{15} - 4_{14}$	100.095	27.5	1.0×10^{-5}	33	38.9±3.3	10.67	0.52	70.7	7.8	9
o − CH_2CO	$5_{14} - 4_{13}$	101.981	27.8	1.1×10^{-5}	33	33.3±3.2	10.65	0.47	66.6	7.8	9
o − CH_2CO	$7_{17} - 6_{16}$	140.127	40.0	2.9×10^{-5}	45	30.6±4.2	10.60	0.51	56.5	11.8	5
p − CH_2CO	$5_{05} - 4_{04}$	101.037	14.5	1.1×10^{-5}	11	29.5±3.9	10.68	0.73	37.7	8.0	5
p − CH_2CO	$7_{07} - 6_{06}$	141.438	27.2	3.1×10^{-5}	15	31.1±7.0	10.68	0.69	42.5	17.0	3

Note: All temperatures are given in the main beam temperature scale.

[a] Blended with the $5_{32} - 4_{31}$ line.

[b] Blended with the $7_{34} - 6_{33}$ line.

Table 7.4: Observation parameters of the deep integrations of the CH_3CHO lines detected towards the PDR and dense core.

Molecule	Transition	ν GHz	E_u K	A_{ul} s^{-1}	g_u	Line area mK km s^{-1}	Velocity km s^{-1}	FWHM km s^{-1}	T_{peak} mK	RMS mK	S/N
				PDR							
CH_3CHO-E	$5_{15}-4_{14}$	93.595	15.8	2.5×10^{-5}	22	57.5± 2.5	10.75	0.63	86.0	5.2	16
CH_3CHO-E	$5_{05}-4_{04}$	95.947	13.9	2.8×10^{-5}	22	81.6± 3.0	10.67	0.68	113.5	6.1	19
CH_3CHO-E	$5_{14}-4_{13}$	98.863	16.6	3.0×10^{-5}	22	68.2± 3.5	10.68	0.61	104.7	8.0	13
CH_3CHO-E	$6_{16}-5_{15}$	112.254	21.2	4.5×10^{-5}	26	41.8± 4.1	10.59	0.47	83.4	11.1	8
CH_3CHO-E	$6_{06}-5_{05}$	114.940	19.4	5.2×10^{-5}	26	88.2±15.3	10.65	0.67	124.3	32.0	4
CH_3CHO-E	$7_{07}-6_{06}$	133.831	25.9	8.2×10^{-5}	30	36.2± 7.4	10.70	0.83	41.0	16.6	2
CH_3CHO-E	$7_{16}-6_{15}$	138.285	28.9	8.6×10^{-5}	30	30.6± 4.7	10.60	0.52	54.9	14.5	4
CH_3CHO-E	$8_{18}-7_{17}$	149.505	34.7	1.1×10^{-4}	34	20.5± 4.2	10.81	0.33	59.1	16.8	4
CH_3CHO-A	$5_{15}-4_{14}$	93.581	15.7	2.5×10^{-5}	22	44.3± 2.6	10.66	0.54	76.9	6.0	13
CH_3CHO-A	$5_{05}-4_{04}$	95.963	13.8	2.8×10^{-5}	22	73.1± 2.8	10.70	0.63	108.5	5.8	19
CH_3CHO-A	$5_{24}-4_{23}$	96.274	22.9	2.4×10^{-5}	22	13.5± 2.3	10.55	0.48	26.7	5.6	5
CH_3CHO-A	$5_{23}-4_{22}$	96.633	23.0	2.4×10^{-5}	22	12.3± 1.9	10.68	0.41	28.5	5.1	6
CH_3CHO-A	$5_{14}-4_{13}$	98.901	16.5	3.0×10^{-5}	22	73.8± 3.4	10.73	0.62	112.7	7.7	15
CH_3CHO-A	$6_{16}-5_{15}$	112.249	21.1	4.5×10^{-5}	26	56.0± 5.1	10.68	0.69	76.3	11.4	7
CH_3CHO-A	$6_{06}-5_{05}$	114.960	19.4	5.0×10^{-5}	26	83.6±13.6	10.71	0.67	117.5	28.8	4
CH_3CHO-A	$7_{07}-6_{06}$	133.854	25.8	7.9×10^{-5}	30	30.8± 3.6	10.61	0.39	73.9	11.9	6
CH_3CHO-A	$7_{25}-6_{24}$	135.685	35.0	7.9×10^{-5}	30	15.4± 3.2	10.76	0.29	50.5	13.2	4
CH_3CHO-A	$7_{16}-6_{15}$	138.320	28.8	8.6×10^{-5}	30	52.9± 6.8	10.74	0.49	100.6	17.0	6
				CORE							
CH_3CHO-E	$5_{15}-4_{14}$	93.595	15.8	2.5×10^{-5}	22	34.4±2.2	10.71	0.74	43.5	4.2	10
CH_3CHO-E	$5_{05}-4_{04}$	95.947	13.9	2.8×10^{-5}	22	38.5±2.4	10.66	0.63	57.1	5.4	10
CH_3CHO-E	$5_{14}-4_{13}$	98.863	16.6	3.0×10^{-5}	22	26.6±4.0	10.63	0.60	41.5	8.8	5
CH_3CHO-A	$5_{15}-4_{14}$	93.581	15.7	2.5×10^{-5}	22	26.7±2.0	10.62	0.57	44.1	4.6	10
CH_3CHO-A	$5_{05}-4_{04}$	95.963	13.8	2.8×10^{-5}	22	33.1±3.1	10.67	0.80	38.9	5.7	7
CH_3CHO-A	$5_{14}-4_{13}$	98.901	16.5	3.0×10^{-5}	22	35.5±5.7	10.74	0.74	44.8	9.5	5
CH_3CHO-A	$6_{16}-5_{15}$	112.249	21.1	4.5×10^{-5}	26	16.0±3.5	10.62	0.55	27.2	9.9	3

Note: All temperatures are given in the main beam temperature scale.

Table 7.5: Observation parameters of the deep integrations of the CH_3CCH lines detected towards the PDR and dense core.

Molecule	Transition	ν GHz	E_u K	A_{ul} s^{-1}	g_u	Line area mK km s^{-1}	Velocity km s^{-1}	FWHM[a] km s^{-1}	T_{peak} mK	RMS mK	S/N
				PDR							
CH_3CCH-E	5_1-4_1	85.456	19.5	5.93×10^{-7}	22	15.2± 2.7	10.54	0.60	23.9	6.8	3
CH_3CCH-E	6_1-5_1	102.546	24.4	1.05×10^{-6}	26	16.0± 2.7	10.95	0.60	25.0	7.6	3
CH_3CCH-E	8_1-7_1	136.725	36.7	2.50×10^{-6}	34	16.8± 3.7	10.53	0.60	26.3	12.2	2
CH_3CCH-E	12_1-11_1	205.077	71.2	8.95×10^{-6}	50	22.3± 3.7	10.67	0.60	34.9	7.6	4
CH_3CCH-E	13_1-12_1	222.163	81.9	1.14×10^{-5}	27	15.3± 3.8	10.66	0.60	23.9	7.9	3
CH_3CCH-A	5_0-4_0	85.457	12.3	6.18×10^{-7}	22	14.6± 2.3	10.77	0.60	22.8	5.7	4
CH_3CCH-A	6_0-5_0	102.548	17.2	1.08×10^{-6}	26	10.8± 2.7	10.72	0.60	17.0	7.1	2
CH_3CCH-A	8_3-7_3	136.705	94.6	2.25×10^{-6}	34	15.2± 3.7	10.55	0.60	23.8	11.8	2
CH_3CCH-A	12_0-11_0	205.081	64.0	9.02×10^{-6}	50	22.0± 4.0	10.76	0.60	34.4	7.9	4
CH_3CCH-A	13_0-12_0	222.167	74.6	1.15×10^{-5}	27	14.1± 3.7	10.35	0.60	22.1	7.6	2
CH_3CCH-A	14_3-13_3	239.211	151.1	9.96×10^{-5}	58	28.6± 5.9	10.46	0.60	44.8	12.8	3
CH_3CCH-A	14_0-13_0	239.252	86.1	1.40×10^{-5}	58	54.2± 7.5	10.63	0.60	84.9	16.1	5
				CORE							
CH_3CCH-E	5_1-4_1	85.456	19.5	5.93×10^{-7}	22	13.5± 1.9	10.48	0.50	25.4	5.5	4
CH_3CCH-E	6_1-5_1	102.546	24.4	1.05×10^{-6}	26	20.0± 2.9	10.48	0.50	37.6	8.9	4
CH_3CCH-E	8_1-7_1	136.725	36.7	2.50×10^{-6}	34	27.4± 4.0	10.56	0.50	51.6	14.2	3
CH_3CCH-A	5_0-4_0	85.457	12.3	6.18×10^{-7}	22	16.8± 2.4	10.59	0.50	31.5	6.3	4
CH_3CCH-A	6_0-5_0	102.548	17.2	1.08×10^{-6}	26	25.7± 2.8	10.74	0.50	48.2	8.5	5

Note: All temperatures are given in the main beam temperature scale.
[a] The line width was fixed to improve the gaussian fit.

Chapter 8

Comparison with other environments

8.1 Introduction

Understanding which processes dominate the chemistry in different environments is important to interpret observations because it provides information about the history of the sources, and important physical processes, such as star formation. The different environments that can be found in the ISM include the cold UV-shielded gas, the warm (PDRs) and hot gas associated to star-forming regions, shocked gas also associated with star forming regions, and the diffuse medium. Today, we have a good understanding of the main chemical properties of the different environments, thanks to detailed studies performed in Galactic sources, that start to be considered as templates.

The chemistry in cold gas is dominated by ion-molecule reactions, and is initiated by cosmic rays that ionize H_2. These regions are characterized by large abundances of deuterated species (e.g., DCN), molecular ions (e.g., DCO^+ and N_2H^+) and isomers (e.g., HNC). The hot core regions surrounding protostars are characterized by large temperatures ($T_{\rm kin}$ > 100 K), and present large amounts of complex organic molecules, especially methanol, which is thermally desorbed from dust grains and later triggers an active chemistry in the hot gas. In shocked regions, the gas reaches higher temperatures ($T_{\rm kin}$ > 1000 K). Here, complex molecules are also desorbed from dust grains. In addition, the grains undergo collisions with the gas-phase species and between themselves, leading to their partial destruction through shattering and sputtering processes. The release of silicon into the gas-phase leads to the formation of silicon monoxide (SiO).

Observations towards extragalactic sources has led to the detection of $\sim$ 50 molecules, which is about one third of the molecules detected in our Galaxy. The study of extragalactic sources is complex because the individual gas components are not resolved. Observations in other galaxies probe a mix of cold and hot gas. By comparing the molecular abundances in extragalactic sources with the ones in different Galactic sources, which are better understood, it should be possible to disentangle the different gas components present in other galaxies, and determine what are the processes that dominate the chemistry, either cold, hot-core like, shocked or FUV-induced chemistry.

In this chapter I present a comparison between the chemical properties of the Horsehead nebula and the ones found in other prototypical Galactic PDRs and also the ones found in other Galactic and extragalactic environments. I will start by comparing the Horsehead with other prototypical PDRs, such as the Orion Bar, NGC 7023 and Mon R2. Because the diffuse medium has a similar χ/n to that of the Horsehead, I will also include it in the comparison of the different PDRs. I will then compare the chemistry of the Horsehead with the one in other environments, such as dense cores, low- and high-mass young stellar objects, giant molecular

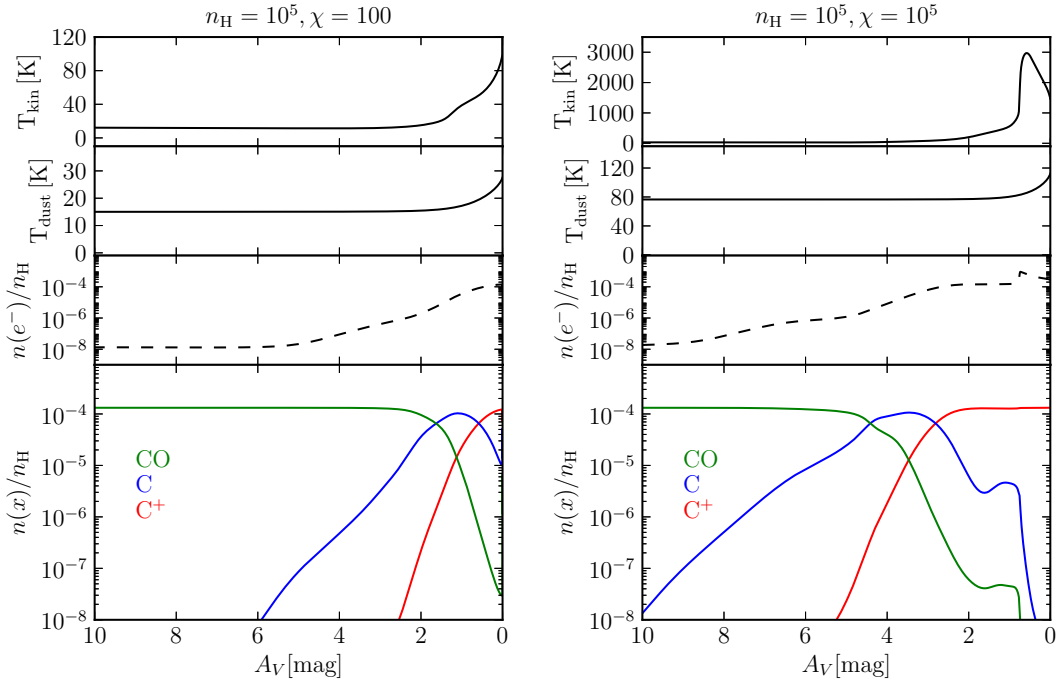

Figure 8.1: PDR models for a cloud with constant density and two different radiation fields representative of low-UV (left) and high-UV (right) PDRs.

clouds in the galactic center, AGN and starburst galaxies.

8.2 Prototypical PDRs

The Horsehead is the only low-UV illuminated PDR that has been studied in detail. Most of the prototypical Galactic PDRs, such as NGC 7023, Orion Bar and Mon R2, are high-UV illuminated PDRs and have been studied in great detail because they are bright at millimeter and sub-millimeter wavelengths, in contrast to the Horsehead where lines are fainter and thus more time-consuming to observe. The different radiation fields produce differences in the chemistry between low and high-UV PDRs. Fig. 8.1 shows two PDR models for a cloud with constant density of 10^5 cm^{-3}, and two different radiation fields of $\chi = 100$ (low-UV) and $\sim 10^5$ (high-UV). In the low-UV case, the kinetic temperature at the edge of the cloud ($A_V \sim 1$) reaches ~ 50 K, while in the high-UV case, the gas temperature at the edge reaches ~ 400 K. Dust grains are also warmer in the high-UV case ($T_{\rm dust} \sim 80$ K) compared to the low-UV case ($T_{\rm dust} \sim 20$ K). The C^+/C/CO transition occurs at different positions in the two models. In the low-UV case, it occurs at $A_V \sim 1$ mag, while in the high-UV case it moves to $A_V \sim 4$ mag as radiation penetrates deeper inside the cloud.

The main characteristics of the Galactic PDRs chosen for this comparison are described next and their physical properties are summarized in Table 8.1. The abundances of different species towards each PDR are listed in Table 8.2.

Table 8.1: Physical properties of prototypical PDRs.

Source	χ (Draine)	$n_{\rm H}$ cm^{-3}	$\chi/n_{\rm H}$	Distance (pc)	Ref.
Horsehead	60	$\sim 6\times10^4$	$\sim 10^{-3}$	400	
Diffuse gas	~ 1	~ 100	$\sim 10^{-2}$	$100-200$ pc	
NGC 7023	2×10^3	$\sim 1\times10^5$	$\sim 10^{-2}$	470	1,2
Orion Bar	10^4-10^5	$\sim 3\times10^5$	$\sim 10^{-2}-10^{-1}$	414	3,4
Mon R2	5×10^5	$\sim 2\times10^6$	$\sim 10^{-1}$	830	5,6,7

References. (1) Fuente et al. (1993); (2) van den Ancker et al. (1997); (3) Fuente et al. (1996); (4) Menten et al. (2007); (5) Rizzo et al. (2003); (6) Ginard et al. (2012); (7) Herbst & Racine (1976)

8.2.1 Horsehead

In order to make a better comparison, I have estimated the abundance of CN, HCN, HNC and N_2H^+ in the Horsehead. These species are all detected in the line survey, and the data will be published in forthcoming papers. To estimate the abundance of CN, I assumed LTE with an excitation temperature of 10 K. For HCN and HNC, RADEX was used to compute the column densities. Because the lines are optically thick, I estimated the abundances of their ^{13}C isotopologues and then used an isotopic ratio of 60 to estimate the abundance of the ^{12}C species. For HN^{13}C, the the collisional rates for HNC were used. For N_2H^+ a fit of the hyperfine structure with CLASS results in low opacities ($\tau \sim 0.1$). Therefore the excitation temperature cannot be determined. For this reason I estimated the N_2H^+ abundance using the integrated intensity of all the hyperfine lines and assumed an excitation temperature of 10 K. N_2H^+ is expected to arise from the cold gas. Indeed, the lines are brighter towards the dense core, but they are also observed at the PDR position. Assuming that the N_2H^+ emission arises from a filament of $\sim 25''$ centered at the dense core, I find that 80% of the flux detected at the PDR corresponds to beam pick-up from the dense core due to the large beam size ($27''$) at 3 mm. ^{13}CN lines are brighter towards the PDR. Only two hyperfine components are detected towards the dense core. This emission probably arises in the foreground lower density layer in the dense core line of sight, and the measured CN abundance is thus considered as an upper limit.

8.2.2 NGC 7023

The reflection nebula NGC-7023 consists of a sheet of dense material that is illuminated by the central Herbig B3Ve star HD 200775. The birth of this star created a cavity in the molecular cloud, and three PDRs were formed in the surrounding gas, one to the north-west (NW), another one to the south (S), and the last one further away to the east (E). The three PDRs are viewed approximately edge-on.

The abundances reported in Table 8.2 are taken from Fuente et al. (2003) and Fuente et al. (1993) for the PDR-peak position, corresponding to the north-west PDR. The HCO abundance is taken from Schilke et al. (2001b). The assumed H_2 column density to compute

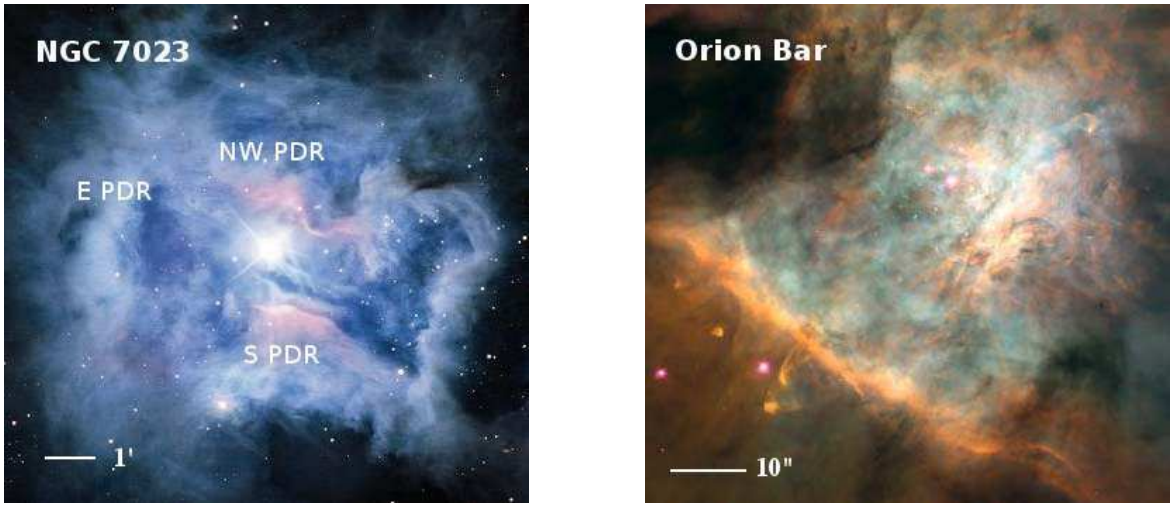

Figure 8.2: *Left:* NGC 7023. Credit: Jean-Charles Cuillandre (CFHT), Hawaiian Starlight, CFHT. *Right:* Hubble image of the Orion Bar. Credit: NASA, Hubble Space Telescope.

the abundances is 1.1×10^{22} cm^{-2}.

8.2.3 Orion Bar

The Orion Bar is a prototypical high-UV illumination PDR, located between the Orion molecular cloud and the HII region surrounding the Trapezium cluster. Due to its proximity and nearly edge-on geometry, it has been used extensively in the past decades to test theoretical models (e.g., Parise et al. 2009; Goicoechea et al. 2011; Nagy et al. 2013). The Orion Bar consists a low density ($n_{\rm H} \sim 10^4 - 10^5$ cm^{-3}) gas component. In order to explain the observed high-J CO lines (up to $J = 21$), CO^+, OH and other high-temperature tracers, some authors (e.g., Lis & Schilke 2003; Goicoechea et al. 2011) have invoked the presence of dense ($n_{\rm H} \sim 10^6$ cm^{-3}) clumps, which are very hot in their surface, or a gas component with very high pressures. The presence of clumps is still debated.

The abundances reported in Table 8.2 are taken from Fuente et al. (2003) and Fuente et al. (1996) for the ionization front (IF) position. The HCO and HCO^+ column densities are taken from Schilke et al. (2001b). The assumed H_2 column density is 6.5×10^{21} cm^{-2}. The HCS^+ abundance is taken from (Leurini et al. 2006), and corresponds to the clump medium (Orion Bar (HCN) position of Schilke et al. 2001a). The H_2CO and CH_3OH abundances are taken from Jansen et al. (1995), and correspond to the molecular peak position. For C_4H and N_2H^+, the abundances are taken from Cuadrado et al. (2014, in prep), and correspond to the IF position.

8.2.4 Mon R2

Monoceros R2 is a complex star forming region. It contains the closest and brightest Galactic ultracompact HII region, which was created by the interaction of the central infrared source IRS1 (see Fig. 8.3) with its host molecular cloud. The central star associated to IRS1 is a

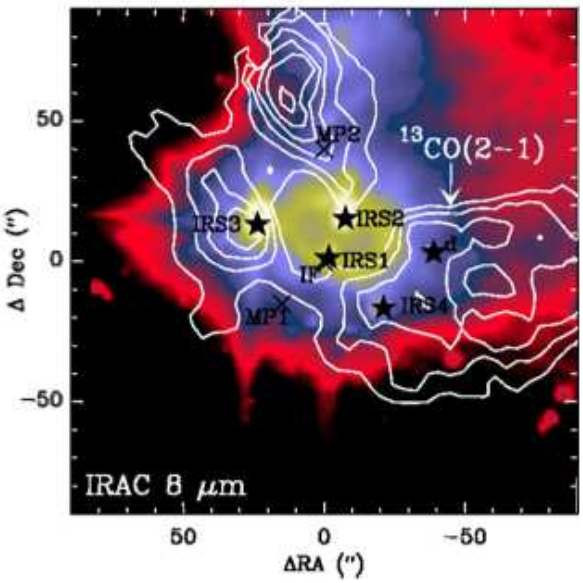

Figure 8.3: IRAC 8 μm image of Mon R2 with ^{13}CO contours. Figure from Ginard et al. (2012).

B0V star. A PDR was formed in the surroundings of the ultracompact HII region.

The abundances listed in Table 8.2 are taken from Ginard et al. (2012) and Rizzo et al.

Table 8.2: Abundances with respect to H_2 (in units of 10^{-11}), towards prototypical PDRs and the diffuse medium.

	Horsehead PDR	NGC 7023 North PDR	Orion Bar IF	Mon R2 IF	Mon R2 MP2	Diffuse medium
CO^+	< 0.1	3	6	1	-	-
HCO^+	180	40	260	120	84	300
HOC^+	0.8	0.4	3	0.3	-	4
HCO	168	29	110	< 7	17	83
$H^{13}CO^+$	3	3	12	2	1.4	5
CN	690	370	1800	< 1680	1140	3000
HCN	130	83	650	420	228	430
HNC	67	44	180	10	16	100
CS	400	45	290	234	198	300
HCS^+	3.4	-	3.9	19	6.5	-
C_2H	2800	340	8700	860	540	3000
c-C_3H_2	220	20	140	20	17	150
C_4H	200	-	130	63	160	< 300
N_2H^+	< 1.7	< 44	1.2	4.9	5.2	-
H_2CO	56	-	600	150	120	630
CH_3OH	24	-	110	-	-	< 1000

Table 8.3: Physical properties of different environments in the ISM.

Type	Source	Distance	Reference
Diffuse medium	BL Lac	$100 - 200$ pc	-
Dense core	L1498	140 pc	Kenyon et al. (1994)
Hot corino	IRAS 16293	120 pc	Loinard et al. (2008)
Hot core	Orion KL	414 pc	Menten et al. (2007)
G.C. GMC	Sgr B2(N)	7.9 kpc	Reid et al. (2009)
Starburst galaxy	M82	3.6 Mpc	Freedman et al. (1994)
AGN	NGC 1068	14.4 Mpc	Bland-Hawthorn et al. (1997)
high$-z$ galaxy	FG0.89	$z = 0.89$	Wiklind & Combes (1996)

(2003). Ginard et al. (2012) performed a 3 mm and 1 mm spectral line survey towards three positions in Mon R2: the ionization front (IF), a molecular peaks to the south of IRS1 (MP1) and a second molecular peak farther to the north (MP2). Table 8.2 displays the reported abundances for the IF and MP2 positions. The CO^+, $H^{13}CO^+$ and HOC^+ abundances are taken from Rizzo et al. (2003). The abundances of CS, CN and HCN are derived from their ^{13}C isotopologues, assuming $^{12}C/^{13}C = 60$. The assumed H_2 column density is 5.6×10^{22} cm^{-2} and 7.6×10^{22} cm^{-2} for the IF and MP2 positions, respectively.

8.3 Other environments

Several different environments were chosen for this comparison. These include the diffuse gas, which resembles the properties of PDRs, a dense core in addition to the one associated to the Horsehead, a low-mass protostar (hot-corino), a high-mass protostar (hot-core), giant molecular clouds in the galactic center, and three extragalactic sources, including a starburst, an AGN and a high-z galaxy. The targeted sources and their distances are listed in Table 8.3. Table 8.4 summarizes the abundances with respect to H_2 of several species in the different environments and their main characteristics are described next.

8.3.1 Diffuse medium

The diffuse ISM has typical densities of ~ 100 cm^{-3} and radiation fields of $\chi \sim 1$. It can therefore be considered as a very low density and low-UV field PDR. In spite of the low densities and low shielding from dust, polyatomic molecules exist in diffuse clouds ($A_V \lesssim 1$), and they are unexpectedly abundant. Because of the low densities, diffuse clouds hardly ever present molecular emission in any species beside CO (Liszt & Lucas 2000). The molecular abundances are therefore derived from the mm-wave absorption spectra towards background sources. For this comparison, I include the measured abundances toward the blazar BL Lac (B2200+420) from Lucas & Liszt (2000), Liszt & Lucas (2001) and Lucas & Liszt (2002). The HCO^+ abundance is scaled from the $H^{13}CO^+$ abundance assuming $^{12}C/^{13}C = 60$.

8.3.2 Dense core: L1498

L1498 is considered to be a starless core because it is not associated to any IR point source (Beichman 1986) or 1.2 mm point sources (Tafalla et al. 2002). It is a relatively isolated dense core located in the Taurus complex, with a central density of $\sim 9 \times 10^4$ cm^{-2} and a kinetic temperature of ~ 10 K (Tafalla et al. 2004, 2006).

Tafalla et al. (2006) made maps of L1498 in several molecular lines from 15 different species with the IRAM-30 m telescope. They derived the radial abundance profile for each species using a non-LTE Monte Carlo code, with the aim of studying the depletion towards the core center. These abundances are reported in Table 8.4. The C_2H abundance is taken from Padovani et al. (2009) and the HCN and HNC abundances are taken from Padovani et al. (2011). The $^{13}CN/H^{13}CN$ abundance ratio was recently computed by Hily-Blant et al. (2013) to be ~ 0.6. The CN abundance listed in Table 8.4 for L1498 is derived from this ratio and the HCN abundance derived by Padovani et al. (2011). These studies were performed by the same group and the abundances were computed with the same radiative transfer code.

8.3.3 Hot corino: IRAS 16293-2422

IRAS 16293-2422 (hereafer IRAS 16293) is the prototypical low-mass protostar, with a rich line spectrum. It is located in the ρ Ophiuchi star-forming region, at a distance of ~ 120 pc (Loinard et al. 2008). IRAS 16293 has a complex structure. It is a protobinary system, and its two components (A and B) are separated by 480 AU in projection ($\sim 4''$). The south-east component A consists of two bipolar outflows (Mizuno et al. 1990), two centimeter sources (A1 and A2; Wootten 1989) and two submillimeter sources (Aa and Ab; Chandler et al. 2005). Several complex molecules have been detected in both A and B sources, arising from the hot corino region (e.g., Bottinelli et al. 2004b; Kuan et al. 2004; Bisschop et al. 2008). Fig. 8.5 shows the 670 GHz continuum map of IRAS 16293 at a resolution of $0.32'' \times 0.18''$ from ALMA (Loinard et al. 2013). The A and B components are not resolved by single-dish

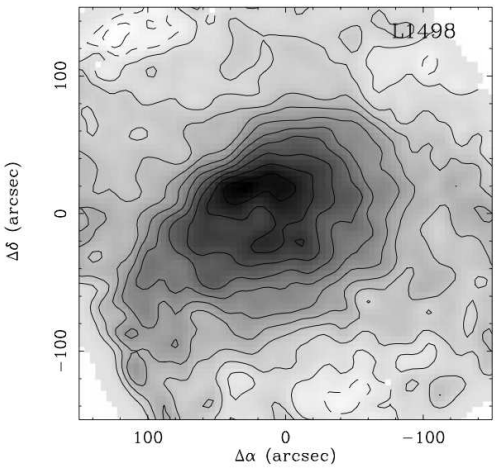

Figure 8.4: 1.2 mm continuum map of L1498. Figure from Tafalla et al. (2004).

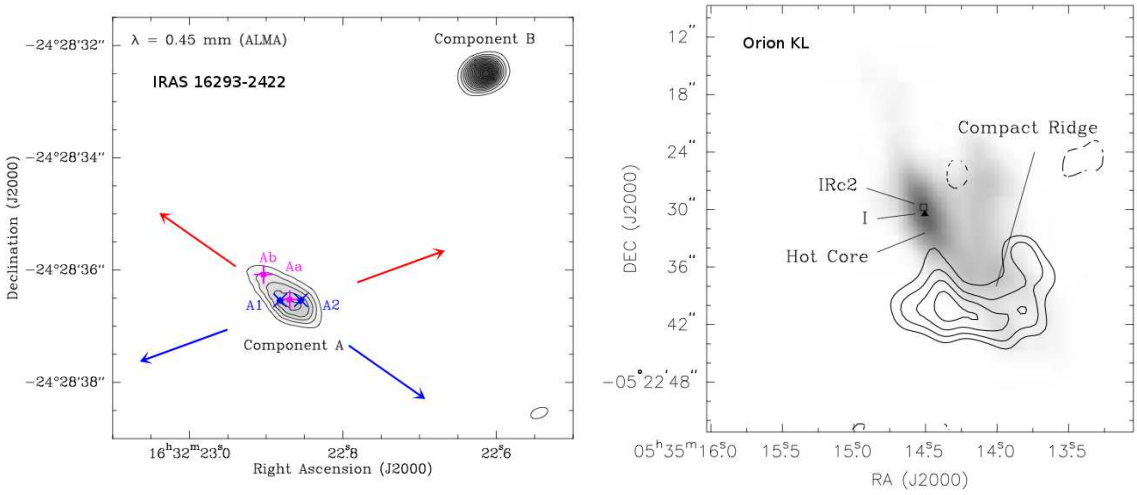

Figure 8.5: *Left:* Sub-millimeter ($\lambda = 0.45$ mm) continuum image of the IRAS 16293-2422 system from ALMA. The two main components (A and B) are shown, and the direction of the two outflows driven from component A are indicated. The submillimeter peaks Aa and Ab and the centimeter sources A1 and A2 are also shown. Figure from Loinard et al. (2013). *Right:* Composite image of the Orion KL region observed with the BIMA array. The HCOOH emission is shown in contours and overlaid on the 1 mm continuum emission (gray scale). The Hot Core and Compact Ridge shown are shown. Image from Liu et al. (2002).

telescopes, but they have different velocities: 3.9 $\mathrm{km\,s^{-1}}$ (A) and 2.7 $\mathrm{km\,s^{-1}}$ (B) (Caux et al. 2011).

van Dishoeck et al. (1995) performed a millimeter and submillimeter line survey of IRAS 16293 in the 230 and 345 GHz windows with the CSO and JCMT telescopes. They derived beam-averaged abundances assuming LTE and statistical equilibrium calculations for those species for which collisional coefficients were available. It is important to notice that the abundances reported in Table 8.4 are not corrected for beam dilution, and therefore contain mixed information on the different components (A and B sources, and the surrounding envelope). The abundances are computed for a H_2 column density 2×10^{23} $\mathrm{cm^{-2}}$. A more recent line survey of this source is the one performed by Caux et al. (2011). Unfortunately, the column densities of the detected species have not been computed yet.

8.3.4 Hot core: Orion KL

Orion KL is the closest high-mass star-forming region, at a distance of 414 pc (Menten et al. 2007). Because it has a rich molecular spectrum, it has been the target for numerous millimeter and submillimeter line surveys (e.g., Tercero et al. 2010, 2011). The region contains several spatial components (e.g., hot core, compact ridge, extended ridge, and plateau). The Hot Core and the Compact Ridge are separated by only ∼5800 AU, and present chemical differences. The Hot Core is rich in nitrogen-bearing molecules, while the Compact Ridge is rich in oxygen-bearing molecules (e.g., Blake et al. 1987; Liu et al. 2002; Friedel & Snyder 2008). These two components cannot be resolved with single-dish telescopes, but they can

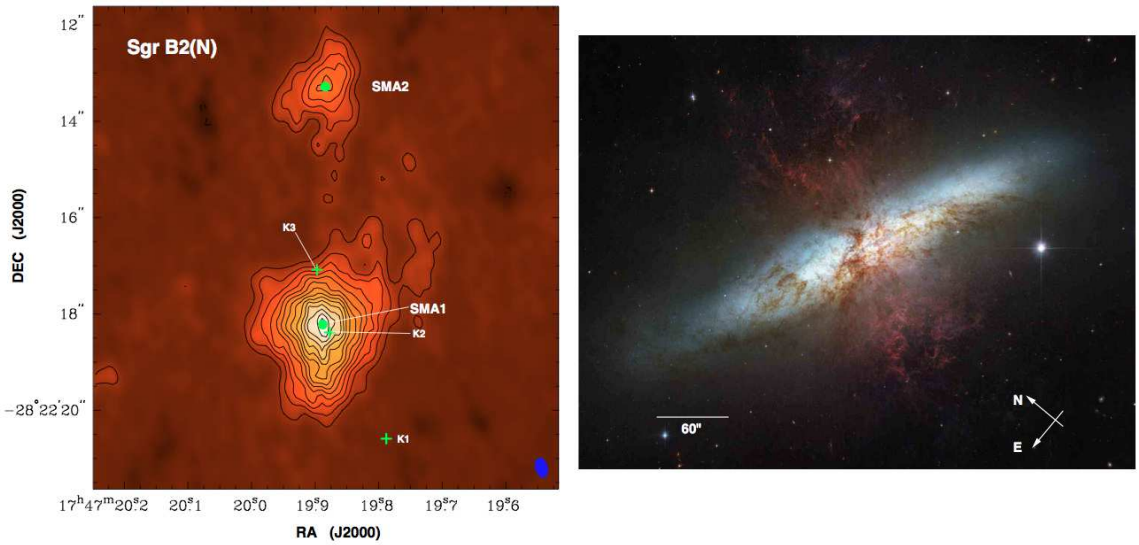

Figure 8.6: *Left:* SMA continuum map of Sgr B2(N) at 850 μm, where the two hot cores (SMA1 and SMA2) are shown. Figure from Qin et al. (2011). *Right:* Hubble image of the M82 galaxy. Credit: NASA, ESA, and The Hubble Heritage Team (STScI/AURA).

be separated by their different velocities. The Hot Core consists of clumps of very dense ($\sim 10^6$ cm^{-3}), warm ($\sim$ 200 K) material with systemic velocities of $\sim 2.5 - 7.5\,\mathrm{km\,s^{-1}}$ (Comito et al. 2005).

For this comparison, the abundances towards the Orion KL Ridge are taken from Blake et al. (1987). For C_2H, C_3H_2, C_4H, CN, HCN, HNC, HC_3N, CS, CO^+, HCO^+, HCO and CH_3CCH, the abundances listed in Table 8.4 correspond to the Extended Ridge, and for H_2CO, CH_3OH, CH_3CN, CH_2CO, HCOOH and CH_3CHO, the abundance correspond to the Compact Ridge.

8.3.5 Galactic center GMC: Sgr B2(N)

The Sagittarius B2 molecular cloud (hereafter Sgr B2) is the most massive ($5-10\times10^6$ M$_\odot$ Lis & Goldsmith 1990) star forming region in our Galaxy. It is located at a projected distance of $\sim$ 100 pc from the Galactic center, which is located at $\sim$ 8 kpc from the Sun (Reid et al. 2009). Sgr B2 contains two main sites of extremely active high-mass star formation, Sgr B2(N) and Sgr B2(M), which are separated by $\sim$ 1.8 pc in projection (corresponding to $\sim 48''$). Sgr B2(N) has been the place of discovery of many of the most complex molecules discovered in the ISM so far. A few examples are: glycoaldehyde ($CH_2(OH)CHO$ Hollis et al. 2000), acetamide (CH_3CONH_2 Hollis et al. 2006), aminoacetonitrile (NH_2CH_2CN Belloche et al. 2008a) and ethyl formate (C_2H_5OCHO Belloche et al. 2009). Sgr B2(N) contains two hot core sources separated by 0.2 pc in projection ($5''$). Fig. 8.6 shows the 850 μm continuum map of Sgr B2(N) at a resolution of $0''.4 \times 0''.24$ from ALMA (Qin et al. 2011). The two hot cores (SMA1 and SMA2) are not resolved spatially by single-dish telescopes, but they can be separated in velocity.

Belloche et al. (2013) performed an unbiased, spectral line survey at 3 mm (in addition to partial surveys at 2 and 1.3 mm) towards Sgr B2(N) and (M) with the IRAM-30m telescope. They detected 56 different molecules (plus 66 isotopologues) towards Sgr B2(N), and computed their column densities with a simple LTE model, that takes into account optical depth effects and beam dilution. For HC_3N, H_2CO, CH_3OH, CH_3CN, CH_2CO, CH_3CCH, $t-HCOOH$ and CH_3CHO, the abundances reported in Table 8.4 correspond to the column densities derived by Belloche et al. (2013) for one of the hot core sources (SMA1; which has a systemic velocity of 64 $\mathrm{km\,s^{-1}}$, a source size of $\sim 2''$ and $T_{\rm rot} \sim 100$ K) divided by a H_2 column density of 1.8×10^{25} $\mathrm{cm^{-2}}$ (Belloche et al. 2008b). The reported abundance for the other molecules correspond to the column densities derived by Belloche et al. (2013) for a more extended (size $\sim 200''$) and colder ($T_{\rm rot} \sim 20$ K) component, divided by a H_2 column density of 3.0×10^{24} $\mathrm{cm^{-2}}$ (Nummelin et al. 2000). These two groups of molecules will be treated separately.

8.3.6 Starburst galaxy: M82

M82 is the prototype starburst galaxy because of its high star-forming activity. It is the nearest (3.6 Mpc) best-studied example of this class of galaxies. It is believed that the high star-formation rate (~ 9 $\mathrm{M_\odot\ yr^{-1}}$ Strickland et al. 2004) in M82 was caused by the interactions with its companion M81 (e.g., Sun et al. 2005), which is located $36'$ south from M82. M82 is viewed nearly edge-on. The central region shows two emission peaks, the north-east (NE) and south-west (SW) molecular lobes (e.g., García-Burillo et al. 2002), which are likely part of a nuclear ring of warm gas and dust heated by stars. The central ∼1 kpc region contains a large number of prominent bright clumps, with many hundreds of young massive star clusters. The supernova remnants and stellar winds from massive stars generate superwinds or outflows (e.g., García-Burillo et al. 2001). As a result, large PDRs are created in the central region of M82, where the chemistry is dominated by the UV field (Fuente et al. 2006, 2008).

Aladro et al. (2011) carried out a partial line survey at 2 and 1.3 mm with the IRAM-30 m telescope towards the NE molecular lobe of M 82. They identified 18 different species, and estimated their column densities assuming LTE. They reported fractional abundances with respect to $C^{34}S$. In order to compute the abundances with respect to H_2, an abundance of 3×10^{-10} is assumed for $C^{34}S$ in M82, which is the abundance derived in the Horsehead PDR and dense core (Goicoechea et al. 2006). This can be done because the CS and $C^{34}S$ abundances do not vary much between the different sources considered here (see Table 8.4).

8.3.7 Active galactic nucleus (AGN): NGC 1068

NGC 1068, also known as M77, is a prototypical AGN galaxy. In the optical, it looks like a normal barred spiral galaxy. Active star-forming regions are concentrated along the spiral arms, where molecular gas is abundant (Schinnerer et al. 2000). At its center it contains an active galactic nuclei (AGN) powered by a supermassive black hole (M= 1.7×10^7 $\mathrm{M_\odot}$ Schinnerer et al. 2000).

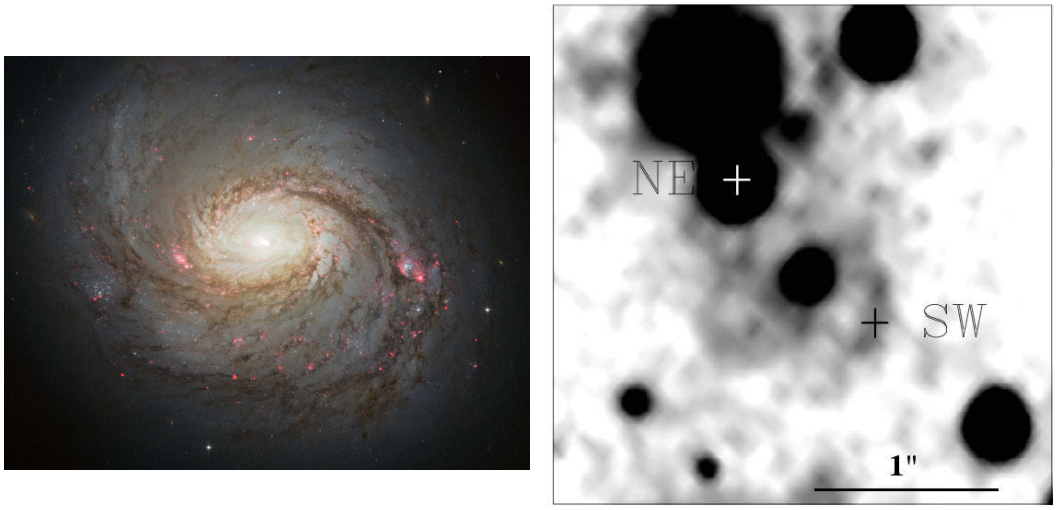

Figure 8.7: *Left:* Hubble image of NGC 1068. Credit: NASA, ESA and A. van der Hoeven. *Right:* Hubble image of the $z = 0.89$ galaxy. The positions of the SW and NE images of the quasar are indicated. Figure from Muller et al. (2011).

Aladro et al. (2013) carried out a 3 mm line survey with the IRAM-30 m telescope in the central $1.5 - 2$ kpc region of NGC 1068. They identified 24 different molecular species (including isotopologues). They computed the column densities assuming LTE. They corrected for beam dilution effects assuming an average source size of $4''$ (derived from interferometric observations) for all the species. They reported abundances with respect to $C^{34}S$. As for M82, a $C^{34}S$ abundance of 3×10^{-10} is assumed here to convert to abundances with respect to H_2.

8.3.8 High-z galaxy: FG0.89

The foreground galaxy FG0.89 is located in front of the quasar PKS 1830-211 ($z = 2.5$). It appears to be a nearly face-on spiral galaxy (Winn et al. 2002). The galaxy acts as a gravitational lens that multiplies the image of the background quasar into two main components. These two components intercept the disk galaxy on either side of its bulge at distances of ~ 2 kpc (SW) and ~ 4 kpc (NE) from the center of the galaxy. Molecular absorption from numerous species is seen in both positions (Muller et al. 2011, and references therein). The two components are separated by $1''$. Fig. 8.7 shows an image of the FG0.89 galaxy from the Hubble telescope.

Muller et al. (2011) performed a 7 mm survey of the molecular absorption lines originating in the disk of the FG0.89 galaxy with the Australia Telescope Compact Array. They detected 28 different species, plus 8 isotopologues, towards the SW absorption region. They computed the column densities assuming LTE, and derived the abundances for a H_2 column density of 2×10^{22} cm^{-2}. They are reported in Table 8.4. The CS abundance is taken from Muller et al. (2006).

Table 8.4: Abundances with respect to H_2 in units of (10^{-11}).

	BL Lac	Horsehead		L1498	IRAS 16293	Orion KL	Sgr B2(N)	M82	NGC 1068	FG0.89SW
	Diffuse	PDR	Core	Core	Hot corino	Hot core	G.C.	Starburst	AGN	$z = 0.98$ galaxy
C_2H	3000	2800	100[a]	800	25	530[c]	67[b]	3546	1875	6242
c-C_3H	15	54	-	-	-	-	-	< 26	-	-
c-C_3H_2	150	220	4.3[a]	160	3.5	8.7[c]	8[b]	132	3	264
C_4H	< 300	200	37[a]	-	-	< 0.8[c]	-	-	-	657
CN	3000	690	< 117	234	10	330[c]	23[b]	546	938	-
HCN	430	130	84	390	190	500[c]	3600[b]	108	264	1520
HNC	100	67	50	500	15	53[c]	160[b]	60	93	509
HC_3N	-	1.3	1.6	100	2.5	13[c]	67	69	114	56
CS	300	400	580	300	-	250[c]	100[b]	660	144	1866
CO^+	-	< 0.1	-	-	-	< 0.1[c]	-	18	-	-
HCO^+	300	180	780	300	180	230[c]	170[b]	490	99	875
HOC^+	4	0.8	-	-	-	-	0.37[b]	12	2.1	16
HCO	83	168	16	-	< 20	< 3.3[c]	-	105	39	65
DCO^+	-	< 0.2	16	5	1.5	-	-	-	-	-
N_2H^+	< 0.4	< 1.7	4.1	17	-	-	16	< 1	19	117
H_2CO	630	56	40	130	70	1700[d]	2800	300	< 2062	1196
CH_3OH	< 1000	24	46	60	440	12000[d]	98000	327	432	850
CH_3CN	< 4	50	1.6	-	15	32[d]	11000	18	6	65
CH_2CO	-	16	4	-	18	67[d]	3300	-	-	88
CH_3CCH	-	89	112	-	65	330[c]	210	3273	-	300
HCOOH	-	11	5	-	< 30	50[d]	83	-	-	-
CH_3CHO	-	13	5	-	< 10	$\lesssim 17$[d]	790	-	-	62

([a]) These abundances correspond to the "Cloud" position (offset $+6'', -4''$) from Pety et al. (2005); ([b]) Extended (others are hot core 1); ([c]) Extended Ridge; ([d]) Compact Ridge.

8.4 Abundance ratios

Comparing absolute abundances (relative to H_2) in different environments is complicated because the method to derive their abundances are not always the same. In some cases, detailed radiative transfer analysis are made, while in most cases LTE is assumed. A more consistent way to compare abundances in different environments is to use abundance ratios between different species. This also eliminates some calibration problems related to the observations. A few abundance ratios which can be used as diagnostic probes of different chemical processes are discussed next.

8.4.1 $HCO/H^{13}CO^+$ and $CO^+/H^{13}CO^+$

The formyl radical (HCO) emits brightly and presents enhanced abundances in FUV-illuminated regions. The abundance ratio (and the integrated line ratio, if the line is optically thin) between HCO and $H^{13}CO^+$ has proven to be an excellent tracer of FUV-induced photochemistry. In the Horsehead PDR, $HCO/H^{13}CO^+ = 56$. Abundance ratios $HCO/H^{13}CO^+ > 10$

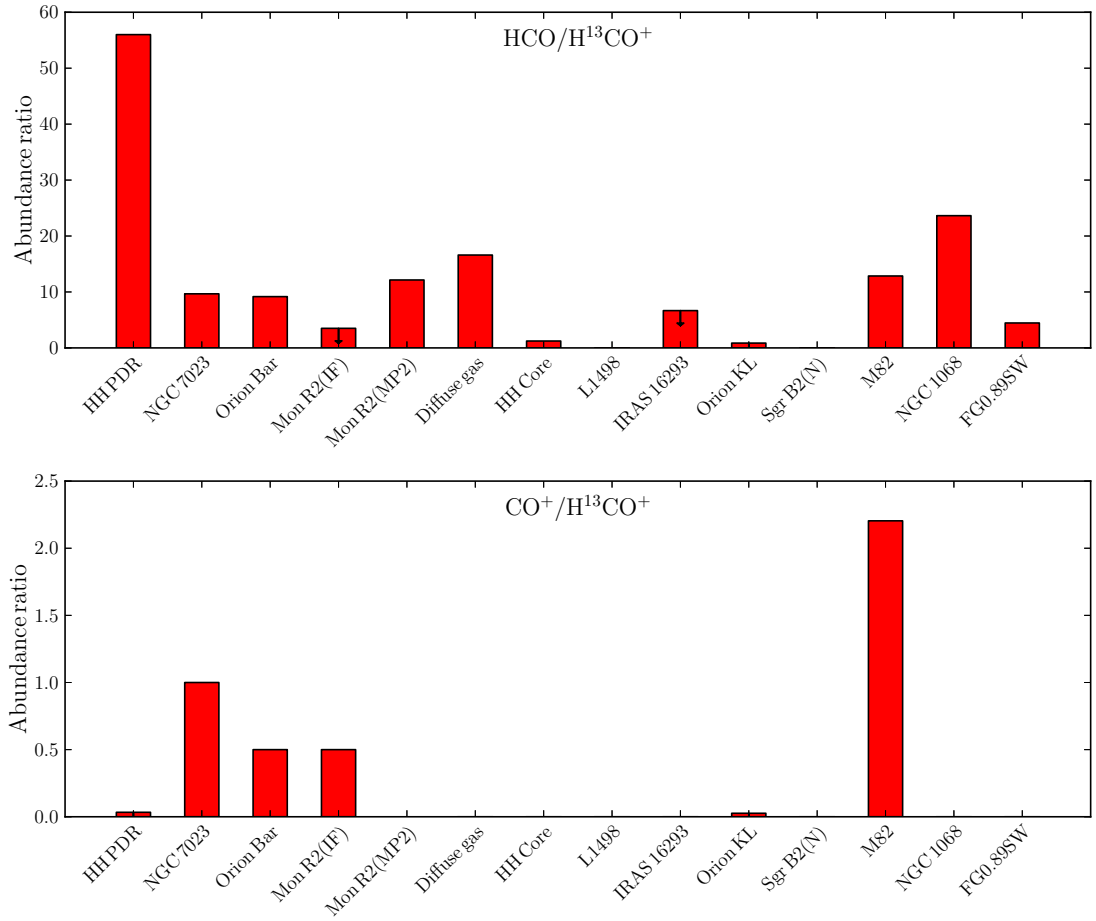

Figure 8.8: Comparison of abundance ratios towards the different sources.

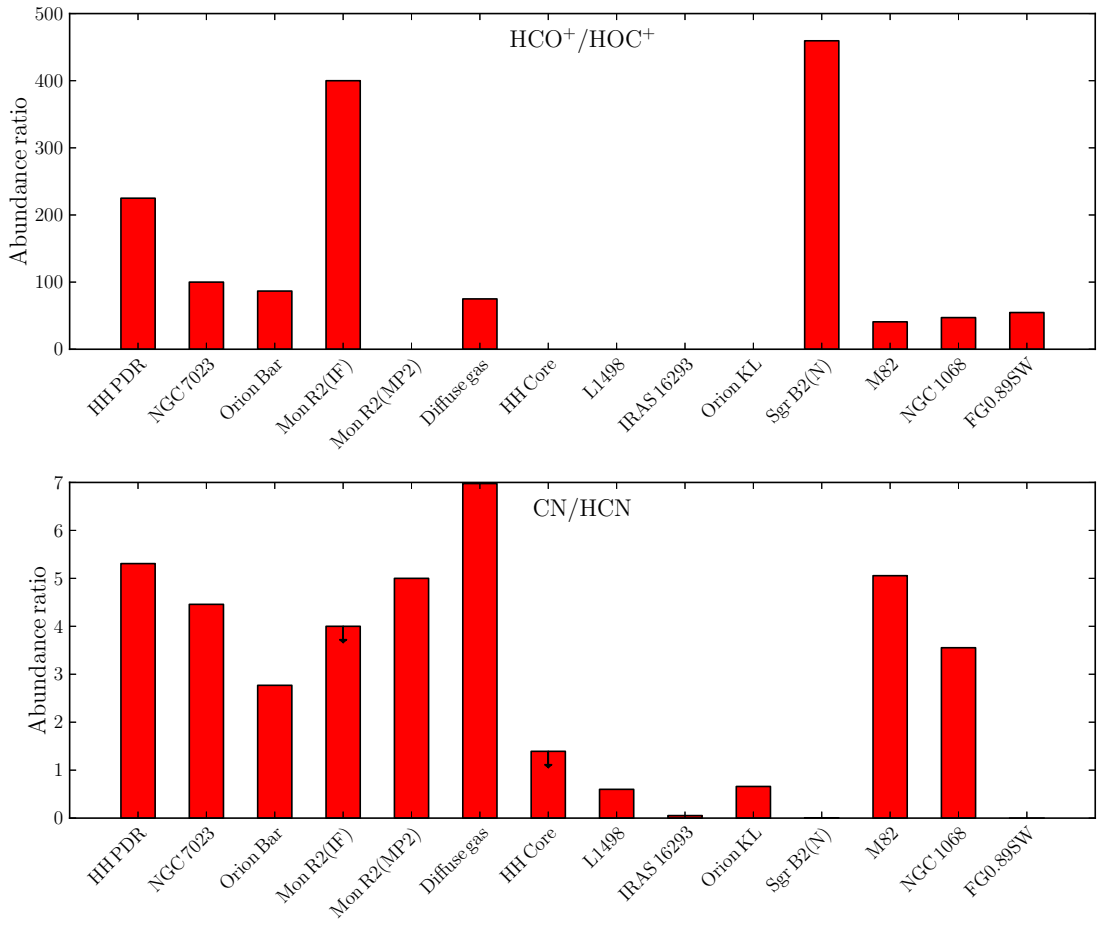

Figure 8.9: Comparison of abundance ratios towards the different sources.

are found in Mon R2(MP2), in the diffuse gas, in the starburst galaxy M82 and in the AGN galaxy NGC 1068. The enhanced HCO abundance found towards M82, suggests that its disk could be viewed as a giant PDR of $\sim$ 650 pc (García-Burillo et al. 2002). In Mon R2, Ginard et al. (2012) derived a higher ratio towards the MP2 position (HCO/$H^{13}CO^+$= 12) than towards the IF position (HCO/$H^{13}CO^+$< 3). They ran a grid of PDR models for different gas densities and radiation fields, and found that HCO/$H^{13}CO^+$> 10 only for $G_0 < 10^3$, *i.e.* in low UV-illumination PDRs. This is consistent with the lower HCO/$H^{13}CO^+$ ratios observed in the Orion Bar and Mon R2(IF). The dense cores, hot core (Orion KL), hot corino (IRAS 16293) and the high$-z$ galaxy, all show HCO/$H^{13}CO^+$ ratios lower than 10.

CO^+ is an excellent tracer of the outermost layers in warm PDRs as it is formed by reactions between C^+ and OH. The endothermic reaction between atomic oxygen and H_2, which leads to the formation of OH, has an activation energy barrier of $\sim$ 4800 K. Therefore, CO^+ can form only in very warm regions. Indeed, CO^+ has been detected only in high-UV illuminated PDRs. Ratios of $CO^+/H^{13}CO^+ > 0.4$ have been observed in NGC 7023, the Orion Bar, Mon R2 (only in the IF position) and in M82. CO^+ has not been detected in the Horsehead, but Goicoechea et al. (2009b) derived an upper limit for its column density,

which translates into a low abundance ratio of $CO^+/H^{13}CO^+ < 0.03$. Ginard et al. (2012) did not detect CO^+ towards the MP2 position in Mon R2 either. From their grids of models, they found that $CO^+/HCO^+ > 0.005$ ($CO^+/H^{13}CO^+ > 0.3$) only when $G_0 > 1000$. The higher $HCO/H^{13}CO^+$ and lower CO^+/HCO^+ ratios found towards the MP2 position than towards the IF position in Mon R2 led the authors to classify the PDR towards MP2 as a low-UV PDR, similar to the Horsehead, and the PDR towards the IF position as a high-UV PDR. M82 presents the highest $CO^+/H^{13}CO^+$ ratio (2.2) among all sources.

In summary, the $HCO/H^{13}CO^+$ and $CO^+/H^{13}CO^+$ abundance ratios are therefore excellent diagnostic to differentiate between high- and low-UV PDRs.

8.4.2 HCO^+/HOC^+

In molecular clouds, HOC^+ (which is formed by $H_3^+ + CO$) is not abundant because it is rapidly converted into HCO^+ by reacting with H_2:

$$HOC^+ + H_2 \rightarrow HCO^+ + H_2. \tag{8.1}$$

This leads to a large abundance ratio of $HCO^+/HOC^+ = 2000 - 6000$ in molecular clouds (Apponi & Ziurys 1997). In PDRs, on the other hand, the abundance of the reactive ion HOC^+ is enhanced, because new formation routes involving the abundant species C^+ (in high and low-UV PDRs) and CO^+ (in high-UV PDRs) are open:

$$C^+ + H_2O \rightarrow HCO^+/HOC^+ \tag{8.2}$$

$$CO^+ + H_2 \rightarrow HCO^+/HOC^+. \tag{8.3}$$

The first reaction favors the formation of HOC^+ (with a 16/84 branching ratio), while the second one has a 50/50 branching ratio.

In the Horsehead PDR, the HCO^+/HOC^+ abundance ratio is ~ 225. The other Galactic PDRs considered here, all present ratios of $HCO^+/HOC^+ \leq 400$, much lower than the values found towards molecular clouds. The diffuse medium, M82, NGC 1068 and FG0.89SW, also show low ratios ($HCO^+/HOC^+ < 100$). Sgr B2(N) presents the highest value, but still much lower than the one found towards molecular clouds. Note that HOC^+ is not detected in either dense core considered here.

The HCO^+/HOC^+ ratio is thus a good tracer of FUV-induced chemistry.

8.4.3 CN/HCN

CN and HCN are thought to be good tracers of high density ($n_H > 10^4$ cm^{-3}) gas. The CN/HCN abundance ratio is also a good tracer of enhanced UV field (with CN/HCN>1; Fuente et al. 1993). Indeed, the photodissociation of HCN, that leads to the formation of CN, is efficient in PDRs. Theoretical models show that the CN/HCN ratio decreases from ~ 10 in the PDR to ~ 0.1 in the shielded regions (Boger & Sternberg 2005). Ginard et al. (2012) showed that for the range of parameters they considered ($\chi = 10-100, n_H = 10^4-10^7$ cm^{-3}), the CN/HCN ratio does not depend on the UV-field, but it rather traces the density of the gas. The observed CN/HCN abundance ratio is $\sim 2.7 - 5.3$ in the Galactic PDRs considered

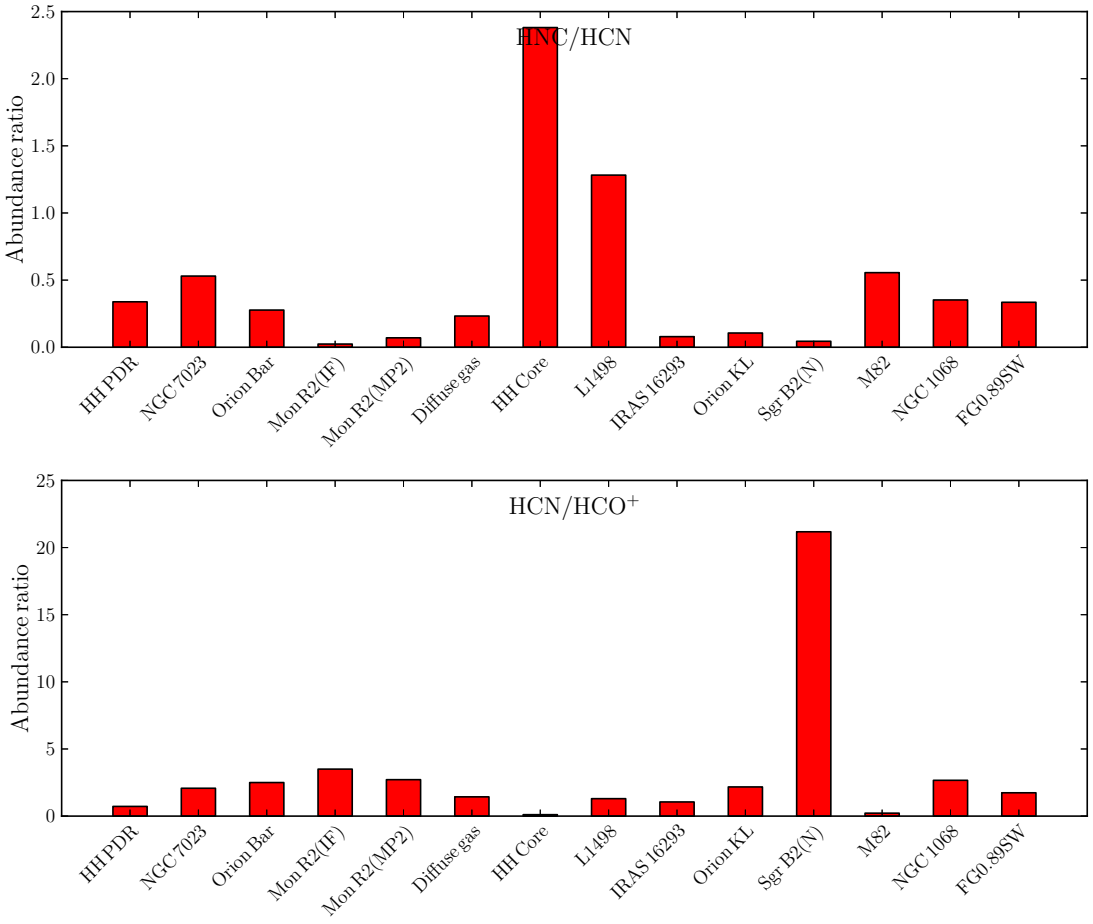

Figure 8.10: Comparison of abundance ratios towards the different sources.

here, consistent with the theoretical predictions. The diffuse gas, M82 and NGC 1068 also show CN/HCN ratios larger than 1. In contrast to the PDRs, the dense cores and hot core and hot horino sources all show much lower CN/HCN ratios ($\lesssim 1$).

CN/HCN ratios larger than 1 are thus good tracers of FUV-induced chemistry.

8.4.4 HNC/HCN and HCN/HCO$^+$

Gas-phase chemistry models predict that the HNC/HCN ratio should be close to unity in cold gas (Herbst et al. 2000). Indeed, HNC/HCN= 1.2 in L1498 and HNC/HCN= 2.3 in the Horsehead dense core. The other warmer sources all show HNC/HCN abundance ratios lower than 1, consistent with the theoretical prediction.

In extragalactic studies, the HNC/HCN and HCN/HCO$^+$ line ratios are considered to be a good diagnostics to differentiate between AGN and starburst environments (e.g., Krips et al. 2008; Loenen et al. 2008). Indeed, the HCN/HCO$^+$ ratio is $\sim$ 10 times larger in the AGN galaxy NGC 1068, than in M82. On the other hand, similar values to that of NGC 1068 are found in the Galactic PDRs.

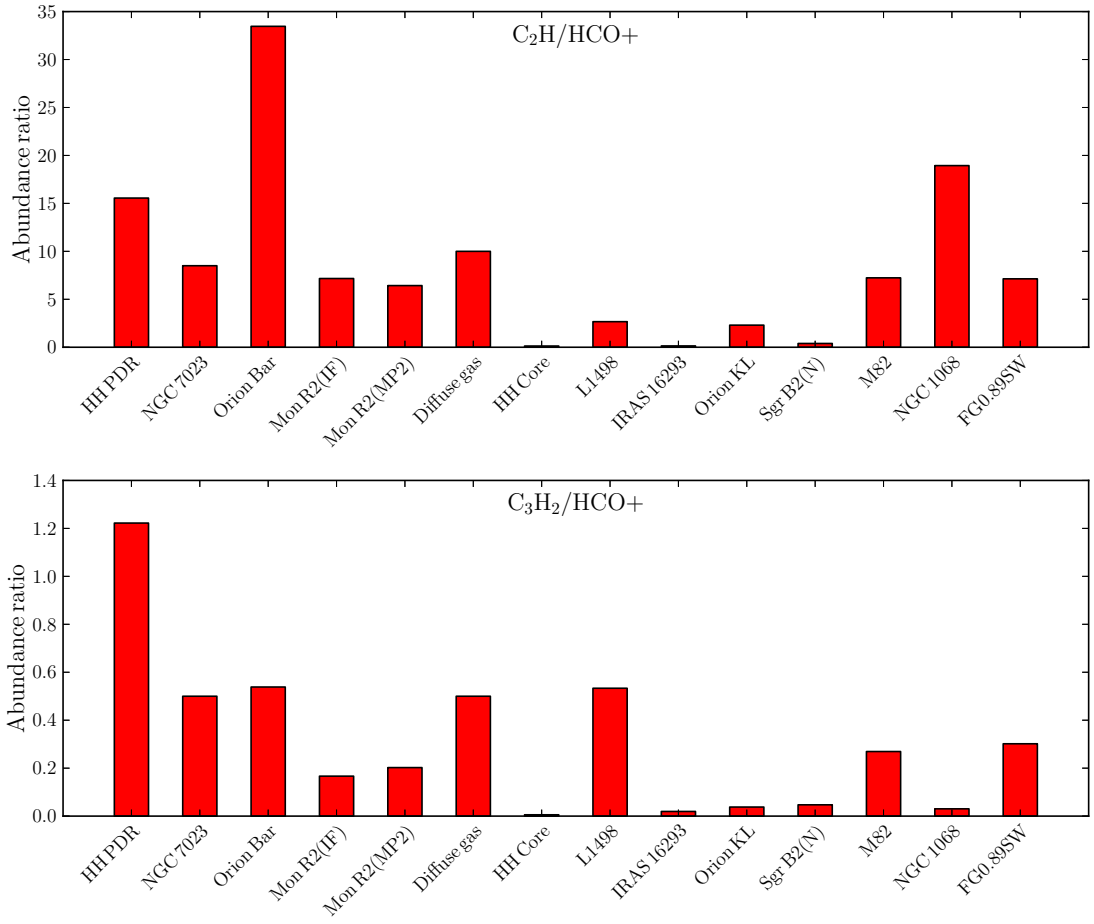

Figure 8.11: Comparison of abundance ratios towards the different sources.

8.4.5 C_2H/HCO^+ and C_3H_2/HCO^+

The abundance of hydrocarbons is enhanced in PDRs, as seen in Fig 8.11. C_2H and C_3H_2 are also abundant in the diffuse medium. The largest C_2H/HCO^+ and C_3H_2/HCO^+ abundance ratios are observed towards the Galactic PDRs, while the lowest ratios are observed towards the hot core and hot corino sources. The hydrocarbons are much more abundant in the dense core L1498 than in the Horsehead dense core.

8.4.6 N_2H^+/H_2CO

N_2H^+ is thought to be the best tracer of cold ($T_{\rm kin} < 10$ K) gas. Indeed, most species start to freeze-out onto grains at these low temperatures, and therefore are no longer observable in the gas-phase. N_2H^+, on the other hand, survives in the gas-phase at low temperatures because CO, the main destruction partner of N_2H^+, is depleted onto grains. As seen in Fig. 8.12, the two dense cores considered here show the largest N_2H^+/H_2CO abundance ratios. The high-z galaxy, FG0.989SW, also presents a large N_2H^+/H_2CO, which indicates the presence of a large amount of cold gas.

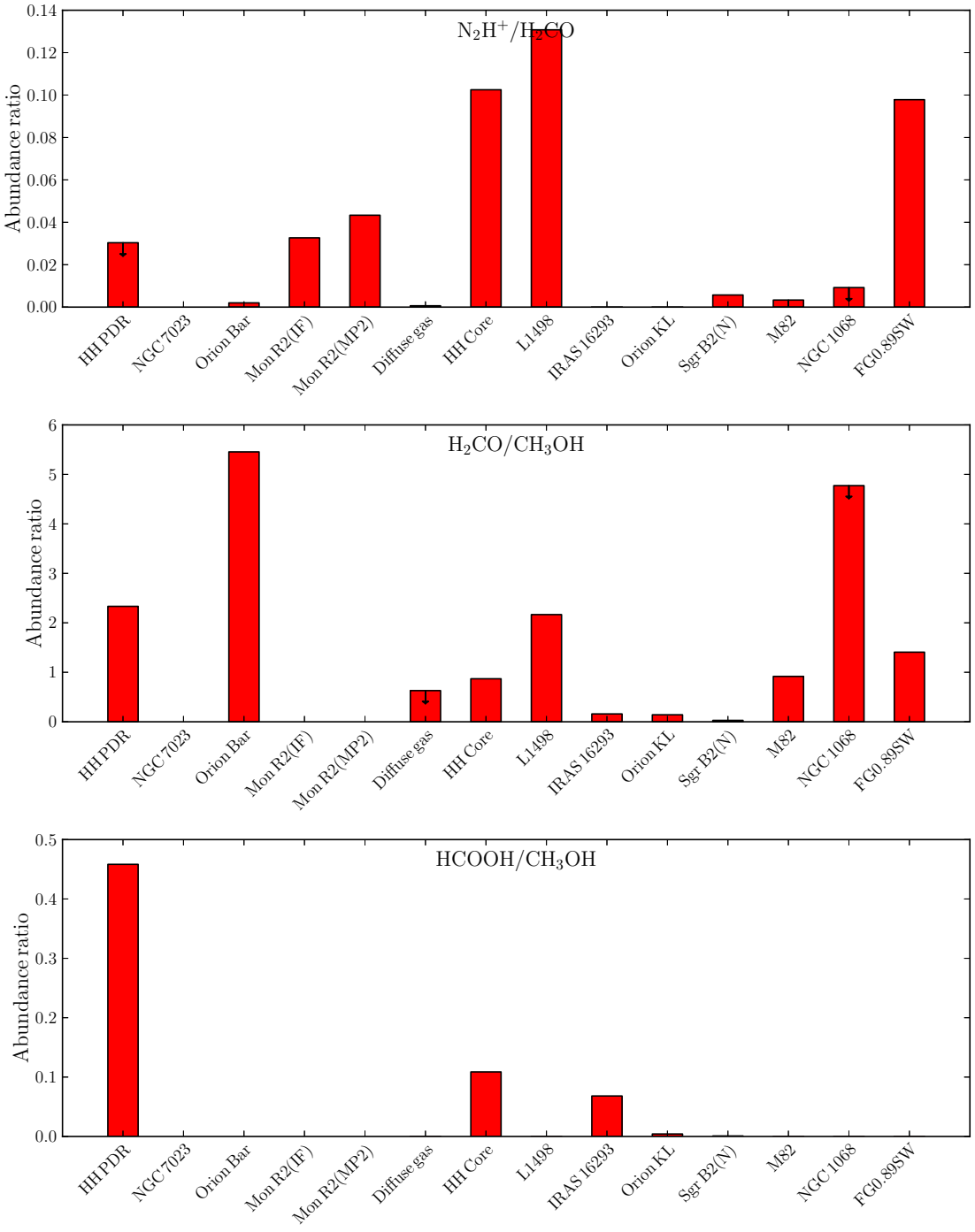

Figure 8.12: Comparison of abundance ratios towards the different sources.

8.4.7 H_2CO, HCOOH, CH_2CO, CH_3CHO and CH_3CCH relative to CH_3OH

The abundance ratios of the complex molecules H_2CO, HCOOH, CH_2CO, CH_3CHO and CH_3CCH with respect to methanol are all much lower in the hot core and hot corino sources,

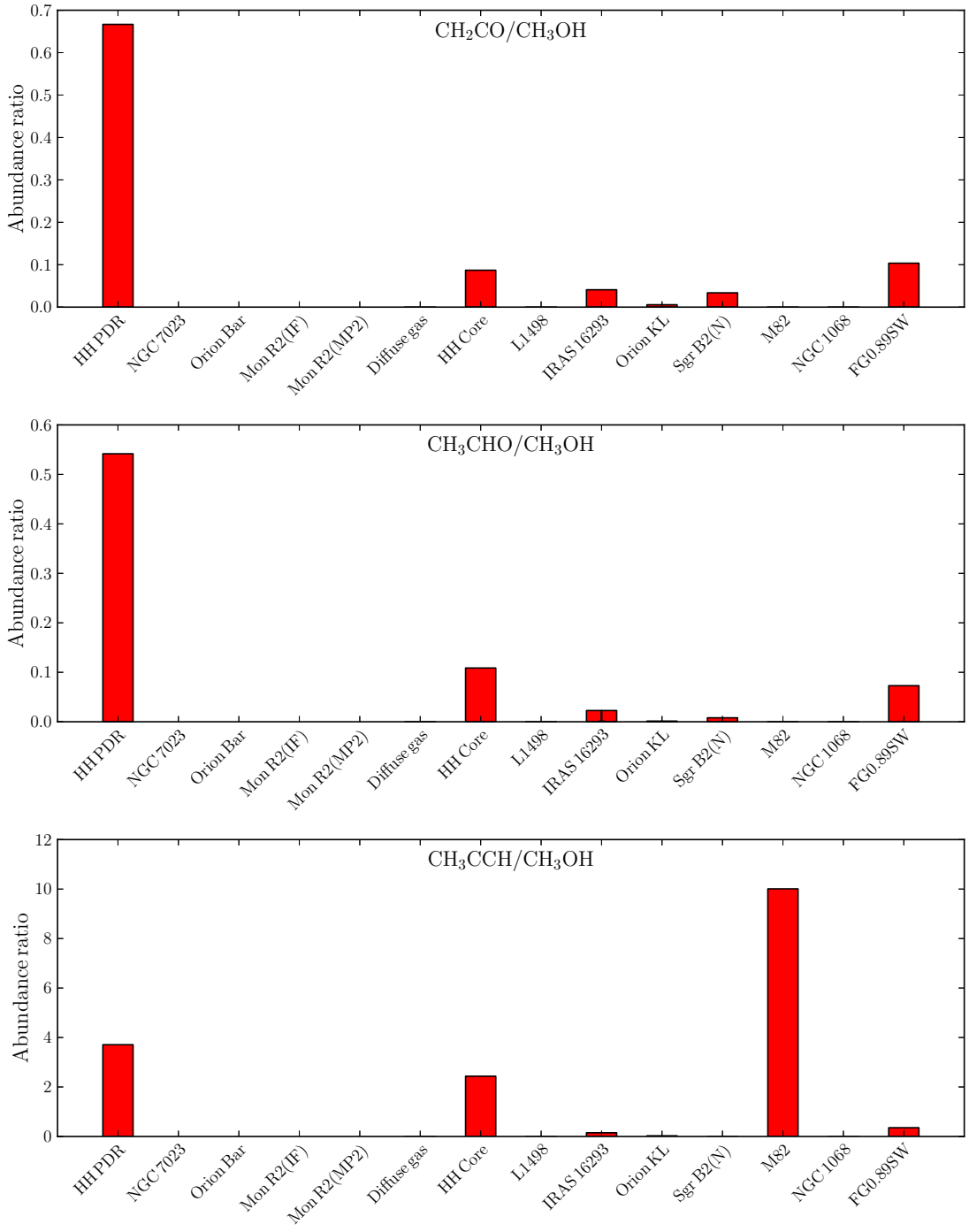

Figure 8.13: Comparison of abundance ratios towards the different sources.

IRAS 16293, Orion KL and Sgr B2(N), than in the Horsehead PDR. The H_2CO/CH_3OH ratio is larger in the Galactic PDRs where their abundances have been measured: the Horsehead PDR and the Orion Bar. This ratio is also large in the dense core L1498, M82 and FG0.98SW.

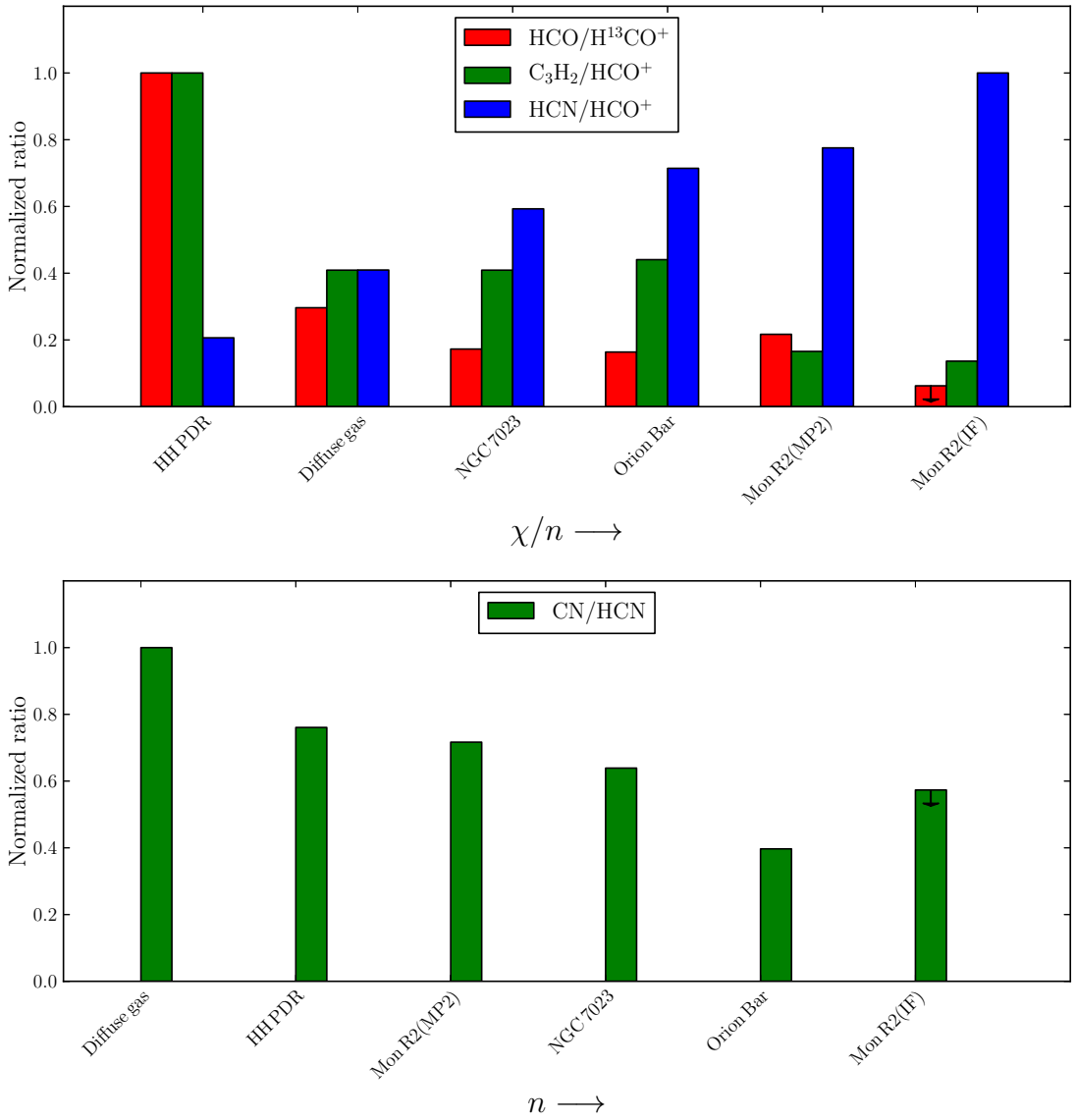

Figure 8.14: Abundance ratios that show a trend with the χ/n (upper) and n (lower) of the prototypical PDRs and the diffuse medium.

M82 presents a large CH_3CCH abundance, and a much larger CH_3CCH/CH_3OH ratio than the rest of the sources. It would be interesting to measure the CH_3CCH abundance in the high-UV Galactic PDRs, and see if a large CH_3CCH/CH_3OH ratio has a correlation with the radiation field.

8.5 Tracers of χ/n and density in PDRs

A few of the ratios discussed above show a correlation or a trend with χ/n or n in the Galactic PDRs. Fig. 8.14 shows these abundance ratios, where the different sources have been sorted

by increasing χ/n or n. The $HCO/H^{13}CO^+$ and C_3H_2/HCO^+ ratios decrease with χ/n, while the HCN/HCO^+ ratio increases with χ/n. The CN/HCN ratio decreases with density.

The radiation field and density at the Mon R2(MP2) position are not well known. The trends in Fig. 8.14 show that Mon R2(MP2) has a χ/n that is in between that of the Orion Bar and Mon R2(IF), and a density that is in between that of the Horsehead PDR and NGC 7023 ($6 \times 10^4 - 10^5$ cm^{-3}). This translates into a radiation field $6 \times 10^2 < \chi < 10^4$. As mentioned before, the low $CO^+/H^{13}CO^+$ ratio suggests $\chi < 10^3$. Therefore, the radiation field in Mon R2(MP2) can be constrained to $6 \times 10^2 < \chi < 10^3$.

8.6 Abundance estimator

In order to classify the different sources, and inspired by Martín et al. (2006) and Muller et al. (2011), I have calculated an abundance estimator defined as,

$$\chi_{ij} = \frac{1}{N} \sum_{k=1}^{N} \left| \log_{10} \left(\frac{X_{ik}}{X_{jk}} \right) \right|, \tag{8.4}$$

where X_{ik} are the abundance ratios k in the Horsehead PDR, X_{jk} are the same abundance ratios k in source j, and N is the total number of ratios considered. The resulting abundance estimator will depend strongly on the chosen ratios. In order to be consistent, only ratios that have been measured in all the sources are considered. The ratios are the HNC/HCN, HCN/HCO^+, C_2H/HCO^+ and C_3H_2/HCO^+. The result is shown in the upper panel of Fig. 8.15. The distance to zero indicates the degree of similarity with the Horsehead PDR, the closest ones being the most similar. In this case NGC 7023 would be more similar to the Horsehead than the diffuse medium and Mon R2(MP2), which is unlikely. In order to improve to comparison, I have included two additional ratios. These are the CO^+/HCO^+ and CN/HCN ratios. CO^+ has not been measured in Mon R2(MP2) or the diffuse medium, and only an upper limit is available for the Horsehead PDR. Because we expect low CO^+ abundances in low-UV PDRs, its abundance was fixed to the upper limit derived in the Horsehead for the three sources. The CN abundance in Mon R2(IF) was also fixed to the upper limit derived in the same position. The result is shown in the lower panel of Fig. 8.15. In this case, a more consistent result is obtained. The diffuse medium is found to be closest to the Horsehead PDR, followed by Mon R2(MP2), NGC 7023, M82, Orion Bar, and finally Mon R2(IF). This indicates that M82 is more similar to high-UV illuminated PDRs, such as the Orion Bar, than to the Horsehead.

Figure 8.16 shows the abundance estimator between the Horsehead PDR and the other environments. Here, the ratios included are HNC/HCN, HCN/HCO^+, C_2H/HCO^+, C_3H_2/HCO^+ and N_2H^+/H_2CO. Non-detections and upper limits were not considered in the abundance estimator. The figure shows that the diffuse medium has closer abundance ratios to the Horsehead PDR than the rest of the sources, followed by M82. Next in this sequence is the high-z galaxy FG0.98SW, the dense core L1498, the AGN Galaxy NGC 1068. Finally, there is the hot corino IRAS 16293 and the two hot cores, Orion KL and Sgr B2(N), which show the most different abundance ratios compared to the Horsehead. The Horsehead dense core

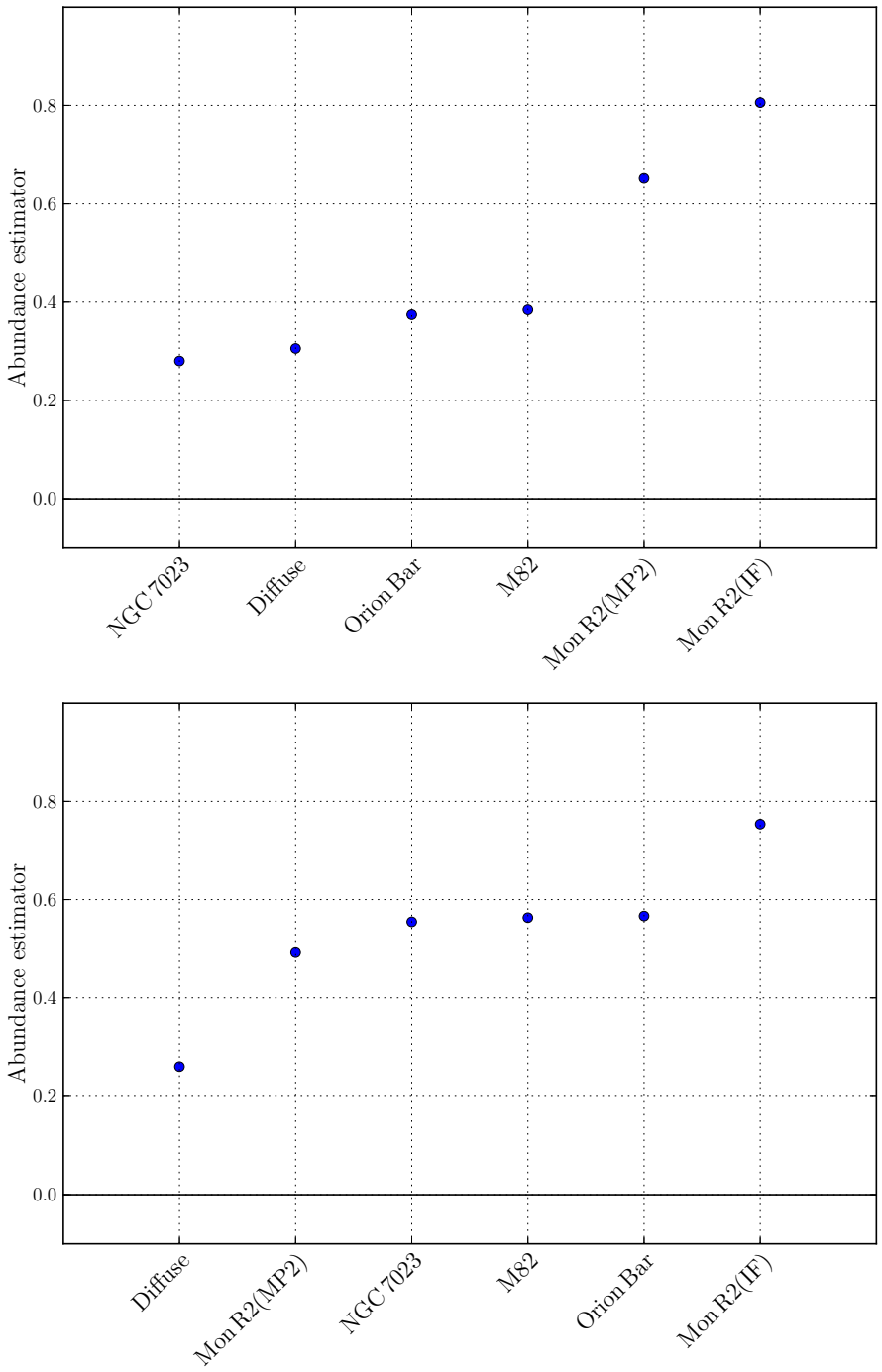

Figure 8.15: Abundance estimator between the Horsehead PDR and the other prototypical PDRs, as well as the diffuse medium and M82. Only the HNC/HCN, HCN/HCO^+, C_2H/HCO^+ and C_3H_2/HCO^+ are considered in the upper panel. In the lower panel two additional ratios are included: CO^+/HCO^+ and CN/HCN.

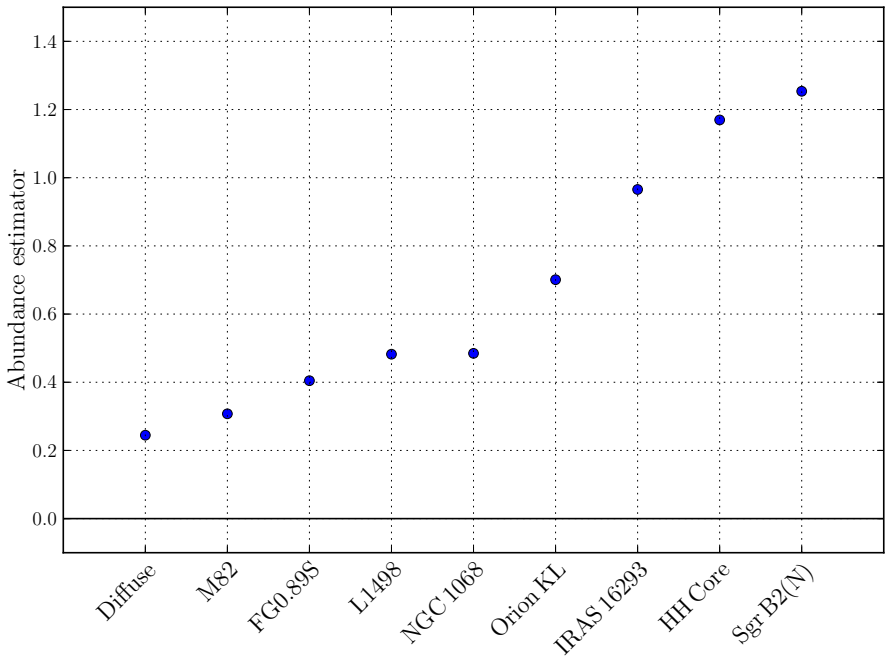

Figure 8.16: Abundance estimator between the Horsehead PDR and other environments.

is also far away from the Horsehead PDR in this sequence. In general the dense core L1498 and the one in the Horsehead show different chemistries. However, any interpretation from such a comparison should be considered carefully, as the result is biased to the selection of ratios. With the coming results of complete line surveys it will be possible to obtain consistent set of observations, with measured abundances or upper limits for a larger amount of molecules, that will enable to use this type of analysis to compare the chemistry in different environments.

8.7 Summary

In this chapter, the diagnostic power of molecular lines has been proven. I have compared the abundances of different species in different environments and obtained chemical diagnostics that can be used to determine the dominant chemical processes from molecular lines observations. The main results are summarized next.

- The $HCO/H^{13}CO^+$, $CO^+/H^{13}CO^+$, HCO^+/HOC^+ and CN/HCN ratios are good tracers of FUV radiation. However, low $CO^+/H^{13}CO^+$ ratios can also indicate low-UV fields.
- The CN/HCN ratio is a good tracer of density in FUV illuminated regions.
- The $HCO/H^{13}CO^+$, C_3H_2/HCO^+ and HCN/HCO^+ ratios are good tracers of χ/n. $HCO/H^{13}CO^+$ and C_3H_2/HCO^+ decrease with increasing χ/n, while HCN/HCO^+ in-

creases with increasing χ/n. The radiation field can be determined with these ratios once the density has been constrained with the CN/HCO^+ ratio.

- The starburst galaxy M82 can be viewed as a giant PDR (García-Burillo et al. 2002). The HCO/$H^{13}CO^+$ and HCO^+/HOC^+ ratios and the abundance of hydrocarbons relative to HCO^+ are similar to those of the Orion Bar and NGC 7023. In addition, CO^+ is abundant in M82 which suggests the presence of warm gas. All this indicates that M82 is a PDR with chemical properties closer to high-UV PDRs, like the Orion Bar. However, the CN/HCN and HCN/HCO^+ ratios are closer to those of the Horsehead PDR, which suggests that M82 also contains low-UV PDRs.

- The abundance estimator between the Galactic PDRs, M82 and the diffuse medium considering the HNC/HCN, HCN/HCO^+, C_2H/HCO^+, C_3H_2/HCO^+, CO^+/$HCO^+$and CN/HCN ratios, results in the following sequence: diffuse gas, Mon R2(MP2), NGC 7023, M82, Orion Bar and Mon R2(IF). In this sequence the former are more similar to the Horsehead, and the latter are most different ones. In this scenario, M82 is closer to the high-UV PDRs.

- The abundance estimator between the Horsehead and the other environments considering the ratios HNC/HCN, HCN/HCO^+, C_2H/HCO^+, C_3H_2/HCO^+ and N_2H^+/H_2CO, results in the following sequence: Diffuse gas, M82, FG0.89S, L1498, NGC 1068, Orion KL, IRAS 16293, Horsehead dense core and Sgr B2(N). In this case, the diffuse gas and M82 are closer to the Horsehead, while the hot core and hot corino sources are the most different ones.

- The dense core L1498 presents very different abundances compared to the Horsehead dense core. This could suggest that they are at different stages of evolution.

The molecular lines used in this chapter to compare the chemistry in different environments are brigh rotational lines in the millimeter and sub-millimeter from well-known species. All these lines are and will be routinely observed with the broadband receivers of ALMA, and in the future NOEMA, when observing different sources such as protostars, protoplanetary disks and extragalactic nuclei, with unprecedented angular resolution. The abundance ratios discussed here can be easily used to obtain a qualitative indicator of the role of UV radiation in each object.

Chapter 9

Conclusions and Perspectives

9.1 The Horsehead: a benchmark to chemical models

Molecular lines are used to trace the structure of the interstellar medium and the physical conditions of the gas in different environments, from high-z galaxies to proto-planetary disks. However, the interpretation of molecular observations for most of these objects is hampered by the complex source geometries, and the small angular sizes in the sky that prevent us from resolving the different gas components, and hence to know which specific region each molecule really traces. Therefore, in order to fully benefit from the diagnostic power of the molecular lines, the formation and destruction paths of the molecules must be quantitatively understood. This challenging task requires the contribution of theoretical models, laboratory experiments and observations. Well-defined sets of observations of simple *template* sources are key to benchmark the predictions of theoretical models. In this respect, the Horsehead nebula has proven to be a good template source of low-UV field irradiated environments because it is close-by ($\sim$ 400 pc), it has a simple geometry (edge-on) and the gas density is well constrained. Moreover, in contrast to other Galactic PDRs, like the Orion Bar and Mon R2 which present large radiation fields ($\chi \simeq 10^4 - 10^5$), the Horsehead is illuminated by a weaker radiation field ($\chi \sim 60$) and thus better resembles the majority of the FUV-illuminated neutral gas in the Galaxy. Furthermore, the dust grains in the Horsehead have temperatures of $\simeq 20 - 30$ K, which is not enough to thermally desorb the ices, and therefore it offers a clean environment to isolate the role of grain surface chemistry and subsequent photo-desorption.

With the purpose of providing a benchmark to chemical models we have performed a complete and unbiased line survey of the Horsehead with the IRAM-30 m telescope. Two particular positions were observed: the PDR, corresponding to the peak of the HCO emission, where the gas is warm ($T_{\rm kin} \sim 60$ K), and the dense-core, a cold ($T_{\rm kin} \lesssim 20$ K) condensation located less than $40''$ away from the PDR edge, where HCO^+ is highly deuterated. The survey covers the 3, 2 and 1 mm bands, which are appropriate for the detection of low-lying rotational lines of molecules, with an unprecedented combination of bandwidth, high spectral resolution and high sensitivity that enables a detailed comparison between the chemistry in FUV-illuminated and FUV-shielded gas. The line density at 3 mm is, on average, 5 and 4 lines/GHz in the PDR and dense core, respectively. At 2 and 1 mm, the line density is 1 line/GHz in both the PDR and dense core. The contribution of molecular lines to the total flux at 1.2 mm is estimated to be 14% at the PDR and 16% at the dense core. Approximately 30 species (plus their isotopologues) are detected with up to 7 atoms in the PDR and the dense core.

This thesis is focused on the observation and analysis of the Horsehead WHISPER survey,

complemented by high-resolution PdBI maps of specific species. The scientific results of this survey include the detection of CF^+ (fluoromethylidynium), a new diagnostic of the FUV-illuminated gas; the detection of a new species in the ISM, tentatively attributed to the small hydrocarbon C_3H^+ (propynylidynium); the detection of the complex organic molecules H_2CO (formaldehyde), CH_3OH (methanol) and CH_3CN (methyl cyanide), which reveal that photo-desorption of ices is an efficient mechanism to release molecules into the gas phase; and the first detection of the complex organic molecules, HCOOH (formic acid), CH_2CO (ketene), CH_3CHO (acetaldehyde) and CH_3CCH (propyne) in a PDR. These results are summarized next.

9.1.1 CF^+: a tracer of C^+ and a measure of the fluorine abundance

CF^+, which was only detected in the Orion Bar before, was detected toward the illuminated edge of the Horsehead nebula. The CF^+ ion, which is formed by reactions of HF and C^+, is expected to be the second most important fluorine reservoir, after HF, in regions where C^+ is abundant. Theoretical models predict that there is a significant overlap between CF^+ and C^+ at the edges of molecular clouds. Therefore, we propose that CF^+ can be used as a proxy of C^+, but that can be observed from ground-based telescopes, unlike C^+ for which we need to go to space. This can be a powerful tool, because the [C II] 157.8 μm line is the main cooling mechanism of the diffuse gas, and the cooling of the medium, which allows the gas to compress, is a crucial step in the formation of new stars. Moreover, given the simple chemistry of fluorine, the CF^+ column density is proportional to the column density of HF. Assuming that in molecular clouds, all fluorine is in its molecular form, the elemental abundance of fluorine can be derived directly from CF^+ observations. Finally, because the Horsehead shows narrow emission lines, in contrast to other PDRs like the Orion Bar, we were able to resolve the two hyperfine components in the CF^+ $J = 1 - 0$ line and to compare with *ab initio* computations of the CF^+ spin rotation constant. The CF^+ spin rotation constant was computed specifically for these observations. The Horsehead is thus a good laboratory for precise spectroscopic studies of species present in FUV-illuminated environments.

9.1.2 Detection of a new molecule in space, tentatively attributed to l-C_3H^+

Thanks to the sensitive observations and large bandwidth covered by the Horsehead WHISPER line survey, a consistent set of 8 lines were detected towards the PDR position, that could not be associated to any transition listed in the public line catalogs. The observed lines can be well fitted with a linear rotor model, implying a $^1\Sigma$ ground electronic state. The deduced rotational constant value is close to that of C_3H. We thus attribute the detected lines to the small hydrocarbon l-C_3H^+.

However it was never detected before, C_3H^+ is usually included in chemical networks because ion-molecule reactions with this cation are thought to be the most important gas-phase channels to form other small hydrocarbons (Turner et al. 2000; Wakelam et al. 2010), like C_3H and C_3H_2, which have been detected in a large variety of sources, from diffuse to dark clouds. C_3H and C_3H_2 have been found to be $\sim$1 order of magnitude more abundant

in PDRs than current pure gas-phase models predict. An additional formation mechanism is therefore needed. One possibility to explain the observed high abundance of hydrocarbons in PDRs is the so called *Top-Down* model. In this scenario polycyclic aromatic hydrocarbons (PAHs) are fragmented into small hydrocarbons in PDRs due to the strong UV fields (e.g., Fuente et al. 2003; Teyssier et al. 2004; Pety et al. 2005). In the same way, PAHs are formed by photo-evaporation of very small grains (e.g., Berné et al. 2007; Pilleri et al. 2012). The discovery of C_3H^+, which is an intermediate species in the gas-phase formation scenario of small hydrocarbons, brings further constraints to the formation pathways of the small hydrocarbons. Indeed, we find a l-C_3H^+ abundance which is too low to explain the observed abundance of the other related small hydrocarbons by means of pure gas-phase chemical reactions. This is the first clear example of the formation of small molecules from larger ones.

The attribution of the unidentified lines to l-C_3H^+ has been questioned by Huang et al. (2013), because their theoretical calculations of the spectroscopic constants of C_3H^+ differ from the ones inferred from our observations. Fortenberry et al. (2013) proposed that a more plausible candidate is the hydrocarbon anion C_3H^-. However, if the unknown species is the anion, it would be the first anion detected in the Horsehead, and the ratio of C_3H^- to neutral C_3H would be ∼57%, which is higher than any anion to neutral ratio detected in the ISM so far[1]. The lines have been detected in several other environments, like the Orion Bar (Cuadrado et al. in prep) and Sgr B2 (McGuire et al. 2013), which confirms the presence of the carrier in the ISM. However, the lines were not detected in the dark cloud TMC 1, where other anions have been already detected. The observations thus favor the assignment of the unidentified species to the hydrocarbon cation, l-C_3H^+. However, a direct measurement in the laboratory is necessary to provide a definitive assignment and close the controversy created by these observations in the Horsehead.

9.1.3 Photo-desorption of dust grain ice mantles: H_2CO and CH_3OH

Relatively simple organic molecules, like H_2CO and CH_3OH, are key species in the synthesis of more complex molecules in the ISM, that could eventually end up in proto-planetary disks, and hence in new planetary systems. They are also used to probe the temperature and density of the gas in different astrophysical sources. It is therefore of great interest to understand how these molecules form. Both H_2CO and CH_3OH have been detected in a wide range of interstellar environments such as dark clouds, proto-stellar cores and comets, with high abundances ($10^{-6}-10^{-9}$) with respect to total hydrogen. Unlike H_2CO, which can be formed efficiently in both the gas-phase and on the surfaces of dust grains, CH_3OH is thought to be formed mostly on the ices, through the successive additions of hydrogen atoms to adsorbed CO molecules.

We observed several millimeter lines of H_2CO and CH_3OH toward the PDR and dense core positions in the Horsehead. The inferred abundances from the observations were compared to PDR models that include either pure gas-phase chemistry or both gas-phase and grain surface chemistry. The observations suggest that, at the PDR, both H_2CO and CH_3OH are mostly formed on the surface of dust grains, probably through the successive hydrogenation

[1]For reference, the abundance fraction of C_6H^-, relative to the neutral, has been found to vary from 1.4% to 4.4% in several sources (Cordiner et al. 2013; McCarthy et al. 2006).

of CO ices and are subsequently released into the gas-phase through photo-desorption. At the dense core position, the observations suggest that H_2CO is formed mainly in the gas phase, while methanol is formed in the ices at the surface of dust grains and it is subsequently photodesorbed into the gas phase. The different formation routes for H_2CO at the PDR and dense core suggested by the models is strengthened by the different ortho-to-para ratios derived from the observations (~ 3 at the dense core, ~ 2 at the PDR).

In addition to the lines detected in the line survey, we obtained high-angular resolution maps of H_2CO and CH_3OH with the IRAM-PdBI. The H_2CO emission map presents a peak at the dense core position, while CH_3OH presents a dip in its emission at the same position. The observations thus suggest that CH_3OH is depleted in the dense core. This way, gas-phase CH_3OH is present in an envelope around the dense core, while H_2CO is present in both the envelope and the dense core itself. Indeed, we expect photo-desorption to be more efficient at the PDR than at the FUV-shielded dense core. We thus conclude that photo-desorption of ices is an efficient mechanism to release species into the gas phase in FUV-illuminated regions.

9.1.4 Nitrile molecules: CH_3CN, CH_3NC and HC_3N

Moderately complex nitriles like CH_3CN and HC_3N are easily detected in (massive) star forming regions. In particular, CH_3CN is a good tracer of the physical conditions in warm and dense regions. We detected several lines of CH_3CN and HC_3N in the PDR and dense core. CH_3NC and C_3N are also detected towards the PDR. The chemistry of HC_3N and CH_3CN is quite different, as we find that CH_3CN is 30 times more abundant in the far-UV illuminated gas than in the far-UV shielded core, while HC_3N has a similar abundance in both positions. The high abundance of CH_3CN inferred in the PDR is surprising because the photodissociation of this complex molecule is expected to be efficient in FUV-illuminated regions. The observed abundance in the PDR cannot be reproduced by current pure gas-phase chemical models. We have shown that photo-desorption is an efficient mechanism to release H_2CO and CH_3OH in the PDR, but the case of CH_3CN is even more extreme as it is 30 times more abundant there than in the dense core, while H_2CO presents similar abundances in both positions. This proves the existence of a relatively efficient gas-phase route to form H_2CO in the dense core, while there is no efficient gas-phase route to form CH_3CN at low temperatures. The most likely explanation for the high CH_3CN abundance at the PDR and low abundance at the dense core is that CH_3CN is produced in the ices through ice photo-processing of N bearing species, and it is released into the gas phase through photo-desorption. The detection of CH_3NC at the PDR, which results in a CH_3NC/CH_3CN isomeric ratio of 0.15, suggests that CH_3NC could also form on the surfaces of dust grains through far-UV irradiation of CH_3CN ices leading to isomerization.

9.1.5 Complex molecules in PDRs

Complex molecules are commonly detected in high-mass star forming regions, and have so far been considered as hot core tracers. They are also detected towards the low-mass version of hot cores, the so called hot-corinos. The complex molecules HCOOH, CH_2CO, CH_3CHO,

and CH_3CCH were detected in the Horsehead PDR and dense core positions with abundances relative to H_2 that are comparable to those derived towards hot core sources. The dominant formation mechanism of these molecules is unclear, although they are thought to form on the surfaces of dust grains. Contrary to the case of CH_3CCH, which presents similar abundances in the PDR and dense core, the abundances of HCOOH, CH_2CO, CH_3CHO are ~ 3.4 times higher towards the PDR than the dense core, which suggests that their formation is enhanced in the presence of far-UV photons. This could be the result of a more efficient photo-desorption in the PDR, due to the larger radiation field compared to the dense core. But it could also indicate that the formation on the grains itself is more efficient in the PDR, due to a higher mobility of the molecules in the ice mantles. Gas-phase formation routes cannot be excluded though, and more studies on the formation of complex molecules from gas-phase precursors are needed.

The detection of these molecules in other environments besides hot cores, like in prestellar cores (Bacmann et al. 2012) and now in PDRs, suggests that they can also form in the cold gas and in FUV-irradiated warm gas. We have shown that complex molecules can survive in the presence of far-UV radiation, and their formation could even be enhanced due to the radiation. This opens the possibility of detecting complex molecules in other FUV-illuminated regions, such as protoplanetary disks, in the future.

9.1.6 Chemical diagnostics

By comparing the abundances of different species derived in the Horsehead with those derived in other environments, we have obtained chemical diagnostics that can be used to determine the dominant chemical processes from molecular line observations. The $HCO/H^{13}CO^+$, $CO^+/H^{13}CO^+$, HCO^+/HOC^+ and CN/HCN abundance ratios are found to be good tracers of far-UV radiation. The incident radiation field and gas density present in PDRs can be constrained by comparing certain abundance ratios with template sources. For example, the $HCO/H^{13}CO^+$, C_3H_2/HCO^+ and HCN/HCO^+ ratios are good tracers of χ/n, while the CN/HCO^+ ratio is a good tracer of density. An abundance estimator was used to classify different sources. It is concluded that the chemical characteristics of the Horsehead PDR are closer to those of the diffuse gas and the starburst galaxy M82, while the hot core and hot corino sources are the most chemically different. The comparison between different sources suggests that M82 resembles more the high-UV PDRs, like the Orion Bar and Mon R2, than the Horsehead. The abundance ratios described in this thesis involve species that will be routinely observed with the current and future instruments, and can thus be easily used to obtain a qualitative indicator of the role of far-UV radiation in different objects.

9.2 On the impact of instrumental progresses in radioastronomy on astrochemistry

With the recent progresses in radioastronomy, the field of astrochemistry is now in a golden age. The Herschel space telescope has gathered observations of simple molecules and dust towards a variety of different environments, such as the diffuse medium, PDRs, star forming

regions, protoplanetary disks and high-z galaxies, providing important scientific results of the chemistry and physics of the ISM. In addition to delivering the most detailed images of the Cosmic Microwave Background (CMB), the relic radiation from the Big Bang, the Planck space telescope contributed to the field of astrochemistry by providing large scale images of the cold ISM in the Galaxy. ALMA has also started to operate with a limited number of antennas, and has already generated impressive results in the field of astrochemistry, star and planet formation, in addition to nearby and high-z galaxies. Future ALMA observations will certainly bring many new discoveries when it reaches its full capabilities.

It is expected that ALMA will spend a maximum of 25% of the time observing at millimeter wavelengths, and most of the time at sub-millimeter wavelengths. The NOEMA project, that will operate at millimeter wavelengths, aims at upgrading the PdBI. When completed it will thus become an important and necessary complement to ALMA. Three main upgrades will be made. The first one is to increase the number of 15-m antennas, from the current 6 to 12, implying a larger collecting area and a better image quality as the number of baselines will be 4 times the current one. The second upgrade involves the extension of the larger baseline, from 800 to 1600 m, implying an angular resolution twice as better as the current one (between $0.2''$ and $2''$). The third upgrade will involve a new generation of receivers spanning 4 times the current total bandwidth, from 8 to 32 GHz, implying a sensitivity in continuum observations that will be 4 times better, or the possibility to cover 4 times the current frequency range in the same time. These are the receivers currently used at the IRAM-30 m telescope, and are the most powerful millimeter receivers that exist today.

Thanks to the tremendous current capabilities of the instruments at the 30 m telescope, it is possible to do complete and unbiased spectral line surveys with an unprecedented sensitivity and spectral resolution, and in a reasonable amount of time. The Horsehead WHISPER line survey is the first of its kind, and several other line surveys are either currently under completion or recently completed. Moreover, because of the new capabilities most of the heterodyne observations at the 30 m will result in a line survey. This has been a major step in astrochemistry, because it is now possible to have a full chemical inventory of a variety of different environments. In this context, the comparison between the chemistry in different objects will allow us to understand the chemical evolution from cold prestellar cores to protoplanetary disks. In the near future, observation with NOEMA will also deliver line surveys but at much better angular resolution, thus enabling us to spatially separate the different gas components. High-angular resolution observations will also reduce the level of line confusion present in current observations of complex sources, such as Sgr B2. These will lead to the discovery of new molecules in the ISM, and hopefully prebiotic molecules such as glycine, will be detected for the first time. In addition to spectral line surveys, the capabilities of the new IRAM instruments will allow us to study complete samples of specific types of sources, and obtain statistics about the chemical properties in different environments. Moreover, the imaging capabilities of the current and future telescopes will allow us to obtain information about the spatial distribution of the molecular emission for many different lines at the same time. For example, at the 30 m it is now possible to observe several lines of both methanol and formaldehyde, together with DCO^+, DCN and N_2H^+, all in one setup. The freeze-out of these species and the formation of H_2CO and CH_3OH on grains can thus be studied by observing maps of $\sim 200'' \times 200''$ for 12 different pre/protostellar cores in only

45 hours. With ALMA and NOEMA, similar studies will be possible for a reduced number of sources but at much better angular resolution. One consequence of the new instruments is the large amount of data produced by every observation. In this respect, comparisons with simple sources using estimators, like the ones discussed in this thesis, will become useful tools to deal with a large amount of data sets.

In order to fully benefit from all the advances in (sub)-millimeter observations, great progress must also be made in the current modeling tools. This includes the need for spectroscopic constants, collisional rates, photodissociation rates, and formation/destruction rates in general. For example, the conversion from observed line intensities to accurate molecular abundances is still an important problem. While high-density and high-temperature environments, like hot cores, can be safely modeled assuming local thermal equilibrium, lower density environments, like the Horsehead, need a non-LTE approach to compute the molecular abundances. For this, it is necessary to know how molecules are excited, and the collisional rates must be available. Another important problem is the interplay between the gas-phase and solid-phase chemistry, which has become a key topic in astrochemistry. Although many advances have been made in the last few years thanks to laboratory studies, there are numerous physical parameters related to grain surface processes that are not well known and are needed to properly compare the observations with theoretical models.

Appendix A

Rotational diagrams

When the source fills the beam the column density in the upper level can be written as

$$N_u = \frac{8\pi k\nu^2 W}{hc^3 A_{ul}} \left(\frac{\tau}{1 - e^{-\tau}} \right) \tag{A.1}$$

(Goldsmith & Langer 1999), where ν is the line frequency, W is the integrated line intensity, A_{ul} is the Einstein coefficient for spontaneous emission and τ is the opacity of the line. For an optically thin line we obtain

$$N_u^{\text{thin}} = \frac{8\pi k\nu^2 W}{hc^3 A_{ul}} \tag{A.2}$$

Under Local Thermodynamic Equilibrium (LTE) conditions, all excitation temperatures are the same, and the energy levels are populated following Boltzmann's law:

$$N_u = \frac{N}{Z} g_u e^{-E_u/kT} \tag{A.3}$$

where N is the total column density of the molecule, g_u and E_u are the degeneracy and the energy of the upper level and Z is the partition function, given by

$$Z = \sum_i g_i e^{-E_i/kT} \tag{A.4}$$

Taking the logarithm we obtain

$$\ln \frac{N_u}{g_u} = \ln \frac{N}{Z} - \frac{E_u}{kT} \tag{A.5}$$

Therefore, a plot of the natural logarithm of N_u/g_u versus E_u/kT will yield a straight line, where the inverse of the slope gives the rotational temperature, which should be equal to the kinetic temperature if all levels were thermalized, and the intersection with the ordinate axis gives the total column density of the molecule.

Equation A.5 can be expressed as

$$\ln \frac{N_u^{\text{thin}}}{g_u} + \ln C_\tau = \ln \frac{N}{Z} - \frac{E_u}{kT} \tag{A.6}$$

where $C_\tau = \frac{\tau}{1-e^{-\tau}} \leq 1$ is the opacity correction factor.

Bibliography

Abergel, A., Teyssier, D., Bernard, J. P., et al. 2003, A&A, 410, 577 (Cited on pages 18 and 19.)

Agúndez, M., Cernicharo, J., Guélin, M., et al. 2008, A&A, 478, L19 (Cited on pages 23 and 46.)

Agúndez, M., Cernicharo, J., Waters, L. B. F. M., et al. 2011, A&A, 533, L6 (Cited on page 32.)

Aladro, R., Martín, S., Martín-Pintado, J., et al. 2011, A&A, 535, A84 (Cited on pages 24, 25, 44 and 140.)

Aladro, R., Viti, S., Bayet, E., et al. 2013, A&A, 549, A39 (Cited on pages 25 and 140.)

André, P., Men'shchikov, A., Bontemps, S., et al. 2010, A&A, 518, L102 (Cited on pages 5 and 6.)

Anthony-Twarog, B. J. 1982, AJ, 87, 1213 (Cited on page 19.)

Apponi, A. J. & Ziurys, L. M. 1997, ApJ, 481, 800 (Cited on page 145.)

Araya, E., Hofner, P., Kurtz, S., Bronfman, L., & DeDeo, S. 2005, ApJS, 157, 279 (Cited on page 93.)

Arzoumanian, D., André, P., Didelon, P., et al. 2011, A&A, 529, L6 (Cited on page 5.)

Asplund, M., Grevesse, N., Sauval, A. J., & Scott, P. 2009, ARA&A, 47, 481 (Cited on pages 1 and 35.)

Avery, L. W., Amano, T., Bell, M. B., et al. 1992, ApJS, 83, 363 (Cited on page 24.)

Bacmann, A., Taquet, V., Faure, A., Kahane, C., & Ceccarelli, C. 2012, A&A, 541, L12 (Cited on pages xi, 118, 125, 126 and 161.)

Bakes, E. L. O. & Tielens, A. G. G. M. 1994, ApJ, 427, 822 (Cited on page 9.)

Ball, J. A., Gottlieb, C. A., Lilley, A. E., & Radford, H. E. 1970, ApJ, 162, L203 (Cited on page 57.)

Bally, J., Lanber, W. D., Stark, A. A., & Wilson, R. W. 1987, ApJ, 312, L45 (Cited on page 3.)

Barnard, E. E. 1913, ApJ, 38, 496 (Cited on page 17.)

Barnard, E. E. 1919, ApJ, 49, 1 (Cited on page 17.)

Bates, D. R. 1983, ApJ, 270, 564 (Cited on page 94.)

Beichman, C. A. 1986, in Astrophysics and Space Science Library, Vol. 124, Light on Dark Matter, ed. F. P. Israel, 279–292 (Cited on page 137.)

Belloche, A., Garrod, R. T., Müller, H. S. P., et al. 2009, A&A, 499, 215 (Cited on pages 117 and 139.)

Belloche, A., Menten, K. M., Comito, C., et al. 2008a, A&A, 482, 179 (Cited on pages 25, 117 and 139.)

Belloche, A., Menten, K. M., Comito, C., et al. 2008b, A&A, 492, 769 (Cited on page 140.)

Belloche, A., Müller, H. S. P., Menten, K. M., Schilke, P., & Comito, C. 2013, ArXiv e-prints (Cited on pages 25, 139 and 140.)

Benjamin, R. A., Churchwell, E., Babler, B. L., et al. 2003, PASP, 115, 953 (Cited on page 5.)

Bergin, E. A., Phillips, T. G., Comito, C., et al. 2010, A&A, 521, L20 (Cited on page 25.)

Bergin, E. A. & Tafalla, M. 2007, ARA&A, 45, 339 (Cited on page 5.)

Bergman, P., Parise, B., Liseau, R., & Larsson, B. 2011, A&A, 527, 39 (Cited on page 57.)

Berné, O., Joblin, C., Deville, Y., et al. 2007, A&A, 469, 575 (Cited on pages ix, 45 and 159.)

Bernstein, M. P., Dworkin, J. P., Sandford, S. A., Cooper, G. W., & Allamandola, L. J. 2002, Nature, 416, 401 (Cited on page 57.)

Biham, O. & Lipshtat, A. 2002, Phys. Rev. E, 66, 056103 (Cited on page 13.)

Bisschop, S. E., Jørgensen, J. K., Bourke, T. L., Bottinelli, S., & van Dishoeck, E. F. 2008, A&A, 488, 959 (Cited on page 137.)

Bisschop, S. E., Jørgensen, J. K., van Dishoeck, E. F., & de Wachter, E. B. M. 2007, A&A, 465, 913 (Cited on pages 14, 60, 117, 121, 124, 125 and 126.)

Blake, G. A., Sutton, E. C., Masson, C. R., & Phillips, T. G. 1987, ApJ, 315, 621 (Cited on pages 24, 117, 138 and 139.)

Bland-Hawthorn, J., Lumsden, S. L., Voit, G. M., Cecil, G. N., & Weisheit, J. C. 1997, Ap&SS, 248, 177 (Cited on page 136.)

Bockelée-Morvan, D., Lis, D. C., Wink, J. E., et al. 2000, A&A, 353, 1101 (Cited on page 93.)

Boger, G. I. & Sternberg, A. 2005, ApJ, 632, 302 (Cited on page 145.)

Boogert, A. C. A., Huard, T. L., Cook, A. M., et al. 2011, ApJ, 729, 92 (Cited on page 59.)

Boogert, A. C. A., Pontoppidan, K. M., Knez, C., et al. 2008, ApJ, 678, 985 (Cited on page 59.)

Bottinelli, S., Boogert, A. C. A., Bouwman, J., et al. 2010, ApJ, 718, 1100 (Cited on page 59.)

Bottinelli, S., Ceccarelli, C., Lefloch, B., et al. 2004a, ApJ, 615, 354 (Cited on page 93.)

Bottinelli, S., Ceccarelli, C., Neri, R., et al. 2004b, ApJ, 617, L69 (Cited on page 137.)

Bottinelli, S., Ceccarelli, C., Williams, J. P., & Lefloch, B. 2007, A&A, 463, 601 (Cited on pages 14 and 60.)

Boulares, A. & Cox, D. P. 1990, ApJ, 365, 544 (Cited on page 20.)

Bowler, B. P., Waller, W. H., Megeath, S. T., Patten, B. M., & Tamura, M. 2009, AJ, 137, 3685 (Cited on page 21.)

Brown, W. A. & Bolina, A. S. 2007, MNRAS, 374, 1006 (Cited on page 60.)

Cami, J., Bernard-Salas, J., Peeters, E., & Malek, S. E. 2010, Science, 329, 1180 (Cited on page 3.)

Caris, M., Giesen, T. F., Duan, C., et al. 2009, Journal of Molecular Spectroscopy, 253, 99 (Cited on page 45.)

Caselli, P., Keto, E., Bergin, E. A., et al. 2012, ApJ, 759, L37 (Cited on pages 14 and 60.)

Caux, E., Kahane, C., Castets, A., et al. 2011, A&A, 532, A23 (Cited on pages 27 and 138.)

Cazaux, S. & Spaans, M. 2009, A&A, 496, 365 (Cited on page 13.)

Cazaux, S., Tielens, A. G. G. M., Ceccarelli, C., et al. 2003, ApJ, 593, L51 (Cited on pages 93 and 117.)

Cazzoli, G., Cludi, L., Puzzarini, C., & Gauss, J. 2010, A&A, 509, A1 (Cited on page 35.)

Cazzoli, G., Puzzarini, C., & Lapinov, A. V. 2004, ApJ, 611, 615 (Cited on page 35.)

Ceccarelli, C., Loinard, L., Castets, A., Tielens, A. G. G. M., & Caux, E. 2000, A&A, 357, L9 (Cited on page 57.)

Cernicharo, J. & Guelin, M. 1987, A&A, 183, L10 (Cited on page 31.)

Cernicharo, J., Guélin, M., & Kahane, C. 2000, A&AS, 142, 181 (Cited on pages 24, 25 and 44.)

Cernicharo, J., Kahane, C., Guelin, M., & Gomez-Gonzalez, J. 1988, A&A, 189, L1 (Cited on page 93.)

Cernicharo, J., Waters, L. B. F. M., Decin, L., et al. 2010, A&A, 521, L8 (Cited on page 25.)

Chandler, C. J., Brogan, C. L., Shirley, Y. L., & Loinard, L. 2005, ApJ, 632, 371 (Cited on page 137.)

Charnley, S. B., Tielens, A. G. G. M., & Millar, T. J. 1992, ApJ, 399, L71 (Cited on pages 57 and 94.)

Codella, C., Benedettini, M., Beltrán, M. T., et al. 2009, A&A, 507, L25 (Cited on page 93.)

Codella, C., Ceccarelli, C., Lefloch, B., et al. 2012, ApJ, 757, L9 (Cited on pages 57 and 60.)

Codella, C. & Moscadelli, L. 2000, A&A, 362, 723 (Cited on page 57.)

Comito, C., Schilke, P., Phillips, T. G., et al. 2005, ApJS, 156, 127 (Cited on pages 24, 25, 27 and 139.)

Compiègne, M., Abergel, A., Verstraete, L., et al. 2007, A&A, 471, 205 (Cited on page 45.)

Cordiner, M. A., Buckle, J. V., Wirström, E. S., Olofsson, A. O. H., & Charnley, S. B. 2013, ApJ, 770, 48 (Cited on page 159.)

Cummins, S. E., Linke, R. A., & Thaddeus, P. 1986, ApJS, 60, 819 (Cited on pages 24, 117 and 120.)

Cuppen, H. M., van Dishoeck, E. F., Herbst, E., & Tielens, A. G. G. M. 2009, A&A, 508, 275 (Cited on page 59.)

Danger, G., Bossa, J.-B., de Marcellus, P., et al. 2011, A&A, 525, A30 (Cited on page 94.)

de Vicente, P., Martín-Pintado, J., Neri, R., & Colom, P. 2000, A&A, 361, 1058 (Cited on pages 93 and 94.)

Desert, F.-X., Boulanger, F., & Puget, J. L. 1990, A&A, 237, 215 (Cited on page 2.)

D'Hendecourt, L. B. & Leger, A. 1987, A&A, 180, L9 (Cited on page 9.)

Downes, D., Wilson, T. L., Bieging, J., & Wink, J. 1980, A&AS, 40, 379 (Cited on page 57.)

Draine, B. T. 1978, ApJS, 36, 595 (Cited on pages 6, 7, 8, 19, 44 and 60.)

Draine, B. T. 2011, Physics of the Interstellar and Intergalactic Medium (Cited on pages 1 and 2.)

Dulieu, F., Congiu, E., Noble, J., et al. 2013, Scientific Reports, 3 (Cited on page 14.)

Dutrey, A., Guilloteau, S., & Guelin, M. 1997, A&A, 317, L55 (Cited on page 44.)

Elsila, J. E., Dworkin, J. P., Bernstein, M. P., Martin, M. P., & Sandford, S. A. 2007, ApJ, 660, 911 (Cited on page 117.)

Elsila, J. E., Glavin, D. P., & Dworkin, J. P. 2009, Meteoritics and Planetary Science, 44, 1323 (Cited on page 117.)

Emprechtinger, M., Monje, R. R., van der Tak, F. F. S., et al. 2012, ApJ, 756, 136 (Cited on page 32.)

Federman, S. R. & Allen, M. 1991, ApJ, 375, 157 (Cited on page 58.)

Federman, S. R., Sheffer, Y., Lambert, D. L., & Smith, V. V. 2005, ApJ, 619, 884 (Cited on page 32.)

Fortenberry, R. C., Huang, X., Crawford, T. D., & Lee, T. J. 2013, ApJ, 772, 39 (Cited on pages ix, 46 and 159.)

Freedman, W. L., Hughes, S. M., Madore, B. F., et al. 1994, ApJ, 427, 628 (Cited on page 136.)

Friedel, D. N. & Snyder, L. E. 2008, ApJ, 672, 962 (Cited on page 138.)

Friedel, D. N., Snyder, L. E., Turner, B. E., & Remijan, A. 2004, ApJ, 600, 234 (Cited on page 24.)

Fuchs, G. W., Cuppen, H. M., Ioppolo, S., et al. 2009, A&A, 505, 629 (Cited on page 59.)

Fuente, A., García-Burillo, S., Gerin, M., et al. 2006, ApJ, 641, L105 (Cited on page 140.)

Fuente, A., García-Burillo, S., Usero, A., et al. 2008, A&A, 492, 675 (Cited on page 140.)

Fuente, A., Martin-Pintado, J., Cernicharo, J., & Bachiller, R. 1993, A&A, 276, 473 (Cited on pages 133 and 145.)

Fuente, A., Rodrıguez-Franco, A., Garcıa-Burillo, S., Martın-Pintado, J., & Black, J. H. 2003, A&A, 406, 899 (Cited on pages ix, 44, 133, 134 and 159.)

Fuente, A., Rodriguez-Franco, A., & Martin-Pintado, J. 1996, A&A, 312, 599 (Cited on pages 133 and 134.)

Garay, G., Köhnenkamp, I., Bourke, T. L., Rodríguez, L. F., & Lehtinen, K. K. 1998, ApJ, 509, 768 (Cited on page 57.)

García-Burillo, S., Martín-Pintado, J., Fuente, A., & Neri, R. 2001, ApJ, 563, L27 (Cited on page 140.)

García-Burillo, S., Martín-Pintado, J., Fuente, A., Usero, A., & Neri, R. 2002, ApJ, 575, L55 (Cited on pages 140, 144 and 154.)

Garrod, R., Park, I. H., Caselli, P., & Herbst, E. 2006, Faraday Discussions, 133, 51 (Cited on pages 59 and 125.)

Garrod, R. T. 2013, ApJ, 765, 60 (Cited on page 117.)

Garrod, R. T., Weaver, S. L. W., & Herbst, E. 2008, ApJ, 682, 283 (Cited on pages 57 and 94.)

Geppert, W. D., Hamberg, M., Thomas, R. D., et al. 2006, Faraday Discussions, 133, 177 (Cited on page 59.)

Gerin, M., Goicoechea, J. R., Pety, J., & Hily-Blant, P. 2009, A&A, 494, 977 (Cited on pages 22, 23 and 121.)

Gerin, M., Kaźmierczak, M., Jastrzebska, M., et al. 2011, A&A, 525, A116 (Cited on page 44.)

Gerin, M., Lesaffre, P., Goicoechea, J. R., et al. 2007, in Molecules in Space and Laboratory (Cited on page 45.)

Gibb, E., Nummelin, A., Irvine, W. M., Whittet, D. C. B., & Bergman, P. 2000a, ApJ, 545, 309 (Cited on page 94.)

Gibb, E. L., Van Brunt, K. A., Brittain, S. D., & Rettig, T. W. 2007, ApJ, 660, 1572 (Cited on page 44.)

Gibb, E. L., Whittet, D. C. B., Boogert, A. C. A., & Tielens, A. G. G. M. 2004, ApJS, 151, 35 (Cited on page 59.)

Gibb, E. L., Whittet, D. C. B., Schutte, W. A., et al. 2000b, ApJ, 536, 347 (Cited on page 59.)

Ginard, D., González-García, M., Fuente, A., et al. 2012, A&A, 543, A27 (Cited on pages 25, 93, 133, 135, 136, 144 and 145.)

Glavin, D. P., Burton, A. S., Elsila, J. E., et al. 2013, in Lunar and Planetary Institute Science Conference Abstracts, Vol. 44, Lunar and Planetary Institute Science Conference Abstracts, 1189 (Cited on page 117.)

Goicoechea, J. R., Compiègne, M., & Habart, E. 2009a, ApJ, 699, L165 (Cited on pages 60 and 126.)

Goicoechea, J. R., Joblin, C., Contursi, A., et al. 2011, A&A, 530, L16 (Cited on page 134.)

Goicoechea, J. R. & Le Bourlot, J. 2007, A&A, 467, 1 (Cited on page 7.)

Goicoechea, J. R., Pety, J., Gerin, M., Hily-Blant, P., & Le Bourlot, J. 2009b, A&A, 498, 771 (Cited on pages 23, 24, 67 and 144.)

Goicoechea, J. R., Pety, J., Gerin, M., et al. 2006, A&A, 456, 565 (Cited on pages 23, 68, 121 and 140.)

Goldsmith, P. F. & Langer, W. D. 1999, ApJ, 517, 209 (Cited on pages 63 and 165.)

Gonzalez Garcia, M., Le Bourlot, J., Le Petit, F., & Roueff, E. 2008, A&A, 485, 127 (Cited on page 11.)

Gratier, P., Pety, J., Guzmán, V., et al. 2013, A&A, 557, A101 (Cited on pages 95 and 125.)

Green, S. D., Bolina, A. S., Chen, R., et al. 2009, MNRAS, 398, 357 (Cited on page 60.)

Groesbeck, T. D., Phillips, T. G., & Blake, G. A. 1994, ApJS, 94, 147 (Cited on page 24.)

Gry, C., Boulanger, F., Nehmé, C., et al. 2002, A&A, 391, 675 (Cited on page 13.)

Guzmán, V., Pety, J., Goicoechea, J. R., Gerin, M., & Roueff, E. 2011, A&A, 534, A49 (Cited on pages 63, 65, 66 and 68.)

Guzmán, V., Pety, J., Gratier, P., et al. 2012a, A&A, 543, L1 (Cited on pages 34 and 35.)

Guzmán, V., Roueff, E., Gauss, J., et al. 2012b, A&A, 548, A94 (Cited on page 34.)

Guzman, V. V., Goicoechea, J. R., Pety, J., et al. 2013, ArXiv e-prints (Cited on pages 63, 65, 66 and 68.)

Habart, E., Abergel, A., Walmsley, C. M., Teyssier, D., & Pety, J. 2005, A&A, 437, 177 (Cited on page 19.)

Habing, H. J. 1968, Bull. Astron. Inst. Netherlands, 19, 421 (Cited on page 7.)

Hatchell, J., Thompson, M. A., Millar, T. J., & MacDonald, G. H. 1998, A&AS, 133, 29 (Cited on page 94.)

Herbst, E., Terzieva, R., & Talbi, D. 2000, MNRAS, 311, 869 (Cited on page 146.)

Herbst, E. & van Dishoeck, E. F. 2009, ARA&A, 47, 427 (Cited on pages 3, 94, 117 and 124.)

Herbst, W. & Racine, R. 1976, AJ, 81, 840 (Cited on page 133.)

Herschel, W. 1811, Royal Society of London Philosophical Transactions Series I, 101, 269 (Cited on page 17.)

Hily-Blant, P., Pineau des Forêts, G., Faure, A., Le Gal, R., & Padovani, M. 2013, A&A, 557, A65 (Cited on page 137.)

Hily-Blant, P., Teyssier, D., Philipp, S., & Güsten, R. 2005, A&A, 440, 909 (Cited on pages 19, 20, 22 and 26.)

Hirashita, H. & Omukai, K. 2009, MNRAS, 399, 1795 (Cited on page 3.)

Hollenbach, D. J. & Tielens, A. G. G. M. 1999, Reviews of Modern Physics, 71, 173 (Cited on pages 1, 2, 6 and 8.)

Hollis, J. M., Lovas, F. J., & Jewell, P. R. 2000, ApJ, 540, L107 (Cited on pages 117 and 139.)

Hollis, J. M., Lovas, F. J., Remijan, A. J., et al. 2006, ApJ, 643, L25 (Cited on pages 117 and 139.)

Huang, X., Fortenberry, R. C., & Lee, T. J. 2013, ApJ, 768, L25 (Cited on pages ix, 45, 46 and 159.)

Hudson, R. L. & Loeffler, M. J. 2013, ApJ, 773, 109 (Cited on page 124.)

Hudson, R. L., Moore, M. H., Dworkin, J. P., Martin, M. P., & Pozun, Z. D. 2008, Astrobiology, 8, 771 (Cited on page 93.)

Huntress, Jr., W. T. & Mitchell, G. F. 1979, ApJ, 231, 456 (Cited on page 94.)

Iglesias-Groth, S., García-Hernández, D. A., Cataldo, F., & Manchado, A. 2012, MNRAS, 423, 2868 (Cited on page 2.)

Indriolo, N., Neufeld, D. A., Seifahrt, A., & Richter, M. J. 2013, ApJ, 764, 188 (Cited on page 32.)

Ioppolo, S., Cuppen, H. M., van Dishoeck, E. F., & Linnartz, H. 2011, MNRAS, 410, 1089 (Cited on page 125.)

Irvine, W. M., Friberg, P., Kaifu, N., et al. 1989, ApJ, 342, 871 (Cited on page 118.)

Jansen, D. J., Spaans, M., Hogerheijde, M. R., & van Dishoeck, E. F. 1995, A&A, 303, 541 (Cited on page 134.)

Jewell, P. R., Hollis, J. M., Lovas, F. J., & Snyder, L. E. 1989, ApJS, 70, 833 (Cited on page 24.)

Jiang, X., Wang, J., & Gu, Q. 2011, MNRAS, 418, 1753 (Cited on page 44.)

Johansson, L. E. B., Andersson, C., Elder, J., et al. 1985, A&AS, 60, 135 (Cited on page 24.)

Johansson, L. E. B., Andersson, C., Ellder, J., et al. 1984, A&A, 130, 227 (Cited on page 24.)

Jørgensen, J. K., Schöier, F. L., & van Dishoeck, E. F. 2005, A&A, 437, 501 (Cited on pages 14, 57 and 60.)

Jura, M. 1974, ApJ, 191, 375 (Cited on page 13.)

Kaifu, N., Ohishi, M., Kawaguchi, K., et al. 2004, PASJ, 56, 69 (Cited on page 24.)

Keane, J. V., Tielens, A. G. G. M., Boogert, A. C. A., Schutte, W. A., & Whittet, D. C. B. 2001, A&A, 376, 254 (Cited on page 125.)

Keeler, J. E. 1908, Publications of Lick Observatory, 8, 1 (Cited on page 17.)

Kenyon, S. J., Gomez, M., Marzke, R. O., & Hartmann, L. 1994, AJ, 108, 251 (Cited on page 136.)

Kramer, C., Stutzki, J., & Winnewisser, G. 1996, A&A, 307, 915 (Cited on page 17.)

Krips, M., Neri, R., García-Burillo, S., et al. 2008, ApJ, 677, 262 (Cited on page 146.)

Kuan, Y.-J., Huang, H.-C., Charnley, S. B., et al. 2004, ApJ, 616, L27 (Cited on page 137.)

Lada, E. A., Bally, J., & Stark, A. A. 1991, ApJ, 368, 432 (Cited on page 17.)

Langer, W. D., Velusamy, T., Pineda, J. L., et al. 2010, A&A, 521, L17 (Cited on page 33.)

Le Bourlot, J., Le Petit, F., Pinto, C., Roueff, E., & Roy, F. 2012, A&A, 541, A76 (Cited on pages 9 and 13.)

Le Petit, F., Barzel, B., Biham, O., Roueff, E., & Le Bourlot, J. 2009, A&A, 505, 1153 (Cited on page 13.)

Lee, C. W., Cho, S.-H., & Lee, S.-M. 2001, ApJ, 551, 333 (Cited on page 24.)

Lepp, S. & Dalgarno, A. 1988, ApJ, 335, 769 (Cited on page 9.)

Lesaffre, P., Gerin, M., & Hennebelle, P. 2007, A&A, 469, 949 (Cited on page 45.)

Leung, C. M., Herbst, E., & Huebner, W. F. 1984, ApJS, 56, 231 (Cited on page 94.)

Leurini, S., Parise, B., Schilke, P., Pety, J., & Rolffs, R. 2010, A&A, 511, 82 (Cited on pages 14, 57 and 60.)

Leurini, S., Rolffs, R., Thorwirth, S., et al. 2006, A&A, 454, L47 (Cited on page 134.)

Leurini, S., Schilke, P., Menten, K. M., et al. 2004, A&A, 422, 573 (Cited on pages 57 and 62.)

Leurini, S., Schilke, P., Wyrowski, F., & Menten, K. M. 2007, A&A, 466, 215 (Cited on page 62.)

Li, D. & Goldsmith, P. F. 2012, ApJ, 756, 12 (Cited on page 93.)

Lindberg, J. E., Aalto, S., Costagliola, F., et al. 2011, A&A, 527, A150 (Cited on page 93.)

Lis, D. C. & Goldsmith, P. F. 1990, ApJ, 356, 195 (Cited on page 139.)

Lis, D. C. & Schilke, P. 2003, ApJ, 597, L145 (Cited on page 134.)

Liszt, H. & Lucas, R. 2000, A&A, 355, 333 (Cited on page 136.)

Liszt, H. & Lucas, R. 2001, A&A, 370, 576 (Cited on page 136.)

Liszt, H., Sonnentrucker, P., Cordiner, M., & Gerin, M. 2012, ApJ, 753, L28 (Cited on page 44.)

Liu, S.-Y., Girart, J. M., Remijan, A., & Snyder, L. E. 2002, ApJ, 576, 255 (Cited on page 138.)

Loenen, A. F., Spaans, M., Baan, W. A., & Meijerink, R. 2008, A&A, 488, L5 (Cited on page 146.)

Loinard, L., Torres, R. M., Mioduszewski, A. J., & Rodríguez, L. F. 2008, ApJ, 675, L29 (Cited on pages 136 and 137.)

Loinard, L., Zapata, L. A., Rodríguez, L. F., et al. 2013, MNRAS, 430, L10 (Cited on pages 137 and 138.)

Low, F. J., Young, E., Beintema, D. A., et al. 1984, ApJ, 278, L19 (Cited on page 3.)

Lucas, R. & Liszt, H. S. 2000, A&A, 358, 1069 (Cited on pages 44 and 136.)

Lucas, R. & Liszt, H. S. 2002, A&A, 384, 1054 (Cited on page 136.)

Mackay, D. D. S. 1999, MNRAS, 304, 61 (Cited on page 94.)

Mackey, J. & Lim, A. J. 2010, MNRAS, 403, 714 (Cited on page 21.)

Mangum, J. G., Darling, J., Henkel, C., & Menten, K. M. 2013, ApJ, 766, 108 (Cited on page 57.)

Mangum, J. G., Darling, J., Menten, K. M., & Henkel, C. 2008, ApJ, 673, 832 (Cited on page 57.)

Mangum, J. G. & Wootten, A. 1993, ApJS, 89, 123 (Cited on pages 57 and 60.)

Maret, S., Ceccarelli, C., Caux, E., et al. 2004, A&A, 416, 577 (Cited on page 57.)

Martín, S., Krips, M., Martín-Pintado, J., et al. 2011, A&A, 527, A36 (Cited on page 25.)

Martín, S., Mauersberger, R., Martín-Pintado, J., Henkel, C., & García-Burillo, S. 2006, ApJS, 164, 450 (Cited on pages 25 and 151.)

Mathis, J. S., Rumpl, W., & Nordsieck, K. H. 1977, ApJ, 217, 425 (Cited on page 7.)

Matthews, H. E., Friberg, P., & Irvine, W. M. 1985, ApJ, 290, 609 (Cited on page 118.)

Mauersberger, R., Henkel, C., & Sage, L. J. 1990, A&A, 236, 63 (Cited on page 93.)

Mauersberger, R., Henkel, C., Walmsley, C. M., Sage, L. J., & Wiklind, T. 1991, A&A, 247, 307 (Cited on page 93.)

McCarthy, M. C., Gottlieb, C. A., Gupta, H., & Thaddeus, P. 2006, ApJ, 652, L141 (Cited on page 159.)

McGuire, B. A., Carroll, P. B., Loomis, R. A., et al. 2013, ArXiv e-prints (Cited on pages ix, 46 and 159.)

Meier, D. S. & Turner, J. L. 2005, ApJ, 618, 259 (Cited on page 57.)

Melnick, G., Gull, G. E., & Harwit, M. 1979, ApJ, 227, L29 (Cited on page 6.)

Men'shchikov, A., André, P., Didelon, P., et al. 2010, A&A, 518, L103 (Cited on page 5.)

Menten, K. M., Reid, M. J., Forbrich, J., & Brunthaler, A. 2007, A&A, 474, 515 (Cited on pages 133, 136 and 138.)

Millar, T. J., Herbst, E., & Bettens, R. P. A. 2000, MNRAS, 316, 195 (Cited on page 44.)

Mispelaer, F., Theulé, P., Aouididi, H., et al. 2013, A&A, 555, A13 (Cited on page 126.)

Mizuno, A., Fukui, Y., Iwata, T., Nozawa, S., & Takano, T. 1990, ApJ, 356, 184 (Cited on page 137.)

Monje, R. R., Emprechtinger, M., Phillips, T. G., et al. 2011a, ApJ, 734, L23 (Cited on page 32.)

Monje, R. R., Phillips, T. G., Peng, R., et al. 2011b, ApJ, 742, L21 (Cited on page 33.)

Mookerjea, B., Ossenkopf, V., Ricken, O., et al. 2012, A&A, 542, L17 (Cited on page 33.)

Muñoz Caro, G. M., Meierhenrich, U. J., Schutte, W. A., et al. 2002, Nature, 416, 403 (Cited on page 57.)

Müller, H. S. P., Thorwirth, S., Roth, D. A., & Winnewisser, G. 2001, A&A, 370, L49 (Cited on page 118.)

Muller, S., Beelen, A., Guélin, M., et al. 2011, A&A, 535, A103 (Cited on pages 25, 118, 141 and 151.)

Muller, S., Guélin, M., Dumke, M., Lucas, R., & Combes, F. 2006, A&A, 458, 417 (Cited on page 141.)

Mumma, M. J. & Charnley, S. B. 2011, ARA&A, 49, 471 (Cited on page 57.)

Nagy, Z., Van der Tak, F. F. S., Ossenkopf, V., et al. 2013, A&A, 550, A96 (Cited on page 134.)

Neufeld, D. A., Schilke, P., Menten, K. M., et al. 2006, A&A, 454, L37 (Cited on page 32.)

Neufeld, D. A., Sonnentrucker, P., Phillips, T. G., et al. 2010, A&A, 518, L108 (Cited on page 32.)

Neufeld, D. A. & Wolfire, M. G. 2009, ApJ, 706, 1594 (Cited on page 31.)

Neufeld, D. A., Wolfire, M. G., & Schilke, P. 2005, ApJ, 628, 260 (Cited on pages 31 and 32.)

Neufeld, D. A., Zmuidzinas, J., Schilke, P., & Phillips, T. G. 1997, ApJ, 488, L141 (Cited on page 32.)

Nummelin, A., Bergman, P., Hjalmarson, Å., et al. 2000, ApJS, 128, 213 (Cited on pages 24 and 140.)

Öberg, K. I., Boamah, M. D., Fayolle, E. C., et al. 2013, ApJ, 771, 95 (Cited on pages 117 and 125.)

Öberg, K. I., Boogert, A. C. A., Pontoppidan, K. M., et al. 2008, ApJ, 678, 1032 (Cited on page 59.)

Öberg, K. I., Boogert, A. C. A., Pontoppidan, K. M., et al. 2011, ApJ, 740, 109 (Cited on page 59.)

Öberg, K. I., Garrod, R. T., van Dishoeck, E. F., & Linnartz, H. 2009a, A&A, 504, 891 (Cited on pages 14 and 60.)

Öberg, K. I., Linnartz, H., Visser, R., & van Dishoeck, E. F. 2009b, ApJ, 693, 1209 (Cited on pages 14 and 60.)

Öberg, K. I., van Dishoeck, E. F., & Linnartz, H. 2009c, A&A, 496, 281 (Cited on page 60.)

Olmi, L., Cesaroni, R., & Walmsley, C. M. 1996, A&A, 307, 599 (Cited on page 94.)

Padovani, M., Walmsley, C. M., Tafalla, M., Galli, D., & Müller, H. S. P. 2009, A&A, 505, 1199 (Cited on page 137.)

Padovani, M., Walmsley, C. M., Tafalla, M., Hily-Blant, P., & Pineau Des Forêts, G. 2011, A&A, 534, A77 (Cited on page 137.)

Pardo, J. R., Cernicharo, J., Goicoechea, J. R., & Phillips, T. G. 2004, ApJ, 615, 495 (Cited on page 93.)

Parise, B., Leurini, S., Schilke, P., et al. 2009, A&A, 508, 737 (Cited on page 134.)

Perault, M., Omont, A., Simon, G., et al. 1996, A&A, 315, L165 (Cited on page 5.)

Perryman, M. A. C., Lindegren, L., Kovalevsky, J., et al. 1997, A&A, 323, L49 (Cited on page 17.)

Pety, J., Goicoechea, J. R., Hily-Blant, P., Gerin, M., & Teyssier, D. 2007, A&A, 464, L41 (Cited on pages 22, 23 and 26.)

Pety, J., Teyssier, D., Fossé, D., et al. 2005, A&A, 435, 885 (Cited on pages ix, 23, 26, 44, 142 and 159.)

Philipp, S. D., Lis, D. C., Güsten, R., et al. 2006, A&A, 454, 213 (Cited on page 17.)

Phillips, T. G., Bergin, E. A., Lis, D. C., et al. 2010, A&A, 518, L109 (Cited on page 32.)

Pickett, H. M., Poynter, R. L., Cohen, E. A., et al. 1998, J. Quant. Spec. Radiat. Transf., 60, 883 (Cited on page 118.)

Pilleri, P., Montillaud, J., Berné, O., & Joblin, C. 2012, A&A, 542, A69 (Cited on pages ix, 45 and 159.)

Pilleri, P., Treviño-Morales, S., Fuente, A., et al. 2013, A&A, 554, A87 (Cited on page 44.)

Pontoppidan, K. M., Boogert, A. C. A., Fraser, H. J., et al. 2008, ApJ, 678, 1005 (Cited on page 59.)

Pound, M. W., Reipurth, B., & Bally, J. 2003, AJ, 125, 2108 (Cited on pages 20, 21 and 22.)

Purcell, C. R., Balasubramanyam, R., Burton, M. G., et al. 2006, MNRAS, 367, 553 (Cited on pages 93 and 95.)

Qi, C., Öberg, K. I., Wilner, D. J., & Rosenfeld, K. A. 2013, ApJ, 765, L14 (Cited on pages 44 and 57.)

Qin, S.-L., Schilke, P., Rolffs, R., et al. 2011, A&A, 530, L9 (Cited on page 139.)

Rangwala, N., Maloney, P. R., Glenn, J., et al. 2011, ApJ, 743, 94 (Cited on page 33.)

Reid, M. J., Menten, K. M., Zheng, X. W., Brunthaler, A., & Xu, Y. 2009, ApJ, 705, 1548 (Cited on pages 136 and 139.)

Reipurth, B. 1983, A&A, 117, 183 (Cited on page 21.)

Reipurth, B. & Bouchet, P. 1984, A&A, 137, L1 (Cited on pages 20 and 21.)

Remijan, A. J., Hollis, J. M., Lovas, F. J., Plusquellic, D. F., & Jewell, P. R. 2005, ApJ, 632, 333 (Cited on page 93.)

Remijan, A. J., Milam, S. N., Womack, M., et al. 2008, ApJ, 689, 613 (Cited on page 93.)

Rimmer, P. B., Herbst, E., Morata, O., & Roueff, E. 2012, A&A, 537, A7 (Cited on page 45.)

Rizzo, J. R., Fuente, A., Rodríguez-Franco, A., & García-Burillo, S. 2003, ApJ, 597, L153 (Cited on pages 133, 135 and 136.)

Roberts, I. 1903, ApJ, 17, 72 (Cited on page 17.)

Russell, R. W., Melnick, G., Gull, G. E., & Harwit, M. 1980, ApJ, 240, L99 (Cited on page 6.)

Russell, R. W., Melnick, G., Smyers, S. D., et al. 1981, ApJ, 250, L35 (Cited on page 6.)

Sakai, N., Ceccarelli, C., Bottinelli, S., Sakai, T., & Yamamoto, S. 2012, ApJ, 754, 70 (Cited on page 57.)

Sandell, G., Reipurth, B., Menten, C., Walmsley, M., & Ungerechts, H. 1986, in Astrophysics and Space Science Library, Vol. 124, Light on Dark Matter, ed. F. P. Israel, 295 (Cited on pages 17 and 21.)

Schaerer, D. & de Koter, A. 1997, A&A, 322, 598 (Cited on page 17.)

Schilke, P., Benford, D. J., Hunter, T. R., Lis, D. C., & Phillips, T. G. 2001a, ApJS, 132, 281 (Cited on pages 24 and 134.)

Schilke, P., Groesbeck, T. D., Blake, G. A., & Phillips, T. G. 1997, ApJS, 108, 301 (Cited on pages 24 and 25.)

Schilke, P., Pineau des Forêts, G., Walmsley, C. M., & Martín-Pintado, J. 2001b, A&A, 372, 291 (Cited on pages 25, 27, 133 and 134.)

Schinnerer, E., Eckart, A., Tacconi, L. J., Genzel, R., & Downes, D. 2000, ApJ, 533, 850 (Cited on page 140.)

Schloerb, F. P., Snell, R. L., & Young, J. S. 1983, ApJ, 267, 163 (Cited on page 93.)

Schutte, W. A., Boogert, A. C. A., Tielens, A. G. G. M., et al. 1999, A&A, 343, 966 (Cited on page 124.)

Sellgren, K., Werner, M. W., Ingalls, J. G., et al. 2010, ApJ, 722, L54 (Cited on page 3.)

Snow, T. P., Destree, J. D., & Jensen, A. G. 2007, ApJ, 655, 285 (Cited on pages 32 and 35.)

Snyder, L. E., Buhl, D., Zuckerman, B., & Palmer, P. 1969, Physical Review Letters, 22, 679 (Cited on page 57.)

Sobolev, V. V. 1957, Soviet Ast., 1, 678 (Cited on page 66.)

Solomon, P. M., Jefferts, K. B., Penzias, A. A., & Wilson, R. W. 1971, ApJ, 168, L107 (Cited on page 93.)

Sonnentrucker, P., Neufeld, D. A., Phillips, T. G., et al. 2010, A&A, 521, L12 (Cited on pages 32 and 35.)

Stark, A. A. & Bally, J. 1982, in Astrophysics and Space Science Library, Vol. 93, Regions of Recent Star Formation, ed. R. S. Roger & P. E. Dewdney, 329–333 (Cited on page 17.)

Sternberg, A. & Dalgarno, A. 1989, ApJ, 338, 197 (Cited on page 6.)

Storey, J. W. V., Watson, D. M., & Townes, C. H. 1979, ApJ, 233, 109 (Cited on page 6.)

Strickland, D. K., Heckman, T. M., Colbert, E. J. M., Hoopes, C. G., & Weaver, K. A. 2004, ApJ, 606, 829 (Cited on page 140.)

Sun, W.-H., Zhou, X., Chen, W.-P., et al. 2005, ApJ, 630, L133 (Cited on page 140.)

Sutton, E. C., Jaminet, P. A., Danchi, W. C., & Blake, G. A. 1991, ApJS, 77, 255 (Cited on page 24.)

Sutton, E. C., Peng, R., Danchi, W. C., et al. 1995, ApJS, 97, 455 (Cited on page 57.)

Suzuki, H., Kaifu, N., Ohishi, M., Miyaji, T., & Ishikawa, S. 1987, in IAU Symposium, Vol. 115, Star Forming Regions, ed. M. Peimbert & J. Jugaku, 90 (Cited on page 17.)

Tafalla, M., Myers, P. C., Caselli, P., & Walmsley, C. M. 2004, A&A, 416, 191 (Cited on page 137.)

Tafalla, M., Myers, P. C., Caselli, P., Walmsley, C. M., & Comito, C. 2002, ApJ, 569, 815 (Cited on page 137.)

Tafalla, M., Santiago-García, J., Hacar, A., & Bachiller, R. 2010, A&A, 522, A91 (Cited on page 57.)

Tafalla, M., Santiago-García, J., Myers, P. C., et al. 2006, A&A, 455, 577 (Cited on page 137.)

Tercero, B., Cernicharo, J., Pardo, J. R., & Goicoechea, J. R. 2010, A&A, 517, A96 (Cited on pages 24, 25 and 138.)

Tercero, B., Vincent, L., Cernicharo, J., Viti, S., & Marcelino, N. 2011, A&A, 528, A26 (Cited on page 138.)

Teyssier, D., Fossé, D., Gerin, M., et al. 2004, A&A, 417, 135 (Cited on pages ix, 23, 44 and 159.)

Tielens, A. G. G. M. & Allamandola, L. J. 1987, in Astrophysics and Space Science Library, Vol. 134, Interstellar Processes, ed. D. J. Hollenbach & H. A. Thronson, Jr., 397–469 (Cited on page 60.)

Tielens, A. G. G. M. & Hagen, W. 1982, A&A, 114, 245 (Cited on page 125.)

Tielens, A. G. G. M. & Hollenbach, D. 1985a, ApJ, 291, 747 (Cited on page 6.)

Tielens, A. G. G. M. & Hollenbach, D. 1985b, ApJ, 291, 722 (Cited on pages 6 and 11.)

Tielens, A. G. G. M., McKee, C. F., Seab, C. G., & Hollenbach, D. J. 1994, ApJ, 431, 321 (Cited on page 3.)

Tielens, A. G. G. M. & Whittet, D. C. B. 1997, in IAU Symposium, Vol. 178, IAU Symposium, ed. E. F. van Dishoeck, 45 (Cited on page 59.)

Townes, C. H. & Schawlow, A. L. 1975, Microwave spectroscopy. (Cited on page 34.)

Tremblin, P., Audit, E., Minier, V., & Schneider, N. 2012, A&A, 538, A31 (Cited on page 21.)

Tudorie, M., Cacciani, P., Cosléou, J., et al. 2006, A&A, 453, 755 (Cited on page 58.)

Turner, B. E. 1971, ApJ, 163, L35 (Cited on page 93.)

Turner, B. E. 1989, ApJS, 70, 539 (Cited on page 24.)

Turner, B. E. 1991, ApJS, 76, 617 (Cited on page 24.)

Turner, B. E., Herbst, E., & Terzieva, R. 2000, ApJS, 126, 427 (Cited on pages ix, 43, 44 and 158.)

Ungerechts, H. & Thaddeus, P. 1987, ApJS, 63, 645 (Cited on page 3.)

van den Ancker, M. E., The, P. S., Tjin A Djie, H. R. E., et al. 1997, A&A, 324, L33 (Cited on page 133.)

van der Tak, F. F. S., Black, J. H., Schöier, F. L., Jansen, D. J., & van Dishoeck, E. F. 2007, A&A, 468, 627 (Cited on page 66.)

van der Tak, F. F. S., Ossenkopf, V., Nagy, Z., et al. 2012, A&A, 537, L10 (Cited on page 32.)

van der Werf, P. P., Isaak, K. G., Meijerink, R., et al. 2010, A&A, 518, L42 (Cited on page 33.)

van Dishoeck, E. F., Blake, G. A., Jansen, D. J., & Groesbeck, T. D. 1995, ApJ, 447, 760 (Cited on pages 117 and 138.)

Verstraete, L., Leger, A., D'Hendecourt, L., Defourneau, D., & Dutuit, O. 1990, A&A, 237, 436 (Cited on page 9.)

Vinogradoff, V., Duvernay, F., Danger, G., et al. 2013, A&A, 549, A40 (Cited on page 126.)

Wakelam, V., Smith, I. W. M., Herbst, E., et al. 2010, Space Sci. Rev., 156, 13 (Cited on pages ix, 43 and 158.)

Ward, M. D. & Price, S. D. 2011, ApJ, 741, 121 (Cited on page 124.)

Ward-Thompson, D., Kirk, J. M., André, P., et al. 2010, A&A, 518, L92 (Cited on page 5.)

Ward-Thompson, D., Nutter, D., Bontemps, S., Whitworth, A., & Attwood, R. 2006, MNRAS, 369, 1201 (Cited on pages 21 and 22.)

Warren, Jr., W. H. & Hesser, J. E. 1977, ApJS, 34, 115 (Cited on page 17.)

Watanabe, N. & Kouchi, A. 2002, ApJ, 571, L173 (Cited on page 59.)

Watanabe, N., Nagaoka, A., Shiraki, T., & Kouchi, A. 2004, ApJ, 616, 638 (Cited on page 59.)

Whalen, D. J. & Norman, M. L. 2008, ApJ, 672, 287 (Cited on page 21.)

Wiklind, T. & Combes, F. 1996, Nature, 379, 139 (Cited on page 136.)

Winn, J. N., Kochanek, C. S., McLeod, B. A., et al. 2002, ApJ, 575, 103 (Cited on page 141.)

Wolf, M. 1903, MNRAS, 63, 303 (Cited on page 17.)

Wolfire, M. G., McKee, C. F., Hollenbach, D., & Tielens, A. G. G. M. 2003, ApJ, 587, 278 (Cited on page 1.)

Wootten, A. 1989, ApJ, 337, 858 (Cited on page 137.)

Wyrowski, F., Schilke, P., Thorwirth, S., Menten, K. M., & Winnewisser, G. 2003, ApJ, 586, 344 (Cited on page 93.)

Young, K. E., Lee, J., Evans, II, N. J., Goldsmith, P. F., & Doty, S. D. 2004, ApJ, 614, 252 (Cited on page 57.)

Zhang, Y., Kwok, S., & Nakashima, J.-i. 2009, ApJ, 700, 1262 (Cited on page 44.)

Zhou, S., Jaffe, D. T., Howe, J. E., et al. 1993, ApJ, 419, 190 (Cited on page 17.)

Zhu, C., Krems, R., Dalgarno, A., & Balakrishnan, N. 2002, ApJ, 577, 795 (Cited on page 31.)

Ziurys, L. M., Apponi, A. J., & Phillips, T. G. 1994, ApJ, 433, 729 (Cited on page 31.)